Tectonics and Magmatism in the Basin and Range Province of the Western United States

Thesis

Tectonics and Magmatism in the Basin and Range Province of the Western United States

A thesis submitted for the Degree of Doctor of Philosophy

TIMOTHY KEITH BRADSHAW

Department of Earth Sciences
October 1991

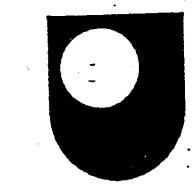

ProQuest LLC
789 East Eisenhower Parkway
P.O. Box 1346
Ann Arbor, MI 48106 - 1346

ABSTRACT

The nature and geochemistry of Miocene magmatism coeval to major extension is studied in detail along the Colorado River between 34-36°N. A tectonomagmatic model is proposed and developed into a general model for the Basin and Range.

Mafic magmas are divided into three groups on the basis of geochemistry: group 1 (most recent) magmas have [Nb/La] >1, and Sr and Pb isotope ratios indistinguishable from OIB, these basalts are thought to derive by ≤10% melting of an asthenospheric source; group 2 & 3 magmas have [Nb/La] <1 and elevated Sr and Pb isotope ratios suggesting a sub-continental lithospheric mantle (SCLM) source. Group 3 magma geochemistry is rather variable, but consistent with an increasing degree of partial melting (1-14%) of a trace element enriched garnet lherzolite source with time. Group 2 magmas have HREE, Y and Sc enriched relative to groups 1 & 3, although relatively depleted LILE and LREE. It is argued that the group 2 & 3 sources are related by depth and that melting in the SCLM progressed to shallower, less enriched, levels with time.

Intermediate to high silica magmas display a positive $^{87}Sr/^{86}Sr$ vs. SiO_2 correlation and evolution to moderately alkaline compositions. Fractionation and AFC processes are insufficient to replicate the observed geochemical variations, instead these magmas are modelled by binary mixing between mafic and silicic endmember melts. The distribution and volume of these 'hybrid' magmas suggests that a ductile melting zone developed in the middle crust, which dominated the Miocene crustal extension.

Geophysical evidence, combined with plate tectonic reconstructions and the changes in magma geochemistry with time, indicate that plate tectonics was the driving force behind extension and magmatism. The influence of a mantle plume is thought to be unnecessary, rather SCLM melting was initiated by heat input from the asthenosphere as it re-equilibrated to fill the 'void' left by the northward migration of the Farallon Plate beneath the W. USA.

ACKNOWLEDGEMENTS

I would first like to thank my supervisors Chris Hawkesworth and Gail Mahood, but particularly Chris for ideas, criticisms, cryptic comments and for generally letting me get on with it. A number of other people have also (helpfully ?) influenced the science herein, including: Jon Davis, Simon Inger, Janet Hergt, Beatrice Luais, Tim Elliott, and Phil Gravestock. Without doubt, Phil deserves the greatest credit, if only for staying interested throughout.

Thanks also to: Pete Webb, Tim Brewer and John Watson, for XRF data; Nick Rogers, for INAA; Kay Chambers and the rest of the cutting room crew, for more than enough thin sections; and, Mabs, Frank, Peter van Calsteren, Tim and Janet, for at least trying to make the isotope lab a bearable experience. Phil Gans, Gail, Eugene Smith and David Ormerod helped out a great deal whilst I was in the States.

Numerous people deserve a mention for maintaining morale (if not morality), including all the people I've played squash and tennis against (particularly Mark George and Phil Wilby), and those who turned out for the six-a-side cricket. Of special 'merit' are: Marcy (excellent entertainment value in the office); Andy and Jim for putting up with me at home; Janet, for chats 'in the bath' (!!); Sam Jones, for arguing politics; Sara, for intriguing hair cuts and fine chocolate brownies; Trasher, Yatesy and everyone else for enjoyable summer schools; and the departmental grapevine for rumour control. All the aforementioned plus Dave Jackson, Kate, Leon, Arlëne, Dentinho, Simon Lomas, Jugsy, J-D-P, etc. etc. for helping me drink away much of my grant over the last three years. Talking of which, this work was funded by a NERC grant, although the Harrahs Del Rio Casino at Laughlin (Nevada) also 'contributed' to fieldwork expenses.

Finally, I wish to thank my parents (and the rest of my family), for always providing encouragement, 'Red Cross' parcels, good food, and for never doubting my decision to do a Phd. I promise to try and get a proper job now!

Plate 1. Lake Havasu along the Colorado River, Arizona.

"Another day in Paradise....?"

CONTENTS

CHAPTER 1a Introduction

CHAPTER 1b Fundamentals of geology in the W. USA

CHAPTER 2 The Colorado River Trough: regional geology and Cenozoic volcanism

CHAPTER 3 The Origin and Significance of Syn-extensional Volcanism in the Colorado River Trough

CHAPTER 4 A progressive melting model for basaltic volcanism in the Colorado River Trough of the W. USA

CHAPTER 5 Extension and Magmatism in the Basin and Range Province, W.USA: a Role for Mantle Plumes?

CHAPTER 6 The adaptation of Pearce Element Ratio diagrams to complex higher silica systems

CHAPTER 7 Summary and Concluding Remarks

APPENDIX FIGURES & TABLES

Introduction

"I have found that California is a prodigiously large place"

wrote Josiah Whitney (first director of the California State Geological Survey) when tasked with making a detailed survey of the state and its surrounding provinces in 1860. Indeed it is, and along the whole eastern margin of the state (and up to 1300km east of that) lies probably the world's largest area of intracontinental extension that is currently sub-aerial, and therefore accessible. Not surprisingly this area (known as the Basin and Range because of its typical physiography) has been subjected to almost every conceivable method of geological survey since Josiah Whitney's time. However, understanding how the extensional province works still presents a major scientific challenge.

Although the province continues to extend, the most intense period of crustal extension occurred earlier in the Cenozoic and it was accompanied by voluminous magmatic activity. While structural and seismic surveys have allowed geologists to unravel the extensional history of the Basin and Range from a retrospective point of view, the magmatism coeval with extension presents an opportunity to investigate the role of both the crust and mantle *during* extension. For example, whether the lithospheric mantle extended as well as the crust, and whether the crust and/or the lithospheric mantle and/or the asthenosphere melted to produce the magmatism. Thus, this thesis presents a geochemical study of some of the syn-extensional magmatism, and interpretations are made about how the extension and magmatism may have been linked.

The main area studied is the Colorado River Trough (CRT), a corridor of major extension along the California-Arizona-Nevada borders. Comparative sample suites were also collected from Yerrington and the Caliente Caldera in the Great Basin (see figures 1 and 2). These three areas were chosen because of favourable access conditions and good existing structural control, at least in terms of the degree of crustal extension. Furthermore, the CRT is unusual in the amount of mafic magmatism that occurred throughout the main extensional

period and, intuitively, it is preferable to study such magmas when attempting to investigate the role of the mantle during extension.

0.1 Objectives

The main objectives of this study are to:

i) characterise the nature and geochemistry of the magmatism within the CRT and to establish the differences and similarities between magmatism in the CRT and the rest of the Basin and Range;

ii) examine how the magmas may have interacted with the crust geochemically and how this may have been influenced by the tectonic state of the crust, or vice versa;

iii) determine the source(s) of the CRT mafic magmatism;

iv) investigate any geochemical changes in this magmatism with time and how they may have related to changes in the nature of extension and/or the magma sources;

v) attempt to answer the fundamental question of whether the extension drives the magmatism, or vice versa;

vi) finally, produce an overall model for the extension and magmatism in the Basin and Range by considering the results of this study and those of previous workers in the Great Basin. This will combine not just geochemical evidence but also plate tectonics and geophysics to provide a fully integrated model.

An additional aim was to have used $^{39}Ar/^{40}Ar$ dating techniques to constrain geochemical changes with time or extension to within the limits of currently available age resolution. Unfortunately the data (to have been provided by Stanford University, California) was unavailable at the time of writing this thesis. However, good stratigraphic control on sample localities and accurate published dates for various marker horizons across the CRT have proven to be sufficient.

0.2 Thesis layout

This thesis has been laid out and written in such a way that much of it can be published with only minor modification. The second part of this chapter provides an insight into the geology of the western United States as a background to this new work. In particular the nature of the Cenozoic crustal extension is reviewed, as are the distribution of Cenozoic magmatism and some of the models for magmatism in the Basin and Range.

Chapter 2 is written in the style of a 'United States Geological Survey Open File Report' and provides a detailed account of the local geology and Cenozoic magmatism in the CRT. Chapter 3 examines crust-magma interactions in some detail and considers the nature of crustal extension in the CRT; this chapter is designed for inclusion in the 'Geological Society of America Bulletin'. Chapter 4 (for 'Earth and Planetary Science Letters') concentrates on the CRT basaltic magmatism and the nature of the mantle source. Chapter 5 is written in the style of a contribution for 'Geology' and discusses potential models for the initiation of magmatism, based on the conclusions of the previous chapters, and relates this to plate tectonics.

Chapter 6 is already in press with 'Contributions to Mineralogy and Petrology'. This chapter covers background information about Pearce Element Ratio (PER) modelling, a technique that is used in Chapter 2 to assess the importance of fractionation in the evolution of CRT magmas. The application of PER models is discussed and improvements to the general methodology of their use are proposed. A combined major and trace element model for the CRT magmas is then suggested which is comparable to the results of more traditional trace element modelling presented in Chapter 3.

Points raised in the preceeding chapters are briefly summarised in Chapter 7, accompanied by some concluding remarks about Cenozoic magmatism and extension in the western United States in general.

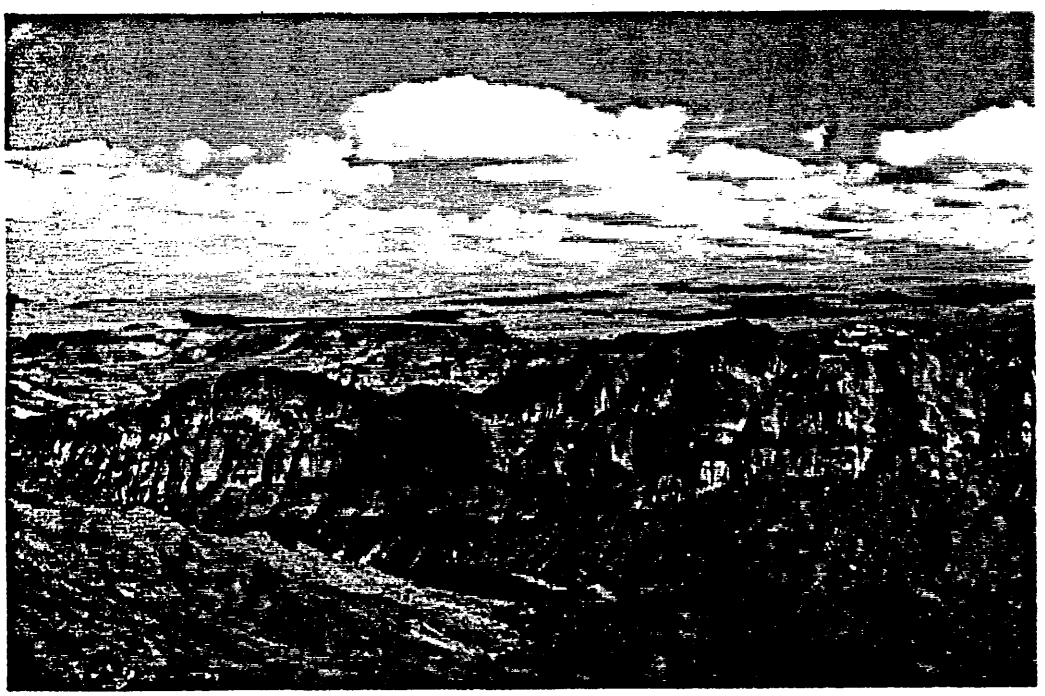

Plate 2. A view looking east across the Colorado River Trough from above the Oak Creek Canyon in the Eldorado Mountains. The Grand Wash Cliffs on the edge of the Colorado Plateau are just visible in the far distance, and the flat topped hill in the middle distance is Malpais Mesa (capped by a post-extensional basalt flow). The striped cliff in the foreground is composed of various cooling units of the Tuff of Bridge Springs, a late syn-extensional eruption. The dissected topography and red-brown exposure of volcanic rocks in the remainder of the photograph is typical of the Cenozoic extensional provinces.

Fundamentals of geology in the western USA

1.1 Introduction

In this part of the chapter, a summary of the geological history of the western United States is presented. Pre-Cenozoic geology is outlined in terms of tectonic provinces and then the general aspects of Cenozoic extension and volcanism are described. It is intended that this should provide an insight into the complex fabric of the continent and how this might influence later tectonics and magmatism. The possible relationship of structural development within the continent to the wider plate tectonic framework is also discussed. Finally, published models for the distribution of Cenozoic extension and volcanism are considered and a general model for the Great Basin is proposed. Subsequent chapters will then build on this and attempt to link processes in the Great Basin to those that might be inferred further south.

1.2 Plate Tectonic Framework

Present plate configurations off the western coast of North America are displayed in figure 1a, with a comparative reconstruction for 52Ma in figure 1b (Engebretson et al 1985). The second of these diagrams represents the fairly stable tectonic condition between the end of Cretaceous compression and the onset of Cenozoic extension. As such, this is the basic framework around which models linking plate tectonic processes to Cenozoic intra-continental events must be constructed. The development of these plate configurations and their influence on Cenozoic magmatism and tectonics will be discussed throughout the following sections and in Chapter 5. However, the important characteristics of the plate motions since 150Ma are summarised in table 1.

A long period of steep-angled subduction ended at ≈80Ma and was abruptly followed by

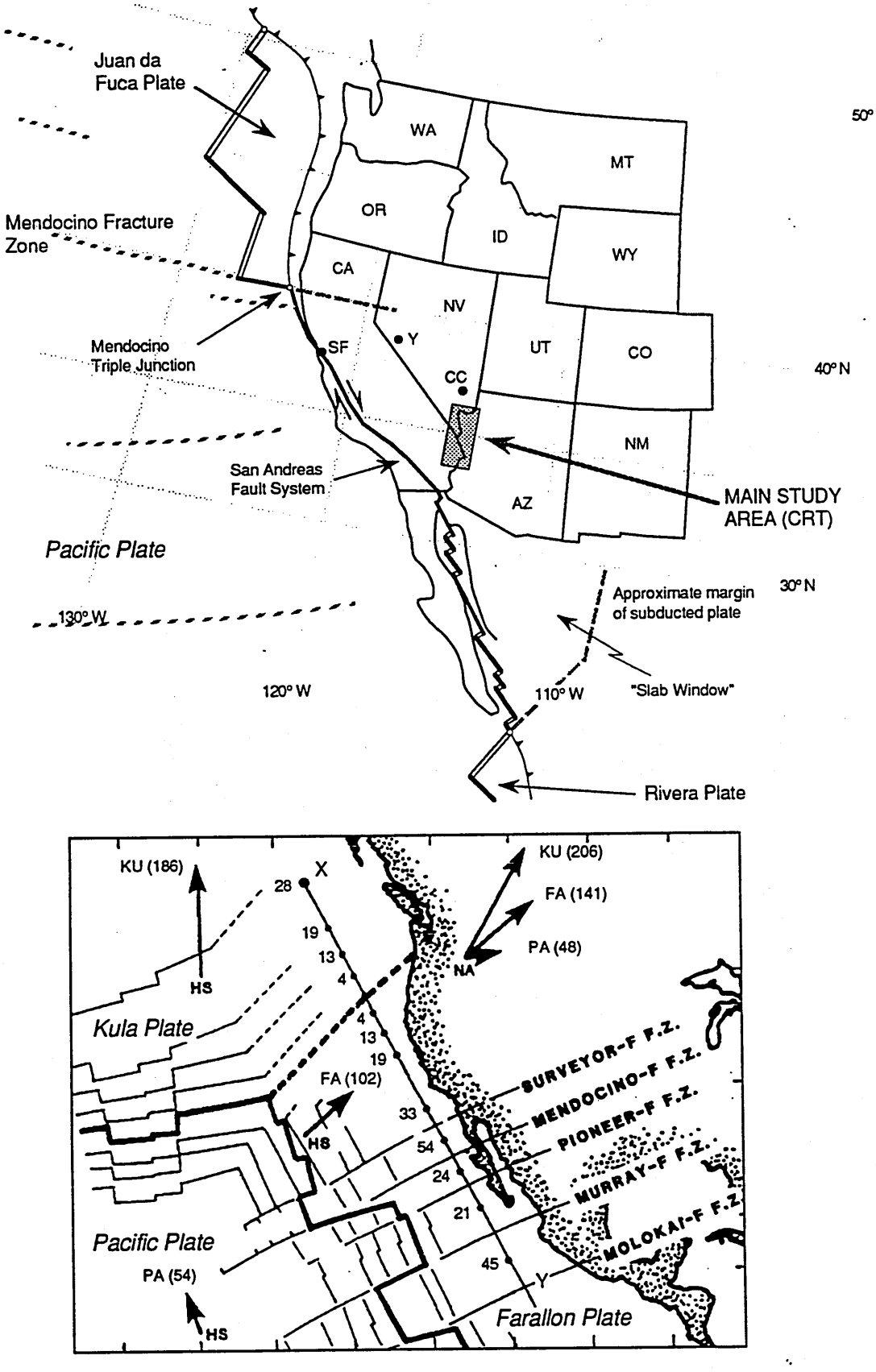

Figure 1a. Current plate tectonic framework of the west coast of North America (adapted from Engebretson et al 1985) showing the Colorado River Trough (CRT), Yerrington (Y) and the Caliente Caldera (CC). SF=San Fransisco. **1b.** Plate reconstruction for 52Ma indicating relative plate motion directions and rates (in brackets; km m.y.$^{-1}$) relative to the hotspot reference frame, HS, and the North American Plate, NA (Engebretson et al 1985). Numbers along X-Y line are the approximate age (m.y.) of the Farallon Plate (FA) being subducted at that latitude at 52Ma. KU= Kula Plate, PA= Pacific Plate.

shallow-angle subduction and more rapid plate convergence. Increase in oceanic plate activity at this time appears to have been a global phenomenon. In the western United States

Time (Ma)	Age of plate subducting at latitude of San Francisco (my)	Westward motion of N.America (km/my)	Convergence rate with Farallon Plate (km/my)	Latitude of Mendocino Fracture Zone	Main geological events in the western US.
0	-	10	40	40°N	
10	15	10	40	36·5°N	*Extensional Orogeny*
25	10	15	45	32°N	28Ma MTJ develops
50	35	45	150	25°N	
75	125	25	110	-	*Compressional Orogeny*
100	150	30	80	-	
150	?	30	10	-	

Table 1. Plate motion data from Engebretson et al (1984; 1985), Oldow et al (1989), based on the global hot-spot reference frame.

it was coincident with the Sevier/Laramide compressional orogenies, which continued until ≈55Ma (Dickinson et al 1988). Subsequent to this, the convergence rate slowed significantly as the age (and therefore the thickness) of the oceanic plate at the subduction zone reached a minimum. It is predicted that these changes induced a relative tensional regime in the western North American Plate, the timing of which roughly corresponds to the period of the Cenozoic extensional orogeny. It is therefore likely that the two are genetically linked.

At ≈28Ma the Mendocino Fracture Zone and Farallon Ridge arrived at the subduction zone, generating the Mendocino and Rivera Triple Junctions as subduction continued. Since that time, convergence of the Farallon Plate with North America has been oblique and thus the Pacific Plate is now in direct contact with the North American Plate along a lengthening strike-slip boundary. As a result of this there is also an area of the western United States which does not have subducted oceanic plate beneath it at present; the "slab window" of Atwater (1970), figure 1a. Subduction of the remaining Farallon Plate fragment, the 'Juan Da Fuca Plate', continues today beneath the active Cascades Range arc of Oregon,

Washington and British Colombia.

1.3 Tectonic Provinces

Western North America lies in part of the 'Cordilleran' mobile belt stretching from southern Chile to northern Alaska. In the western United States it can be divided into two major provinces with rather different tectonic histories: the Coastal Province and the Foreland Fold Belt (figure 2). The Foreland Fold Belt effectively corresponds to the true continental western United States, established during the Pre Cambrian and Palaeozoic. The Coastal Province then developed on the western margin of this from the early Mesozoic.

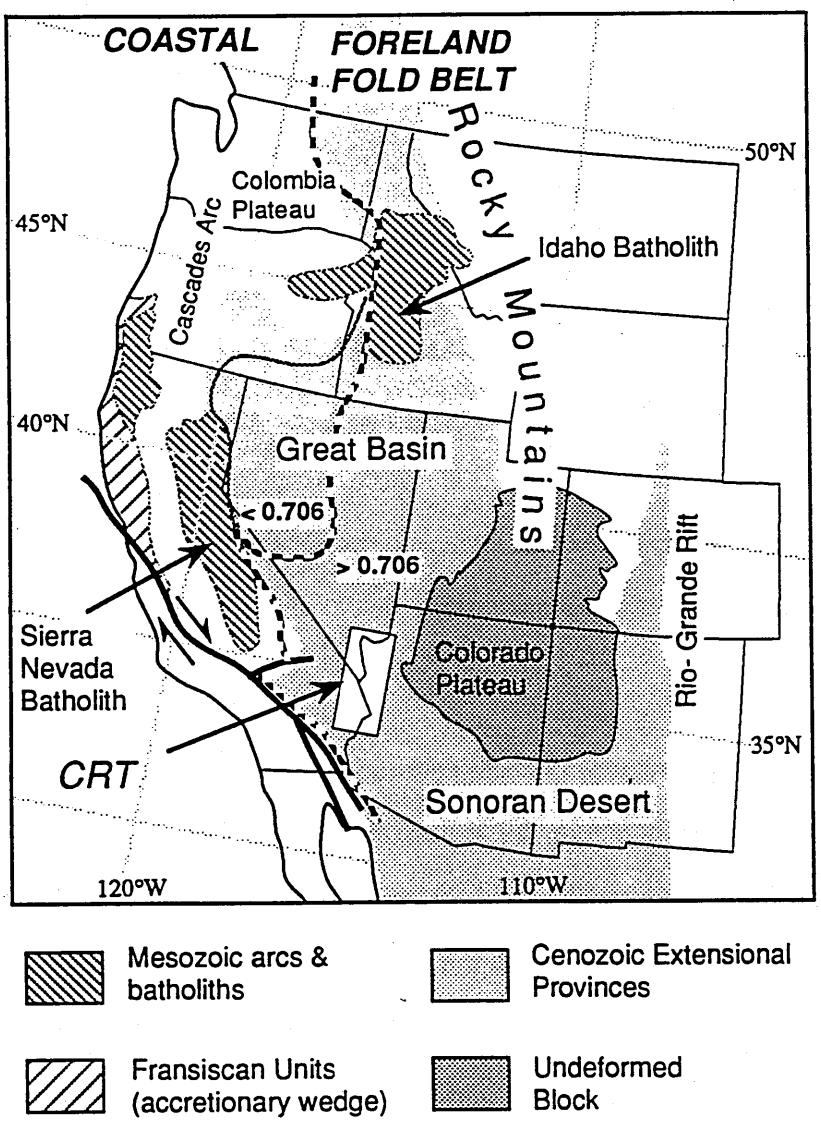

Figure 2. Tectonic provinces in the western United States. The Basin and Range Province is comprised of the Great Basin and Sonoran Desert regions. The hatched line represents the western limit of the Pre Cambrian basement based on Sr isotope determinations (see text). This generally defines the division between the Coastal Province and the Foreland Fold Belt, except in northwest Nevada where the division is to the west of the Sonomia terrain (see section 1.3.2b) marked as the shaded line.

1.3.1 Coastal Province

The Coastal Province provides a record of the subduction of the Farallon Plate during the Mesozoic and Tertiary. However, units within it may be significantly older because the province has effectively grown by the processes of allochthonous terrain accretion since the early Triassic (Coney et al 1980; Ben-Avraham et al 1981). Amongst the terrains, discrete arc (cf.Yerrington district, Nevada), fore arc (Fransiscan units), ophiolitic, and complex continental units can be recognised. The latter of these is represented by the Wrangelia Super Terrain (Saleeby 1983) which is a composite of arc and sedimentary basin sequences developed on Carboniferous to Ordovician aged basement.

In response to oblique subduction, dextral strike slip tectonics have been dominant in the province throughout the Cenozoic. This has resulted in the disruption and northward lateral displacement of the terrains, often over thousands of kilometres (Oldow et al 1989, and references therein).

Close to the eastern margin of the accreted province, a continental volcanic arc developed during the Jurassic and became prominent between 125 and 80Ma (Oldow et al 1989). The core of this arc is now exposed as the Sierra Nevada Batholith; a composite of chemically distinct granodioritic units and smaller dioritic to granitic plutons, collectively termed 'granitoids'. The Idaho Batholith is a more northerly equivalent of this, developed east of the Blue Mountains accreted island arc terrain from 90-75Ma (Clarke 1990).

Apart from in the batholith regions, recent seismic and gravity evidence (Couch and Riddihough 1989) suggests that the average crustal thickness throughout the Coastal Province is only ≈ 20km; it is therefore expected that the lithospheric thickness does not exceed ≈60km. Such thicknesses may be present up to 200km inland and, in combination with increased rates of subduction, it is speculated that this could have permitted the much shallower angle of subduction during the late Cretaceous. This certainly influenced the location of Cretaceous crustal thickening and it may also have had repercussions for extension during the Cenozoic.

1.3.2 Foreland Fold Belt

This province includes the Great Basin - Sonoran Desert region, the Colorado Plateau and the Rocky Mountains. The main study area of the Colorado River Trough (CRT) falls within this province.

1.3.2(a) *Stratigraphy*

The most complete stratigraphic record is preserved in the Great Basin (figure 2) but, equally, the principal interpretations can be applied to the other areas as well.

Sedimentary sequences greater than 8km in thickness are developed in east central Nevada (Drewes 1967; Coats 1987) and are interpreted in terms of a NE-SW trending passive continental margin from the Proterozoic to the Triassic (Oldow 1989). Continental basement to this occurs as scattered Precambrian gneiss and granite complexes within the Foreland Fold Belt. However, these are not exposed in the Great Basin region and, therefore, the western extent of the Precambrian basement has to be inferred. A good approximation can be made by considering the time integrated isotopic history of Mesozoic granite plutons that were derived by melting within the continental crust. In this way the original continental margin is defined by the western limit of plutons having initial strontium isotope ratios of >0.7060 (Kistler and Peterman 1973), see figure 2.

The oldest exposed sediments in the Great Basin are Proterozoic to Cambrian quartzites and conglomerates, which are overlain by an almost continuous succession of dolomite formations through the Palaeozoic and into the Triassic (Spurr 1903; Stewart 1980; Oldow et al 1989). In the west the dolomites are interbedded with shales, siliceous mudstones and chert, indicative of a deep water environment on the margins of the continental shelf. Further east these are replaced by siltstones, limestones and evaporites. This proximal (miogeoclinal) facies became established over the whole region by the middle Triassic and, subsequently, sedimentation evolved towards wholly non marine conditions (Coats 1987).

Across the southern Rocky Mts and the Colorado Plateau a shallow interior seaway

(typically ≤200m deep: Ericksen and Slingerland 1990) provided the locus for sedimentation during the Cretaceous. This was initially open to the Gulf of Mexico through Texas but uplift at the end of the Cretaceous disrupted it into a number of discrete basins; principally the Powder River, Uinta and Green River Basins (Dickinson et al 1988).

The Cenozoic was dominated by volcanic activity, particularly in the Great Basin and Sonoran Desert regions where volcanic sequences often attain thicknesses of >2km (see section 1.4). In contrast to this activity, the bulk of the Colorado Plateau remained essentially amagmatic throughout the Cenozoic, apart from two short episodes of ultra potassic magmatism in the Oligocene and in the Pliocene; represented by the Navajo minettes and Hopi Buttes nephelinites respectively (Roden et al 1979; Ehrenberg 1982a; Alibert et al 1986).

1.3.2(b) *Structural geology*

Three compressional orogenic episodes have affected the Foreland Fold Belt during the Phanerozoic (Oldow et al 1989): the Devonian Antler Orogeny; the Permo-Triassic Sonoma Orogeny; and a major late Cretaceous event, the Sevier /Laramide Orogeny. The main Cenozoic extensional orogeny will be discussed in section 1.4.2 and in succeeding chapters.

The Antler Orogeny peaked during the earliest Carboniferous with the closure of the Antler Basin. This basin contained deep water sediments with arc remnants and became emplaced onto the edge of the continental shelf above the Roberts Mountains Thrust. Units of this "Roberts Mountains Allochthon" were then further deformed during the early Triassic by east-directed thrusting related to the collision of the Sonomia Terrain in northern Nevada (figure 3). Initially the Sonoma Orogeny referred just to this event (Speed 1979), but it is now recognised that the continental margin of the western United States began to undergo a major reorientation from as early as the late Carboniferous (Walker 1988).

Oblique subduction initiated a sequence of NW-SE trending left lateral shear zones during the Permian which displaced rocks of the old Antler Basin into the Mojave Desert,

truncating the western margin of the continent. Active subduction zone magmatism is also recorded in the Mojave Desert at this time (Walker 1988; Burchfiel and Davis 1981). A combination of this truncation and the later collision of the Sonomia Terrain, resulted in a new NW-SE directed trend for the continental margin that still persists today.

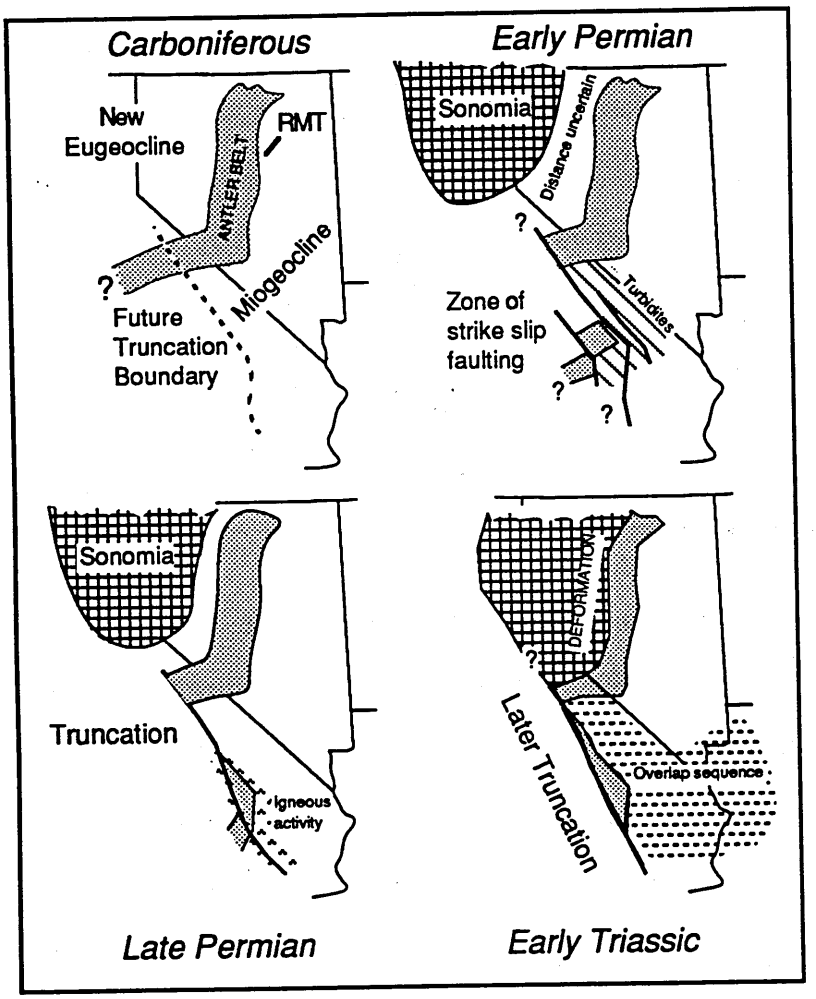

Figure 3. The Sonoma Orogeny and the development of the northwest-southeast trending margin of western North America. The eastern edge of the Antler Belt is the Roberts Mountains Thrust (RMT), see text for details. Figure adapted from Walker et al (1988).

The late Cretaceous Sevier / Laramide Orogeny was the most intense period of intracontinental deformation in the western United States. The Sevier event largely involved thin skinned thrusting, within the sedimentary pile of the Great Basin, as a climax to deformation that began in the middle to late Jurassic (Oldow et al 1989). In the central and southern Rocky Mts this was succeeded by the main Laramide event (75-35Ma, Dickinson et al 1988) which here also affected the previously stable crystalline basement. The deformation associated with both episodes is considered to have developed above a major

decoupling level in the middle or lower crust that may continue as far as 600km eastwards beneath the Great Plains (Oldow et al 1989). A schematic cross section of these structures is presented in figure 4.

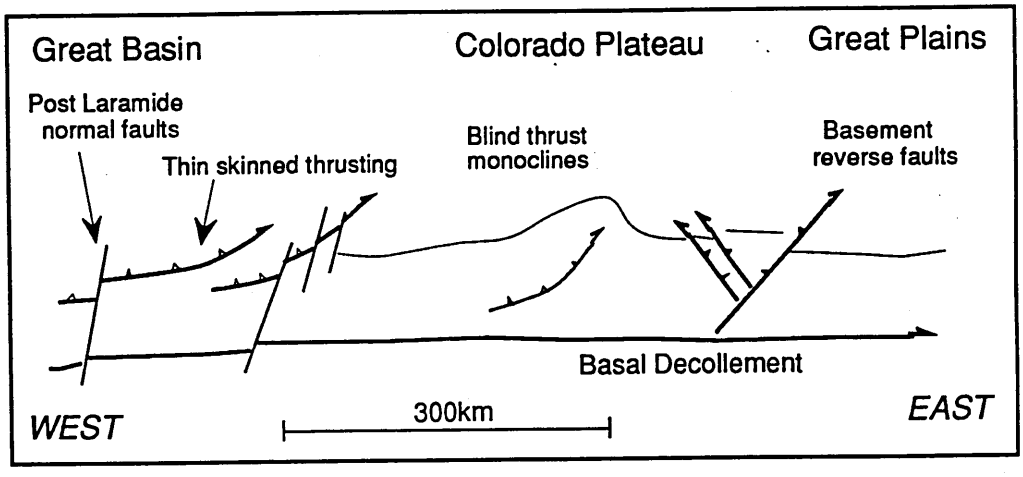

Figure 4. Simplified E-W cross-section from the Great Basin to the Great Plains at approximately 38°N. The basal decollement is suggested to be at 22km depth and further decollements typically occur at or around 9km depth, based on seismic reflection profiles (summarised in Prodehl and Lipman 1989).

By the end of the Laramide Orogeny crustal thickness exceeded 50km (Bird 1984; Hauser and Lundy 1989), indicating crustal thickening[1] factors of between 1·3 and 2 over most of the Province. At this time the region experienced high grade Barrovian style metamorphism and was extensively intruded by peraluminous granitoids. Sr, Nd and Pb isotope ratios (for example, Miller and Bradfish 1980; Farmer and DePaolo 1983) are consistent with derivation of these granitoids from within the continental crust. Patiño Douce et al (1990) consider that melting of miogeoclinal sediments and fertile basement first produced a regional migmatite layer in the middle crust and then mobile granitoid magmas where crustal thickening factors were greatest.

The belt of late Cretaceous compression continues south to Las Vegas and then southeast through the Sonoran Desert. In the Spring Mts (southwest of Las Vegas) a major transition occurs in the tectonic style of deformation, from structures involving supracrustal units to structures predominantly affecting the crystalline basement (Burchfiel and Davis 1988). In

---

[1] Thickening factor = maximum crustal thickness attained / initial crustal thickness.

southeastern Arizona, late Cretaceous deformation is again observed in supracrustal units. However, in the Mojave Desert and in a region just southeast of Las Vegas (approximately coincident with the main study area of this research) there is little evidence of major crustal shortening at this time (Volborth 1973; Oldow et al 1989). Such an abrupt along-strike discrepancy in the degree of shortening between here and the Great Basin necessitates the existence of a major structural break. It has been speculated (Oldow et al 1989) that the Pine Nut strike slip fault observed along the western margin of the Sierra Nevada may continue into this area. But this is not yet substantiated near Las Vegas and it is more likely that a forerunner of the Tertiary conjugate Las Vegas - Lake Mead Shear Zone was responsible.

Current estimates for crustal thickness in the Foreland Fold Belt range from 25-30km in the Basin and Range Province to ≥40km for the Colorado Plateau and the eastern Sierra Nevada (Pakiser 1989).

1.4 The Cenozoic

1.4.1 Patterns of volcanism

The space-time distribution of Cenozoic volcanism provides important evidence for the proposed models concerning the origin of magmatism and extension in the western United States. The distribution pattern represents a constraint that is independent of the geochemistry of the magmatism, but one that must still be satisfied by models based on geochemical interpretations. A number of patterns were initially recognised by Armstrong et al (1969), Lipman et al (1972; see also, Lipman 1980) and Snyder et al (1976), with more detail becoming available through the excellent maps of Stewart and Carlson (1976), and Stewart et al (1977). Their main observation was of a change in the locus of volcanism southwards across the northern Basin and Range with time (figure 5).

Volcanic activity started at ≈43Ma in an arcuate east - west belt across central Nevada and Utah. From 43 to 15Ma this belt migrated south with activity concentrated at its leading (southern) edge. The volcanism was mostly caldera based and the products were dominated

by intermediate to rhyolitic ash flow tuff deposits (Oldow et al 1989; Gans et al 1989; Feeley and Grunder 1991). By 14Ma the volcanic front reached its southern-most limit at ≈37°N and stopped, with the development of the vast Timber Mountain caldera complex (Christiansen et al 1976), and the smaller Kane Springs Wash caldera (Novak 1984).

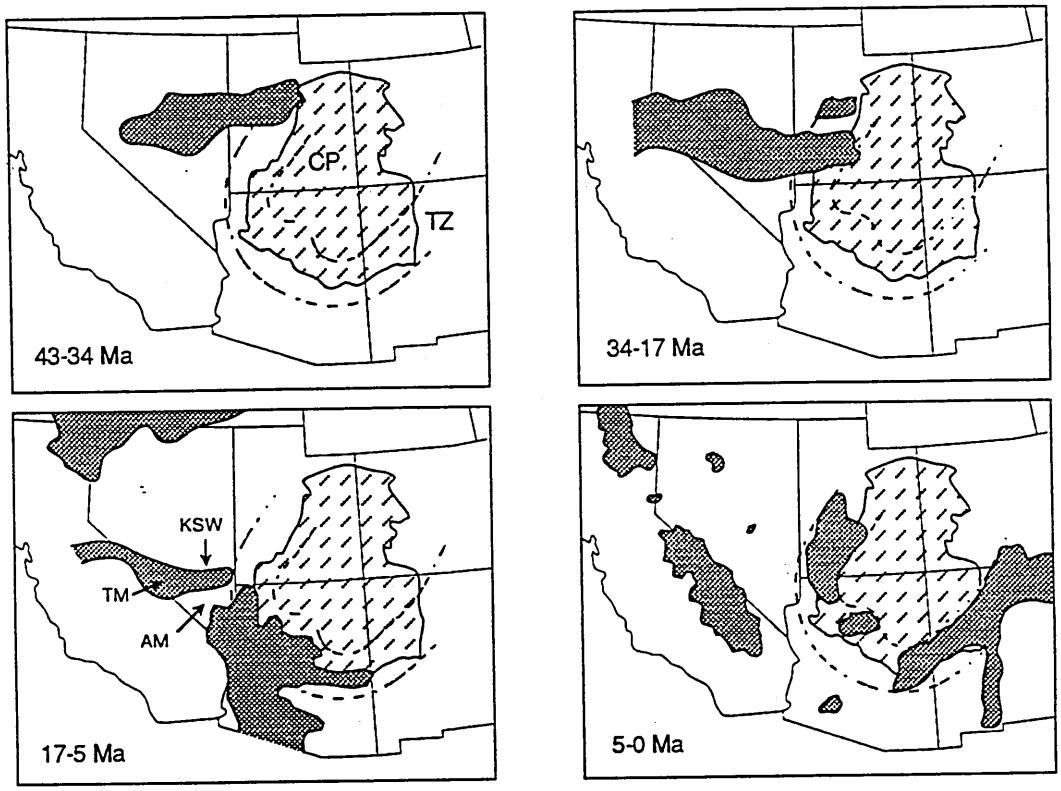

Figure 5. Spread of volcanism (dark shading) in the western United States during the Cenozoic (adapted from Stewart et al 1977 and other references in the text). TZ, the area within the dashed lines, is the transition zone between the Colorado Plateau (CP; diagonal shading) and the extensional provinces. TM= Timber Mountain Caldera. KSW= Kane Springs Wash Caldera. AM= 'amagmatic corridor'.

Between 17-15Ma and 0Ma the locus of volcanism spread out approximately east-west towards the margins of the Great Basin, eventually concentrating along the physiographic transition regions between the Great Basin and the Colorado Plateau and along the Sierra Nevada foothills (Fitton et al 1988). During the Quaternary, volcanism also returned to the middle of the Great Basin at a number of fairly localised centres (such as at Lunar Craters and Yucca Mountain).

The distribution shift at ≈17Ma was also concurrent with a major change in volcanic style towards smaller volcanic vents and predominantly basaltic flows (eg. Leat et al 1988; Ormerod 1988; Fitton et al 1988; Bacon and Metz 1984). Rhyolites were subordinate

except in the Long Valley caldera area of California (Hildreth 1979; Bailey 1987; Wilson and Hildreth 1991) and in the waning phases of earlier Great Basin calderas, such as at Kane Springs Wash until ≈13·4Ma (Novak and Mahood 1986).

From compilations of age data (Glazner and Bartley 1984; Gans et al 1989) the spread of volcanism in the Southern Basin and Range mirrors that observed in the Great Basin. Thus, a south to north migration is indicated between 30 and 10Ma. The Oligo-Miocene sequences consist mainly of volcaniclastic rocks, silicic ash flow tuffs and andesitic lavas. However, compared with the Great Basin, there are more occurrences of andesitic to basaltic flows, particularly along the Colorado River (this study) and in New Mexico adjacent to the Rio Grande Rift (Davis 1991). In the late Tertiary, volcanism became predominantly basaltic or bimodal and, as in the north, it was focussed mainly within the Basin and Range - Colorado Plateau transition zones (Suneson and Luchitta 1983; Perry et al 1987; Bloomfield and Arculus 1989; Fitton et al 1991). Within this region the active centres of volcanism encroached further into the Colorado Plateau with time. In the western Grand Canyon an 80km eastwards shift has been observed since 7Ma (Best and Brimhall 1984). Similar, or faster, rates towards the northeast occur along the southwestern margin of the Colorado Plateau (Wittke et al 1989; Moyer and Esperança 1989; Fitton et al 1991).

Volcanism reached the Lake Mead area by 18Ma (Smith et al 1990; Anderson 1971) where it became localised along the site of the Las Vegas - Lake Mead shear zones with the development of a number of large mafic centres. Active volcanism continued until 5·8 Ma, but the volcanic front did not propagate northwards in this time. Thus, the apparently converging trends of volcanism in the northern and southern Basin and Range provinces did not meet, and are separated by an area north of Las-Vegas (36·2-37°N) that has no history of volcanic activity; the so called 'amagmatic corridor' of Stewart et al (1977).

1.4.2 The nature of extension

Essentially the onset of crustal extension follows the same spatial and temporal patterns as that of the Cenozoic magmatism. Although age correlations (cf. Gans et al 1989, and see

figure 9) suggest that magmatism preceedes extension in any area.

There were apparently two main episodes of extension in the Foreland Fold Belt; an Oligocene-Miocene phase and a late Miocene-Recent phase. The second of these was coincident with the previously mentioned switch to basaltic or bimodal volcanism. Extension was achieved on high angle normal faults that divide the Province into its present characteristic, north-south orientated, depositional basin and mountain range topography (Stewart 1978; Oldow et al 1989). The basins are in fact graben or half graben structures (Hauser et al 1987), which continue to fill with lacustrine, playa and fluvial deposits.

Seismic profiles across the Great Basin reveal that some of the present range bounding faults persist as deep as the lower crust (Allmendinger et al 1983; Hauser et al 1987). However, extension across the Great Basin and other areas subsequent to the basaltic / bimodal volcanism switch amounts to <20% (ß - factor [2] <1·2); for example, Hamilton and Myers (1966) and Stewart (1978) both report a range of extension estimates from 8-18%. In contrast to this, the *average* extension estimate across the same area during the Oligo-Miocene is 100% (ß=2, Hamilton 1987; Gans et al 1989) and in places it exceeds 300% (ß=4, Miller et al 1983; Gans et al 1989; Wernicke et al 1988). The structural morphology of the Oligo-Miocene extension is therefore markedly different to that associated with the later phase of extension.

The characteristic difference is the presence of low angle normal faults, or 'detachment faults' during Oligo-Miocene extension (eg. Wernicke 1981; Miller et al 1983; Rehrig 1986; Howard and John 1987; Davis and Lister 1988; Glazner et al 1989). These may be of great lateral extent and support tectonic offsets of tens to hundreds of kilometres. Generally the faults separate a poorly deformed footwall (the '*lower plate*') from a highly attenuated hanging wall ('*upper plate*'), in which intense imbricate faulting and further low angle

---

[2] Beta - factors are a standard measure of the degree of extension. They relate the change in length of a studied section caused by extension and express it as a fraction of the original length. Thus: $ß = L_1/L_0$, where L_0= original section length, and L_1= length after extension.

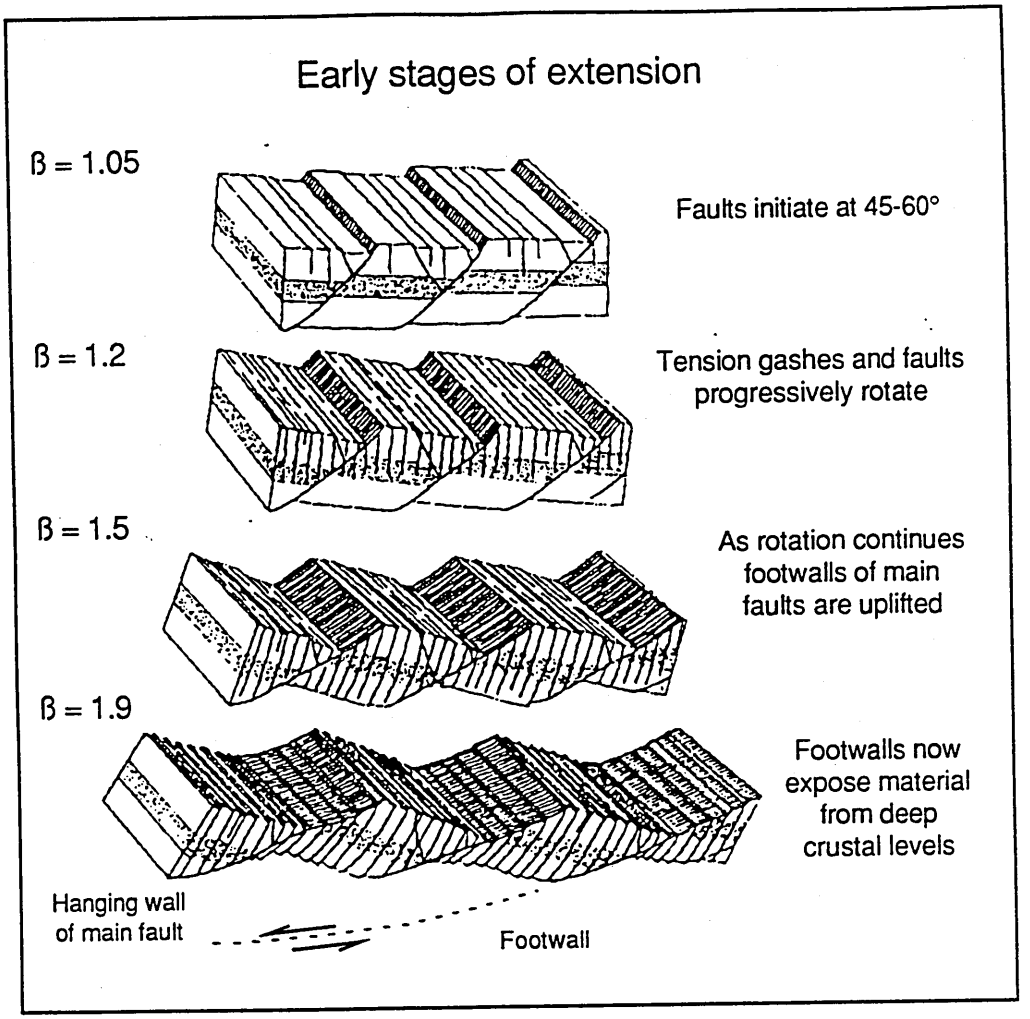

Figure 6. Development of crustal extension by block rotation (after Angelier and Coletta 1983). The hangingwall ('upper plate') of the main fault becomes highly deformed and faults within it rotate relative to the footawll ('lower plate') as extension continues

faults are developed (figure 6). These secondary low angle faults may have initiated as an early generation of high angle faults (at c.60°) that rotated with time, and were then cut by successive fault generations to rotate them further (as in the models of Proffett 1977; Angelier and Coletta 1983; Jackson and McKenzie 1983; McClay and Ellis 1987; Miller 1991). A natural consequence of this type of model is the uplift of the deeper portions of the fault as it rotates, with isostasy providing the main driving force. Thus faults which originally penetrated to the lower crust at moderate to high angles might be expected to uplift and expose material from this depth if they rotated to close to the horizontal. This is one potential model for the formation of major detachment faults as they do typically uplift mid crustal rocks in their footwalls (see references above). Because of the nature of this material, the lower plate units in detachment terrains are commonly termed 'metamorphic core complexes' (figure 7).

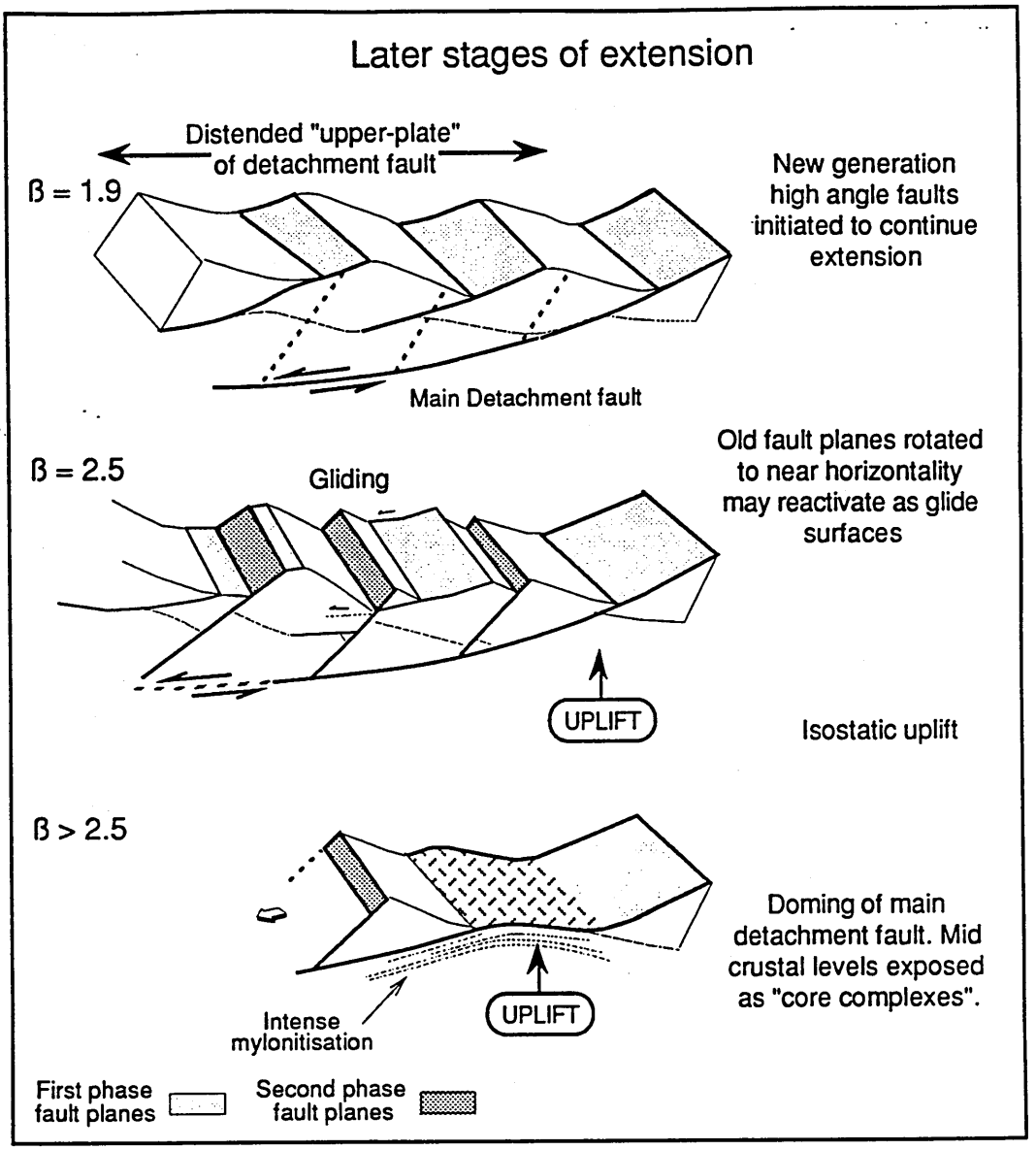

Figure 7. Continued fault development from fig 6. A second phase of high angle faults is initiated. The main phase one detachment fault becomes warped by isostatic uplift, and higher level phase one faults may reactivate as glide surfaces.

However, much controversy still surrounds the formation of low angle normal faults, because it is possible that they can initiate as horizontal features. The Snake Range Décollement in east central Nevada is recognised as one such example by Gans et al (1985), although this is interpreted as a portion of the mid crustal brittle / ductile transition and not a fault *sensu stricto*. Its uplift can be reconciled with the rotation model described above, where the Décollement represents the level at which original high angle faults 'sole-out'.

Contrary to these ideas, a number of workers (eg. John 1987; Davis and Lister 1988)

suggest that all low angle normal faults, including the secondary sets at higher crustal levels, initiate horizontally. However, this incurs tremendous physical problems in the need to supply enough crustal flexure not only to initiate but also to propagate such faults. It *is* possible, but it requires an isostatically uncompensated surface relief of at least 3-5km above the surrounding area prior to extension (Spencer and Chase 1989; Block and Royden 1990). Such extreme relief would have to be very localised (belts 60-120km wide) and this cannot be substantiated in the geological record. Also, no currently active analogue of such horizontal detachment faults has been identified in geophysical sections across the western United States. However, as discussed above, deep penetrating high angle faults are recognised, and thus the rotation-uplift model for general detachment fault formation is favoured in this report (figure 7). By accepting this method, no great difference in the nature of crustal extension needs to be inferred between the Oligo-Miocene and Miocene-Recent phases. Thus, the present high angle range bounding faults could develop into detachment faults under the appropriate conditions.

The distribution of metamorphic core complexes is presented in figure 8, after Wust (1986). It can be observed that they are generally located close to the margins of the Basin and Range Provinces. Because of their nature, it is expected that this also represents the location where maximum crustal extension was attained during the Oligocene-Miocene. If this conclusion can be extrapolated to include the whole lithosphere then the distribution is consistent with extension models proposed by Keen (1985), and summarised in Fitton et al (1988), in which stretching of a large area of lithosphere is predominantly controlled by forces acting at its margins. For the western United States this would relate to stress release at the Pacific margin, resulting from the plate reorganisations outlined in section 1.2.

1.4.3 Modelling the distribution of extension and volcanism

This section briefly outlines some of the possible models which have been proposed for the origin of the extension and volcanism in the Basin and Range Province. These ideas will be developed further in chapters 3, 4 and 5, leading to the presentation of an overall synthesis in chapter 5.

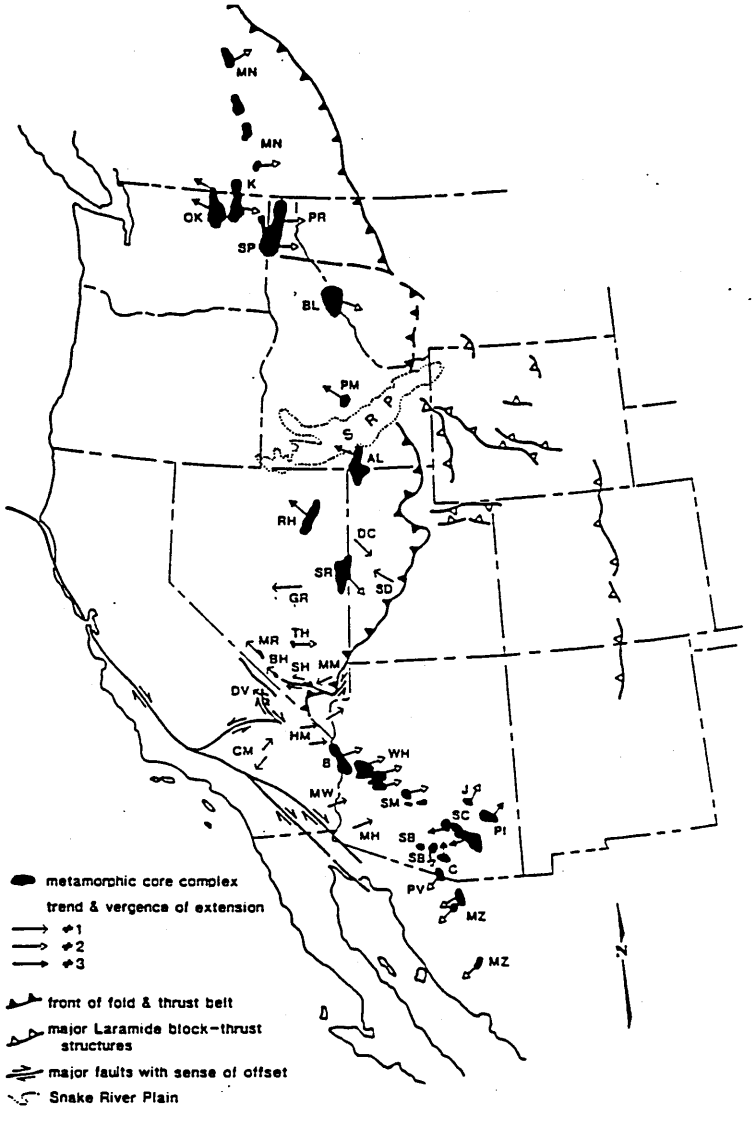

Figure 8. Metamorphic core complex distribution and detachment directions in the Basin and Range Province (after Wust et al 1986). Three criteria have been used to determine detachment directions: a) mylonite fabrics, b) listric fault vergence directions, and c) the assumption that mylonite fabrics develop strongest in the direction of movement. Arrows labelled 1, 2 and 3 represent movement directions determined using criteria a, a+b, and a+b+c respectively. Some of the best studied core complexes are: SR- Snake Range; SC- Pichacho-Santa Catalina; B- Buckskin, Rawhide, Whipple; BH- Bullfrog Hills; HM- Homer Mountains; RH- Ruby Mountains, east Humbolt Range.

1.4.3(a) *The early Cenozoic*

Glazner and Bartley (1984) concluded that the northward migration of volcanism in the southern Basin and Range was genetically linked to the development and motion of the Mendocino Triple Junction (MTJ) at the continental margin (section 1.2). However, Gans et al (1989) correlate the passage of the triple junction / plate edge with the later change to

basaltic and/or bimodal volcanism. This is emphasised in figure 9 (after Gans et al 1989) which displays the relative importance of volcanic activity with time in a sequence of sections from south to north in the Southern Basin and Range. At each locality the bulk of volcanism clearly preceeds the passage of the plate edge (MTJ), but the onset of basaltic or bimodal volcanism always post-dates its passage. Further north, in the Great Basin, Ormerod et al (1988) recognised the passage of the plate edge only as a geochemical change in basaltic magmas, from a lithospheric type to a predominantly Ocean Island Basalt (OIB) type signature after a 2-3m.y time lag. However, data from Gans et al (1989) does suggest that the onset of extension and volcanism in the southern Basin and Range *consistently* pre-dates the passage of the plate edge by ~5 m.y; a relationship which still makes some link between the two an attractive proposition (see chapter 5).

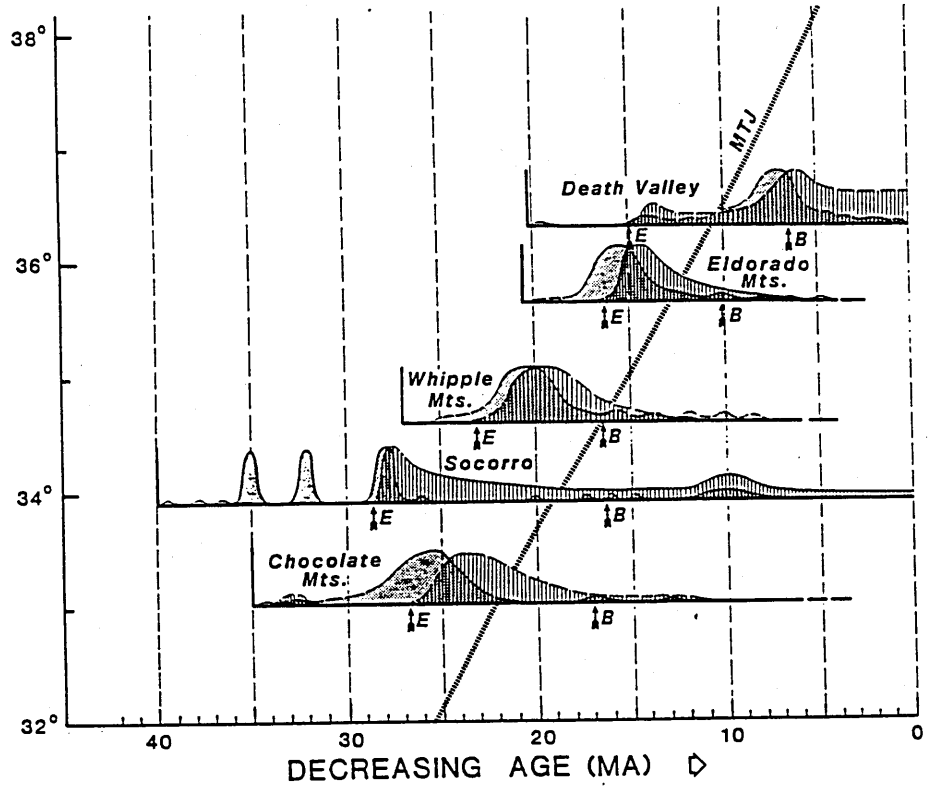

Figure 9. Eruptive rates (shaded) and extensional strain rates (vertical ruling) from selected ranges in the southern Basin and Range, plotted as latitude versus time. E= onset of rapid, high magnitude extension, B= onset of basaltic or bimodal volcanism, MTJ= position of Mendocino Triple Juntion / Fracture Zone with time. See text for details. (Figure adapted from Gans et al 1989).

In the Great Basin the spread of early Cenozoic extension and volcanism is even more difficult to relate to simple plate tectonic processes because the southward migration is

opposite to that that might be predicted from plate motions. Instead, a relationship to previous crustal thickening has been suggested (Sonder et al 1987; Wernicke et al 1987), similar to that proposed for the Himalayas by Dewey (1988), and England & Houseman (1988). The essence of these models, is that thickened continental lithosphere is mechanically weaker (will support less deviatoric stress) than normal lithosphere because its strength profile becomes dominated by that of the crust, its weakest portion (Kuznir and Park 1987). Such lithosphere is unstable and will therefore extend as part of the process of re-establishing a state of stable equilibrium.

However, there appears to be no systematic correlation between the timing or extent of previous crustal thickening and the onset of Tertiary extension and volcanism in the Basin and Range (Gans et al 1989; Gans pers comm). Also, the initial Tertiary magmatism in any area invariably pre-dates extension by a few million years and it is usually the most basic observed in the pre- to syn-extensional sections (Geissman et al 1982; Gans et al 1989). This is consistent with magmatism that is motivated by mantle rather than crustal processes.

In light of this, the early models proposed by Stewart et al (1977), Lipman et al (1972) and Lipman (1980) offer a more tangible explanation for the origin of extension and volcanism in the Great Basin. These models relate the locus of volcanism to a major east-west structural warp in the Farallon Plate which was initiated at ~45Ma, possibly in response to a change in direction of plate motions and the associated decrease in convergence rate of the Farallon Plate with the North American Plate (see section 1.1). If the warp in the Farallon Plate was able to propagate southwards then a situation not unlike subduction zone roll back may have been instigated, with the warp separating an area of deep subduction in the north from one of shallower, more gently dipping subduction beneath central and southern Nevada. Asthenospheric flow into the region 'vacated' by the descending slab might then be sufficient to provide the driving force for extension and volcanism in the Great Basin (figure 10).

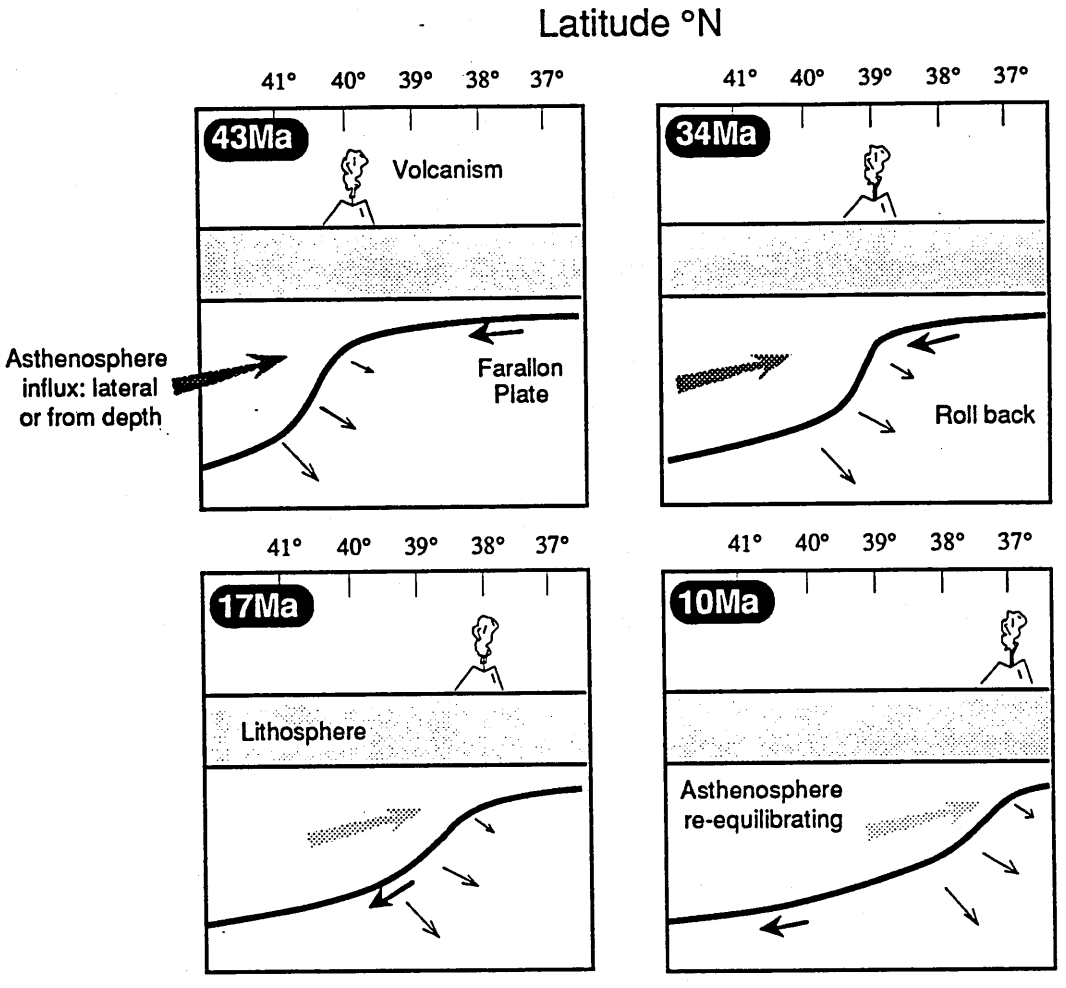

Figure 10. Tectonic model for the onset of extension and volcanism in the Great Basin. Sections are schematic approximately north-south along longitude 120°W. The Farallon Plate (dark line) is shown to be migrating to the north, but subduction is oblique to the section line and there is also a major east directed (into the page) component. A warp in the Farallon Plate makes its southern portion relatively metastable. To re-attain stability the warp develops southwards, effectively 'resubducting' the Farallon Plate to greater depth. Magmatism and extension also progress southwards as asthenosphere from depth flows into higher mantle levels to replace the descending plate; the magmatism may result from decompression melting of this asthenosphere and/or melting of the lithosphere.

1.4.3(b) *The late Cenozoic*

In the late Cenozoic the loci of volcanism moved to the margins of the extensional provinces and it is interesting to note that the centres of volcanism do not coincide with the earlier areas of extreme extension. This can easily be demonstrated by figure 11 which compares figures 5 and 8. The main occurrences of basaltic volcanism in the late Cenozoic clearly define belts adjacent and sub-parallel to the main areas of Oligocene-Miocene extension, but significantly displaced from them towards regions of previously unextended crust.

An analogy to this can be drawn from the distribution of volcanism at some passive continental margins. Here, it is often observed that intense mafic magmatism and the site of oceanic rifting coincide with structural highs in the continental crust *adjacent* to lines of older extensional basins (Mutter et al 1988). The thinned lithosphere of these basins is expected to be relatively strong because the lithospheric strength profile is dominated by that of the mantle (the influence of the weaker crust having been diminished by extension). Thus, initiation of ocean rifting does not occur here but in the thicker, and relatively weaker, crust of the basin margins.

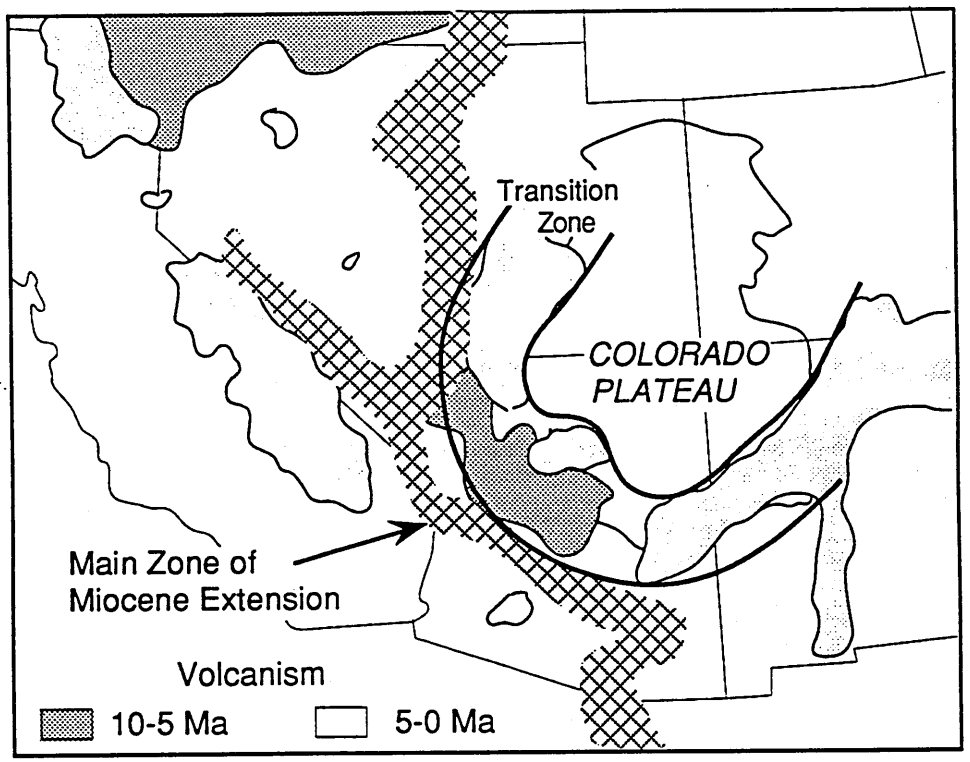

Figure 11. The main zone of early Cenozoic extension and the location of later (≤10Ma) basaltic or bimodal volcanism. The bulk of extension was located towards the margins of the extensional province possibly suggesting a tectonic control at the North American Plate margin (see section 1.4.2). Later volcanism is focussed on the margins of the highly extended zone in regions of relatively unextended, thicker (and therefore weaker), crust.

1.5 Summary

The main points raised in this chapter are concerned with the construction and deformation of western North America during the Phanerozoic. The most significant aspects in relation to this study are the late Cretaceous compressional events and two phases of extension and magmatism which followed during the Cenozoic. The earliest of these Cenozoic events

(Oligo-Miocene in age) was a period of intense extension dominated by the uplift of mid-crustal material beneath 'detachment faults'. This was accompanied by predominantly trachy-andesitic to high silica magmatism, and it is the geochemistry of these rocks that will be considered in more detail in the succeeding chapters. Changes in the geochemistry of rarer basaltic volcanism from this time, and into the second Cenozoic phase (dominated by basaltic and bimodal volcanism), will also be discussed.

It is also important to note the possible models invoked for the origin of magmatism (and extension) in the Great Basin. These are mostly linked to Plate tectonic processes which will be given further consideration in Chapter 5, where a model for the origin of magmatism and extension in the Southern Basin and Range is proposed.

A summary of the main events in the geological history of the western United States is presented in figure 12, below and on the facing page.

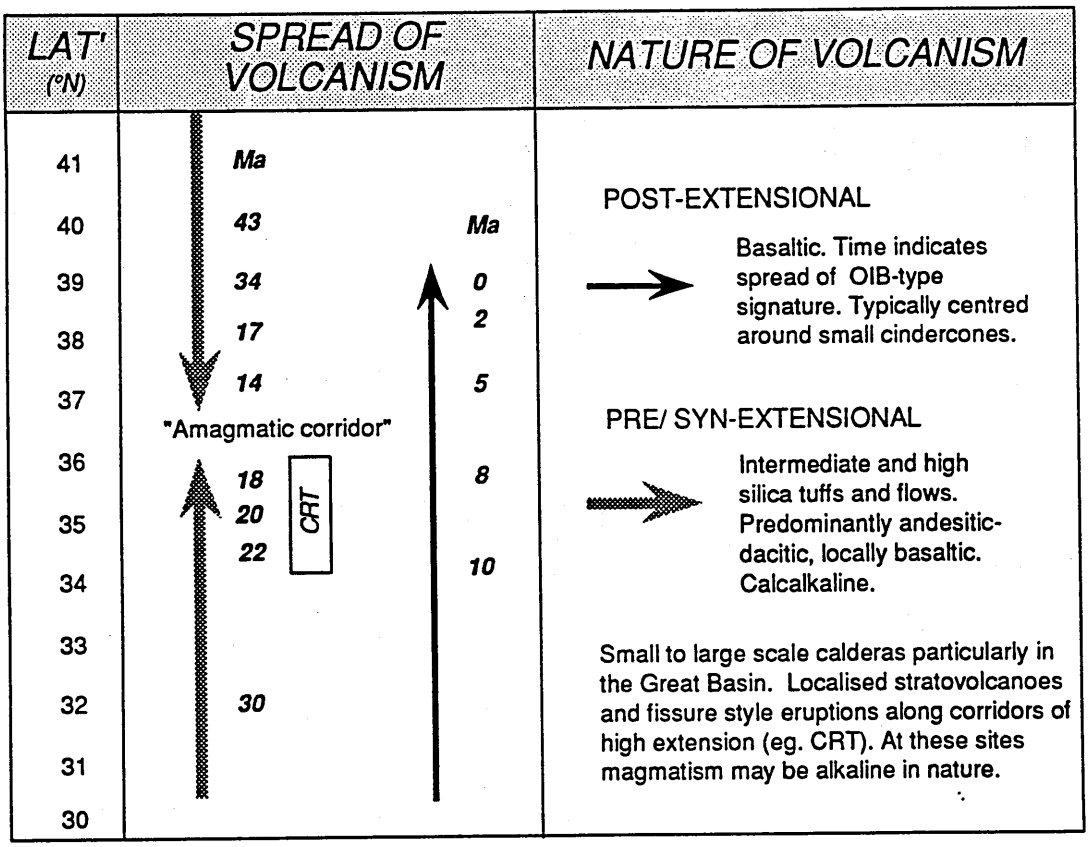

Figure 12a. Detail of Cenozoic magmatic history. **b.** Summary of stratigraphy and tectonic events in the western United States (facing page).

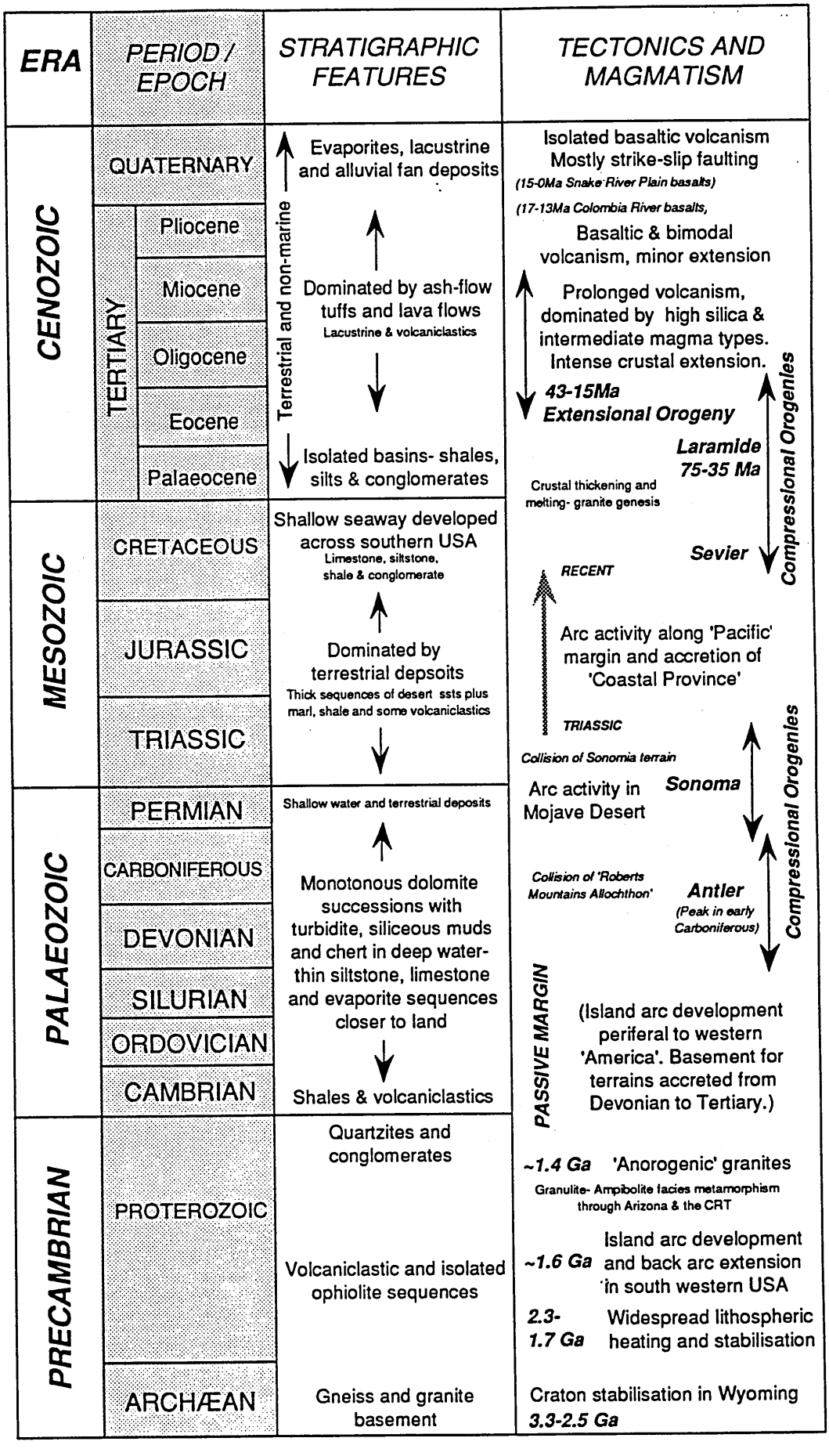
ERA
PERIOD / EPOCH
STRATIGRAPHIC FEATURES
TECTONICS AND MAGMATISM
CENOZOIC
QUATERNARY
TERTIARY
Pliocene
Miocene
Oligocene
Eocene
Palaeocene
Terrestrial and non-marine
Evaporites, lacustrine and alluvial fan deposits
Dominated by ash-flow tuffs and lava flows
Lacustrine & volcaniclastics
Isolated basins- shales, silts & conglomerates
Isolated basaltic volcanism
Mostly strike-slip faulting
(15-0Ma Snake River Plain basalts)
(17-13Ma Colombia River basalts,
Basaltic & bimodal volcanism, minor extension
Prolonged volcanism, dominated by high silica & intermediate magma types.
Intense crustal extension.
43-15Ma
Extensional Orogeny
Laramide
75-35 Ma
Crustal thickening and melting- granite genesis
Sevier
Compressional Orogenies
MESOZOIC
CRETACEOUS
JURASSIC
TRIASSIC
Shallow seaway developed across southern USA
Limestone, siltstone, shale & conglomerate
Dominated by terrestrial depsoits
Thick sequences of desert ssts plus marl, shale and some volcaniclastics
RECENT
Arc activity along 'Pacific' margin and accretion of 'Coastal Province'
TRIASSIC
Collision of Sonomia terrain
Arc activity in Mojave Desert
Sonoma
Compressional Orogenies
PALAEOZOIC
PERMIAN
CARBONIFEROUS
DEVONIAN
SILURIAN
ORDOVICIAN
CAMBRIAN
Shallow water and terrestrial deposits
Monotonous dolomite successions with turbidite, siliceous muds and chert in deep water- thin siltstone, limestone and evaporite sequences closer to land
Shales & volcaniclastics
Collision of 'Roberts Mountains Allochthon'
Antler
(Peak in early Carboniferous)
PASSIVE MARGIN
(Island arc development periferal to western 'America'. Basement for terrains accreted from Devonian to Tertiary.)
PRECAMBRIAN
PROTEROZOIC
ARCHÆAN
Quartzites and conglomerates
Volcaniclastic and isolated ophiolite sequences
Gneiss and granite basement
~1.4 Ga
'Anorogenic' granites
Granulite- Ampibolite facies metamorphism through Arizona & the CRT
~1.6 Ga
Island arc development and back arc extension in south western USA
2.3-1.7 Ga
Widespread lithospheric heating and stabilisation
Craton stabilisation in Wyoming
3.3-2.5 Ga

CHAPTER 2

The Colorado River Trough: Regional geology and Cenozoic volcanism

2.1 Introduction

The Colorado River Trough (CRT) is a relatively low lying physiographic strip in the Sonoran Desert covering the tri state area of California-Nevada-Arizona (figure 1). It stretches 290km north - south between Lake Mead and the town of Parker, and is bounded on the east by the Colorado Plateau. The western margin is defined by the high standing McCullough and New York Mountains in the north, but is less well defined further south. The average elevation for the CRT is below 1075m, compared to its western margin which is above 1500m, and the Colorado Plateau average of 1800m.

Since the Proterozoic the area has generally been in close proximity to the continental margin of North America. This margin was 'active' in the Proterozoic and, after a period of quiescence during the Palaeozoic, it has been active again since the Triassic. During the Miocene the CRT became the locus for an extensional orogeny. Extension exceeded the Basin and Range average of 100% and mid-crustal rocks reached the surface beneath a number of major detachment faults. The extension was accompanied by voluminous basalt to rhyolite volcanism which in places may have reached 5000m in thickness (eg. Anderson 1971).

A summary of this complex geological history is outlined in sections 2.2 and 2.3 with the Cenozoic era being covered in more detail in the second of these sections. The remainder of this report focuses on the nature and geochemistry of the Cenozoic volcanism. Some comparisons are made to volcanism associated with similar extension at Yerrington (west-central Nevada), and to typical Miocene volcanism in the Great Basin.

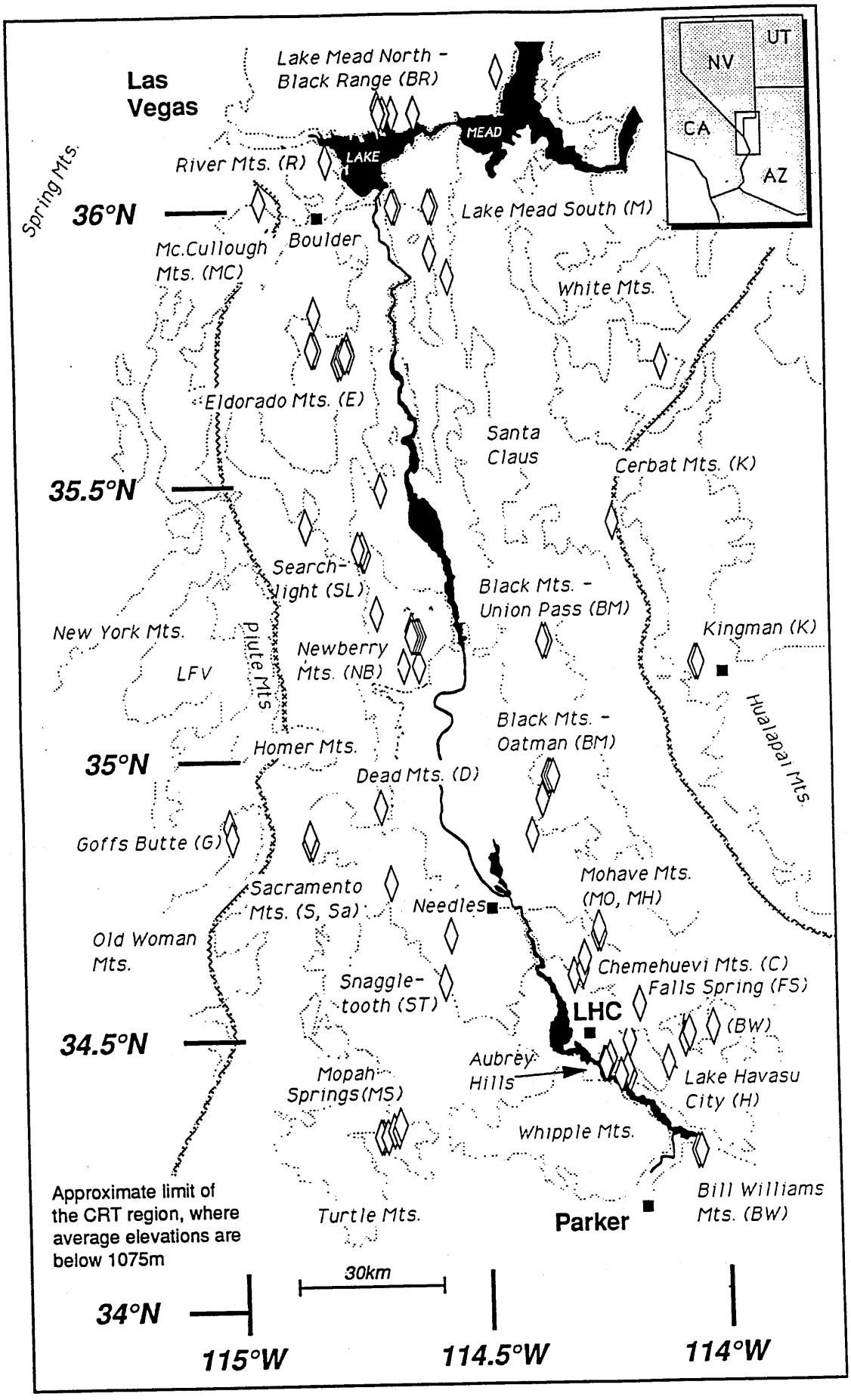

Figure 1. Locality map for sample suites in the CRT region of southern Nevada, California, and Arizona; samples localities as diamonds. The Colorado River and Lake Mead are shown in black. LHC= Lake Havasu City, LFV= Lanfair Valley. Scale approximately 1:1200000.

2.1.1 Sampling and analysis

A total of 167 samples were collected from the CRT region, and a further 28 from the Great Basin. Major and trace element concentrations were determined on all of the samples using XRF techniques and a representative selection has been analysed by neutron activation (INAA), and for strontium and lead isotopes (see Appendix A for analytical information). The results of the detailed trace element and isotopic investigations are presented in succeeding chapters.

The sampling policy was to collect a representative suite along the length of the CRT and also on a number of sections across it (see figure 1), where ever possible covering pre-, syn- and post-extensional lavas. Sampling was biased against volcaniclastic units because of the inherent difficulties both in determining the geochemistry of their primary magmas, and in locating their source vents. Further sampling limitations were introduced by the necessity to avoid localities affected by pervasive alteration.

2.2 Background Geology

Figure 2 is a generalised geology map for the area compiled from published maps of Nevada, Arizona and California. Modifications have been made after Volborth (1973); Davis and Vandendolder (1987); Weide and Faber (1988); and unpublished mapping of E.I.Smith at the University of Las Vegas.

2.2.1 Formation of the Pre-Cambrian basement

The lower Colorado River region has some of the most extensive exposure of Pre-cambrian crystalline basement rocks in the Foreland Fold Belt. As a result, this has been a focal area for detailed isotopic analysis to determine crustal formation ages (principally by Bennett and DePaolo 1987) and, perhaps not surprisingly, this area also proves to be one of the most complex in the western United States (figure 3).

Samarium - neodymium (Sm-Nd) isotope systematics can be used to date the time at which

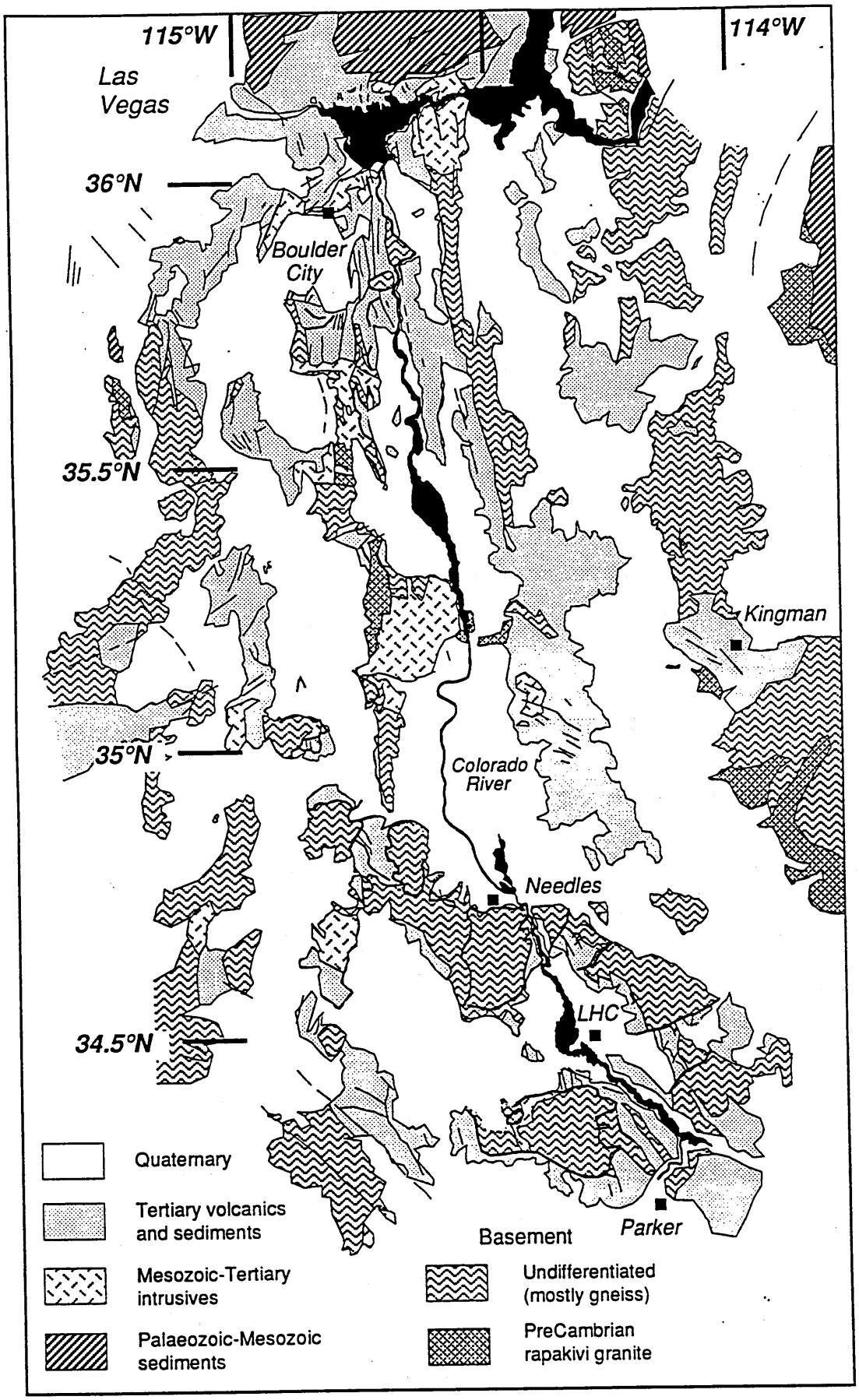

Figure 2. Generalised geology map of the CRT region. See figure 5 for details of structure. LHC= Lake Havasu City. Scale approximately 1:1200000.

the crust (and mantle lithosphere) separated from a convecting mantle source, to leave behind a depleted mantle reservoir. The time at which the initial isotopic compositions of the crust and this depleted mantle reservoir coincide is interpreted as the crust formation age. This is often termed the 'neodymium model age' (T_{DM}). The details and limitations of this Sm-Nd method are presented in Faure (1986), Arndt and Goldstein (1987), and DePaolo et al (1991).

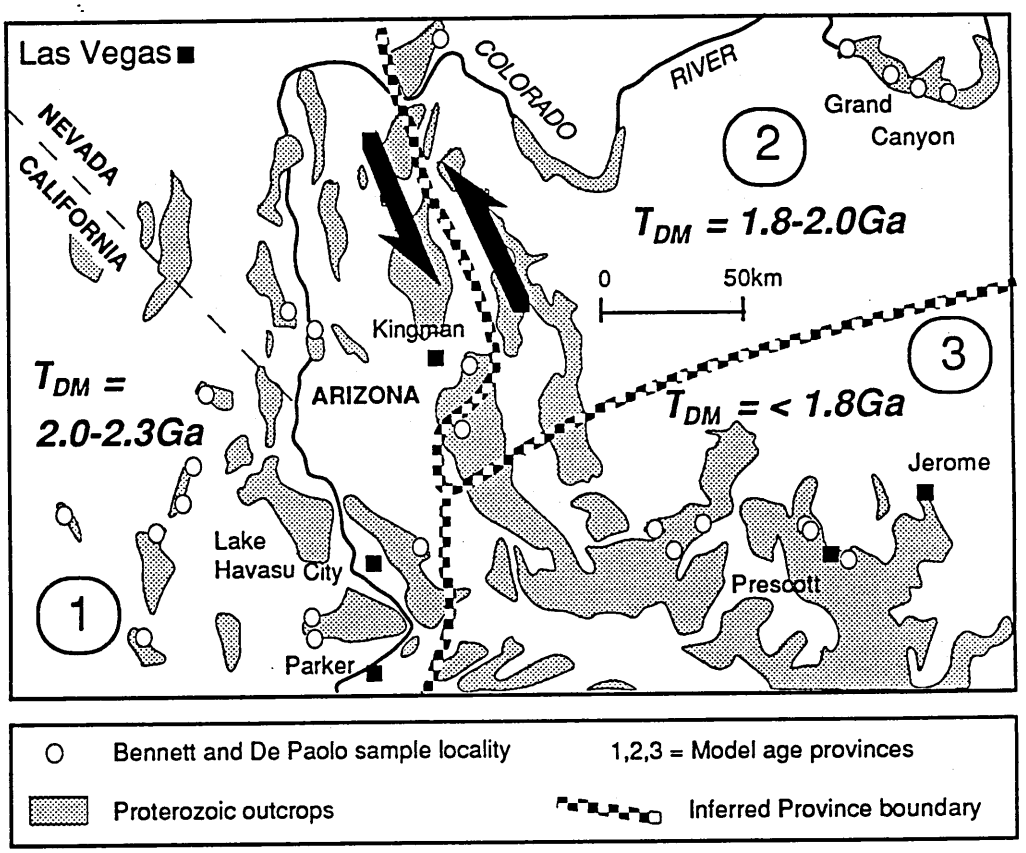

Figure 3. Three distinct crustal provinces meet in the CRT region, based on the evidence of Nd model ages (T_{DM}). A sinestral strike-slip feature is inferred to separate the oldest province in the west from the younger provinces to the east. This figure is adapted from Bennet and DePaolo (1987).

For the Colorado Plateau and southern Arizona, calculated crust formation ages range from 1·7 to 2·3 Ga (Bennett and DePaolo 1987) with a gradual age decrease to the south. However, along the Colorado River the 2·0-2·3Ga 'Province 1', of Bennett and DePaolo, is juxtaposed directly against their 1·7-1·8Ga 'Province 3' (see figure 3). Such a sharp boundary between provinces suggests some structural offset and therefore a north - south trending sinestral strike slip feature has been inferred along this line by Bennett and DePaolo (1987)

This shear or fault probably developed during the Proterozoic, although its existence has yet to be validated in the field. However, it might be anticipated that such a significant crustal lineament would influence younger structural trends in the area. Thus, it may be more than coincidental that the eastern limit of major Cenozoic extension (see figure 5) also follows approximately the same trend as this inferred province boundary.

2.2.2 Nature of the basement rocks and deformation

The Proterozoic basement of Arizona, Nevada and southern California consists mainly of quartzo-feldspathic metasedimentary gneisses and water lain silicic volcanics (Thomas et al 1988). In the Hualapai Mts. a volcanogenic massive sulphide deposit has been recognised (Bennett and DePaolo 1987), suggesting some affinity with an island arc setting. Further to the east, between Flagstaff and Phoenix, an *in-situ* ophiolite sequence has been dated at 1.73Ga (Dann 1991). Over the whole area this early basement was later intruded by porphyritic 'anorogenic' rapakivi granites during a crustal melting event at ≈1·4Ga (Volborth 1973; Bennett and DePaolo 1987; Thomas et al 1988).

Uranium-lead (U-Pb) isotope systematics on zircons consistently reveal gneiss crystallisation ages of between 1·68 and 1·74Ga (Young et al 1989; Burchfiel and Davis 1981; Thomas et al 1988; Bennett and DePaolo 1987; DePaolo et al 1991), which correspond to the main Proterozoic orogenic event in this area. In the Colorado River region the orogeny was characterised by crustal growth and the influx of significant amounts of mantle derived magmas to the crust (DePaolo et al 1991). The resulting distribution of metamorphic facies are displayed in figure 4, after Thomas et al (1988). Along and adjacent to the CRT there is a slight gradation in facies, from granulite in the McCullough Mts. (Young et al 1989) to high amphibolite facies in the Whipple Mts. The grade then decreases to greenschist facies further southeast towards Tucson (Thomas et al 1988). Using garnet - plagioclase - sillimanite - quartz thermobarometry, a temperature and pressure overlap is calculated between the Whipple and McCullough Mts, with results from both areas indicating conditions in the range of 590-750°C and 2-4 kb. The determining

factor between the two facies may therefore be just one of fluid availability (Thomas et al 1988; Young et al 1989).

Overall, the low pressure - high temperature conditions are consistent with metamorphism occurring in a hot shallow crustal environment. This, combined with an active period of crustal growth, has lead to a proposed back arc extensional setting for the Proterozoic orogenic event (Bender et al 1988; Dann 1991).

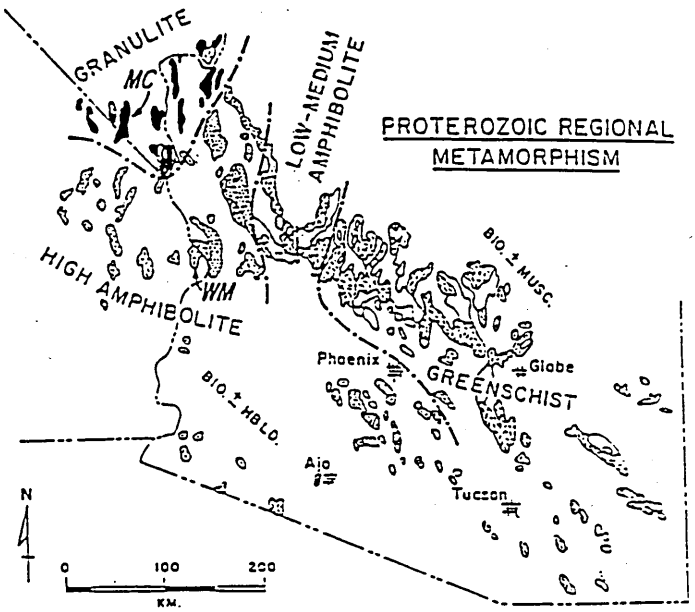

Figure 4. Proterozoic metamorphic facies distribution in the basement rocks of the CRT and southern Arizona (after Thomas et al 1988). Notice that the highest grade facies occur along the Colorado River in southern Nevada. MC= McCullough Mts. WM= Whipple Mts.

2.2.3 Palaeozoic to Early Tertiary

Sedimentary facies and outcrop patterns indicate that a north - south line through the Spring Mts. (southwest of Las Vegas) marked the western edge of emergent land during the late Proterozoic (Burchfiel and Davis 1981). A fairly uniform 1·5km of Palaeozoic sediments (and a more variable thickness of Mesozoic sediments) then covered the area, including the Colorado Plateau (Reynolds et al 1988; Oldow et al 1989).

Arc magmatism commenced in the late Permian, associated with the reconfiguration of the North American plate margin (Walker 1988). It became prominent during the Jurassic with

the position of the arc apparently moving northeastwards (inland) with time (Burchfiel and Davis 1981). The maximum eastward position coincided with the present Newberry and Whipple Mts. up to approximately 70Ma (Volborth 1973; Burchfiel and Davis 1981; Anderson et al 1988), although most of the activity was further to the west. In the Whipple Mts. the core of the arc is represented by the 89±3Ma Whipple Wash suite of granodiorite to tonalite plutons and the 73±3Ma Axtel quartz diorite, all intruded at ≈30km depth (Anderson et al 1988). The Newberry Mts. igneous complex is dominated by a series of large rapakivi granite plutons, with lesser amounts of muscovite granite and hornblende granodiorite (some associated dioritic pods may also be of Cretaceous age). Representatives of each of these have been sampled as part of this study because of their potential as crustal endmembers in the contamination of Cenozoic magmas.

Deformation and metamorphism in the Newberry Mts. during this period of arc activity are limited to minor shear zones and localised heating related to the plutons (Volborth et al 1973; Reynolds et al 1988). However, intra-arc strike slip faults are more prominent in the Mojave Desert to the west, where they are part of a NW-SE trend of similar features from Yerrington to south-central Arizona (Burchfiel and Davis 1988; Busby-Spera 1988). Busby-Spera (1988) considers that this represents a linear graben structure occupied by the volcanic arc between the late Triassic and Middle Jurassic.

The graben acted as a locus for sediment removal from the broad areas of emergence in Arizona and Utah. At Yerrington some marine deposition of terrigenous sands occurred (Proffett and Dilles 1984), but emergence and proximity to the graben permitted complete removal of the sedimentary cover throughout the CRT region. This process continued in the early Tertiary when the CRT formed the northwestern limit of the uplifted Mogollon Highlands block (Reynolds et al 1988). The net result provides a unique situation in the western United States in that subsequent Cenozoic magmatism developed directly onto Proterozoic and Mesozoic crystalline basement rocks.

Late Cretaceous orogenies had a negligible effect within the CRT, but south of Parker structures comparable to those in the Spring Mts. are observed; this is the Maria Fold and

Thrust Belt. The most important regional feature of the late Cretaceous was the apparent underthrusting of a Mesozoic accretionary prism / forearc unit beneath the Mojave Desert (Burchfiel and Davis 1981). Thrusting of this "Rand-Pelona-Orocopia Schist" northeast, below the crystalline continental margin, was coincident with the general shallowing and increased rate of subduction of the Farallon Plate between 80 and 40 Ma (Engebretson et al 1985).

The extent of this schist unit at depth has recently been inferred using oxygen isotope analysis of Cenozoic volcanics that might have been contaminated by passing through it (Glazner and O'Neil 1989). A signature of low $^{87}Sr/^{86}Sr$ ratios but with high $\delta^{18}O$ (9-11‰) is taken as indicative of such contamination. The favoured interpretation for the unit is of an eastward tapering wedge shaped body, underplated beneath the Mojave Desert. But higher $^{87}Sr/^{86}Sr$ and lower $\delta^{18}O$ (7-8‰) values in volcanics from the Mopah Range indicate that the unit probably does not persist below the CRT.

This is important in terms of Cenozoic volcanism because it further simplifies the task of identifying potential crustal contaminants for this magmatism. It has already been noted that sedimentary cover was absent prior to the start of volcanism and that the basement consists predominantly of granulite, which would be unlikely to melt. Therefore, any occurrence of major crustal contamination is likely to be restricted to the mid crust or to lower portions of the upper crust, where melting of Mesozoic granite plutons might provide the contaminant.

2.3 The Cenozoic

2.3.1 Structural fabric of the CRT

A number of workers (eg. Faulds et al 1988; Gans et al 1989; Spencer 1985; Howard and John 1987) recognised that the CRT is approximately coincident with a corridor of extreme east - west extension, figure 5. The northern termination of this corridor is the Las Vegas - Lake Mead Shear Zone which offsets a number of large mafic centres by up to 40km (Weber and Smith 1987). The NW striking part of the shear zone separates the highly extended 'Red Sandstone Basin' in the south from the much less extended 'White Basin' to

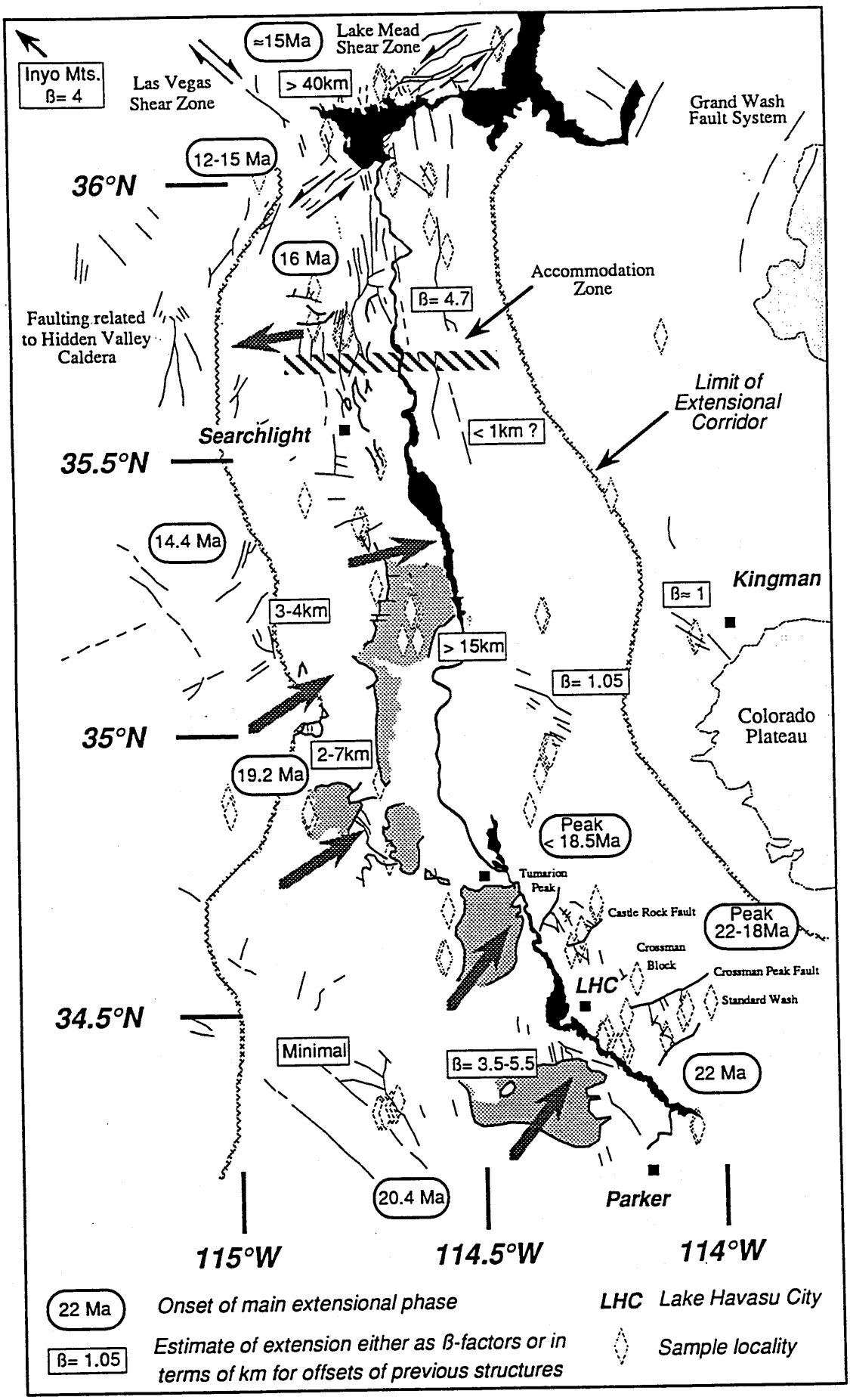
Inyo Mts.
ß= 4
Las Vegas
Shear Zone
≈15Ma
Lake Mead
Shear Zone
> 40km
Grand Wash
Fault System
12-15 Ma
36°N
16 Ma
ß= 4.7
Accommodation
Zone
Faulting related
to Hidden Valley
Caldera
Limit of
Extensional
Corridor
Searchlight
< 1km ?
35.5°N
14.4 Ma
Kingman
ß= 1
3-4km
> 15km
ß= 1.05
35°N
Colorado
Plateau
2-7km
19.2 Ma
Peak
< 18.5Ma
Tumarion
Peak
Castle Rock Fault
Peak
22-18Ma
Crossman
Block
Crossman Peak Fault
LHC
Standard Wash
34.5°N
Minimal
ß= 3.5-5.5
22 Ma
20.4 Ma
Parker
115°W
114.5°W
114°W
22 Ma
Onset of main extensional phase
LHC
Lake Havasu City
ß= 1.05
Estimate of extension either as ß-factors or in
terms of km for offsets of previous structures
Sample locality

←— **Figure 5.** Detail of crustal structures in the CRT region; fine lines represent normal and strike slip faults. Light shading= Colorado Plateau. Dark shading= metamorphic core complexes (see text), with detachment faults marked as thick lines surrounding them. From south to north the core complexes are: the Whipple Mts; Chemehuevi Mts; Sacramento Mts (in three segments); and the Newberry / Dead Mts. A number of other major low angle normal faults (thick lines without shading between) have also been shown. These occur at higher structural levels above the main detachment faults (eg. see figure 6) particularly near Lake Havasu City and in the Eldorado Mts. Large arrows indicate fault vergence direction (the direction of motion of units above the main detachment faults). In the south the direction of movement is towards the northeast or east, but north of a structurally chaotic zone (an 'accommodation zone') in the Eldorado Mts the motion is to the west. Indications of the timing of the onset of extension and the degree of extension are shown in the oblong and rectangular boxes respectively. Data from: Gans et al (1989); Faulds et al (1988); Smith et al (1990); Davis and Lister (1988); Howard and John (1987); Spencer (1985); Weber and Smith (1987); Buesch and Valentine (1986); Neilson (1986); Neilson and Turner (1986); Hazlett (1986); Anderson (1971), Anderson et al (1972); and Smith (1990, perscomm). Scale 1:1200000, 1 inch =30km.

the north (Duebendorfer and Wallin 1991). These authors and Smith et al (1990) model the shear zone as a major transform fault coupled to the Saddle Island detachment fault that is exposed on the western shore of Lake Mead.

It is possible that this shear zone represents an inherent crustal weakness which may previously have been active during the Laramide Orogeny (see Chapter 1b). At that time it apparently prevented compressional strain in the Great Basin from being transmitted into the CRT, whereas in the Tertiary it then prevented extensional strain from being transmitted the other way.

Within the extensional corridor the structural fabric is defined both by the strike of normal faults and of Cenozoic dyke swarms. In the Eldorado and Newberry Mts. these trend approximately north-south, although near Searchlight, some east-west dykes are aligned parallel to a small strike slip fault. A more important strike slip feature cuts east-west through the Eldorado and Black Mts. at c.35·7°N. Although there are very few dykes here, it is a zone of intense faulting and mineralisation representing the boundary between two major tectonic domains. Faulds et al (1988) describe this feature as an accommodation zone separating east-tilted strata (westerly verging extension) in the north, from west-tilted strata (easterly verging extension) in the south.

South of the Newberry Mts. the fault vergence directions vary between 030 and 075. (Respectively: the minimum value for the Whipple Mts. from Davis and Lister 1988, and the maximum value for the Sacramento Mts. from Spencer 1985). Syn-extensional dykes

would be expected to have orientations orthogonal to this direction, and parallel to the axis of maximum extension (eg. strike at 145±20°). However throughout this southern region, syn-extensional dykes strike at c.110±15°. Spencer (1985) considers that this deviation from the expected value is a result of a component of secondary extension, produced as a consequence of the variable main extension direction.

Extension in the early to middle Miocene is characterised by intense normal faulting, block rotation and the development of low angle normal faults. In the CRT low angle faults are observed on a number of scales, from those that involve just high level Cenozoic cover sequences (as in parts of the Eldorado Mts.) to a series of true detachment faults, uplifting deep crustal rocks as metamorphic core complexes. These detachment faults are now exposed in a chain between the Newberry and Whipple Mts, that then continues southeast across Arizona (Anderson et al 1988; Reynolds et al 1988). A schematic cross section through the CRT at roughly 34·5°N is shown in figure 6 from Howard and John (1987).

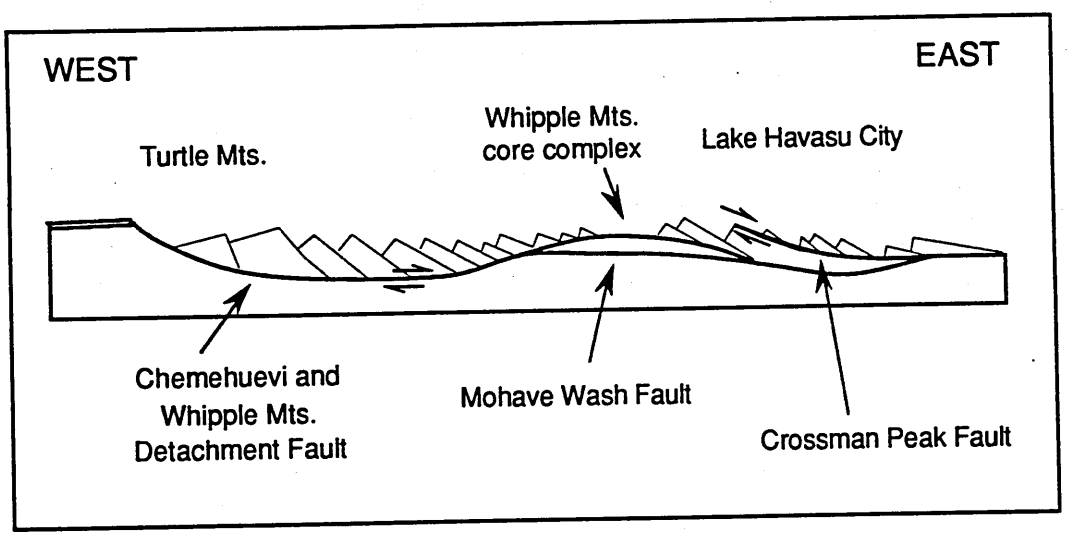

Figure 6. Schematic cross-section through the upper crust, east-west through the vicinity of Lake Havasu City. Adapted from Howard and John (1987). The Crossman Peak fault is probably an early generation high angle fault reactivated as a later glide surface.

2.3.2 The degree and timing of extension and uplift

The onset of extension (and volcanism) is apparently diachronous along the CRT. Extension began at ≈22Ma in the Whipple Mts, 19Ma in the Sacramento Mts. and 16Ma in the Eldorado Mts. In each case the period of extension lasted less than 10m.y. and it often

appears to have peaked over an interval of just 2-3m.y. (cf. Gans et al 1989; Davis and Lister 1988; Gail Mahood *perscomm*). Where no direct dating of tilted strata or fault gouge material is available, the timing of extension can be inferred relative to a constant time marker across the region. The Peach Springs Tuff, which covers the lower Colorado River area and parts of the Mojave Desert and Colorado Plateau, probably has an origin somewhere in the weakly extended Black Mts. (Glazner et al 1986) or in the Lanfair Valley (Hillhouse and Wells 1991) and thus makes a suitable marker. The tuff has been dated at 18.5±0·2Ma using $^{40}Ar/^{39}Ar$ methods (Nielson et al 1990).

Around Lake Havasu City the tuff is often only gently tilted (10-30°) and it may form a sharp angular unconformity with the syn-extensional volcanics below. However, in places it is tilted up to 70° and palaeomagnetic studies reveal tectonic rotations ranging from 37° clockwise to 51° anticlockwise (Wells and Hillhouse 1989). Near Needles, the tuff is prominent as a highly tilted unit with an average dip of between 30 and 60°. Thus it can be inferred that deposition of the Peach Springs Tuff was syn- to post-extensional near Lake Havasu City, but was pre-extensional further north.

In the Whipple Mts. Davis and Lister (1988) calculate c.16±4km of uplift over a period of 2m.y., responsible for exposing mid-crustal levels below a detachment fault surface. The degree of extension here is in excess of 100% (ß factor >2, Davis and Lister 1988), and it may be as high as 250-450% (ß= 3·5 - 5·5) based on the extension calculated for similar structures in the Snake Range of east central Nevada (Miller et al 1983; Gans et al 1985). Similarly, reconstruction of the Anderson (1971) cross section through the Eldorado Mts. reveals an average ß factor of 4·7. However, the amount of extension declines rapidly away from the corridor axis, ß= 1·05 in the Black Mts. at Oatman, and ≤1·5 along the whole western margin of the corridor (see caption to figure 5 for references).

Although most of the extension was concentrated during the early and middle Miocene, high angle normal faults were active along the margins of the CRT in the late Cenozoic (≤10Ma). These faults were particularly associated with the uplift of the Colorado Plateau, which culminated between 7 and 4 Ma (Eaton 1986).

2.3.3 The nature of volcanism

Unlike in the Great Basin where volcanism was predominantly caldera based, only one small caldera structure is identified in the vicinity of the CRT. This is the Hidden Valley caldera in the McCullough Mts, active at c.11Ma (Smith et al 1990). The remainder of the Miocene volcanism in the Lake Mead area is concentrated in three large mafic stratovolcanoes located along the Lake Mead Shear Zone (Weber and Smith 1987; Smith et al 1990). A number of possibly high-level subvolcanic plutons are also recognised here and have been assigned to individual volcanoes on the basis of comparative geochemistry (Weber and Smith 1987; Larsen and Smith 1990). Such Tertiary intrusives, mostly of monzogranite composition, with subordinate diorite and granodiorite, are not recorded elsewhere in the CRT. Neither are volcanic sections of similar thicknesses to the 5000m observed in the Eldorado Mts. (Anderson 1971), and thus both may be consequences of the long term localisation of volcanism along the Lake Mead Shear Zone. The shear zone would have provided both a pathway and focus for volcanism during the Miocene, and may also have participated in the exhumation of intrusive equivalents to some of this volcanism.

On the margins of the CRT much smaller stratovolcanoes are recognised, and even individual cinder cones can be identified in the least extended areas, such as around Kingman. Often the small stratovolcanoes developed rhyolitic plugs in the final stages of activity and these now form prominent spires rising above the surrounding tilt block terrain. They are particularly distinctive in the Black Mts above Oatman and in the Mopah Range (figure 7).

Towards the axis of the extensional corridor, individual volcanic centres cannot be recognised because of the extreme nature of extension. However, Miocene dyke swarms throughout the core complexes are parallel, rather than radial, which suggests that eruptions were of fissure style or based around short lived stratovolcanoes, active over a wide area at any one time. The only occurrence of radial structures in the CRT is in association with the Hidden Valley Caldera (see figure 5).

The general eruptive style for the CRT is therefore considered to be of lava flows (mostly basaltic to andesitic), with explosive volcanism playing a subordinate role. This is in marked contrast to the high silica ash flow volcanism prevalent in the Great Basin during the Eocene-Miocene extensional phase.

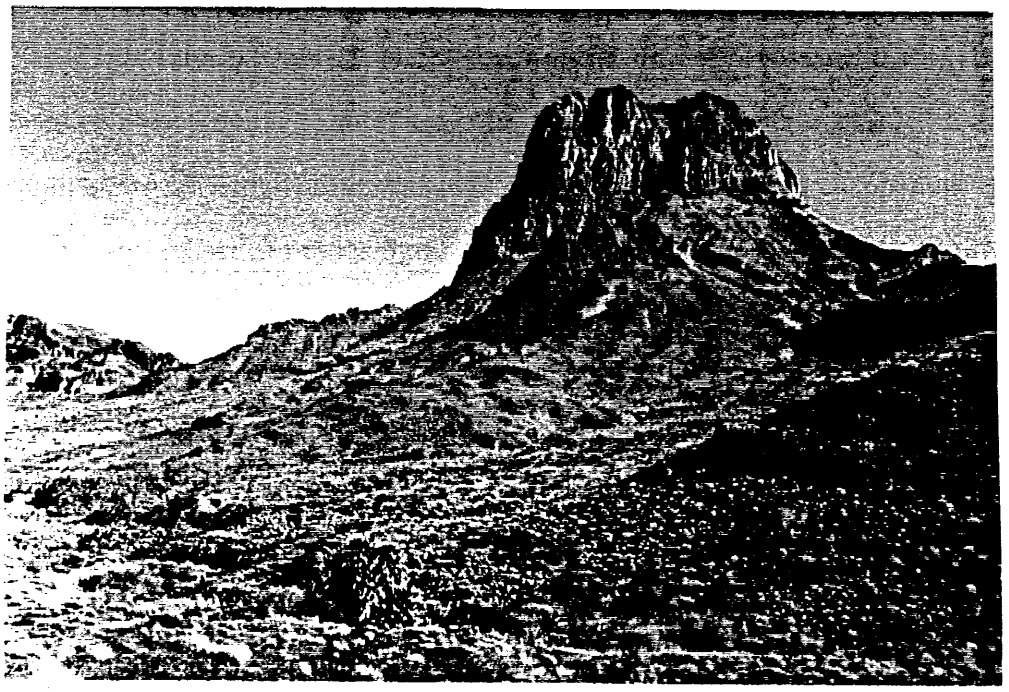

Figure 7. Mopah Peak from sample locality MS-3. Late stage rhyolitic plug protruding through a thick sequence of tilted andesitic flows in the fore ground. Palm trees approximately 20 feet high.

2.4 Geochemistry and Petrography

2.4.1 Classification

Pre- and syn-extensional rocks are mostly considered together in this report because of their similar geochemical trends and close temporal relationship. In the field they are readily identified by their pink-brown or pale grey colour, much of which is a product of surficial alteration. Post-extensional lavas are easily identified by their morphology, forming horizontal flows typically capping flat-topped mesas. They are also temporally distinct, occurring between 5 and 10m.y. after the syn-extensional magmatism; consequently, these flows are less altered and appear relatively pristine in the field.

Post-extensional magmatism typically comprises of basalts and basaltic andesites with lesser amounts of trachyte and rhyolite. In the field, the silica distribution is bimodal although the actual 'silica gap' is fairly narrow. Pre- and syn-extensional magmatism has a more continuous silica distribution from 45-80 wt% silica with a mean at ≈58wt% silica. But again, samples from individual areas can exhibit a bimodal distribution (45-58 and >66 wt% SiO_2), or cluster between 58 and 66 wt% SiO_2. Using the total alkali vs. silica classification of Cox et al (1979) most rocks fall close to the alkaline - sub-alkaline divide and they can generally be termed basalts and trachyandesites (figure 8). At the high silica end, rhyolites and dacites are most abundant although some of the late syn-extensional rocks are more enriched in alkalies and can be classified as trachytes.

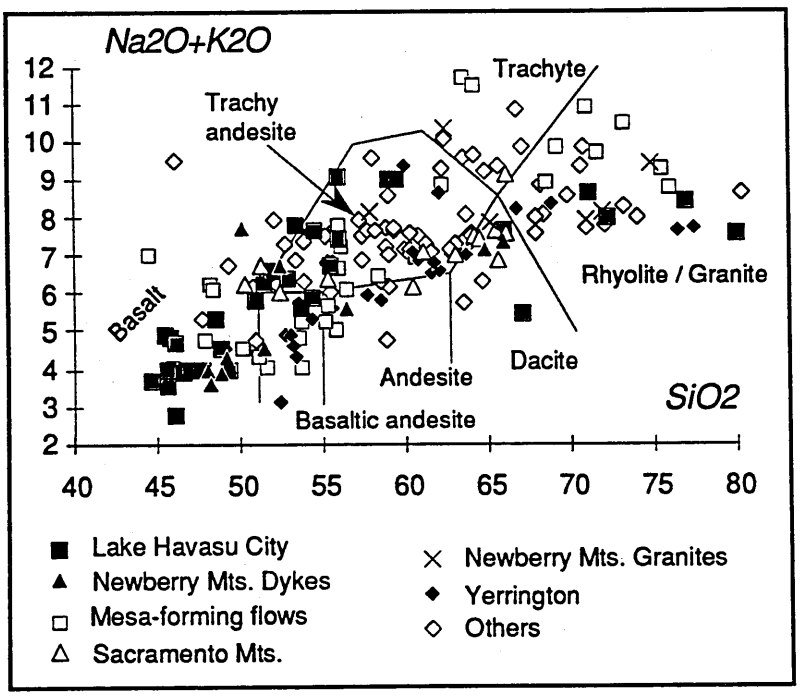

Figure 8. Total alkali versus silica (wt%) classification for the whole set of samples covered in this report (adapted after Cox et al 1979; LeBas et al 1986). Open squares are post-extensional samples.

Most of the pre- and syn-extensional basaltic volcanism is concentrated near Lake Mead and along the axis of the extensional corridor between Lake Havasu City and the Newberry Mountains. Regions that are peripheral to the axis (eg. Oatman, Searchlight, Sacramento Mts. and Mopah Springs) have a tendency towards trachyandesitic and rhyodacitic compositions. This suggestion of a link between the amount of extension and magma compositions is discussed in detail in chapters 3 and 4.

A summary of the stratigraphy for each sampled section is presented in figure 9, along with the relationships to the main episodes of extension and radiometric ages where available.

2.4.2 Petrography

The broad range of silica contents results in great petrographic diversity and thus only the general features will be discussed here. However, some important geochemical divisions can also be identified petrographically and these are examined in more detail.

2.4.2(a) *Basalts*

Pre-extensional basalts have been recognised in the Lake Havasu City area. Typically samples are porphyritic, but with ≤10% phenocrysts (up to 1·5mm) in a finely crystalline groundmass. The phenocryst assemblages consist of clinopyroxene and orthopyroxene, with or without olivine, or just of olivine. Olivine crystals tend to be euhedral, although in most samples they have been either partially or totally pseudomorphed by chlorite and serpentine. Even where fresh, the phenocrysts are mantled with iddingsite. Pyroxene phenocrysts are generally subhedral and may occur in small crystal clots with plagioclase. The groundmass mineralogy is dominated by fine plagioclase laths and granular clinopyroxene in proportions of approximately 70:30, with plagioclase forming the interstitial material. Crystalline opaque minerals are also an important component and may constitute up to 5% of the bulk rock. In a few samples rare micro-phenocrysts (xenocrysts?) of plagioclase, and quartz xenocrysts with disequilibrium textures can be observed (see section 2.4.2b).

Most of the mesa-forming post-extensional basalts have very similar bulk mineralogy and textures to the pre-extensional basalts, but generally with fewer groundmass opaques, just olivine in the phenocryst assemblage and little or no orthopyroxene. Others are more distinct, having <5% phenocrysts (olivine and plagioclase) and a greater proportion of groundmass clinopyroxene. Although still granular, adjacent clusters of clinopyroxene grains may be in near optical continuity and therefore produce a pseudo-ophitic or

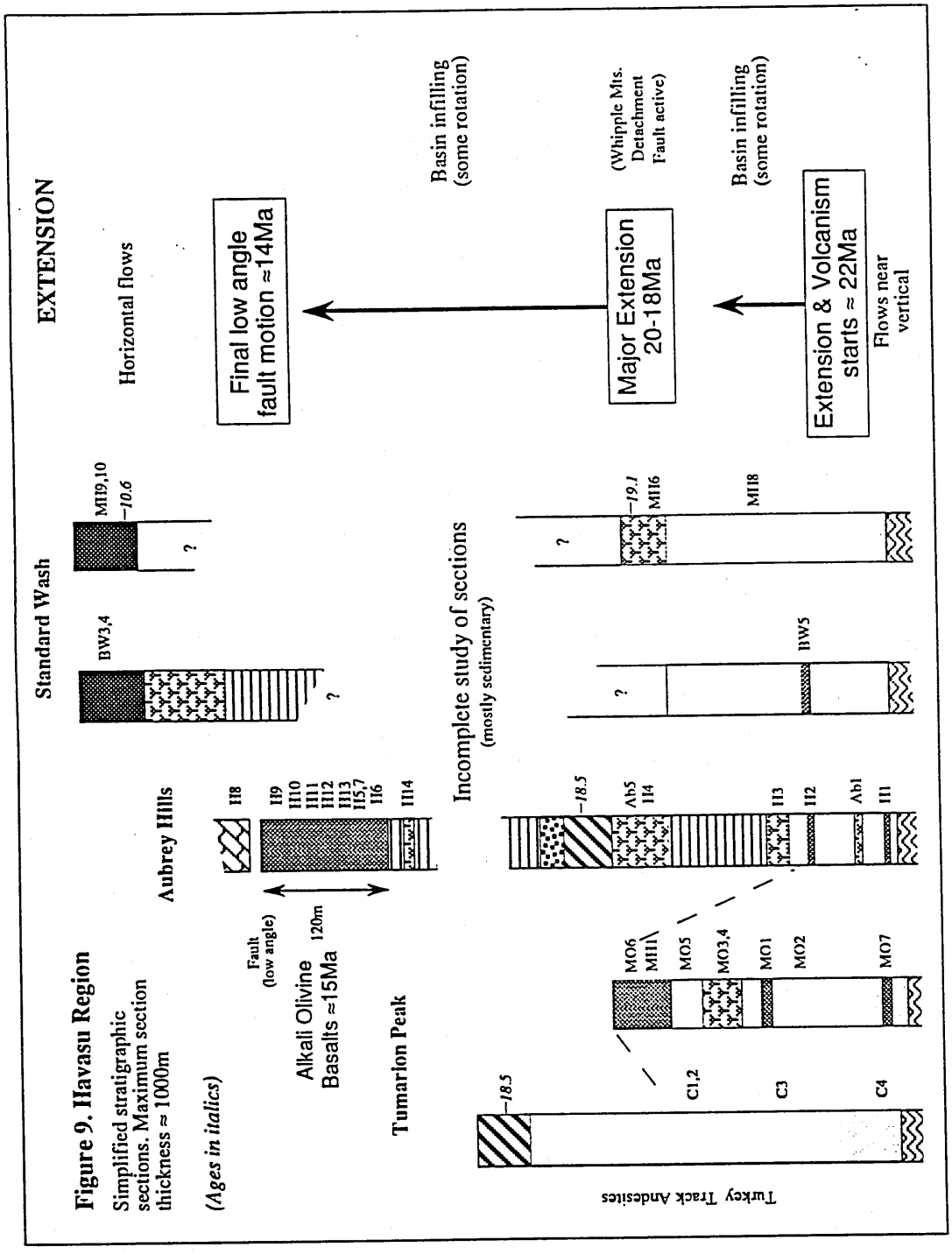

Figure 9. Havasu Region

Simplified stratigraphic sections. Maximum section thickness ≈ 1000m

(Ages in italics)

Note on age data. Havasu Region: Peach Springs Tuff Ar-Ar age, Neilson et al (1990), 18.5±0.2 Ma. Sample MH6 Ar-Ar age from Phil Gans perscomm. Other ages are whole rock K-Ar dates reported in Neilson (1986) eg. post-extensional basalts at 10.6±0.27 Ma, Turkey Track Andesites at 19.8±0.5 Ma, and oldest LHC lavas dated at 21.5Ma. Neilson (1986) also reports correlative stratigraphy between various sections within and around Lake Havasu City.

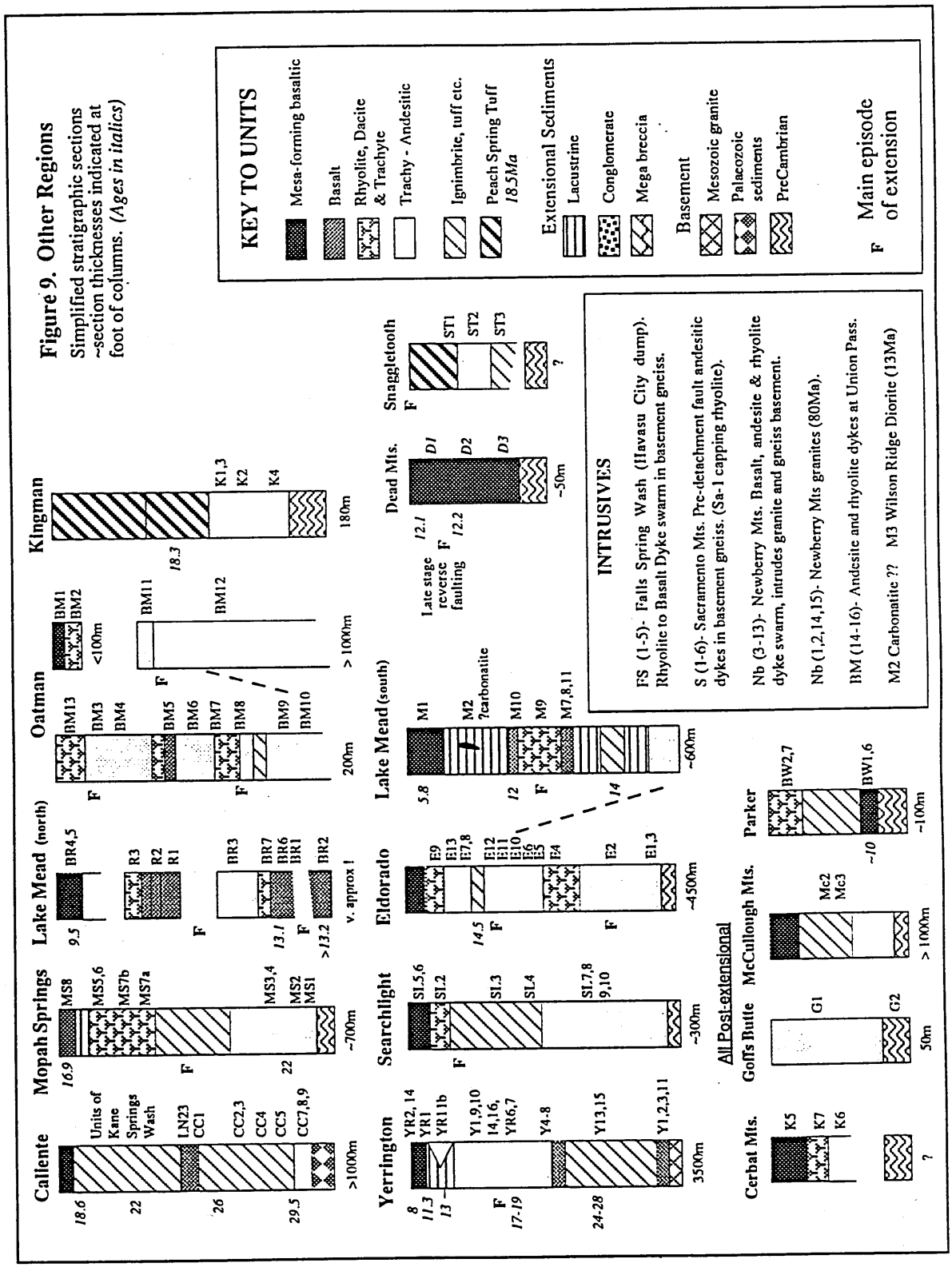

Note on age data from other regions. Yerrington: K-Ar, Proffett and Dilles (1984). Caliente: K-Ar, Best et al (1989). Mopah Springs region: K-Ar dates listed in Neilson and Turner (1986). Dead Mts & Sacramento Mts: K-Ar, Spencer (1985); Ar-Ar on sample Sa-1, Phil Gans perscomm (14.5Ma). Lake Mead & Eldorado Mts: K-Ar, Anderson et al (1972).

'ophimottled' texture with the groundmass plagioclase laths. In sample BW4, optically continuous clinopyroxene patches stretch for over 35mm. Rather more disequilibrium textures are observed in the mesa-forming basalts than in pre-extensional flows.

A third distinct type of basalt has been identified for the first time in the Miocene Basin and Range, at Lake Havasu City. These are alkali olivine basalts erupted at ≈15Ma in the Aubrey Hills, just prior to the final phase of local extension. The basalts are much coarser than those discussed above and they contain fresh olivine phenocrysts up to 2mm long; olivine is also present in the groundmass and constitutes 5-10% of the rock. The groundmass is the most distinctive feature of these basalts, displaying a classic sub-ophitic texture with oikocrysts of Ti-augite up to 3mm long partially enclosing coarse labradorite feldspar laths (figure 10). Interstitial material consists mostly of plagioclase with lesser amounts of opaque minerals; the latter grow along crystal boundaries as wedges and slivers up to 0·5mm long, quite unlike the granular to cubic nature observed in the other basalts. A few occurrences of tiny isotropic patches in the groundmass may be analcime, thus confirming the classification as true alkali basalts.

Basalts with similar textural relationships are observed as dykes in the Newberry Mts. However, the mafic phases have all been totally altered to secondary assemblages of bright green chlorite and amphibole. On the basis of petrography it is suggested that these basalts be regarded as essentially the same magma type as that of the Aubrey Hills, or to an intermediate stage between that and the post-extensional basalts. The latter may be more likely because the dyke samples appear to contain less groundmass olivine than the Aubrey Hills lavas.

2.4.2(b) *Disequilibrium textures*

Disequilibrium textures occur in many of the basalts although they are most commonly observed in the post-extensional samples. The textures are identified within or around plagioclase and quartz of apparent xenocrystic origin.

Plagioclase xenocrysts are predominantly square to rectangular, rather than lath shaped, and

Figure 10. Thin section of sample H6, 15Ma alkali-olivine basalt from Lake Havasu City. **10a** (above) in plane polarised light, **10b** (below) in crossed polarised light. The slide is coarse grained and consists mostly of large clinopyroxene crystals sub-ophitic with plagioclase laths. High releif groundmass and phenocryst olivine crystals are also visible.

can be much larger than the normal groundmass plagioclase crystals. They often display complex zoning, Carlsbad rather than lamellar twinning, and a deeper grey birefringence, which suggests a certain percent of K-feldspar component. Crystal edges may appear corroded, ragged, broken or rounded as a result of marginal resorption into the melt, and any embayments are filled with groundmass material. Within the crystal cores, or occasionally confined to individual zones, sieve-like textures are observed (figure 11a). The 'holes' in the sieve consist of brown glass and pyroxene, evidence of extreme internal melting which, as in figure 11a, can be seen to nucleate along the cleavage. At later stages crystals often develop a clear overgrowth rim in equilibrium with the melt. This tends to produce a reverse zonation from albitic or andesine cores to labradorite rims, consistent with microprobe analyses of similar textures in the Mojave Desert (Glazner 1989).

Quartz xenocrysts are often polycrystalline with relict igneous textures (ie. 120° grain intersections). They invariably have rounded and deeply embayed margins and have developed complex reaction rims. The inner part of the reaction rims consist of clear or brown glass and this is surrounded by a wider zone of clinopyroxene crystals. Towards the outer margins of the rim the pyroxenes are commonly granular, but closer to the xenocryst they occur as laths and acicular masses projecting into the areas of glass. Lath terminations within the glass rim are hollow, indicative of rapid crystal growth at the edges in response to quenching of the basalt against the xenocryst (Cox et al 1979), figure 11b. Occasionally the whole xenocryst is replaced, but their presence can still be inferred from the distinctive pyroxene textures which remain.

Because the xenocrysts appear to be of igneous affinity, two possibilities arise for their origin:

i) they are crustal material of igneous origin, and therefore probably derived from the Mesozoic granites, or

ii) they are reworked crystals from earlier, more evolved Cenozoic magmas.

The major and trace element geochemistry of these two 'contaminants' is likely to be very similar, but they should have significantly different isotope ratios (see chapter 3).

Figure 11a. Thin section of sample BW4 in plane polarised light. Large euhedral plagioclase phenocryst displaying an extreme example of a sieve textured core and a clear overgrowth rim. The crystal is also partially corroded (bottom right). Notice the somewhat similar groundmass texture to sample H6 in figure 10, although finer grained and without olivine.

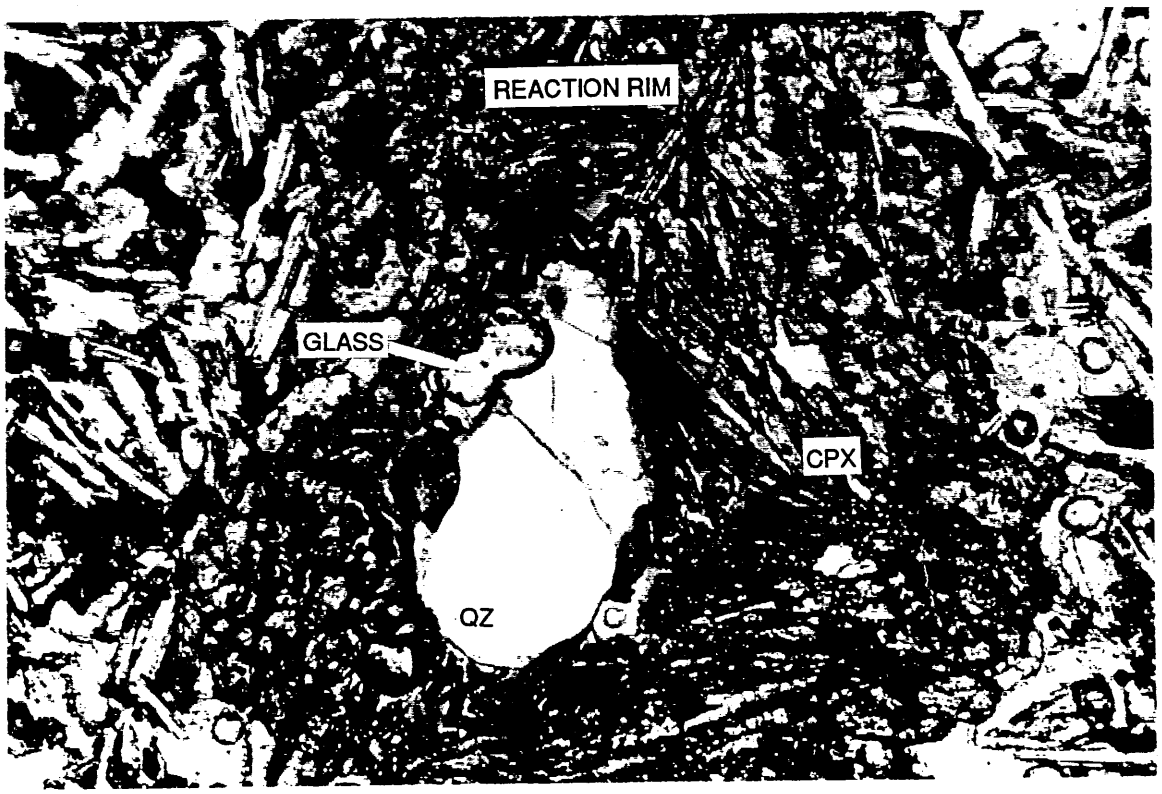

Figure 11b Sample BR4 in plane polarised light. Poly crystalline quartz xenocryst with complex reaction rim (mostly granular and acicular clinpyroxene) and area of partial melting (labelled 'glass').

An important point to note is that samples with the greatest proportion of disequilibrium textures (ie. BW3, BR4) generally have higher silica contents than other associated basalts. Therefore the addition of xenocryst material, such as that described, may be an important process in the evolution of basalts to higher silica magmas.

2.4.2(c) *Trachyandesites*

Quartz xenocrysts with reaction rims are absent in the trachyandesites, although disequilibrium textured plagioclases are observed. Typically, samples are highly porphyritic (>30% phenocryst content is not uncommon) with the phenocryst assemblages consisting of plagioclase, clinopyroxene and orthopyroxene. Phenocrysts and microphenocrysts of these, plus opaque minerals, often form as clots with interstitial plagioclase. These 'glomerocrysts' have primary igneous textures and are not replacement features after xenocrysts. Olivine phenocrysts occur in some of the more basic samples and may show resorption (as in sample SL6), which suggests equilibrium crystallisation.

Hornblende and biotite become more important as the mafic phenocryst phase in rocks with higher silica contents. However, plagioclase phenocrysts (andesine composition) are always the most abundant and plagioclase is also the dominant groundmass phase. Clinopyroxene and opaque minerals are much less abundant in the groundmass than they are in the basalts. Trachytic flow textures are common and in some units these are visible to the naked eye. One example of which are the 'Turkey Track' andesites of Lake Havasu City, so named because of the orientation of plagioclase phenocrysts up to 30mm long.

Many samples contain some plagioclase and clinopyroxene phenocrysts that appear to have undergone a long crystallisation history. These large phenocrysts usually display complex zoning and twinning, and it is sometimes possible to identify distinct cores which have been abraded and then overgrown (see figure 12). The cores of some clinopyroxene phenocrysts contain small, high relief, inclusions which may be grains of spinel. Clinopyroxene pheocrysts are often also associated with large, euhedral, apatite crystals. Microprobe analyses of augite phenocrysts from the Eldorado Mts. (Appendix A) show no

pronounced chemical differences between crystals, nor between core and rim samples, apart from normal zoning to lower CaO and higher FeO at the margins. If the crystals had been entrained as xenocrysts, a greater spread of composition would have been expected. Thus it is likely that they are merely recirculated phenocrysts from the main magma batch rather than being fragments of country rock.

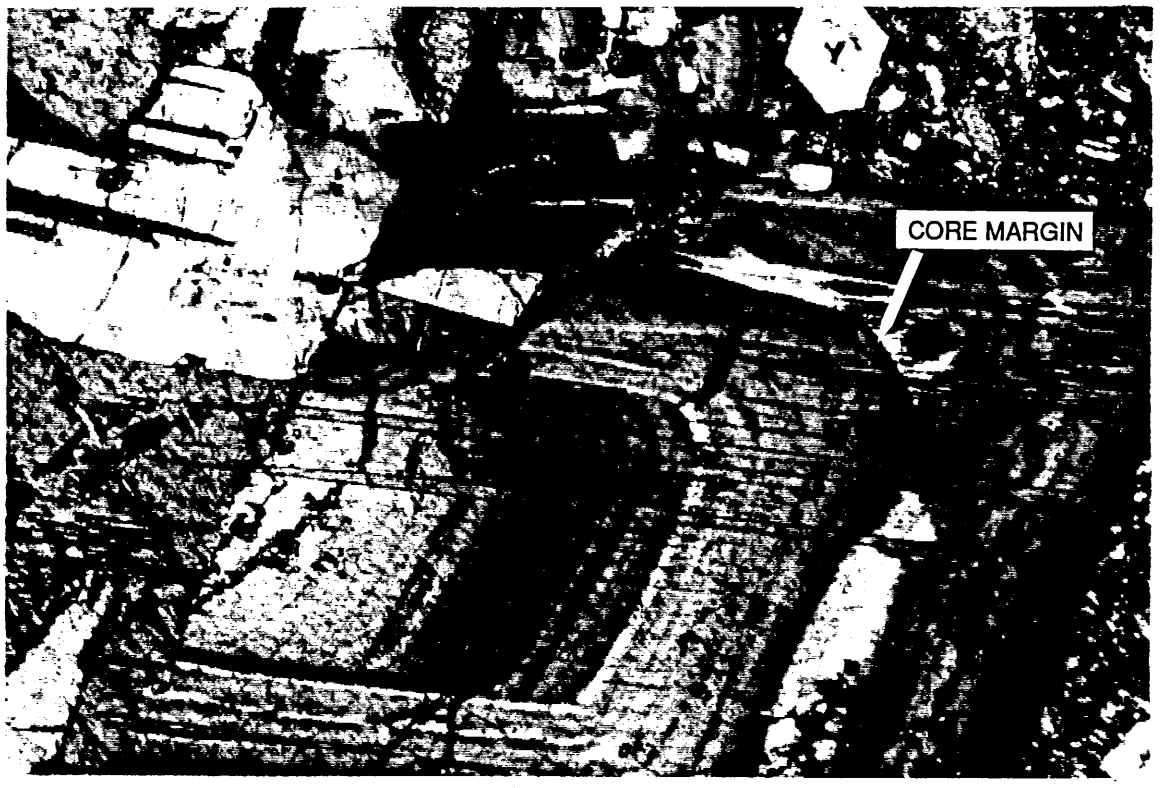

Figure 12 Thin section of sample Y9 in cross polarised light. Complex zoning and twinning in large plagioclase phenocryst. Note the abraded core and later overgrowth.

2.4.2(d) *High silica rocks*

Some of the highest silica samples (ie. E4 and MO4) are vitrophyres and many of the other rhyolites and dacites have holohyaline groundmasses. Phenocryst assemblages are again dominated by plagioclase (oligoclase to andesine composition), with biotite, hornblende, sanidine and quartz also present. Plagioclase phenocrysts have stubby or rectangular forms and invariably display complex twinning and zoning. In sample SA1 the quartz crystals are rounded and partially resorbed, although they are not multigranular and therefore not considered to be xenoliths. Similar quartz resorption is a common feature of high silica

rocks (Cox et al 1979) and may relate to changes in the quartz stability field with pressure. Tuttle and Bowen (1958), and Winkler (1979), observed that the quartz-orthoclase cotectic in the quartz-albite-orthoclase system moves towards higher silica levels at lower pressures. Therefore quartz crystallised on the cotectic at high pressure will become unstable as the magma decompresses.

Quartz and feldspar xenocrysts are present in rhyolites from the Lake Mead area (eg. R3A and R3B). They can be distinguished from the SA1 type phenocrysts by their irregular shape, multigranular nature and lack of resorption features. The grains occur in partially disaggregated masses, as discrete rock fragments or as stringers elongated in the flow direction. This latter feature is of note because it emphasises that mechanical processes are potentially very important in mixing magmas and their contaminants.

2.4.2(e) *Kaersutite occurrences*

The alkali basaltic samples R2 and M2 from near Lake Mead contain crystals of kaersutitic amphibole. In R2 kaersutite is abundant in the phenocryst assemblage with orthopyroxene and clinopyroxene. At the M2 locality it occurs as megacrysts up to 10 by 4cm. In both cases the crystals are very fresh, but typically abraded (rounded) or ragged, and they are mantled by a rim of granular opaque oxide minerals indicating a disequilibrium reaction. Such characteristics suggest a xenocrystic origin.

Sample M2 is from a small pod-like body near Hoover Dam which intrudes post-extensional sediments and therefore represents the most recent phase of magmatism in the CRT (≈2Ma). Besides kaersutite, large crustal xenoliths and smaller olivine and clinopyroxene xenoliths (of mantle origin?) are also very abundant (described by Wilshire et al 1985). The rock is dominated by a partially devitrified groundmass and contains a high proportion of large calcite crystals. These do not appear to be part of an alteration assemblage, but occur as veins and small pods within the intrusion. The veining is often intense although confined to the intrusion, and therefore the calcite may be of primary magmatic origin. If this is the case, M2 might almost be classified as a carbonatite; a

conclusion that is consistent with the abundance of xenolith material because carbonatites are recognised as having extreme magmatic intrusion rates through the lithosphere (Le Bas *personal communication*).

2.4.3 Major and trace element variations

The variations in selected major and trace elements for the pre/syn- and post-extensional magmatic rocks are illustrated in figures 13-19. These highlight aspects of the overall trends, although a number of suites have been plotted individually (as in figure 10) to demonstrate some of the typical intra-suite variations. Silica is chosen as the standard against which the variations in other elements are portrayed because of its suitability for comparing samples from a great compositional range. The use of MgO or Mg# is inappropriate because their effectiveness is limited for discrimination in highly evolved samples, and they induce bias in rocks where olivine has been a major cumulate or fractionating phase.

CaO and Fe_2O_3.t display linear decreases in concentration with increasing silica. MgO, TiO_2 and P_2O_5 also decrease, but show a marked scatter at <55 wt% SiO_2. Na_2O does not vary significantly with silica, while K_2O is the only major element which has a pronounced positive correlation with silica (figure 13). Some of the scatter above the main K_2O trend is generally consistent with slightly lower Na_2O contents and also with higher or extremely variable Rb, Cs and U concentrations. These suggest that hydrous alteration has been a factor. However, only the freshest samples were collected and analysed. Moreover, the observed alteration is relatively insignificant compared to the pervasive alteration described by Glazner (1988) in the Mojave Desert where rocks affected by post-crystallisation potassium metasomatism have K_2O and Rb contents increased by up to 220% and Na_2O decreased by nearly 60%.

The scatter of P_2O_5, and also of Ba and Sr, in the low silica samples (figures 13 & 14) appears to be even more extreme, but there are reasonable positive correlations between Ba-P_2O_5, Sr-P_2O_5 and Ba-Sr. These correlations imply that the scatter is systematic and relates

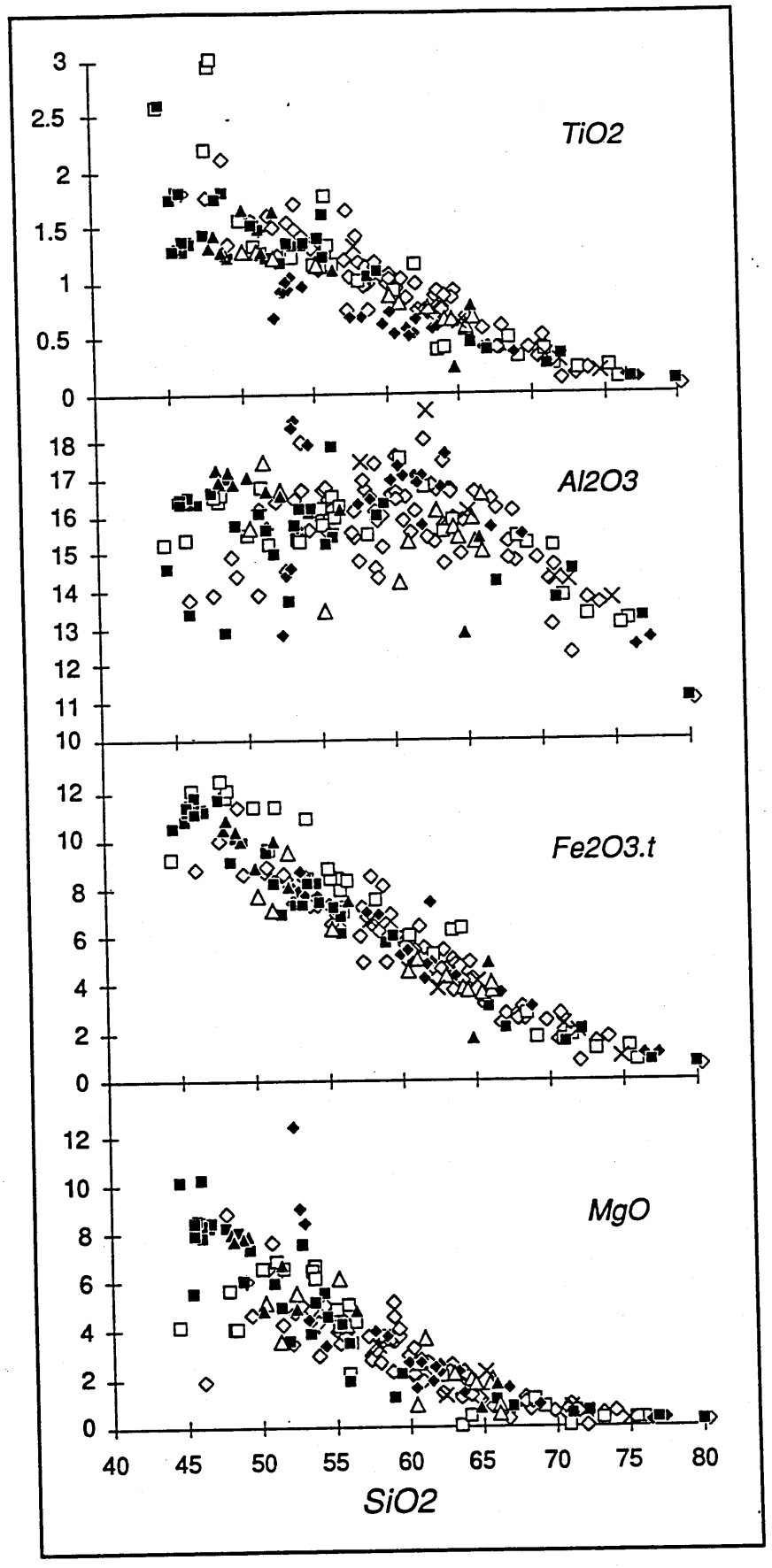

Figure 13. Weight percent oxide variations with silica for all samples covered in this report. See figure 8 for key to individual sample suites. Note the low TiO2 and high Al2O3 contents in the 15Ma alkali olivine basalts from Lake Havasu City, and in the Newberry Mts. dykes (cluster of filled squares at low silica & filled triangles respectively). Fe2O3.t= Total iron expressed as Fe3+.

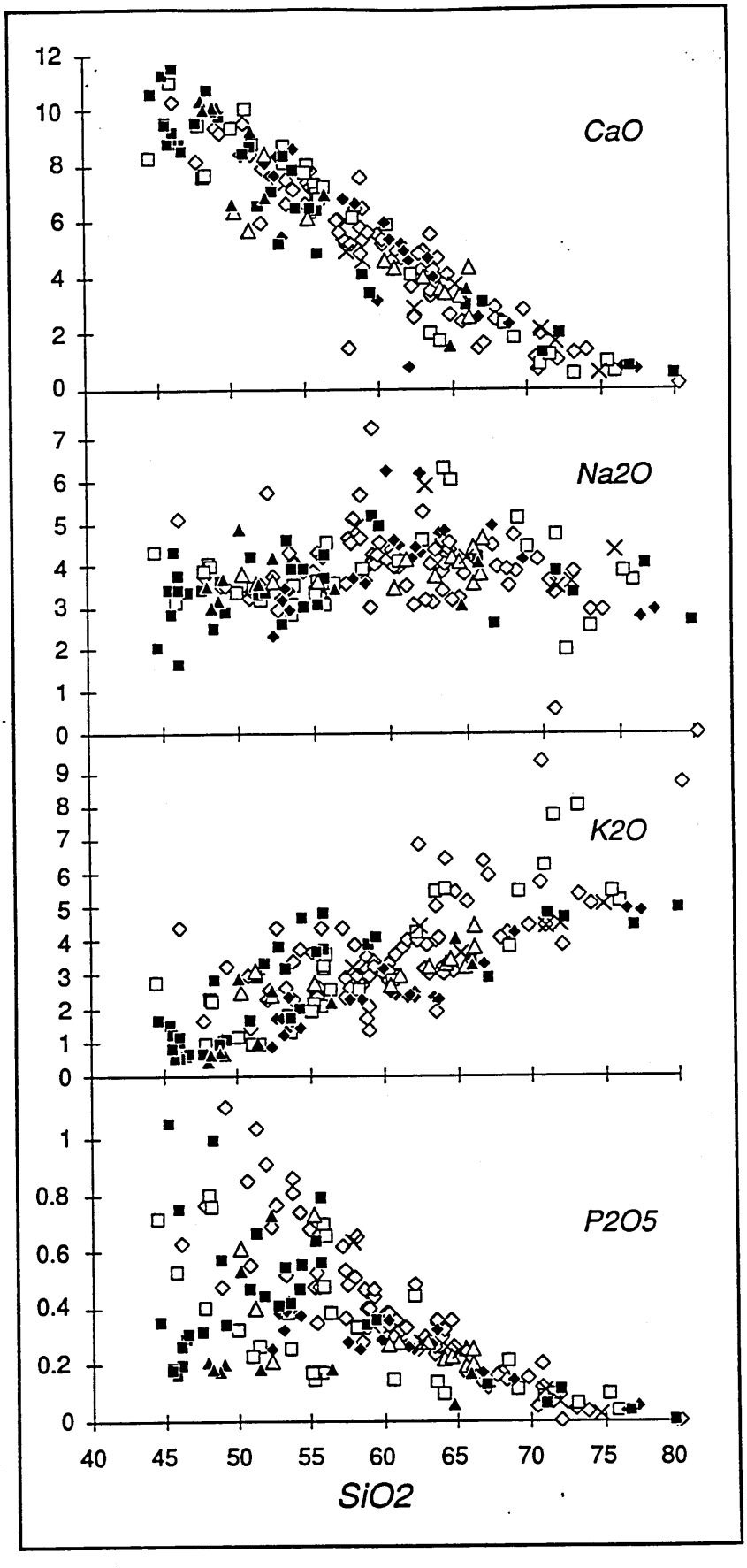

Figure 13. (cont) Note the decreased scatter in P2O5 abundances with increasing silica and the slight inflexion in the K2O graph above 70wt% silica. Post-extensional samples (open squares) typically display a similar range of major element variability to the pre/syn-extensional samples

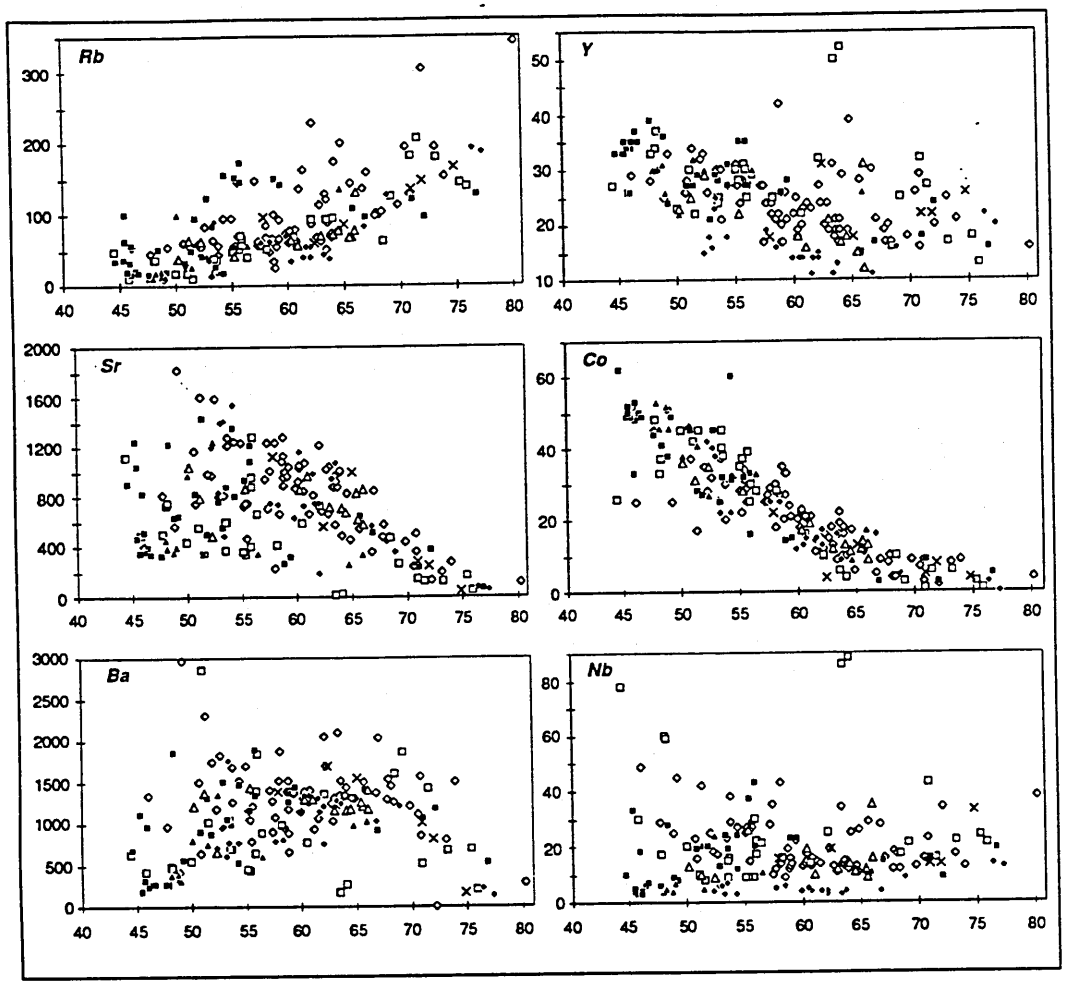

Figure 14. Trace element variations (ppm) versus silica content (wt%). Key as figure 8. Although the data are obviuosly scattered there is some positive correlation with Rb and Ba, and negative correlations with Co, Sr and Y. See text for discussion.

to a function which is not adequately expressed in terms of silica; for instance, a source characteristic, degree of partial melting, or a combination of these (see chapter 4 for discussion). The variability is almost certainly not related to alteration because each of the elements display strong positive correlations with the light rare earth elements (LREE: ie. Ce and Nd) which are not readily mobilised by hydrothermal action.

Al_2O_3 concentrations are fairly high and average at about 16 wt% (figure 13). However, Al_2O_3 and Sr contents start to decline above ≈56 wt% SiO_2 in response to plagioclase fractionation. Similarly, further inflexion points on the other major and trace element graphs may also correspond to particular phases becoming more or less dominant in the

fractionating assemblage (Cox et al 1979):

i) The levelling-off of K_2O above ≈70 wt% SiO_2 correlates with a decrease in Ba contents, suggesting K-feldspar fractionation. This also gives rise to slight inflexions in the other silica variation diagrams.

ii) Co, Cr, Sc and MgO trends inflect at ≈65 wt% SiO_2, as do the Fe_2O_3.t and CaO trends very slightly, suggesting the cessation of clinopyroxene fractionation.

iii) Scatter of MgO, Cr, Ni and Co in samples below 55 wt% SiO_2 is an artefact of the representation against silica. Sc, Cr, Ni and Co all have positive correlations with MgO and therefore the variation is likely to be a function of olivine and clinopyroxene fractionation, which would be consistent with petrography. The degree of fractionation is discussed in section 2.5.1b.

TiO_2 vs. SiO_2 variation can be resolved into a number of individual trends. Samples from Yerrington plot with consistently lower TiO_2 than those from the CRT, and they also have relatively lower Y, Heavy Rare Earth Element (HREE) and Zr contents, and slightly higher CaO. TiO_2 contents decline with increasing silica in all the suites with >47wt% silica, but the CRT data split into two distinct groups at low silica. A scattered high-TiO_2 group includes early basalts from Lake Havasu City and Lake Mead, and the post-extensional basalts. The second group is more coherent and comprises primarily of the 15Ma alkali olivine basalts from Lake Havasu City, the Newberry Mts. dykes, and basaltic dykes from the Sacramento Mts. Samples in this group have generally lower trace element contents (particularly P_2O_5, Sr, Ba, Ta, Nb and Zr), but higher Y, compared to the rest of the CRT data set. They also form distinct clusters at slightly higher Al_2O_3 and MgO content than expected for their low levels of silica. The group is more easily distinguished on figure 15 which includes only samples with <50wt% SiO_2. The alkali olivine basalts plot at much lower values of Ti/Y and P_2O_5 and have rather restricted ranges of both. Note that Ti/Y remains roughly constant, at ≈220, in the Lake Havasu City alkali olivine basalts because an increase in Y with silica (figure 14) is matched by a slight increase in TiO_2 with silica (figure 13). This is in agreement with the general petrography of these samples, which suggests that ilmenite was not a fractionating phase.

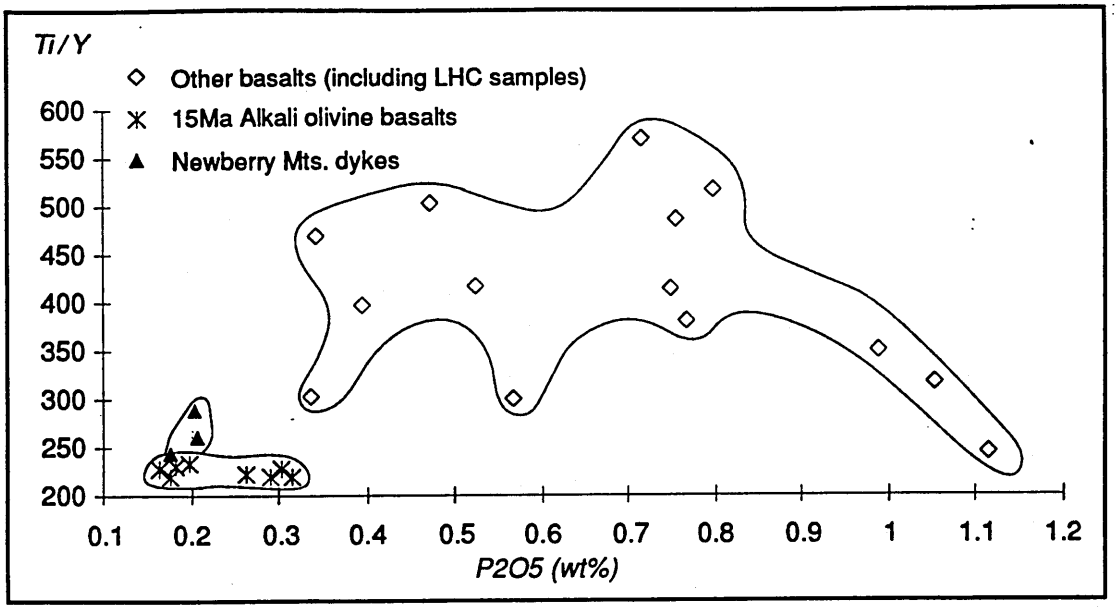

Figure 15. Ti/Y versus P2O5, for samples having <50wt% silica, to discriminate between the 15Ma alkali olivine basalts and other CRT pre/syn-extensional and post-extensional basalts.

The variation of Nb and Zr with silica (figures 14 and 16) is not as pronounced as for some of the other trace elements. A slight positive correlation is observed within the Newberry Mts. dykes and Lake Havasu City alkali olivine basalt suites, particularly between Zr and silica. More significant increases in Zr with silica occur in suites from Oatman, the Eldorado Mts. and in some of the post-extensional suites (related samples from a number of these groups are highlighted on figure 16). The largest increase in Zr, ≈600ppm (with a 30wt% increase in silica), is observed between the post-extensional basalts BW1&6 and their associated trachytes BW2&7. However, it is also apparent that much of the data spread is towards increasing silica either without increase in Zr (or Nb) or with a gradual decrease in Zr content. Such trends are clearly displayed by the Yerrington and Sacramento Mts. suites.

The overall pattern for the CRT suites is that of a convergence of trends towards ≈185 ppm Zr and ≈72 wt% SiO_2.[1] Detailed examination reveals that this trend is generally defined through the lowest silica members from each individual group of related samples. Similar convergence of sample trends at high levels of silica is also observed on many of the other

[1] The few samples which are displaced below the convergence trend to much lower Zr contents above 75 wt% SiO_2 are likely to have fractionated zircon.

major and trace element variation diagrams. In particular those of P_2O_5, TiO_2, Al_2O_3 and Sr vs. silica. Trend convergence is mostly towards compositions similar to those of the suite of granite analyses from the Newberry Mts. (eg. samples Nb2, Nb14 and Nb15).

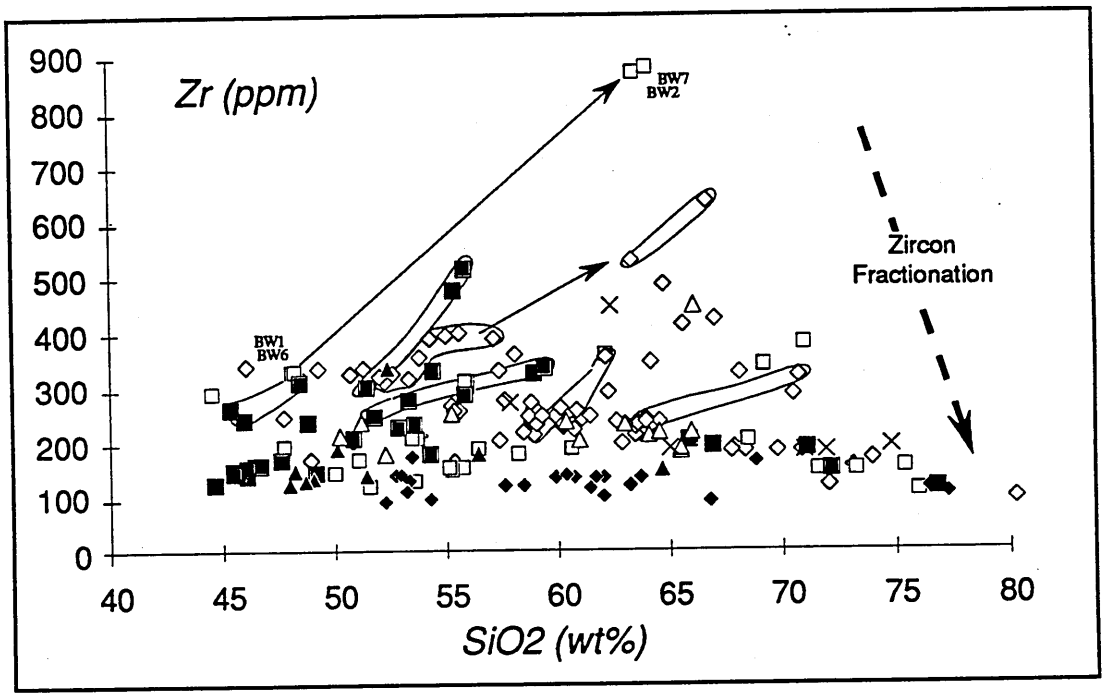

Figure 16. Zr (ppm) versus SiO2 (wt%). Arrows and circled data points link samples from various suites thought to be related by fractionation. However, note that the predominant trend is for a slight decrease in the Zr content with increasing silica. Samples from Yerrington (filled diamonds) consistently have the lowest Zr contents and display little variation with silica.

2.4.3(a) *Mantle normalised diagrams*

For trace element comparisons it is often useful to normalise data to a standard composition, and to display the results either as trace element ratio diagrams or as multi-element plots ('spidergrams'). Spidergrams have the advantage of permitting rapid evaluation of the general trace element abundance patterns within and between groups of samples. A number of such diagrams are therefore presented in figure 17. Primitive mantle abundance values from Sun and McDonough (1989), are taken as the normalising factor for each element. The element order on figure 17 represents generally increasing mantle compatibility from left to right across the diagrams. Thus, Pb and Rb are the least compatible elements while Sc is significantly more compatible with respect to mantle mineral phases such as pyroxene and olivine.

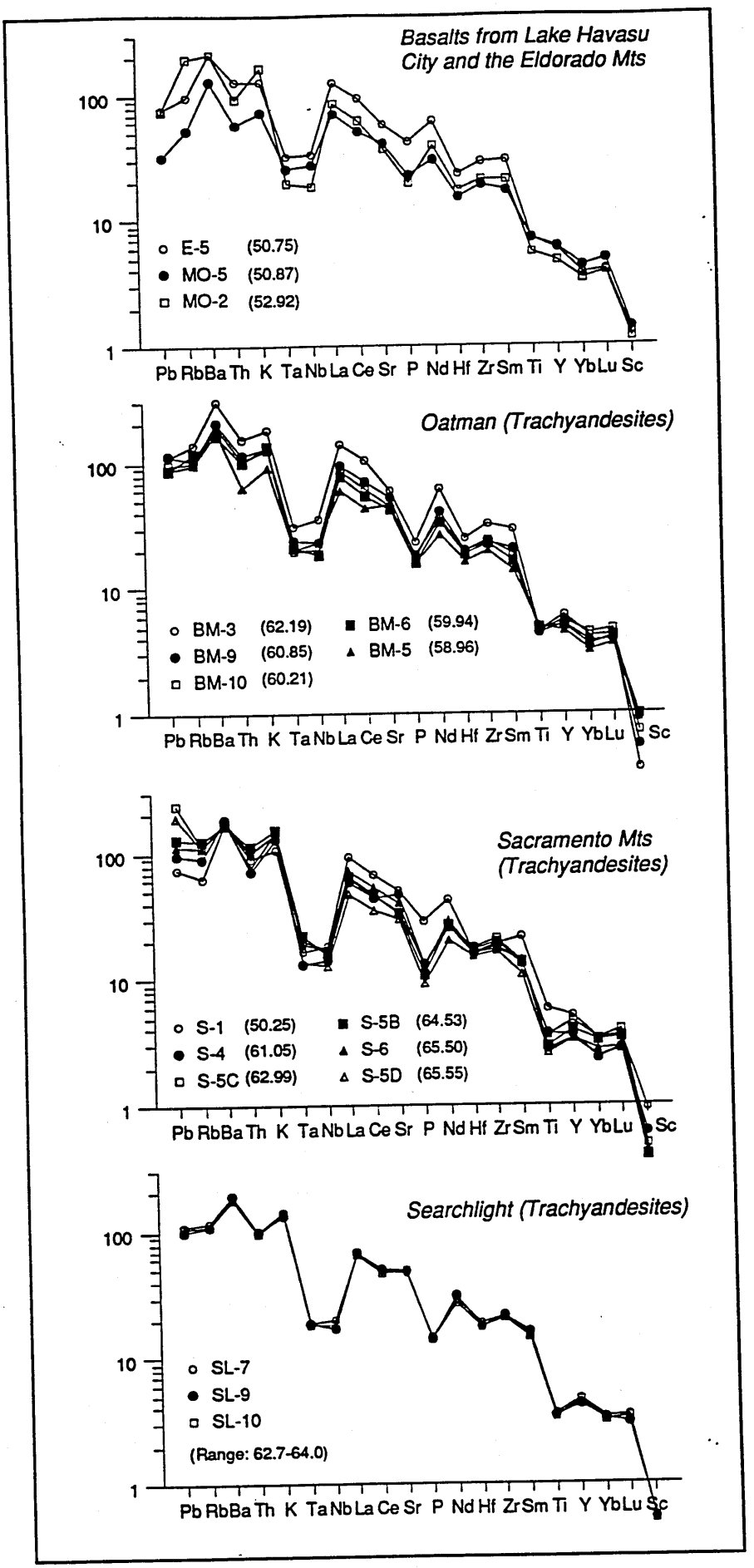

Figure 17. Incompatible trace element diagrams for representative pre/syn-extensional samples from the CRT. Trace element abundances are normalised to the primitive mantle abundances of Sun and McDonough (1989).

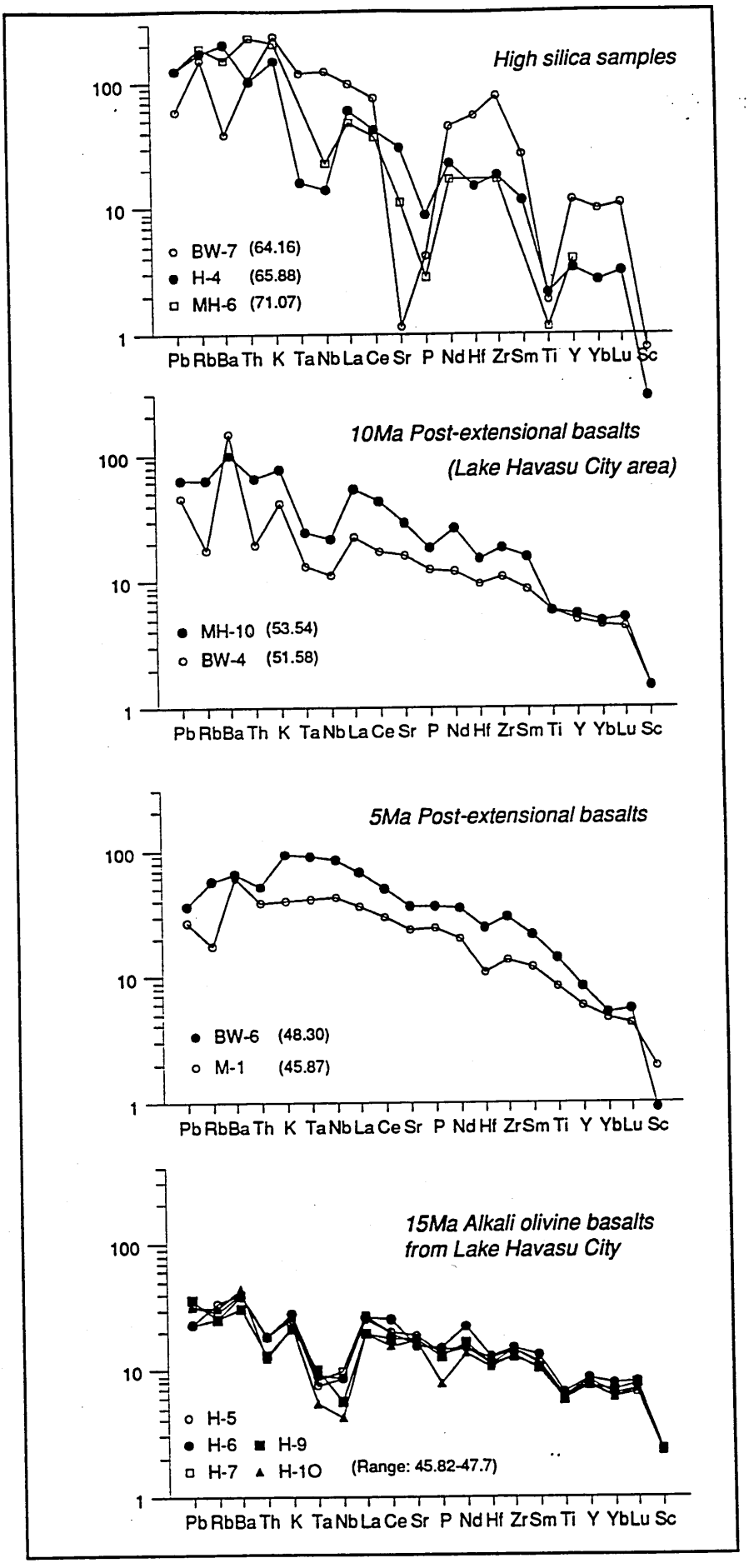

Figure 17. (cont) Note: weight percent silica contents are given in brackets. High silica sample BW7 is a space / time correlative to post-extensional basalt BW6. Post-extensional samples are representatives from the mesa basalt group on previous diagrams.

In all the samples, trace element abundances are significantly enriched above those of the primitive mantle. Typically the samples have high LREE/HREE ratios and show maximum enrichment of the Large Ion Lithophile Elements (LILE). A peak at Ba is often observed which is apparently a characteristic feature of many lavas from the western United States (for example: Fitton et al 1991; Bacon 1990; Gans et al 1989). Pre- and syn-extensional basalts, and many of the trachyandesites, have High Field Strength Element (HFSE) abundances of approximately 25 times primitive mantle (ie. Ta, Nb, P, Hf, and Zr). The LREE, Sr and LILE are enriched above this level and this tends to produce a Ta-Nb 'trough'[2] on the spidergrams.

The other HFS elements (Ti and Y) and the HREE generally have abundances of approximately 3 to 6 times primitive mantle. This generates a pronounced step between Zr-Sm and Ti on the spidergrams; the step enlarges with increasing silica because of the negative TiO_2 vs. SiO_2 correlation. Similarly, the slight negative anomaly of P, relative to the adjacent REE's, also increases with silica. In the higher silica samples negative anomalies may also develop for Eu, Sr and Ba as the degree of plagioclase (and alkali feldspar) fractionation increases. Although the resulting trace element patterns in the high silica rocks sometimes appear quite wayward, the underlying patterns often still reflect those of their related basalts and trachyandesites.

The three spidergrams of trachyandesite suites are almost identical, although the Sacramento Mts. dykes have rather more scattered Pb and Rb abundances. These samples are older than the other trachyandesites presented in figure 17 and are slightly more altered. Samples in the Oatman suite cover a range of just 3·2wt% SiO_2 but a consistent positive correlation is evident between the trace element and silica contents (apart from Ti and P); the correlation is only strongly inversed for Sc. Analogous patterns of correlation are not observed in the Sacramento Mts. suite, even though they might have been anticipated to be even more strongly developed here because this suite covers a range of ≈15 wt% SiO_2.

---

[2] Mantle normalised La/Nb and K/Nb ratios >1 produce such a trough on the spidergrams.

Post-extensional basalts fall into two groups, although not exactly along the same divisions suggested by their petrography. One group displays many of the pre/syn-extensional basalt characteristics such as the Nb trough and Ba peak, but the anomalies are generally not as well developed. Trace element abundances also tend to be lower on average. The second group is rather more distinctive with a much smoother convex upwards pattern and no Ta-Nb trough. Infact the abundance peak is often located at Ta or Nb. These samples do not display an HFSE plateau at 25 times primitive mantle values, although the overall REE abundance levels are comparable with those of the pre/syn- extensional basalts.

The 15Ma alkali olivine basalts from Lake Havasu City are again distinct from the other basaltic samples. Samples in this suite have the lowest trace element abundances, and spidergram patterns that are essentially flat (particularly for the REE) by comparison with the other basalts. The Zr-Sm to Ti step is much shallower and the Ba peak is less well developed, but a negative anomaly at Th is more prominent. The low Ti/Y ratios and greater abundance of the HREE's produces a slight plateau (at ≈8-10 times primitive mantle) towards the more compatible end of the spidergram. Despite all of these differences the overall shape of the spidergram bears more resemblance to that of the pre/syn-extensional basalts (and the MH10, BW4 type post-extensional basalts) than to the much younger[3] BW6 and M1 type basalts.

2.4.3(b) *Summary of main geochemical features*

The previous sections have outlined the general geochemistry of magmatism in the CRT. Some of the important features to note include:

i) the large range of magma compositions, from 44-80 wt% SiO_2;

ii) major and trace element trends which typically become less scattered towards high silica levels, and often appear to trend towards the position of granitic samples from the Newberry Mts;

[3] Ages of post-extensional basalts: MH10, BW4 ≈ 10Ma; BW6, M1 ≈ 5Ma.

iii) evidence from MgO, K_2O and the transition metals of the possibility of fractionation throughout the CRT suites;

iv) high trace element concentrations in all the CRT samples and irregular, convex upwards, spidergram patterns with a prominent trough at Ta-Nb. This is evident both spatially and temporally as many of the post-extensional samples have similar geochemistry to the pre/syn-extensional samples;

v) the recognition of two basalt types which are distinct from the main CRT basalts: one occurs in the most recent phase of post-extensional magmatism and is characterised by a smooth spidergram signature and no Ta-Nb trough; the second type occurs as 15Ma alkali-olivine basalts at Lake Havasu City which have a similar spidergram shape to the typical basalts although with relatively enriched HREE, Y and Sc concentrations and low Ti/Y ratios.

This variety of geochemistry presents a complex problem for identifying how magmas may be related to one another and particularly how they might evolve to higher levels of silica. However, some of the major element trends alone (figure 13) can be used to characterise the overall nature of the CRT magmatism in general terms. This is a useful starting point for developing geochemical models, and therefore the main distinction between alkaline and tholeiitic or calc-alkaline trends is discussed below before more detailed models are considered in section 2.5.

2.4.3(c) *Alkaline, tholeiitic and calc-alkaline evolution trends*

In figure 18a the low silica end of the total alkali versus silica diagram (figure 8) is shown in more detail for samples from the CRT. The alkaline/sub-alkaline divide is reproduced from Perry et al (1987), after Irvine and Baragar (1971). Clearly, most of the CRT samples, irrespective of age or locality, can be classified as alkaline, although roughly only one third of the samples indicated are nepheline normative. Within the nepheline normative sub-group are the 15Ma alkali olivine basalts from Lake Havasu City, and the few post-extensional samples that have the distinctive absence of a Ta-Nb trough on trace element spidergrams (see previous sections).

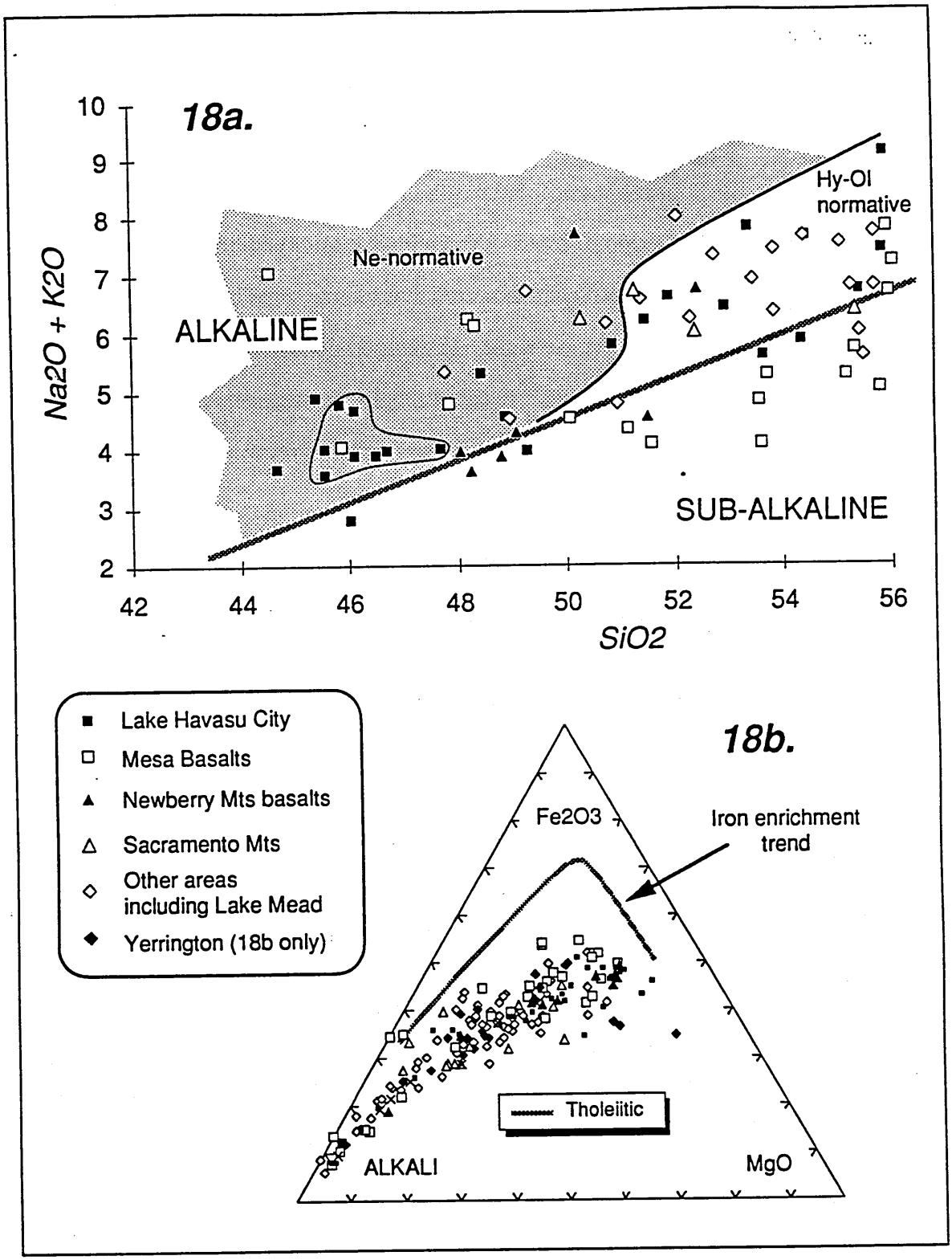

Figure 18a. Detail of the total alkali versus silica diagram for CRT basaltic samples. Samples in shaded field are ne-normative. 15Ma alkali olivine basalts from Lake Havasu City are circled. The thick shaded line separates sub-alkaline (below) from alkaline samples (above). See text for details. **18b.** Weight percent 'AFM' diagram with trend indicated for the general evolution of tholeiitic suites. Most of the samples lie below this trend and fall in the field typically defined by alkaline suites. ALKALI= Na2O+K2O. Fe2O3= total iron content expressed as Fe2O3.

Many of the samples that fall in the sub-alkaline field are post-extensional and at higher silica levels a few of these are quartz normative. The typical trace element geochemistry (represented by the 10Ma post-extensional basalts illustrated in figure 17) is reasonably similar to that of the main group of basalts. Typically, the sub-alkaline basalts have only moderate Al_2O_3 contents (c. 16wt%) and therefore these samples are classified as tholeiitic, rather than calc-alkaline. However, in figure 18b there is no obvious development of a trend towards the iron enrichment that is typical of tholeiitic evolution. This may indicate that the build up of iron within the magma system was limited in some way, possibly by the fractionation of oxide phases such as magnetite and ilmenite.

Despite the alkaline nature of most of the CRT samples, it is interesting to note the lack of evolved samples in figure 8 with a high alkali content and low silica (eg. phonolites). Rather, the bulk of evolved CRT samples are moderate to low alkali dacites and rhyolites.

2.5 Geochemical modelling

In this section some simple major and trace element models are presented for the geochemistry of the Cenozoic magmatism in the CRT. The importance of fractionation during the evolution of the magmas to higher levels of silica is evaluated, as are the basalts in terms of the likely degree of fractionation from primary basaltic magmas. Possible relationships between some of the main basaltic magma types are also discussed in the final part of the section.

2.5.1 Evolution to higher levels of silica

It has already been noted that some of the major and trace element trends displayed by the CRT sample suites may be related to crystal fractionation. From petrographic evidence, the main fractionating phases are likely to be olivine, clinopyroxene and plagioclase, as well as some opaque oxide minerals (eg. ilmenite and magnetite).

The actual occurrence of fractionation is easily demonstrated by considering the variation of elements which are highly incompatible in the phases that are fractionating. Such elements have bulk crystal/liquid distribution coefficients (bulk 'D' values) below unity and therefore the concentration of these elements within the magma will show a pronounced increase as fractionation proceeds. Although, if the body of magma represents a closed system, the observed increase in concentration is only relative, because the absolute abundance of the element has not changed.

A useful element for evaluating fractionation is Zr because it is compatible only in zircon and other trace phases which fractionate at high levels of silica (ie. above 68wt% SiO_2 under most normal magmatic conditions)[4]. Thus, the major increases in Zr vs. SiO_2 described in section 2.4.3 (and marked on figure 16) can be reproduced by the fractionation of phases in which Zr is incompatible. However, the underlying trend of increasing silica with a slight decrease in Zr content cannot be reconciled in this way. Instead, a model is required where by the Zr content of the magma is effectively diluted as the silica content increases. Two processes which might be responsible for this are direct assimilation of crustal material or combined assimilation and fractional crystallisation (AFC: DePaolo 1981). The petrographic observations of quartz and feldspar xenocrysts (section 2.4.2b) would support the involvement of either of these processes.

2.5.1(a) *Quantitative estimates of fractionation*

Fractionation occurs to some degree in most of the sample suites, either as the primary factor governing the evolution to magmas with higher silica contents, or in combination with crustal assimilation. Therefore it is important to have a quantitative estimate of the amount of fractionation, to evaluate its relative contribution to the general process of evolution.

[4] A full discussion of zircon chemistry and its behaviour in calc-alkaline magmas is presented in chapter 6.

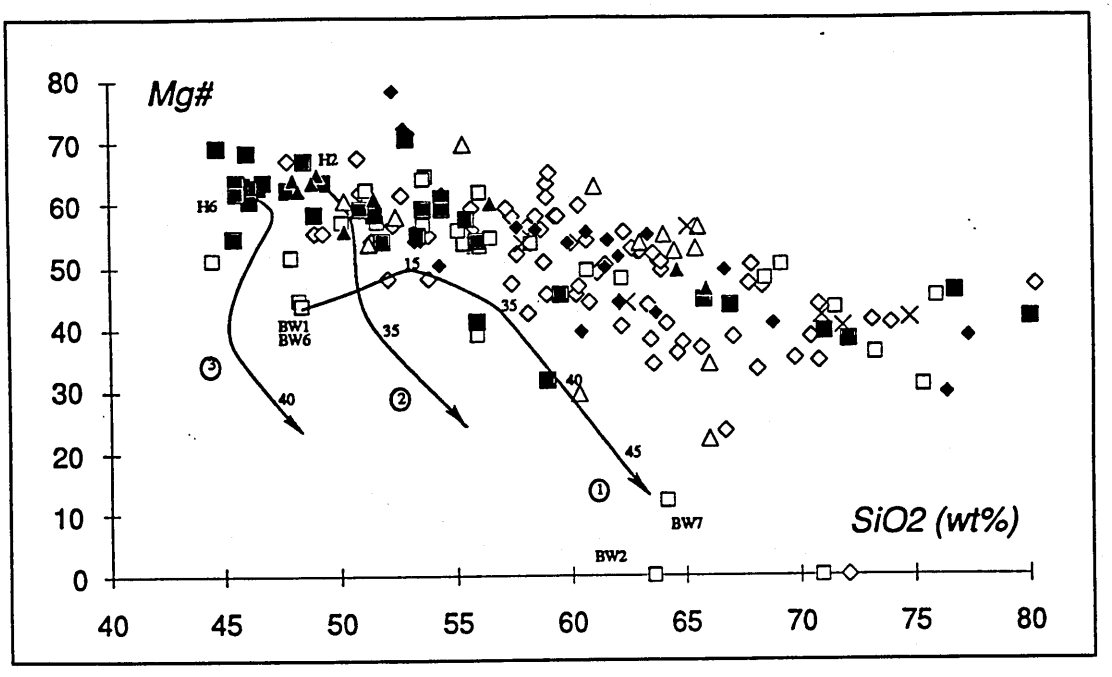

Figure 19. Mg# versus silica wt%. Theoretical 1atm fractionation paths have been calculated from various basaltic endmembers and the degree of fractionation displayed as a wt% (see text for details). Notice that the main sample trend significantly diverges from these models

The widely used computer programmes 'CHAOS' (Nielsen 1989), 'SUPERMIX' (Wright and Doherty 1970) and 'GENMIX' (Le Maitre 1981) permit the generation of theoretical models of fractionation and can provide quantitative as well as qualitative estimates of mineral extraction. Some examples of such theoretical fractionation paths, generated using the CHAOS programme, are illustrated on figure 19. Model 1 apparently reproduces the inferred fractionation link between samples BW1&6 and associated samples BW2&7, and the estimated amount of fractionation from figure 19 is >45wt%. However, BW2&7 are unusual in the context of the overall trends, and thus the theoretical fractionation paths fail to reproduce the observed spread of the remaining CRT analyses. This may be because the CHAOS programme only permits modelling at atmospheric pressure and, while the actual pressure of fractionation for the CRT samples is not directly known, the conditions inferred by the programme might be inappropriate. Thus, it would be useful to assess the possibility and degree of fractionation in an empirical manner, that is independent of pressure.

Pearce Element Ratio (PER) modelling (after Pearce 1968) is a powerful tool in this respect, and the details and limitations of this technique are discussed in chapter 6. In essence, PERs compare data in a form normalised to an element (ω) that is incompatible in

the bulk mineral assemblage which is thought to have fractionated. As described in the previous section, the *absolute* abundance of ω will remain unchanged if the magma behaves as a closed system. Thus, by scaling the change in mineral proportions to the change in ω, it becomes possible to model absolute amounts of mineral fractionation quantitatively.

The effects of pressure can be overcome if the data are considered in terms of standard CIPW normative mineral abundances. Using such standard (molar-) mineral compositions, PER modelling is more robust than other techniques because no assumptions are made about the precise chemistry of the fractionating phases.

Some examples are shown in figure 20 for related samples which fall within the bulk of data on figure 19. In figure 20, Zr is taken as the standard incompatible element, ω, although the ratios are also scaled to the Zr content of the most mafic magma from each studied suite. The samples used in this scaling process are indicated in the figure caption. The vertical axes on figure 20 are in weight percent terms, therefore any vertical difference between individual sample positions, and that of the most mafic sample, can be directly interpreted as a wt% fractionation or cumulation of the normative mineral. For instance, samples within the middle sequence of lavas from the Eldorado Mts. may be related by fractionation:

E5 is the most primitive lava with a Zr concentration of 323ppm, and E10b is the most evolved in the series with a Zr concentration of 385ppm. Thus, the scaling factor for the normative mineral contents of E10b is ~0.84 (ie. 323/385). Sample E5 has a normative diopside content of 17.3wt% and the scaled normative diopside content of E10b is 8.5wt% (reduced from 10.1wt%). Hence, a possible fractionation of approximately 8.8wt% normative diopside between the two samples.

A summary of such calculations is presented in table 1 (page 73).

The results in table 1 indicate that fractionation is important in the post-extensional suites, in the later magmas of the Eldorado Mts and at Oatman, where two cycles of fractionation occur. The general positive correlations between incompatible trace element abundances and silica, noted in section 2.4.3a for the Oatman samples, can now be reconciled with this

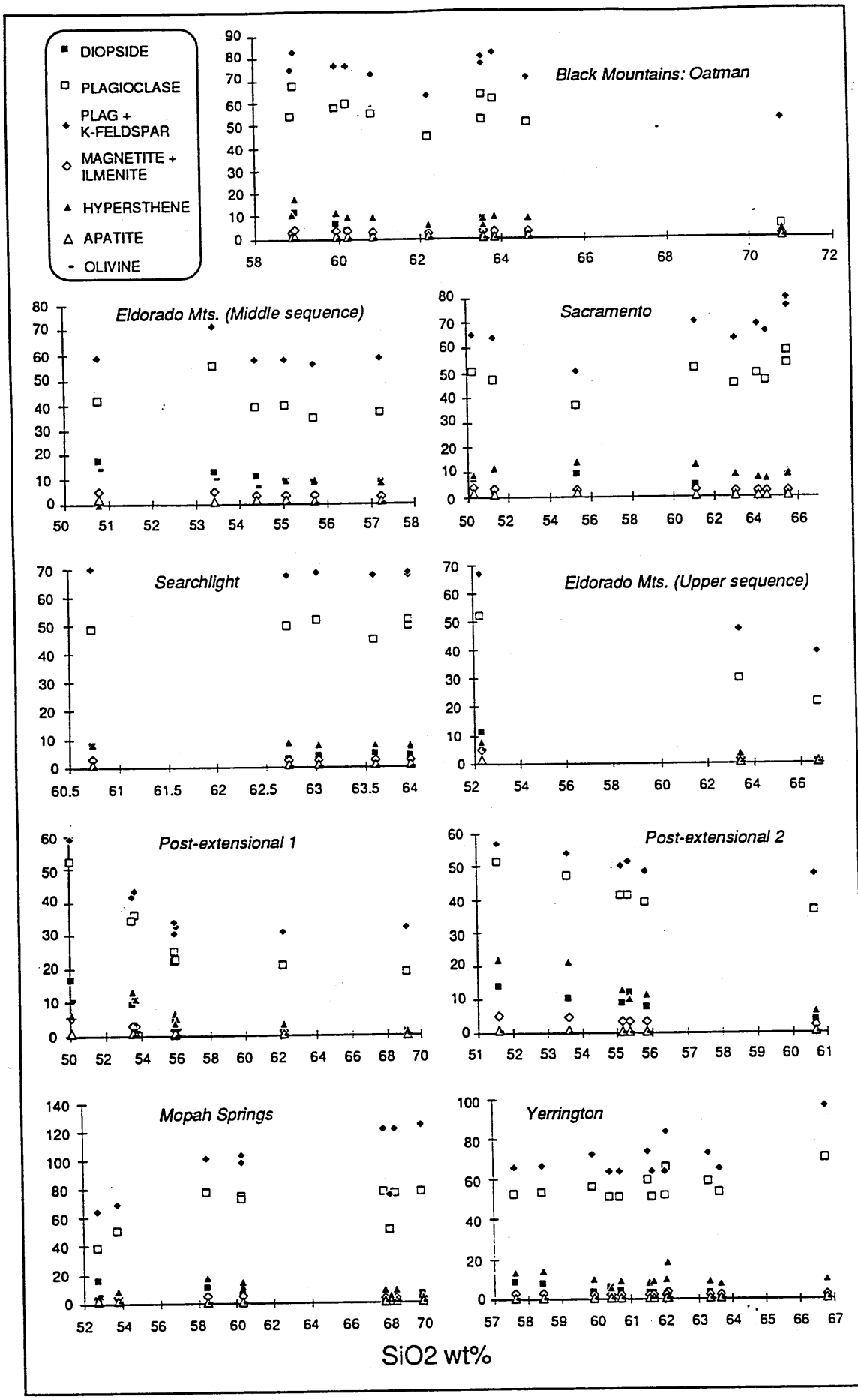

Figure 20. Simple Pearce Element Ratio diagram. Vertical axes are CIPW normative compositions (see key) multiplied by a scaling factor of $[Zr_0 / Zr_i]$, where Zr_0 is the Zr content of the most mafic sample from each suite and Zr_i is the Zr concentration in each individual sample i. From the top anticlockwise the Zr_0 samples used are: BM5, E5, SL3, K5, MS2, Y6, BW4, E7, and S1. See text for discussion.

fractionation. The observed negative correlation between Sc and SiO_2 (see figure 17) is also consistent with the results in table 1 because ≈30 wt% of the overall fractionating assemblage is pyroxene, in which Sc is highly compatible. As anticipated from the major element data, PER modelling predicts that opaque oxides and/or apatite fractionate to some extent in virtually all of the investigated sample suites.

Suite	Silica Range (wt% SiO_2)	Phase Fractionation %						*Total wt % Fractionation*
		Di	PL	Mt+Il	HY	Ol	Ap	
Oatman	58.9-62.2	10.7	22.9	2.2	11.9	0	0.1	*47.8*
Oatman	63.5-70.8	8.4	57.2	2.2	2.3	0	0.6	*70.7*
Post-extn 1	50.0-56.0	11.1	30.3	3.6	-- 10.0 ---		0.2	*55.2*
Post-extn 2	51.5-56.0	10.0	14.9	2.9	15.4	0.3	0.4	*43.9*
Eldorado (Upper)	52.3-66.7	11.4	31.1	3.9	6.4	5.1	1.5	*59.4*
Eldorado (Middle)	50.8-57.2	8.8	5.0	1.8	-- 5.6 --		0.8	*22.0*
Mopah Springs	52.7-69.8	9.6	[38.8]	1.7	1.1	5.4	1.2	*19.0*
Mopah Springs	58.5-69.8	5.0	[0.1]	2.4	14.0	0	0.3	*21.7*
Yerrington	57.6-59.9	8.6	[0.5]	0.9	6.2	0	0	*15.7*
Yerrington	59.9-63.5	3.4	2.5	0.2	2.2	0	[0.1]	*8.3*
Sacramento	51.3-64.5	1.1	0.7	1.6	4.4	1.2	0.3	*9.3*
Post-extn 1	56.0-69.2	4.5	3.4	2.6	-- 5.4 --		0.4	*16.3*
Searchlight	60.7-64.0	3.9	[2.7]	0.5	0.9	0	0.1	*5.4*

Table 1. Weight percent fractionation of normative mineral phases in figure 20. Square brackets denote addition / cumulation of material. Oatman data is split into two cycles fro ease of representation.

Notice from figure 20 that normative K-feldspar (and plagioclase) contents often appear to increase with increasing silica, particularly at high silica contents (eg. at Yerrington and Mopah Springs).The overall degree of fractionation, and particularly the contribution of mafic phases, is much lower in the syn-extensional suites from Searchlight, the Sacramento Mts, Yerrington and Mopah Springs. However, these suites cover similar (or larger) increases in silica to those observed in the other suites.[5]

[5]Mean total fractionation in the upper section of table 1 is 55.4wt%, in the lower section the mean is 15wt%.

The division between the high and low wt% fractionation suites is represented by the two sections to table 1. On average the high wt% fractionation suites record ≈3.7 times the amount of fractionation as the low wt% suites for the same change in silica content. It is possible that this difference is primarily as a result of a difference in the fractionating assemblages. Suites in the high wt% group are dominated by plagioclase fractionation, and non-silicate phases comprise only ≈6 wt% of the fractionating assemblage. In contrast, suites in the low wt% fractionation group are dominated by Ol-Cpx-Opx fractionation, and non-silicate phases comprise up to ≈15 wt% of the assemblage.

Using the fractionating assemblages in table 1, the *maximum* wt% fractionation difference between the two groups, that can be accommodated by the different silica contents of the two assemblages, is only a factor of ≈1.6. The mean difference is calculated as a factor of 1.2, which is less than one third of the observed factor. Therefore, it must be concluded that other processes besides fractionation control the evolution to high silica in these suites, as was implied by the raw major and trace element versus silica variations.

2.5.2 Primary basalts

The main influences on primary basalt magma composition are expected to be source mineralogy, the degree of partial melting, and the extent of trace element enrichment / depletion in the source. To assess and distinguish these factors it is essential to consider samples of primary or near-primary nature, that have not been significantly affected by contamination or fractionation. Thus, in this section, the CRT basalts are evaluated for their potential as representing primary or near primary magmas.

Primary basalts have typically been defined as having Mg#s ≥ 71 (eg. Green et al 1974), but only three samples in the data set meet this criteria, and the petrography of these samples (all from Yerrington) is dominated by euhedral olivine phenocrysts, suggesting at least some olivine accumulation. Most of the CRT basalts have Mg#s between 58 and 70, although this is dependent on assuming a general Fe^{2+} / Fe^{3+} ratio of 0·85; a forced assumption because XRF analysis makes no distinction between Fe^{2+} and Fe^{3+} ions.

Considering the alkaline nature, and therefore potentially higher fO_2 conditions, this assumed ratio may be too high, so that samples could actually have higher Mg#s than presented in figure 19.

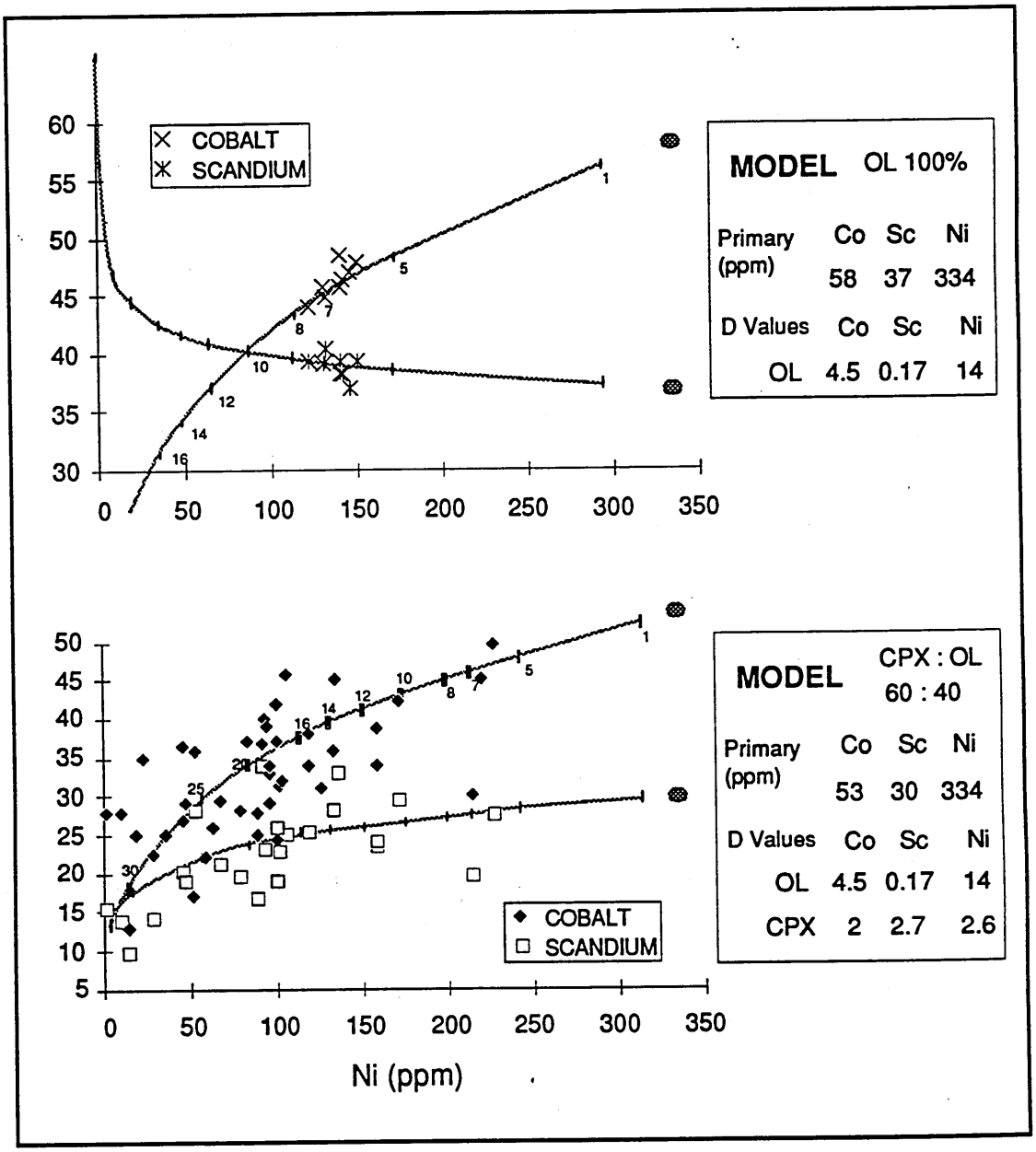

Figure 21. Cobalt (Co) and scandium (Sc) variations with nickel (Ni) content. 15Ma alkali-olivine basalts from Lake Havasu City are plotted in the top part of the diagram, and other CRT basalts in the lower portion. Model fractionation curves are drawn through the data from primary magma compositions indicated by the shaded lozenges. See text for discussion.

Phenocryst assemblages suggest that olivine and / or clinopyroxene have fractionated to some degree in most of the basalt samples. Thus, the distribution of trace elements compatible in these phases (ie. the transition metals) should provide a more realistic constraint than Mg# for the degree of evolution from primary magmas. Variation in the

representative compatible elements Sc, Co and Ni are displayed in figure 21; Ni is highly compatible in olivine, Co is more compatible in olivine than clinopyroxene, and Sc is highly compatible in clinopyroxene with respect to olivine (Henderson 1986). Cr is not considered because of problems arising from its extreme compatibility in the trace phase spinel, which may occur as inclusions in clinopyroxene (see section 2.4.2c).

The 15Ma alkali-olivine basalts from Lake Havasu City display a slight negative correlation between Sc and Ni, suggesting that clinopyroxene was not a fractionating phase. This is in accordance with observed phenocryst assemblages which indicate fractionation only of olivine from their primary magma. The inferred primary basalt magma has Ni and Co concentrations similar to those proposed by Ormerod (1988) for similar basalts in the Big Pine Volcanic Field of California, although the initial Sc content is is estimated to be 12ppm higher. Using this inferred primary basalt composition, the alkali olivine basalt samples can be modelled by between 5 and 8 wt% olivine fractionation (figure 21 top).

The other samples suites have rather more scattered Co-Ni-Sc variations, reflecting the greater spatial and temporal distribution of the samples. However the overall variations can be approximately modelled by a 60:40 ratio of clinopyroxene and olivine fractionation. A similar primary magma is taken as the starting composition, but the range of published clinopyroxene distribution coefficients necessitates that the initial Co and Sc contents be lower than that of the alkali olivine basalt primary magma. Most of the remaining basalt samples can be accommodated by between 5 and 25 wt% fractionation from this second hypothetical primary magma; the rapid decline in Sc at low Ni may indicate that the proportion of fractionating clinopyroxene increases with the degree of evolution (figure 21 lower).

These results suggest that it should be possible to include all of the alkali olivine basalts (and many of the other samples) in the detailed geochemical modelling presented in the following section, and in the succeeding chapters when the nature the basalt source(s) and the degree of partial melting are considered. However it is accepted that some caution must also be applied, and that many of the interpretations will only be of a general nature.

2.5.3 Normative modelling of basaltic samples

Analyses expressed in the form of normative mineral abundances have already been shown to be valuable for interpreting the evolution of sample suites to higher levels of silica. Equally, normative models may also be applied to basaltic suites to interpret the general relationship between samples. Typically this involves the use of phase diagrams, in conjunction with detailed petrographic observations.

2.5.3(a) *The ol-cpx-opx-ne-plag phase diagram*

Most of the CRT samples are alkalic or hypersthene - olivine normative, and olivine, plagioclase and clinopyroxene are observed as the principal phenocryst and groundmass minerals. Thus, the system ol-cpx-opx-ne-plag is probably the most appropriate for interpreting the CRT samples (see figure 22). Samples on this phase diagram have been projected from normative plagioclase, a phase that is present in all of the basalts. Experimental cotectics (liquid lines of multiple saturation) for 1 atmosphere and 8-30kb have been reproduced from Sack et al (1987).

Although the bulk of samples scatter between the two experimental cotectics, there are a number of exceptions, notably samples M2, MO1, H1 and some of the 15Ma alkali olivine basalts from Lake Havasu City. These fall on or adjacent to the cotectics and it is interesting to observe that all of these samples are approximately aphyric (see appendix B for brief petrographic descriptions). In particular, the 15Ma alkali olivine basalts display groundmass intergrowth textures that would be consistent with the cotectic crystallisation of clinopyroxene, plagioclase and olivine.

In section 2.5.2 the 15Ma alkali olivine basalts are modelled by olivine fractionation from a primary magma, and on figure 22 these basalts define an olivine fractionation vector away from the 8-30kb cotectic[6]. The trend intersects the cotectic in the region of experimental

[6] Notice that two of the altered samples from this group are displaced away from this general trend towards more ne-rich compositions.

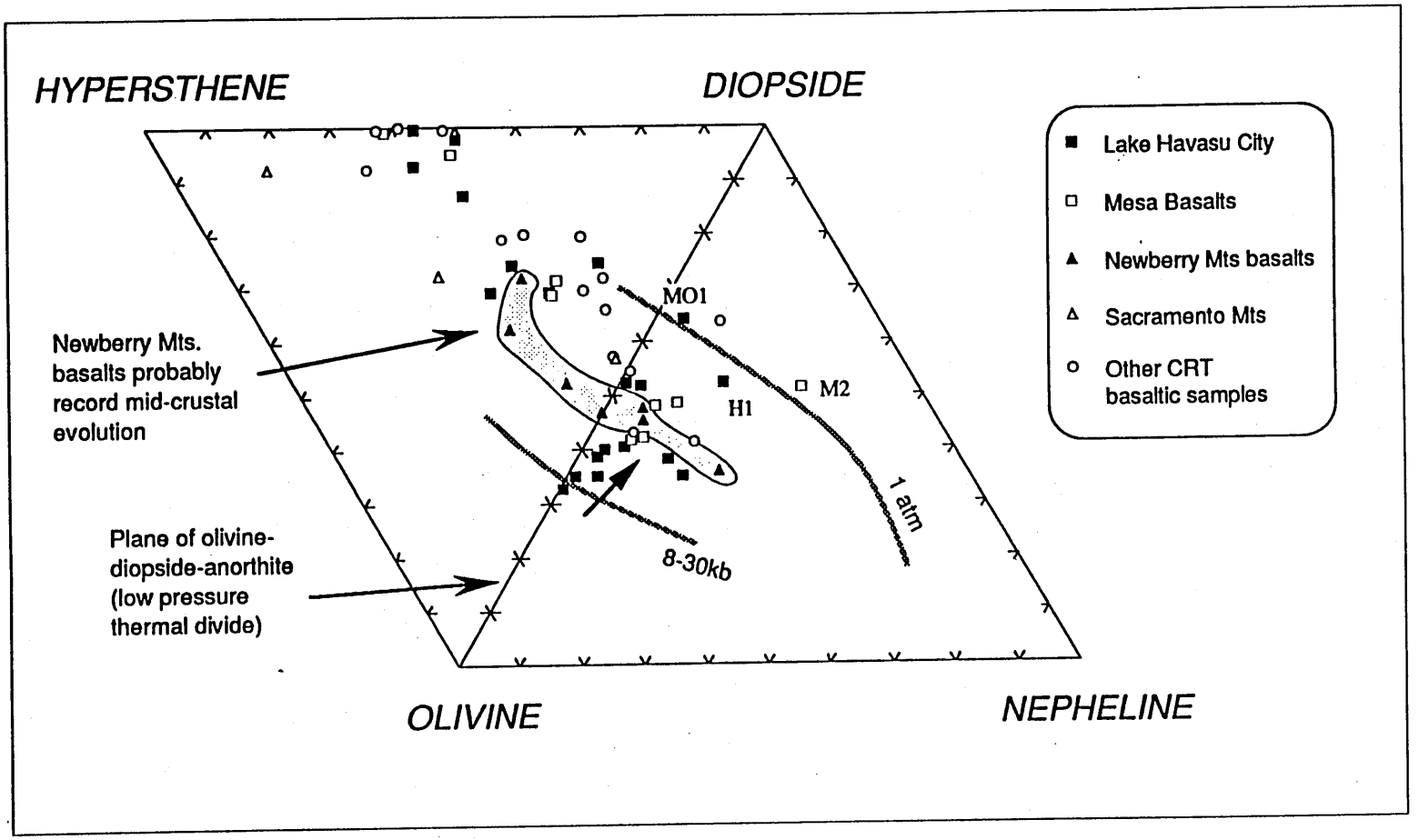

Figure 22. Olivine- clinopyroxene- orthopyroxene- nepheline- plagioclase phase diagram for normative compositions. All samples have ≤56 wt% silica and have been projected from plagioclase. Experimental cotectics (ol-cpx-opx-plag, shaded lines) are reproduced from Sack et al (1987). Solid arrow indicates evolution by olivine fractionation for the 15Ma alkali olivine basalts from Lake Havasu City. See text for discussion.

results for 10kb (Sack et al 1987). The cluster of samples close to the cotectic at this pressure suggests that the basalts probably reached the surface from near Moho depths with only minor re-equilibration.

Basalts that fall on or close to the 1 atmosphere cotectic are some what evolved, recording final equilibration at or near to the Earth's surface. These samples mostly occur in early, possibly pre-extensional, sequences from a number of areas, although some of the samples are post-extensional. Polybaric fractionation is likely to have played a major role in the evolution of the remaining samples that plot between the 1 atmosphere and high pressure cotectics on figure 22. Within this group of samples the Newberry Mts basalts define a trend generally parallel to the two experimental cotectics. This trend crosses the olivine-diopside-plagioclase plane that is described as a thermal divide in Presnall et al (1978), and references therein. This divide is thought to exist at low pressures although between 3 and 5kb it apparently disappears and, at these pressures, magmas may fractionate across the olivine-diopside-plagioclase plane to produce more evolved sub-alkaline rocks from an initially alkaline parent. Thus, it is suggested that the Newberry Mts. basalts may record evolution at some depth within the middle crust or the lower part of the upper crust.

The trace element data described in previous sections of this chapter indicate that there are a number of distinct basalt types in the CRT. However, the normative mineral compositions (and basalt positions projected onto figure 22) are difficult to interpret in terms of how these various basalts may be related to each other. For example, it is not clear whether the 15Ma alkali olivine basalts could be derived from the same primary magma as the typical CRT basalts. Such problems will thus be addressed in the following chapters that concern detailed trace element and isotopic modelling.

2.6 Summary and Discussion of Geochemistry

This report covers the regional geology of the Colorado River Trough (CRT) along the border between Arizona, California and southern Nevada. In particular, the characteristics of Cenozoic magmatism and extension have been described. The CRT is geologically significant in terms of the Cenozoic history of the western United States because it represents a corridor of extreme crustal extension, and it was also the locus of intense magmatism during the Miocene. Some simple geochemical and petrographic features of the magmatism have been discussed and these will form the basis of more detailed work to be presented in the following chapters.

Inherited tectonic features appear to have had at least some influence in localising Cenozoic extension (and probably magmatism) within the CRT. The region is sandwiched between the Lake Mead / Las Vegas Shear Zones, a possible Proterozoic shear feature to the east and the line of a Mesozoic intra-arc graben to the west. However, it is not thought that the area underwent any significant crustal thickening during the Laramide Orogeny.

The axis of the CRT is marked by a semi-continuous line of metamorphic core complexes which represent sections of the middle crust uplifted during extension. The degree of extension is apparently asymmetrical across the CRT and the average value may be in the region of 100%. However, values in excess of 250% are recorded in the vicinity of the core complexes. Parallel dyke swarms and fault orientations indicate that the extension direction varied from northeast-southwest to east-west, going north along the corridor. Similarly, the extension and volcanism spread from south to north with time.

Prior to the onset of Cenozoic extension and magmatism any basement cover sequences in the CRT were completely removed. Thus, early Miocene volcanism developed directly onto an exposed crystalline basement consisting of Proterozoic granulite and Mesozoic arc granites.

Trachyandesitic compositions dominate the early to Middle Miocene volcanic sequences,

although the volcanism was often more basaltic than its Great Basin time equivalents. Much of the basaltic volcanism was alkaline in nature, but a whole range from nepheline to quartz normative magmas are observed. A few, mainly post-extensional, basalts are tholeiitic, however it is suggested from petrographic observations that fractionation of opaque oxide minerals may have suppressed the development of typical iron enrichment trends.

Typical pre- and syn-extensional basalts from the CRT have trace element abundances significantly enriched above primitive mantle values, with maximum enrichment of the LREE and LIL elements. Trace element patterns display a Ta-Nb trough on mantle normalised 'spider' diagrams and a step between Zr/Sm and Ti that generally enlarges with increasing silica. These characteristics also appear in some of the post-extensional basalts, and thus it is likely that much of the CRT basaltic magmatism (irrespective of location or time) is related in some way, perhaps by source. However, a number of the younger post-extensional samples have much smoother spidergram patterns and display no Ta-Nb trough; basalts with similar patterns are classified as being of 'Basin and Range- type' by Fitton et al (1991).

Within the main group of syn-extensional basalts, a geochemically interesting subset is identified in the Lake Havasu City region. These 15Ma alkali olivine basalts have the distinctive Ta-Nb trough, but low Ti/Y ratios, a reduced Zr-Ti step and overall lower concentrations of incompatible trace elements. Such basalts may represent some of the least evolved magmas in the CRT and thus their origin will be discussed in some detail in Chapter 4. It is also worthy of note that the alkali olivine basalts only occur in the region that has undergone the most extreme extension. Therefore a relationship between tectonics and types of magmatism is a possibility.

Geochemical modelling indicates that some of the CRT basaltic magmas (in particular the alkali olivine basalts described above) may have reached the surface directly from deep crustal levels. At these near Moho depths, the magmas apparently came to equilibrium by fractionating predominantly olivine and/or clinopyroxene. Glazner and Ussler (1988; 1989) and Ormerod (1988) record similar high pressure fractionation for basalts in the Mojave

Desert and the Pig Pine Volcanic Field, respectively. Such fractionation may therefore have been a pre-requisite for continued progression of the magmas through the crust. Most of the basaltic sample suites record at least some polybaric evolution (fractionating predominantly plagioclase, olivine and clinopyroxene) probably within the crust. Only a few samples appear to have re-equilibrated onto 1 atmosphere cotectics which may indicate that high-level magma chambers were generally not well developed. Accordingly, basaltic volcanism along the centre of the CRT appears to be related to dyke swarms rather than to localised volcanic features.

Throughout the various CRT sample suites, petrographic evidence supports evolution models to higher silica by both fractionation and crustal assimilation. Poly-crystalline quartz xenoliths are observed in some basaltic samples and plagioclase xenocrysts with complex disequilibrium textures are prominent in samples of both basaltic and trachyandesitic composition. The large change in silica content of some suites displaying only minimal fractionation suggests that mixing of basalt with a high silica contaminant is often the dominant process.

Assimilation could also explain the decreased scatter on many of the major and trace element variation diagrams at high levels of silica. Because, in light of the factors outlined in section 2, it is anticipated that the contaminant would represent a minimum eutectic melt of granite, and therefore be of restricted chemical composition (Winkler 1979; Patiño Douce et al 1990). Mixing of such a contaminant with initially variable basaltic magmas will naturally induce convergence in chemical trends as the proportion of contaminant increases. Furthermore, assimilation dominated processes would be consistent with the observed evolution from predominantly alkaline basalts towards rhyolite and dacite compositions, rather than towards phonolitic compositions.

More detailed evolution models based on the interpretation of isotopic and trace element data will be presented in the following chapter. Here, the relative contributions of AFC processes and direct assimilation to produce higher silica magmas will be assessed. Possible links between magmatism and tectonics are also explored in chapter 3 in the light

of current models proposed for crustal extension in the western United States..

In Chapter 4 the least evolved samples from the CRT will be modelled in an attempt to define the trace element and isotopic composition of their source(s). Relationships between the various basalt groups (and their sources) will be discussed, as will any implications these might have for the geochemical development of the basaltic magmatism with time.

The Origin and Significance of Syn-extensional Volcanism in the Colorado River Trough (W.USA)

3.1 Introduction

The influence of tectonics on magmatism (and vice versa) is exemplified in continental areas by the general association of tholeiitic basalts or bimodal volcanism and crustal extension (for example, in the Paraná Basin, the East African Rift and the Tertiary Volcanic Province of NW Scotland). In contrast, intermediate silica and calc-alkaline volcanism is normally associated with the compressional tectonic regimes prevalent above subduction zones (eg. in the Andes, and the Cascades Range). However, much of the volcanism accompanying Eocene-Miocene extension in the Basin and Range Province of the western United States is characterised by intermediate to high silica magma types (eg. Glazner 1989; Gans et al 1989; Feeley and Grunder 1991; Smith et al 1990). Calc-alkaline evolution trends are often observed in the Great Basin, although predominantly alkaline basalts occur in association with corridors of intense extension. In general, it is only in the later stages of magmatism (typically post-extensional) that basaltic or bimodal volcanism became important. Understanding the origin of the earlier magmas is therefore a crucial step in producing an overall model for the development of the Basin and Range Province.

In general the intermediate to high silica syn-extensional magmas of the Basin and Range have been attributed to one, or more, of the following processes:

i) fractionation from an initially basaltic magma,

ii) fractionation with assimilation of higher silica (crustal) material,

iii) direct mixing between silicic and basaltic magmas.

This paper assesses the merits of each of these processes in detail by considering the geochemical trends displayed throughout rocks from a number of volcanic sequences. The approach is to attach less importance to the localised variations in volcanic style and magma

geochemistry, and to concentrate mainly on recognising and evaluating the overall patterns that emerge.

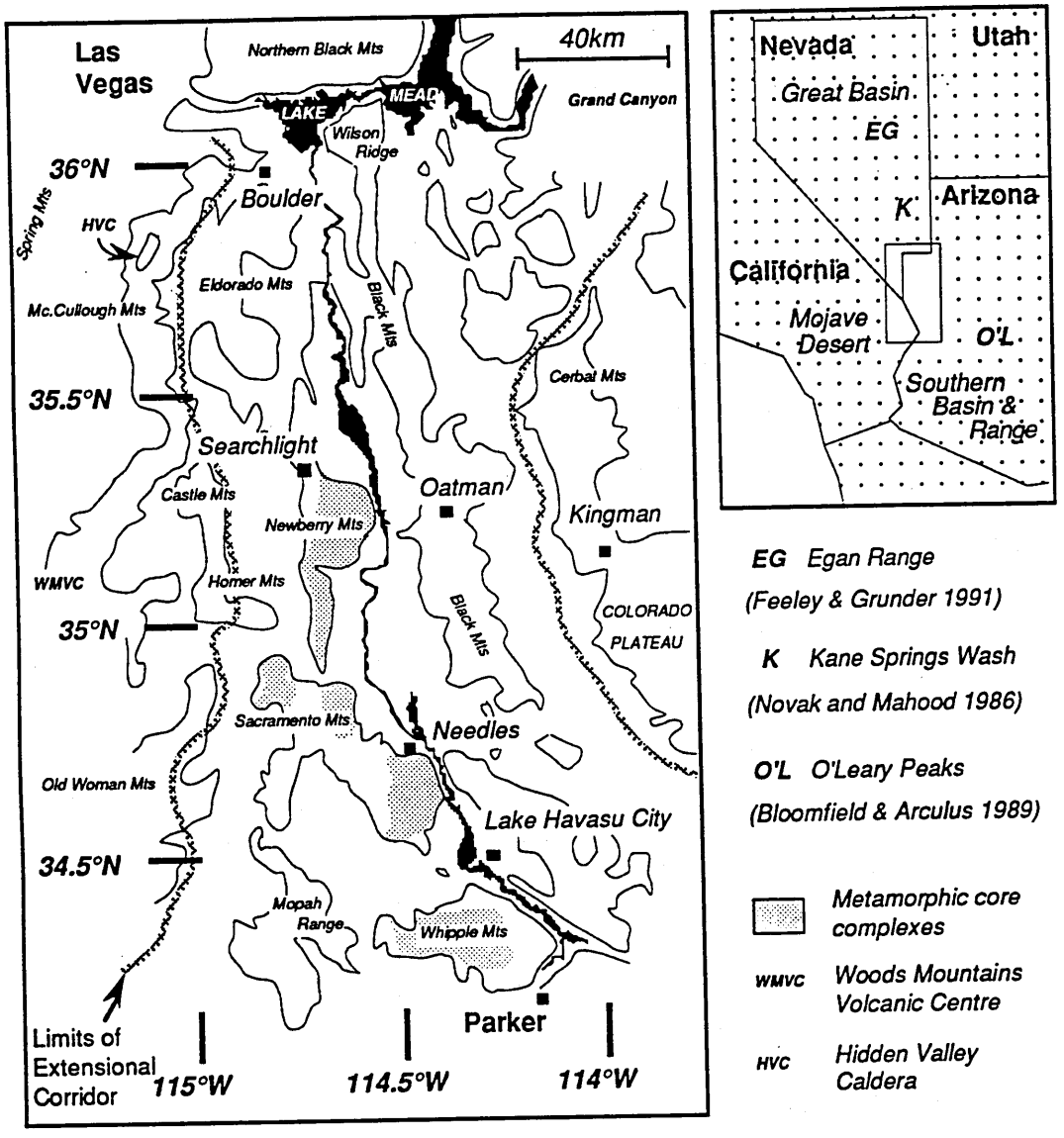

Figure 1. The Colorado River Trough region and the extensional corridor; Colorado River in black. The locations of other suites used for comparison in this study are also indicated. The Woods Mountains Volcanic Centre is a caldera inferred from gravity anomaly data (Mikus and James 1991). This feature, and the Hidden Valley Caldera are the only such structures in the vicinity of the CRT, both lie beyond the margins of the extensional corridor.

The main study area covers volcanism in the Colorado River Trough (CRT), an 80km wide physiographic low along the Colorado River, from Las Vegas in the north to the town of Parker 290km to the south (figure 1). The area lies between the Great Basin and the Southern Basin and Range Province and has been described as a corridor of extreme crustal extension (Howard and John 1987; Davis and Lister 1988). The axis of the corridor is marked by a chain of crystalline 'metamorphic core complexes' (figure 1). These represent

mid-crustal material uplifted beneath low angle detachment faults and potentially indicate localised extension in the range of 250-450% (see Chapter 2). Synextensional volcanism occurred across the whole corridor during the Miocene (~22-15Ma), enabling sample suites to be collected from both the highly extended axis and the poorly extended corridor margins. Comparisons are also made to published data from the Great Basin (Kane Springs Wash and the Egan Range), and to some Miocene-Pliocene fields in the Southern Basin and Range (O'Leary Peaks, see figure 1).

The final part of this study considers how the proposed origin of the intermediate to high silica volcanism might have influenced the structural development of the Colorado River Trough. The conclusions are compared with published structural interpretations of the extensional corridor, and then related to a general model for the development of the Basin and Range Province.

3.2 Volcanism in the Extensional Corridor

Syn-extensional volcanism in the extensional corridor is dominated by intermediate silica (55-66wt% SiO_2) magma types, although samples are recorded over the whole range of silica from 44-80wt%. Most of the samples are highly porphyritic, often with crystals displaying complex zoning and overgrowth of partially resorbed cores, although some of the highest silica rocks are almost aphyric. Basalts and rhyolites are common at the base of many sequences, and alkali-olivine basalt dykes and flows (46-48wt% SiO_2) occur at Lake Havasu City and in the Newberry Mts associated with the final stages of extension (~15Ma). Prominent rhyolitic plugs generally represent the last stage of volcanism throughout the Black Mts and in the Mopah Range.

The spatial distribution of silica variation across the corridor is displayed in figure 2. Notice that the Lake Havasu City suite, from the corridor axis, is bimodal and is dominated by basaltic and basaltic andesite magmas. Brief episodes of bimodal volcanism also occurred in the Castle Mts (Turner and Glazner 1988) and in the vicinity of Lake Mead during the middle Miocene (see figure 1 for locations).

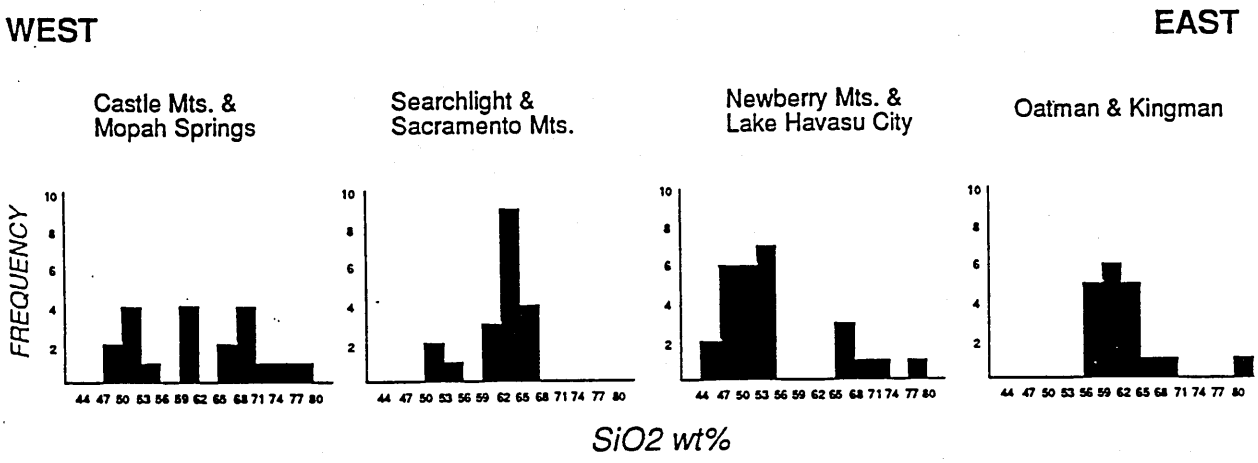

Figure 2. Silica distribution in sample suites from across the extensional corridor, see figure 1 for locations. Castle Mts data from Turner and Glazner (1988). The Newberry Mts and Lake Havasu City suites mark the axis of the corridor. Note that the compositional gap in these suites is the inverse of that displayed by suites from adjacent areas. (15Ma alkali-olivine basalt flows from Lake Havasu City have been represented by just one unit in the 44-47wt% SiO_2 category, in line with their rather limited volumetric abundance).

Because of the intense nature of the extension it is often difficult to assess the original thickness of the volcanic sequences, except on the margins of the extensional corridor. However, reconstruction of the Eldorado Mts complex (Anderson 1972) suggests an original lava pile thickness in excess of 5000m. Away from the corridor axis the thicknesses decline, to ~3100m at Oatman, ≤800m at Mopah Springs (Hazlett 1986) and ~170m at Kingman (Beusch and Valentine 1986).

Three large mafic strato volcanoes and their comagmatic plutons can be distinguished around Lake Mead (Weber and Smith 1987) although no other major individual volcanic centres have been recognised within the extensional corridor. The prominence of dyke swarms, small plugs and even individual cinder cones (eg. in the Kingman area) suggest instead that volcanism mainly occurred in fissure style eruptions and associated with small volcanic structures. This is quite unlike the volcanism in the Great Basin at this time (22-15Ma) which was predominantly based around extensive and long-lived caldera systems.

3.3 Geochemistry

Major element vs. silica variations in the syn-extensional volcanics are typically linear up to ~66wt% SiO_2. However, this would be expected for both fractionation and mixing models of evolution. Such major element variations thus provide little information about the relationship of samples across the range of silica. Consequently the emphasis in this paper is on the trace element and isotopic characteristics of the sample suites, and the general patterns that emerge. A more detailed description of the geochemistry and petrography is presented in chapter 2.

3.3.1 Trace element variations

The basalts considered in this contribution all display trace element abundances above that of the primitive mantle and typical Mid-Ocean Ridge Basalts. However, they have depletions in some of the high field strength elements relative to other similarly incompatible elements. In particular the basalts are characterised by low Ta/La ratios (figure 3a), a feature that is usually common in rocks of orogenic affinities (eg. Gill 1981).

The highly incompatible trace elements Pb, Rb, Th and Ba (and K_2O) generally increase in concentration with increasing silica, although these elements do suffer to some extent from mobilisation by aqueous fluids associated with the extension and fault movements. Zr, Nb and the Rare Earth Elements (REE) are unlikely to be affected by this alteration, but their variation with silica is rather more complex. Individual sample suites may show a pronounced increase in the concentration of these elements with silica, although other suites display either a decrease or almost no variation with increasing silica. The underlying pattern is for a convergence of sample suite trends to ~185ppm Zr and ~15ppm Nb at 66wt% SiO_2. Zr and Nb have reasonable positive correlations with the REE. The concentration of Y generally declines with increasing silica, but above ~66wt% SiO_2 a positive correlation between Y and SiO_2 is often observed. At this point Ba and K_2O concentrations either decline or increase at a lesser rate than at low silica, probably as a result of the onset of K-feldspar and/or biotite fractionation. It is also likely that trace

phases such as zircon appear on the liquidus at these higher silica levels (Chapter 6).

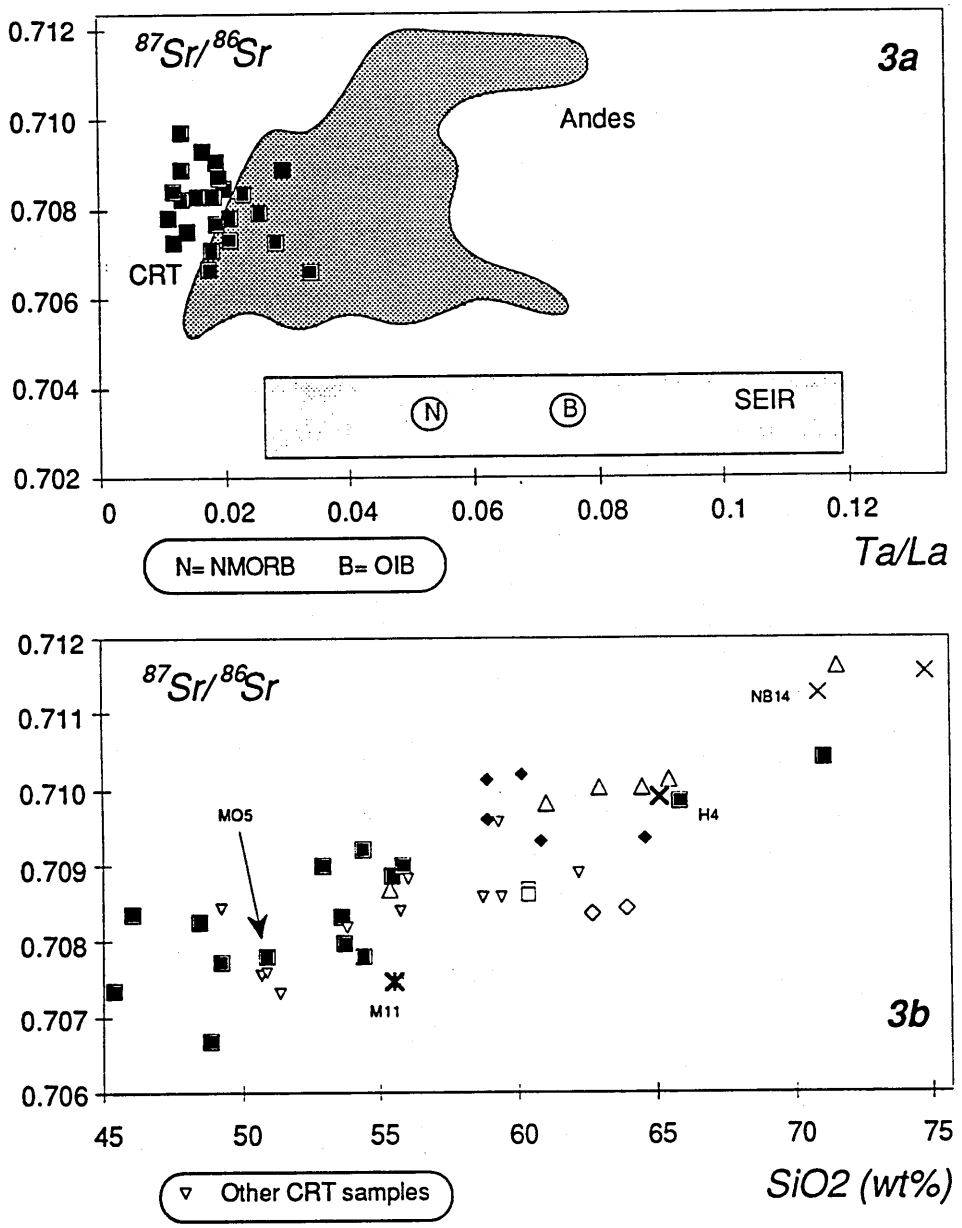

Figure 3a. $^{87}Sr/^{86}Sr$ isotope ratios vs Ta/La for samples from the CRT with <56wt% silica. Comparisons are made to suites from the Andes (OU data base) and average MORB (N) and OIB (B) from Sun and McDonough (1989). The range of data from one ridge segment in the Indian Ocean (SEIR) is also displayed. The CRT samples apparently have strong orogenic affinities. b.$^{87}Sr/^{86}Sr$ isotope ratios vs silica content for syn-extensional samples from the extensional corridor (excluding 15Ma alkali olivine basalts, see Chapter 4). Refer to figure 4 for a general key to the sample suites. Isotope ratios of the granite samples have been time corrected to 20Ma to represent their composition at the time of Tertiary magmatism.

As would be anticipated, Ba/Y, Rb/Y and K/Y ratios increase with silica in the basic and intermediate silica suites, but Ba/Y decreases sharply at higher silica levels. Suites from the extensional corridor also display a large range in the ratios of Ba, Rb and K_2O with Zr and

Nb, although the scatter of data is greater because of the less consistent variability of Zr and Nb concentrations with silica.

3.3.2 Sr isotope variations

$^{87}Sr/^{86}Sr$ isotope ratios increase with silica (figure 3b) and the samples have scattered, but overall positive, correlations between $^{87}Sr/^{86}Sr$ and the trace element ratios discussed in the preceeding section (see figure 7). Basaltic samples range from 0.7065 to 0.7084 with an average of 0.7079 at 50wt% SiO_2. Towards higher silica, samples scatter about a linear array which trends towards the position of Mesozoic granite samples from the Newberry Mts (eg. sample NB14- $^{87}Sr/^{86}Sr$ =0.7113, SiO_2 =71wt%; sample NB11- $^{87}Sr/^{86}Sr$ =0.7099, SiO_2 =65wt%). Some of the data scatter is likely to be the result of alteration, although obviously altered samples have been excluded from this study. Much of the isotopic range displayed by the basaltic samples may reflect source heterogeneities because it is considered that the magmas are derived by melting in the sub-continental lithospheric mantle (see geochemical modelling in Chapter 4).

3.4 Evolution Models

To evaluate if there is any relationship between the typical intermediate to high silica syn-extensional magmatism and crustal extension it is first necessary to consider the likely origin of these magmas. Trace element abundance patterns (see Chapter 2) reveal a marked similarity between the intermediate silica magmas and the less abundant basaltic magmas in the CRT. Thus it is suggested that the magmas may be linked by some evolution process such as those outlined in the introduction.

Trace elements are particularly instructive for defining evolution models because their behaviour under conditions of fractional crystallisation is strictly governed by mineral/melt distribution coefficients (D). The actual behaviour of a specific element is determined from the bulk D-value for the study system, calculated according to the proportions of phases observed, or inferred, to be fractionating (see table 1). Elements with bulk D-values > 1 are compatible in minerals of the fractionating assemblage and the concentration of these

elements in the residual magma will decrease as fractionation proceeds. If the trace element variations do not conform to that anticipated (within reasonable error limits), then it is likely that other processes besides fractional crystallisation were operating.

	D Values						*Bulk D Values for models*			
	Cpx	Plag	Hbl	Opx	OL	Mt+IL	❶	❷	❸	❹
Rb	.05	.1	.25	.001	.006	.01	.049	.066	.11	.16
Ba	.05	.23	.31	.001	.006	.01	.084	.138	.16	.225
K_2O	.03	.17	.6	.01	.007	.0	.06	.101	.208	.35
Nb	.1	.01	1.3	.15	.001	.8	.125	.095	.432	.732
Zr	.1	.01	1.4	.03	.01	.3	.072	.05	.417	.742
Y	.5	.03	2.5	.2	.01	.2	.249	.149	.849	1.35
Sr	.1	1.8	.57	.01	.001	.01	.528	1.01	.669	.787
❶	.4	.27	.0	.12	.13	.08				
❷	.2	.55	.0	.09	.09	.07	Model Mineral			
❸	.4	.27	.25	.0	.0	.08	Proportions			
❹	.15	.27	.5	.0	.0	.08				

Table 1. Crystal/ liquid distribution coefficients used in this study. Data sources: Pearce and Norry (1979); Cox et al (1984); Henderson (1986). The mineral proportions of four model fractionating assemblages, and the corresponding bulk D-values, are indicated See text for discussion. The clinopyroxene and plagioclase dominated model (❶) is taken as the standard for calculating model curves in figures 4-7. Apart from Sr, the bulk D-values resulting from the plagioclase dominated model (❷) are not significantly different to those of ❶, however the hornblende dominated models result in bulk D-values up to an order of magnitude larger.

Trace elements which have similar bulk D-values will be partitioned into the fractionating phases to the same degree and thus the concentration ratios of these elements are unlikely to change with fractionation; similarly, isotopic ratios also remain independent of fractionation. Significant changes in trace element and/or isotopic ratios within a related suite of rocks is therefore another important indicator in identifying processes other than fractionation. In many cases it is also easier to compare different sample suites on the basis of trace element ratios because absolute elemental abundances are naturally prone to inter-suite variation.

In the following models a range of typical syn-extensional basalts and basaltic andesites from 50-55.4 wt% SiO_2 are employed to represent the mafic endmember composition. The

unusual trace element geochemistry of the 15Ma alkali-olivine basalts (see Chapters 2 and 4) probably makes them unsuitable as standard endmember basalts, although they have been indicated on figure 4 for comparative purposes.

3.4.1 Fractionation

Simple crystal fractionation can be expressed by the equation,

① $$C_1\omega / C^{\circ}\omega = F^{(D\omega-1)}$$

(Allegré and Minster 1978) where $C^{\circ}\omega$ is the initial concentration of element ω, $C_1\omega$ is the concentration after fractionation, F is the proportion of melt remaining and D is the bulk D-value of ω between the fractionating phases and the liquid. (Refer to table 1 for D-values and model mineral assemblages used in this paper). To test for fractionation an assemblage of Cpx: Plag: Opx: Ol: Mt+Ilm in proportions of 0.4: 0.27: 0.11: 0.13: 0.08 is taken as a standard. This assemblage is based on general petrographic observations of phenocryst phases and on major element modelling of a fractionated suite in the Eldorado Mts (see Chapters 2 and 6 for a discussion). A model with plagioclase as the principal fractionating phase was also tested, however, the actual effect on the bulk D-values of the trace elements considered in this study is fairly negligable (model ❷ in table 1). The chosen assemblage is therefore thought to be reasonably representative.

Modelled fractionation curves have been added to figures 4-6 based on the assemblage described above. The axes of these diagrams incorporate a trace element ratio, which should not vary considerably with fractionation, versus a trace element abundance which will increase with fractionation because the bulk D-value for the element is <1. The similarity of bulk D-values for Ba, K_2O and Nb results in very little change in the Ba/Nb and K_2O/Nb ratios by fractional crystallisation. However, the greater difference between the D-values for Ba and Y produces a slight increase in Ba/Y ratios with fractionation. Simple fractionation vectors have not been marked on figure 7 because both axes are effectively independent of fractionation, it is therefore important to note the pronounced increase in $^{87}Sr/^{86}Sr$ isotope ratios with increasing Ba/Nb.

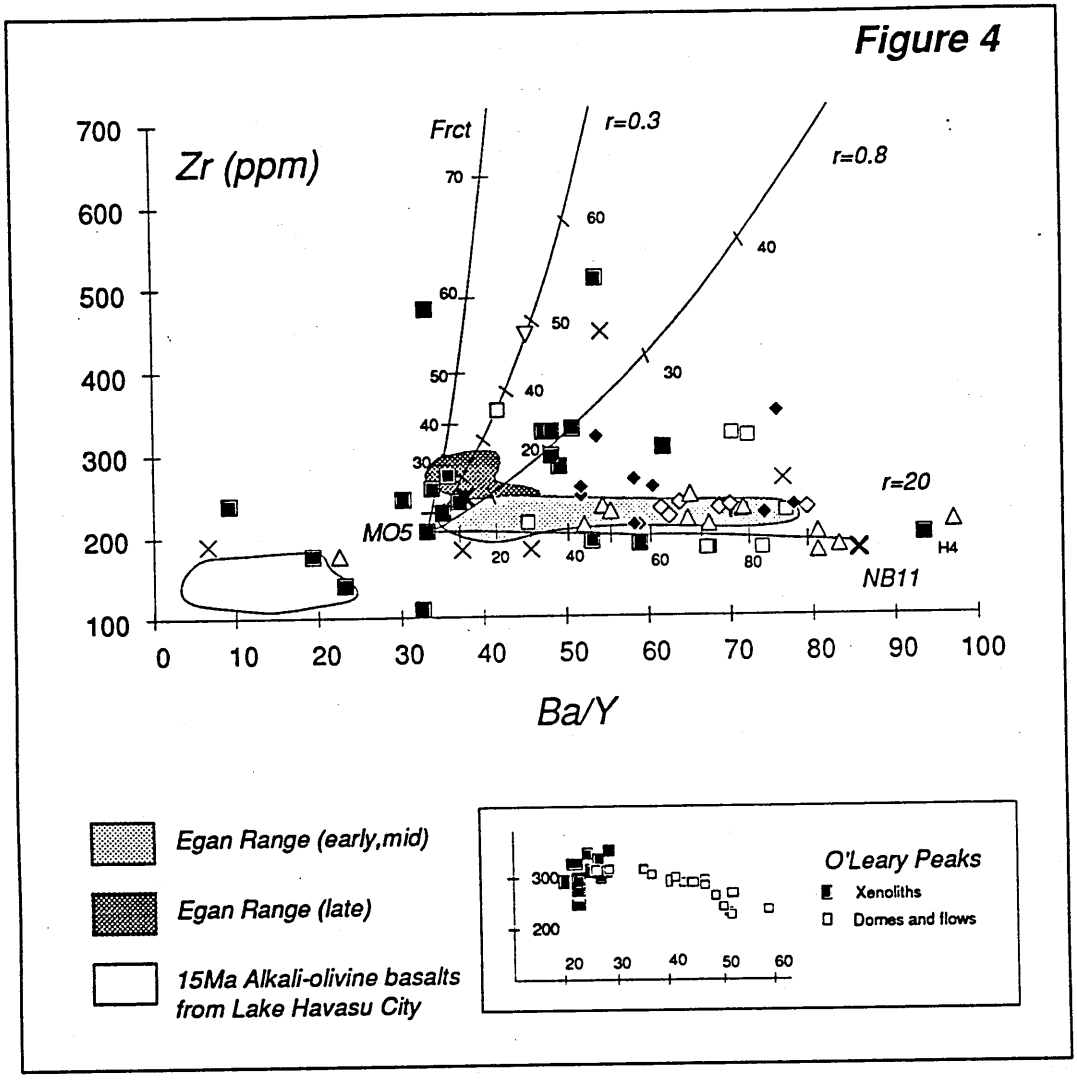

General Key

■ Lake Havasu City	◇ Searchlight
▽ Peach Springs Tuff	□ Mopah Springs
△ Sacramento Mts	◆ Oatman
× 'Granites' (✕ NB11)	✱ M11

Figure 4. Ba/Y vs Zr for sample suites from the extensional corridor, the Egan Range and O'Leary Peaks, inset (xenolith samples are considered to represent mafic melt compositions). Models for simple crystal fractionation (Frct) and AFC (indicated by the 'r' values) have been calculated with model ❶ as the fractionating assemblage (see table 1), and MO5 and NB11 as the mafic and silicic endmembers respectively. Binary mixing conditions are approximated by the r=20 model. Values on model curves indicate degree of evolution from the mafic endmember.

Key to sample groups on other diagrams is as for figure 4, except where stated.

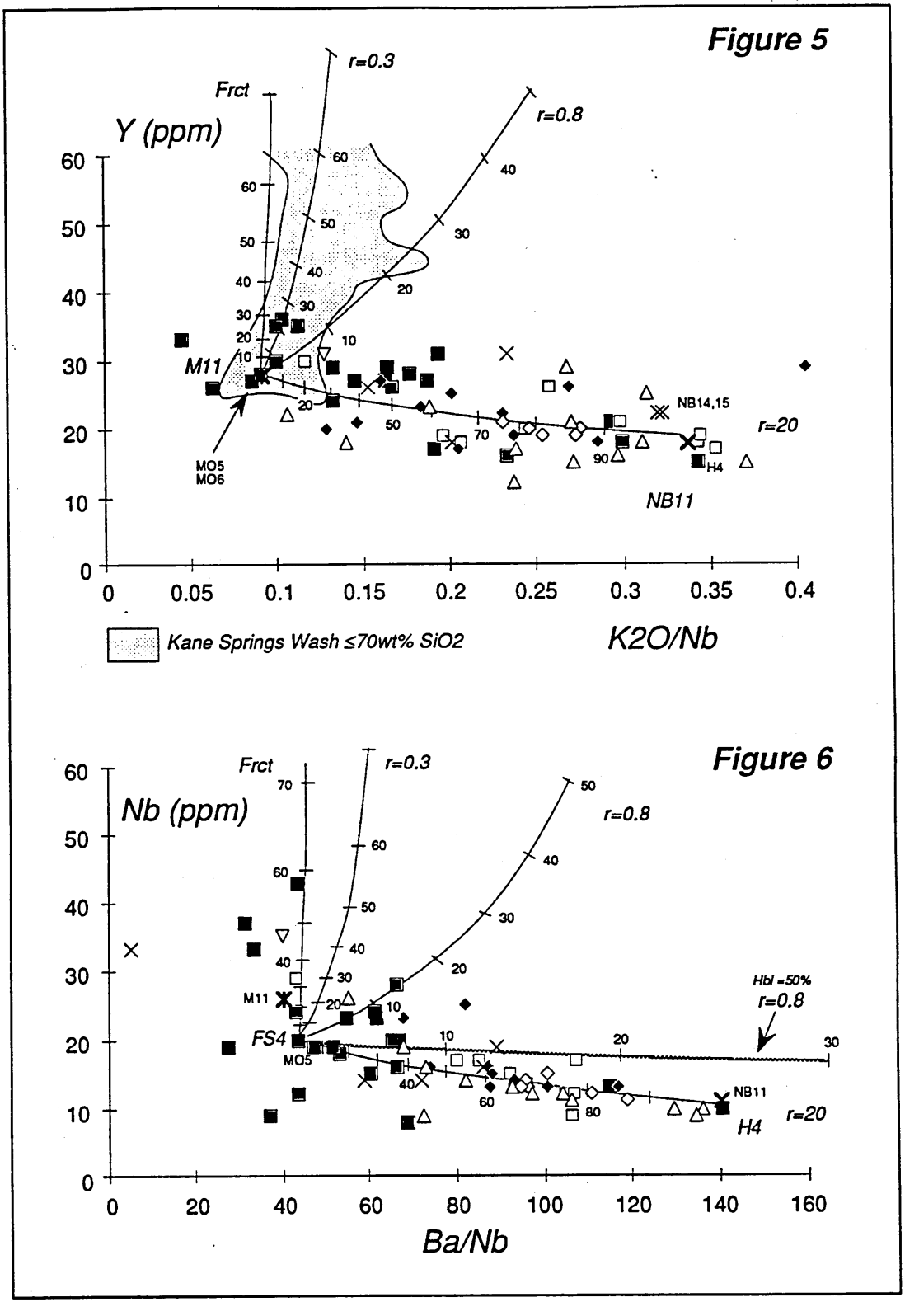

Figure 5. K_2O/Nb vs Y, including the range of data from the Kane Springs Wash caldera in the Great Basin. Models generated as in figure 4 but with M11 as the mafic endmember. Other potential endmember compositions are also labelled. See figure 4 for key to sample suites, table 1 for models.

Figure 6. Ba/Nb vs Nb for extensional corridor samples. Samples FS4 and H4 used as endmember compositions. Hatched line is a hornblende dominated model for the same endmembers, generated using assemblage ❶ in table 1.

Samples from the extensional corridor display a range of Ba/Y from almost 0-100, K_2O/Nb ratios from 0.05-0.4 and Ba/Nb from 2-140. As expected, a number of samples from the Eldorado Mts fall on or close to the modelled fractionation curves, as do some early sequence samples from Lake Havasu City. However, it is apparent that most samples define a trend approximately orthogonal to that modelled for fractionation. The overall trends are towards increasing Ba/Y, K_2O/Nb, and Ba/Nb with only slight increases, or even decreases, in Zr,Y and Nb concentrations. Individual sample suites often define tight linear arrays through this trend (eg. Sacramento Mts and Searchlight samples) although scatter towards higher Zr, Y and Nb is consistently observed in other suites (eg. Mopah Springs and Oatman). Sample suites from O'Leary Peaks (Bloomfield and Arculus 1989), and the Egan Range (Feeley and Grunder 1991) also display similar linear trends orthogonal to the modelled fractionation vector.

These trace element patterns, and the overall positive correlation of $^{87}Sr/^{86}Sr$ isotope ratios with Ba/Nb and SiO_2, suggest that simple fractionation cannot be the dominant process controlling the evolution of the sample suites in this study. Instead it is likely that a contaminant material either mixes with or is assimilated by the basaltic magmas.

3.4.2 Assimilation and Mixing

To model processes involving assimilation and/or magma mixing it is first necessary to define the composition of the potential contaminant. In the extensional corridor the compositional variability of the sample suites indicates that the contaminant has high silica ($\geq$ 65wt% SiO_2), high $^{87}Sr/^{86}Sr$ ($\geq$ 0.709) and at least moderate Ba/Y, K_2O/Nb and Ba/Nb ratios, while maintaining reasonably low Zr, Y and Nb concentrations. Typical contaminants might be either crustal material, or earlier high silica volcanics, which might themselves be the product of fractionation dominated processes. In this latter case assimilation or mixing with a melt of this would produce trace element and isotopic trends indistinguishable from the effects of simple first order fractionation.

Potential crustal endmembers in the extensional corridor are fairly limited because pre-

Cenozoic cover sequences were totally removed from the area prior to the onset of Miocene volcanism (see Chapters 1b & 2). The crystalline basement consists of Proterozoic granulite to high amphibolite facies gneiss (Thomas et al 1988; Young et al 1989) and numerous Mesozoic granite bodies which represent the remnants of arc activity and crustal melting between the Triassic and the late Cretaceous (Burchfiel and Davis 1981). There is little published geochemical data on felsic granulite xenoliths from the south western USA, however, one silicic granulite is analysed in Kempton et al (1990). This sample is reported to have an $^{87}Sr/^{86}Sr$ ratio of 0.8185, combined with low Ba and K_2O, and high Y concentrations (table 2). The resulting Ba/Y ratios of <20, and K_2O/Nb ratios <0.05, would make such a sample unsuitable as the contaminant. However, melting of the granulite basement cannot be ruled out, and indeed the granulites may have contributed to the production of the widespread granite magmas during the Mesozoic.

The Mesozoic 'granites' cover a range of $^{87}Sr/^{86}Sr$ from 0.709 to 0.713 and samples have suitably high Ba and K_2O concentrations, combined with low Zr,Y and Nb (see table 2). Their mineralogy ranges from that of muscovite leucogranite to biotite and hornblende rich diorite and granodiorite. The ubiquitous presence of hydrous phases and the overall geochemistry indicates that these granites could represent the fertile crustal endmember required for the assimilation models. However, rather than direct assimilation / melting of such granite, it is possible that at least some of the assimilant could be in the form of rhyolites or rhyolitic magmas that were originally derived by melting of the granites during the Cenozoic.

3.4.2 (a) *Assimilation and fractional crystallisation (AFC)*

AFC processes, in which assimilation and crystal fractionation occur contemporaneously, can be summarised by the following equation (DePaolo 1981),

② $$C_l\omega = C_m^o\omega\left(F^{-z} + \left[\left(\frac{r}{r-1}\right)\frac{C_a\omega}{zC_m^o\omega}(1-F^{-z})\right]\right)$$

where $C_m^o\omega$ is the initial concentration of ω in the basalt magma, $C_a\omega$ is the concentration of ω in the assimilant and $C_l\omega$ is the resulting concentration. F is the proportion of melt remaining, r is the ratio of mass assimilated to mass crystallised and,

$$z = [(r+D_\omega-1) / (r-1)]$$

where D_ω is the bulk D-value for ω. Under the condition of $r>1$ the term F^{-z} becomes F^z.

The most influential term in equation ② is 'r' which determines the rate at which contaminant material is assimilated into the model system. The heat required to melt the assimilant is provided by the latent heat of crystallisation released during fractionation. Because this latent heat is a finite parameter, the amount of assimilant melting that can be produced as a result of fractionation, is also finite. A maximum value of r=0.5 is suggested by Lum et al (1989) although in deep crustal conditions, where the country rock may already be hot, DePaolo (1981) suggests that values as high as r=1 may be attainable.

Trace element models for r=0.3 and r=0.8 have been added to figures 4-6, using samples MO5, FS4 and M11 as typical basaltic endmembers, and granite NB11 as the assimilant. In figure 5, a late group from the Egan Range and samples from Kane Springs Wash (with ≤70wt% SiO_2) plot about the r=0.3 model. This compares favourably with previous models for magmatism at Kane Springs Wash proposed by Novak and Mahood (1986). Some of the Lake Havasu City samples fall on or close to the r=0.8 models in figures 4 and 6, however, the same samples plot closer to the r=0.3 model in figure 5.

The models can effectively reproduce the observed range of Ba/Y, K_2O/Nb and Ba/Nb ratios, although the amount of fractionation must generally exceed 90%. For such large amounts of fractionation, the incompatible element concentrations would be expected to increase by orders of magnitude. However, this is clearly not the case for Zr, Y and Nb in the sample suites from the extensional corridor. There is also some slight inconsistency between the diagrams, particularly arising from lower Y contents than anticipated in many of the samples.

A possible solution would be to include a phase in the fractionating assemblage which removes Zr, Y and Nb from the melt. Hornblende is a suitable phase, particularly in intermediate silica systems where the hornblende D-values for these elements are all >1 (table 1). Furthermore, hornblende is observed as a trace phase (≤ 5%) in many of the intermediate to higher silica samples from the extensional corridor, although biotite is consistently the more important mafic phase above 62wt% SiO_2.

The effects of minor hornblende fractionation are fairly limited, but a certain degree of success is achieved in modelling Y variations with r=0.5 as the proportion of hornblende is increased to ≥ 20wt% (at the expense of Opx and Ol; ❸, table 1). However, more extreme models, including 50% hornblende (at the expense of Opx, Ol and Cpx) and r=0.8, still fail to reproduce the observed spread of Nb and Zr variations (figure 6). Thus it seems unlikely that hornblende could be a major contributor to the general evolution models.

Isotope modelling. The scatter of $^{87}Sr/^{86}Sr$ isotope data vs. Ba/Nb is displayed in figure 7 for AFC models of r=0.5 and r=∞. Models with r < 0.5 are effectively dominated by fractionation and thus cannot reproduce the observed range of isotope and trace element ratios. As in the trace element models, a number of basaltic endmembers have been utilised (MO5 and M11), although the spread of data suggests that a range of crustal endmembers is now also required (eg. granite samples NB11 and NB14, and the rhyolite H4). But even with a range of endmembers, the models do not fit all the data. For instance, the Searchlight samples fall below all the modelled curves, having high Ba/Nb ratios but low $^{87}Sr/^{86}Sr$. These samples have the highest proportion of hornblende phenocrysts (10-15%), and so it is possible that the magmas evolved away from the general model by hornblende fractionation above 60wt% SiO_2. The amount of hornblende fractionation may be quite small because the hornblende D-value for Ba at high silica is an order of magnitude smaller than that in basaltic systems (Martin 1983), and therefore the Ba/Nb ratio of the magma will increase rapidly with fractionation.

Because each of the contaminant samples has a reasonably high Sr content (288-997 ppm),

the modelled r=0.5 curves approximate to r=∞ for much of their course in figure 7. This makes it difficult to draw any major conclusions from the $^{87}Sr/^{86}Sr$ isotope data, except that the evolution models must include a number of basaltic and crustal endmembers, and AFC conditions of $r \geq 0.5$. The shallow positive slope of the array in figure 7 suggests that the typical crustal endmember has a high Ba/Nb ratio, but only a moderate $^{87}Sr/^{86}Sr$ ratio. A similar pattern is also observed on diagrams of Rb/Ba versus $^{87}Sr/^{86}Sr$. (Note that Rb/Ba ratios typically only fractionate in crustal environments as a result of the large D-value differences between the two elements in alkali feldspar and biotite.)

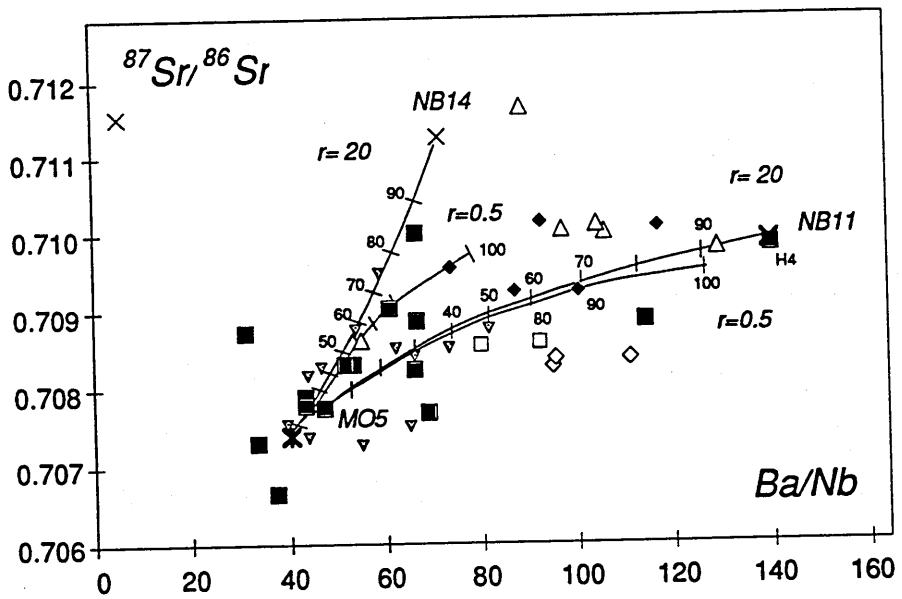

Figure 7. $^{87}Sr/^{86}Sr$ isotope ratios vs Ba/Nb. Granite $^{87}Sr/^{86}Sr$ ratios have been time corrected as in figure 3. Two separate sets of endmembers have been used (MO5 & NB11; M11 & NB14) to generate models with r=0.5 and r=20. Fractionating mineral assemblages and key to sample suites as figure 4 except inverted triangles which are samples from other regions of the CRT, such as Lake Mead.

3.4.2 (b) *Binary mixing*

Binary mixing is a special case of AFC where r=∞. This can generally be approximated by models incorporating r >10, although any model which requires r > 1 must include at least some degree of magma mixing. In the binary mixing model, fractionation plays a subordinate role (technically fractionation does not occur when r =∞) and evolution to higher levels of silica is dominated by the addition of contaminant material in the form of a high silica *melt*. The proportion of melt to basic magma is too great for it to be generated by the latent heat released during crystallisation of the basalt and consequently it must be

regarded as a magma in its own right.

Figures 4-7 display a series of binary mixing models approximated by r =20 between various basaltic endmembers and the granite NB11. These models define curves roughly orthogonal to those for simple fractionation, with increases in Ba/Y, K_2O/Nb, Ba/Nb and $^{87}Sr/^{86}Sr$, but decreases in Nb, Y and Zr concentrations with evolution. The bulk of samples in the suites from the extensional corridor scatter around these modelled curves and similar trends are also apparent in data from the Egan Range and O'Leary Peaks. The coincidence of the data and the modelled curves is significant and, by analogy to the models described above, the amount of scatter can be accommodated by just small amounts of fractionation, and by uncertainty over the exact endmember compositions. It is notable that the least scatter of data is observed in figure 5 where the potential silicic endmembers H4, NB11 and NB14 all lie in approximately the same position.

	Mafic Endmembers				*Silicic Endmembers*			
	MO5	MO6	M11	FS4	NB11	NB14	H4	GN22-5
SiO_2	50.87	53.62	55.41	56.26	65.09	70.95	65.88	73.15
TiO_2	1.51	1.31	1.36	1.32	.63	.35	.45	.46
Al_2O_3	16.06	16.20	16.77	16.20	16.09	14.32	15.24	12.77
Fe_2O_3	9.55	8.24	7.23	7.51	4.10	2.39	3.02	2.92
MnO	.10	.13	.09	.12	.07	.05	.06	.06
MgO	5.93	5.16	4.18	3.83	2.25	.75	1.05	.76
CaO	8.36	8.33	7.83	7.08	3.71	2.14	2.93	1.95
Na_2O	4.15	3.89	3.61	3.59	4.18	3.49	4.21	2.77
K_2O	1.64	1.72	2.38	3.56	3.70	4.48	3.43	3.38
P_2O_5	.47	.41	.52	.48	.25	.11	.18	.10
Rb	33	28	58	96	88	136	109	195
Ba	899	984	1047	873	1539	1007	1405	502
Nb	19	19	26	20	11	14	10	16
Sr	823	874	752	499	997	288	638	144
Zr	207	230	254	246	185	184	199	172
Y	27	74	28	29	59	22	59	19
$^{87}Sr/^{86}Sr$	.7078	.7083	.7074	na	.7099	.7113	.7098	.8185

Table 2. The composition of the mafic and silicic endmembers used to generate the models in figures 4-7. NB11 and NB14 are Cretaceous granites from the Newberry Mts, H4 is an early syn-extensional rhyolite from Lake Havasu City. Samples MO5, MO6 and FS4 are also from the Lake Havasu City area, M11 is from Lake Mead. GN22-5 is a Proterozoic quartzo-feldspathic granulite from southern Arizona, included for comparison (Kempton et al 1990).

3.5 Discussion

Clearly the binary mixing models provide the closest and most consistent fit to the data, although fractionation and endmember variability are likely to have been responsible for some of the scatter. The implication of accepting such a model (± minor fractionation) as the principal control on evolution is that the basaltic and silicic magmas must have been present in the crust at the same time. Two questions then arise, i) how were the silicic melts generated, and ii) at what crustal level did the melting and mixing take place to produce the intermediate silica 'hybrid' magmas?

The depth of magma mixing within the extensional corridor can be inferred from a number of independent observations. Firstly there is little evidence to support the existence of large scale volcanic features across the corridor. For instance, there are no relict caldera collapse structures or prominent mafic volcanic centres, although the corridor does have a well developed parallel dyke fabric (mostly north-south orientated, see Chapter 2). Thus it is unlikely that any significant high-level, and long term, magma chambers developed in which magma mixing could occur. The presence of hybrid magmas in dykes intruded below the Homer and Sacramento Mts Detachment faults (Spencer 1985) also suggests that the melting and mixing level was at some depth (probably below 5km). A more specific constraint can be obtained by considering the likely depth to the fertile source material of the silicic magma, immediately prior to the onset of extension and volcanism.

In the previous section, Mesozoic granite bodies were favoured as the fertile protolith. Pressure-temperature-time models for such granites in the Whipple Mts (Anderson et al 1988) indicate emplacement depths of 7.9 - 9.2kb (~ 29-33km) during the Cretaceous. These plutons were subsequently mylonitised under conditions of 4.5 - 4.7kb (~16km) and 420-580°C at 26 ± 5Ma (Davis and Lister 1988; Anderson et al 1988). Although the granites were intruded by syn-kinematic plutons they did not undergo significant degrees of remelting, so it is reasonable to suggest a depth in excess of 16km for the source of the syn-extensional silicic magmas in this region.

A further value for the source depth can be calculated directly from the normative mineral compositions of the higher silica syn-extensional volcanics. Part of the pressure and temperature sensitive system Q-Ab-An-Or-H_2O (Tuttle and Bowen 1958; Winkler 1979) is displayed in figure 8, with experimental cotectics and data from the extensional corridor. Apart from two pre-extensional rhyolites from Lake Havasu City, all the samples fall in a cluster close to the 4 -5kb cotectics. Again, this represents a minimum pressure estimate because magmas will naturally re-equilibrate if they have long residency times at higher crustal levels subsequent to their formation.

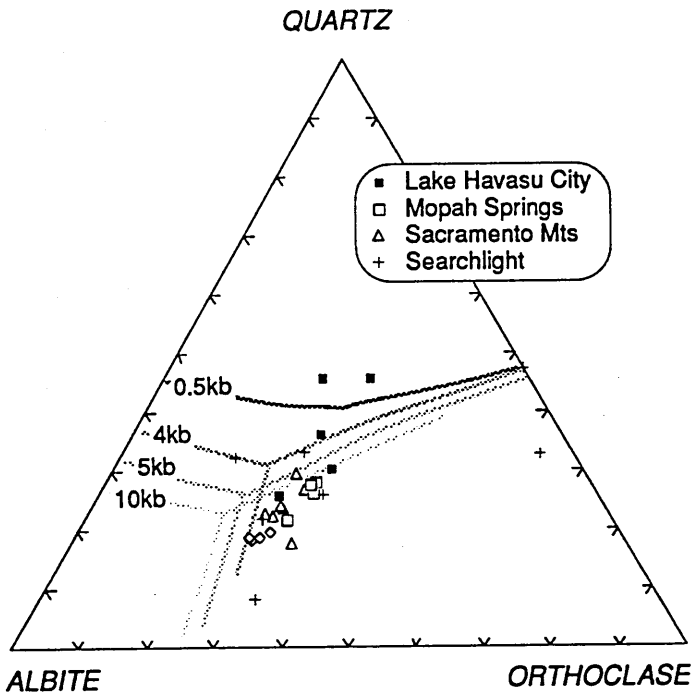

Figure 8. Normative quartz, albite and orthoclase compositions of extensional corridor samples having ≥63 wt% SiO_2 (after Tuttle and Bowen 1958). Experimental cotectics from Winkler (1979). The two samples plotting above the 0.5kb cotectic probably record a final stage of evolution at approximately atmospheric pressure.

In summary, it is proposed that the silicic magmas originated at or below ~16km. The general lack of re-equilibration at lower pressures also suggests that magma mixing occurred at similar depths, and that the two processes were probably coincident. These results are consistent with previous crustal melting depth estimates of ~5kb in the San Francisco Volcanic Field (Bloomfield and Arculus 1989).

Models for the actual origin of the silicic magmas fall into two main categories,

i) melting caused as a result of overthickening of the crust prior to extension

ii) melts generated by direct heat transfer (advective heating) from basaltic intrusions in the Tertiary.

The former is considered to be an important process for generating granitic magmas in the Great Basin during the late Cretaceous Laramide Orogeny (Farmer and DePaolo 1983; Patiño Douce et al 1990). The Sevier Plutonic Belt coincides with the region of maximum crustal thickening in the Great Basin at this time and mobile granitoid magmas were apparently produced where crustal thickening factors (maximum crustal thickness attained / initial crustal thickness) were ≥ 1.5 (Patiño Douce et al 1990). Because the thermal peak within the crust generally post dated the time of maximum crustal thickening, much of the granitic magma generation was post-kinematic.

Sonder et al (1987) suggested that continued thermal relaxation of the lithosphere following the end of the Laramide Orogeny may also have contributed to the production of silicic melts during the Tertiary extensional phase. However, the area immediately south of Lake Mead (coincident with the Tertiary extensional corridor) was not subject to any significant crustal thickening or deformation during the Laramide Orogeny (Oldow et al 1989 and references therein). Laramide compressional strain in the Great Basin was apparently dissipated by a fore-runner of the Lake Mead-Las Vegas Shear Zone in the north, while the eastern limit of crustal thickening occurred in the Spring and Clark Mts to the west of the corridor (Burchfiel and Davis 1988).

Advective melting models (Huppert and Sparks 1988) imply a genetic link between the basaltic and silicic magmas. In this case the silicic melt is generated as a consequence of the intrusion of hot basaltic magma into the crust, and the process of melt formation acts as part of the cooling mechanism for the intrusion. Maximum crustal melting is attained if the heat release is concentrated at a specific depth, which obviously favours situations where basaltic magmas have been intruded in the form of sills. Depending on the local crustal conditions, Huppert and Sparks (1988) suggest that the rate and amount of silicic melt

generation can be quite considerable, for instance a 500m thick sill (at ~1200°C) intruding 'wet' country rock at 750°C will generate nearly 630m of silicic melt in ~25 years. This process is self accelerating because the partially molten zone will form an effective barrier to subsequent intrusions (Koyaguchi 1986). Newly ponded magma will further heat the same crustal level and the amount of melting is expected to be even greater, following the pre-heating effect of the earlier intrusions.

The initial trapping of magma at one level is probably governed by a density contrast or stress barrier within the crust, above which the basaltic magma is no longer buoyant (Gudmundsson 1986; Glazner and Ussler 1988; 1989). In the extensional corridor, it is likely that such a contrast existed between the Mesozoic granite bodies in the middle (or lower) crust and the surrounding Proterozoic granulite. Moreover, the granite bodies also constitute fertile (hydrous and 'warm') material in which crustal melting could be rapidly established.

The Huppert and Sparks model predicts the generation of highly porphyritic magmas with phenocryst populations recording multiple growth episodes. Some residual phenocrysts from the original crustal protolith are also expected. Typically these would be observed as the resorbed nucleii to larger phenocrysts and as partially re-equilibrated 'sieve-textured' phenocrysts. Both of which are abundant features in the hybrid and higher silica magmas from the extensional corridor.

However, the advective model does not specifically generate intermediate silica hybrid magmas, and thus a further stage is required in which magma mixing occurs. In a tectonically active environment mixing by chemical diffusion is likely to be enhanced by mechanical processes, however, to produce the whole range of silica contents observed in the extensional corridor, the magma mixing must go near to completion. This will only occur if the two magmas both behave as liquids at the same temperature and therefore it is only likely if the basaltic endmember represents an evolved composition (Sparks and Marshall 1986). The basaltic endmembers considered so far (MO5, MO6, M11 and FS4) all have MgO <6wt%, Mg# ≤59 and SiO_2 >50wt%. These attributes are generally

consistent with the compositions suggested by Sparks and Marshall (1986) for mafic magmas that would be capable of complete hybridisation with the proposed high silica endmembers. In contrast, the 15Ma alkali-olivine basalts from Lake Havasu City and the Newberry Mts (MgO > 8wt%, SiO_2 < 48wt%) would not have had suitable compositions to enable significant mixing to occur.

To summarise, physical, petrographic and geochemical constraints each suggest that the intermediate silica hybrid magmas in the extensional corridor were produced as a result of magma mixing processes. In its simplest form this can be approximated by a two component (binary) mixing model. However, a range of basaltic and high silica endmember compositions are probably required, and small amounts of fractionation are also suggested. Melts of Mesozoic granites in the middle or lower crust are proposed as the silicic endmember, and melt generation is likely to have been a consequence of advective heating from basaltic magmas trapped along a crustal density barrier. A relationship of silicic magmas to crustal thickening does not seem likely because the required crustal thickening factors were never attained within the extensional corridor.

3.6 The Relationship of Magmatism and Tectonics

The distribution of the hybrid volcanism (figure 2) suggests that the melting and mixing processes proposed for their origin must have operated over almost the entire extensional corridor, although apparently not to any great degree along the corridor axis. The amount of magma involved is considerable, probably in the order of 5km thickness at any point within the corridor [1], and the actual thickness of partially molten crust may be even greater. However, the time periods envisaged for the bulk of volcanic activity at any one point are rather short: 4-5My in the Whipple Mts (Gans et al 1989); ≤ 8My in the Sacramento Mts (Simpson et al 1991); and preliminary $^{40}Ar/^{39}Ar$ data suggest ~ 2-3My for the Eldorado

[1] Assuming a 1km average lava pile thickness across the corridor and a 4:1 ratio of intrusive to extrusive volumes, as can be calculated for the River Mts volcanic field and the associated Wilson Ridge Pluton near Lake Mead. This ratio is probably a minimum estimate, values of between 5:1 and 15:1 are suggested in Gans et al 1989.

Mts (G. Mahood *pers comm*). Tectonic activity appears to have been similarly time restricted (eg. Gans et al 1989; Davis and Lister 1988).

The magma volume and distribution observed in the extensional corridor suggests that partial melting must have occurred as a semi-continuous *zone* in the crust. This probably developed below 16km and continued to some depth, perhaps even to the base of the crust. Such a thermally weakened zone is less able to support applied stress and will respond by ductile deformation. As the ductile zone enlarges it will not only govern the stress distribution at that depth but will begin to dominate the effective strength of the whole continental crust. Kuznir and Park (1987) showed that with conditions of high heat flow, equivalent to that expected during Tertiary magmatism, the strength of the crust reaches a minimum in time periods similar to those quoted above, and crustal failure is inevitable.

Because of the potential for crustal flow, deformation in the ductile zone can be considered as symmetrical. However, upper crustal extension is observed to have an asymmetrical distribution within the corridor, being greater to the west of the axis (Spencer 1985; Howard and John 1987; Davis and Lister 1988). A two-layer model for crustal extension is therefore required. But the dominance of basaltic magmatism along the corridor axis implies that extension rates here were sufficient to provide fault pathways through the ductile zone, before significant hybridisation of the magmas could occur. Effectively the corridor axis behaves like a continental rift, although it is part of a much wider extensional system (see figure 9).

Published geophysical models for the extensional corridor generally agree with the model outlined above. Kruse et al (1991) suggest that lower crustal ductile flow over a wide area is a necessity to explain the apparent lack of crustal thickness differences between the highly extended Lake Mead area and the unextended Colorado Plateau. Similarly, Block and Royden (1990) conclude that regional scale flow in the lower crust is the only reasonable mechanism for maintaining a flat Moho profile, while bringing mid-crustal material to the surface beneath up-doming detachment faults.

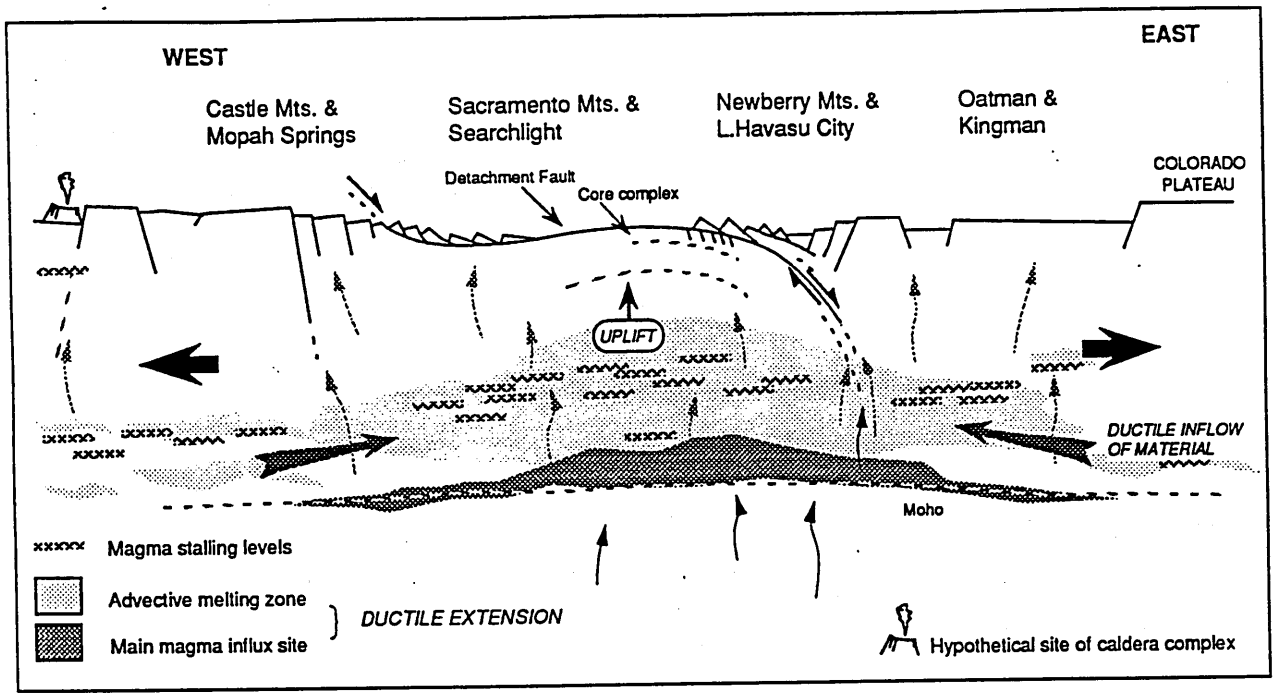

Figure 9. Schematic cross section through the crust of the extensional corridor at 18Ma, for approximately the latitude of Lake Havasu City. The main feature of the model is a large area of the middle and lower crust undergoing ductile extension, while asymmetrical brittle extension occurs in the upper crust. Basaltic magmas initially stall and evolve to some degree at the Moho, before being emplaced at further density / stress barriers higher in the crust (see text for full discussion). The axis of major extension and uplift is marked by the locus of maximum magma intrusion and ductile inflow of material at depth. A hypothetical location for caldera style volcanism has been indicated where magma stalling occurs in the upper crust. Such a location could correspond to the Woods Mountains Volcanic Centre indicated on fig 1.

Structural observations have also lead to a two-layer stretching model, incorporating a significant input of mantle derived basaltic magma, being proposed for extension and volcanism in the Great Basin (Gans 1987; Gans et al 1989). Here, corridors of high extension have been identified, although generally separated by much wider regions of more limited extension. Sample suites from the high extension corridors (eg. the Egan Range) display similar geochemical trends to those of the Colorado River Trough, as do suites from the Southern Basin and Range and the Mojave Desert (the "crustal recycling" of Glazner 1989). A comparable mode of evolution is thus suggested for all these suites. Similarly, a model for thermal weakening of the crust, associated with a high level plutonic complex, has recently been proposed to explain brittle and ductile extension regimes observed at the Questa Caldera along the Rio Grande Rift (Meyer and Foland 1991).

The only major difference between the Colorado River Trough and the Great Basin is that large high level volcanic systems are prevalent in the latter region. This situation could arise due to a combination of two factors in the Great Basin, i) the presence of thick supracrustal units and, ii) a smaller degree of overall extension per unit length in this province. The supracrustal units (absent in the Colorado River Trough) have the potential to provide further density and stress barriers in the upper crust at which even some hybrid magmas might stall. Reduced tectonic activity would enable these high level systems to grow and evolve with only sporadic disruption. Thus, in time, creating an environment in which predominantly dacitic to high silica caldera style eruptions could occur, such as at Kane Springs Wash.

3.7 Conclusions

It is proposed that extension and volcanism throughout the various provinces of the Basin and Range during the Miocene can be attributed to the same fundamental processes (see figure 9):

i) basaltic magma intrusion and trapping at crustal density barriers

ii) extensive crustal melting due to advective heating, followed by mixing of the basaltic and crustal endmember magmas

iii) the development, by thermal weakening in the lower crust, of a regional ductile zone that dominates the overall strength of the crust.

Where and when conditions permit, upper crustal volcanic systems may then develop in which further magmatic evolution can take place.

The critical difference between the Basin and Range and other extensional provinces, such as the East African Rift, is that magma mixing occurs in the Basin and Range over a large area. The mixing can approach completion because the mafic endmembers involved are not primitive basaltic magmas; rather, they have already evolved to some degree, probably at the Moho (see Chapter 2). Crustal extension then follows as a *consequence* of the magmatism and crustal melting.

In contrast, extension in the East African Rift, associated with the opening of the Red Sea, is the the controlling factor on the volcanism in that region. Here the extension not only generates the magmas (by adiabatic decompression melting in the asthenosphere, *cf.* McKenzie and Bickle 1988), but also provides an environment in which the magmas can be rapidly intruded through the crust with only minimal interraction. Limited crustal melting may occur along the walls of dyke conduits but, unless the magmas are emplaced horizontally, the extent of partial melting will be insignificant compared to that inferred in the Basin and Range Province. This scenario favours the development of basalt dominated or slightly bimodal volcanism.

The abundance of basaltic volcanism at Lake Havasu City in the final stages of extension, particularly the 15Ma alkali-olivine basalt flows, suggests that extension here may also have become the driving force for volcanism with time. The origin of these and the other basaltic magmas in the extensional corridor are discussed in the following chapter.

A progressive melting model for basaltic volcanism in the Colorado River Trough of the western USA

4.1 Introduction

Basaltic volcanism became widespread in the Basin and Range provinces of the western United States after approximately 14Ma, following a period of earlier Cenozoic volcanism dominated by trachy-andesite to high silica eruptions. Much of the focus for recent geochemical research has been in the investigation of these later Cenozoic basalts, either in relation to the nature of their mantle source regions or to assess their links with crustal extension (eg. Fitton et al 1988; 1991; Wittke et al 1989; Lum et al 1989; Farmer et al 1989; Ormerod et al 1988). However, the bulk of Cenozoic magmatism and extension in the Basin and Range took place during the Oligocene and early Miocene, generally prior to the onset of basalt dominated volcanism (Gans et al 1989; Davis and Lister 1988).

This contribution presents new geochemical data from a corridor of high extension south of Las Vegas, Nevada, where basaltic volcanism is recorded throughout the main period of crustal extension. Although the basalts are not the most abundant magmas they nevertheless provide an almost unique opportunity in the Basin and Range to investigate the role of the mantle *during* major extension. Time related geochemical changes in the basalts also make it possible to consider the processes involved in the development of the magmatism as the region progressed through pre-, syn-, and finally post-extensional phases. In particular, the extent of partial melting in the mantle, and any changes in the mantle source with time, can be considered in light of changes in the local tectonic state of the crust.

The study area covers the Colorado River Trough (CRT), an 80km wide physiographic low along the Colorado River from Lake Mead in the north to the town of Parker 290km to the south (figure 1). Between approximately 22 and 12 Ma this area extended in a NE-SW

direction by at least 100% and locally up to 250-450% (see Chapter 2). The focus of both extension and magmatism was diachronous along the CRT and spread from south to north during this period. At the northern end of the CRT the Las Vegas / Lake Mead Shear Zone abruptly terminates the extensional corridor and separates this area from a poorly extended section of the Great Basin to the north (Duebendorfer and Wallin 1991). This feature also appears to have been a significant focussing point for basaltic magmatism over the last 15Ma.

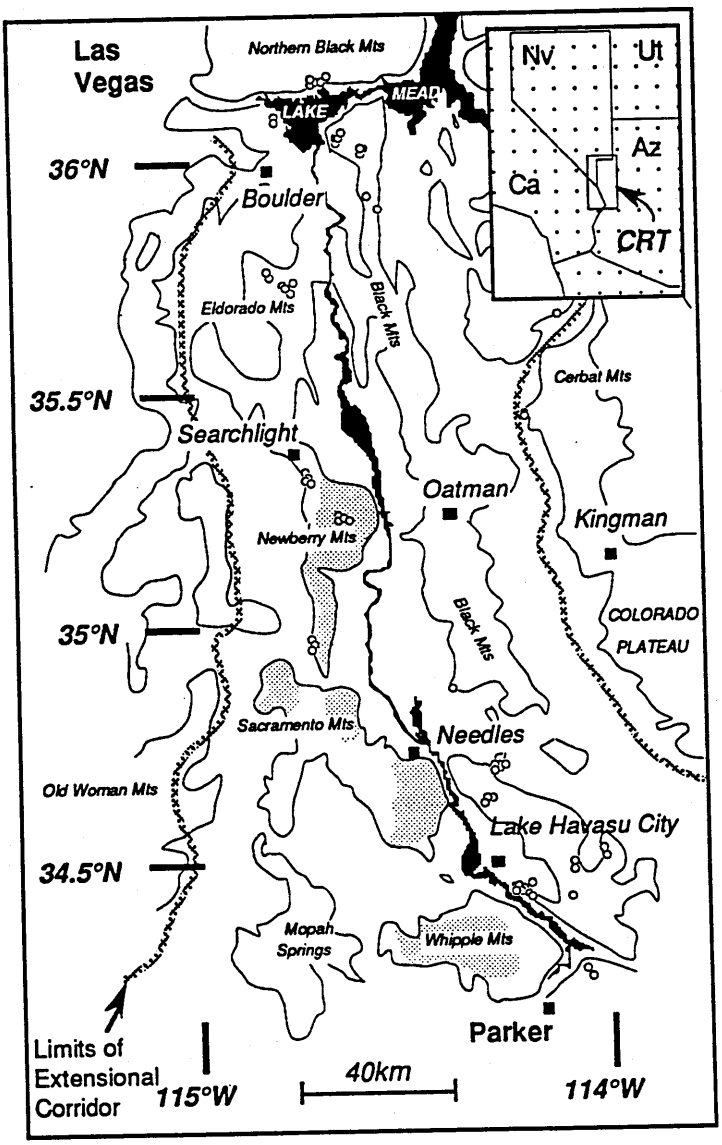

Figure 1. Sample localities in the Colorado River Trough region (circles). Most of the studied samples were collected from around Lake Mead and Lake Havasu City. Post-extensional samples were collected from across the whole region. Shaded areas are metamorphic core complexes. Colorado River shown in black.

Within the CRT, pre/syn- and post-extensional basalts are readily distinguished on the basis of field relations, and these groups can then be further subdivided using geochemical and

petrological criteria. The relationship of these groups and the samples within them are interpreted below, leading to the derivation of a model for magmatic events during extension. The nature of the mantle source for the basalts is also discussed.

4.2 General geochemistry

Most of the studied samples are alkaline or slightly sub-alkaline basalts, trachybasalts and basaltic andesites, all with ≤56wt% SiO_2. Transition metal abundances (eg. Sc, Co, Cr and Ni) and petrographic evidence indicate that all of the samples have undergone at least some olivine and/or pyroxene fractionation, although probably no plagioclase fractionation. In the complex modelling presented in section 4.3.4 (where basalt source compositions are calculated), only the samples from each basalt group that are thought to have undergone the least degrees of fractionation are used[1].

The CRT samples display trace element enrichments above that of the primitive mantle (of Sun and McDonough 1989), although the level of enrichment is highly variable between the individual basalts (see figure 2). The main geochemical feature is that of Large Ion Lithophile Elements (LILE) enriched relative to the Light Rare Earth Elements (LREE), and LREE enrichment relative to the High Field Strength Elements (HFSE) and the Heavy Rare Earth Elements (HREE). This produces an irregular, but generally convex upwards, mantle normalised pattern that typically peaks at Ba (eg. Group 3 on figure 2). Small troughs at P_2O_5 and Hf are other common features and most of the mantle normalised diagrams also display a step between elements considered to be more or less incompatible than Ti. Relative depletion in Ta and Nb with respect to the LREE and LILE produces a Ta-Nb trough such as that commonly observed in island arc volcanism (Gill 1981). The depth of this Ta-Nb trough is fairly constant and this is demonstrated in figure 3 in terms of Nb/La variation, plotted against Ba concentration as an indication of the range of individual trace element abundances.

[1] For the basalt groups described overleaf: the mean degree of fractionation for the group 2 basalts is 7wt%, but the degree is somewhat higher for groups 1 and 3 (24 and 15wt% respectively); thus, errors on the modelled source for groups 1 and 3 are higher than for group 2.

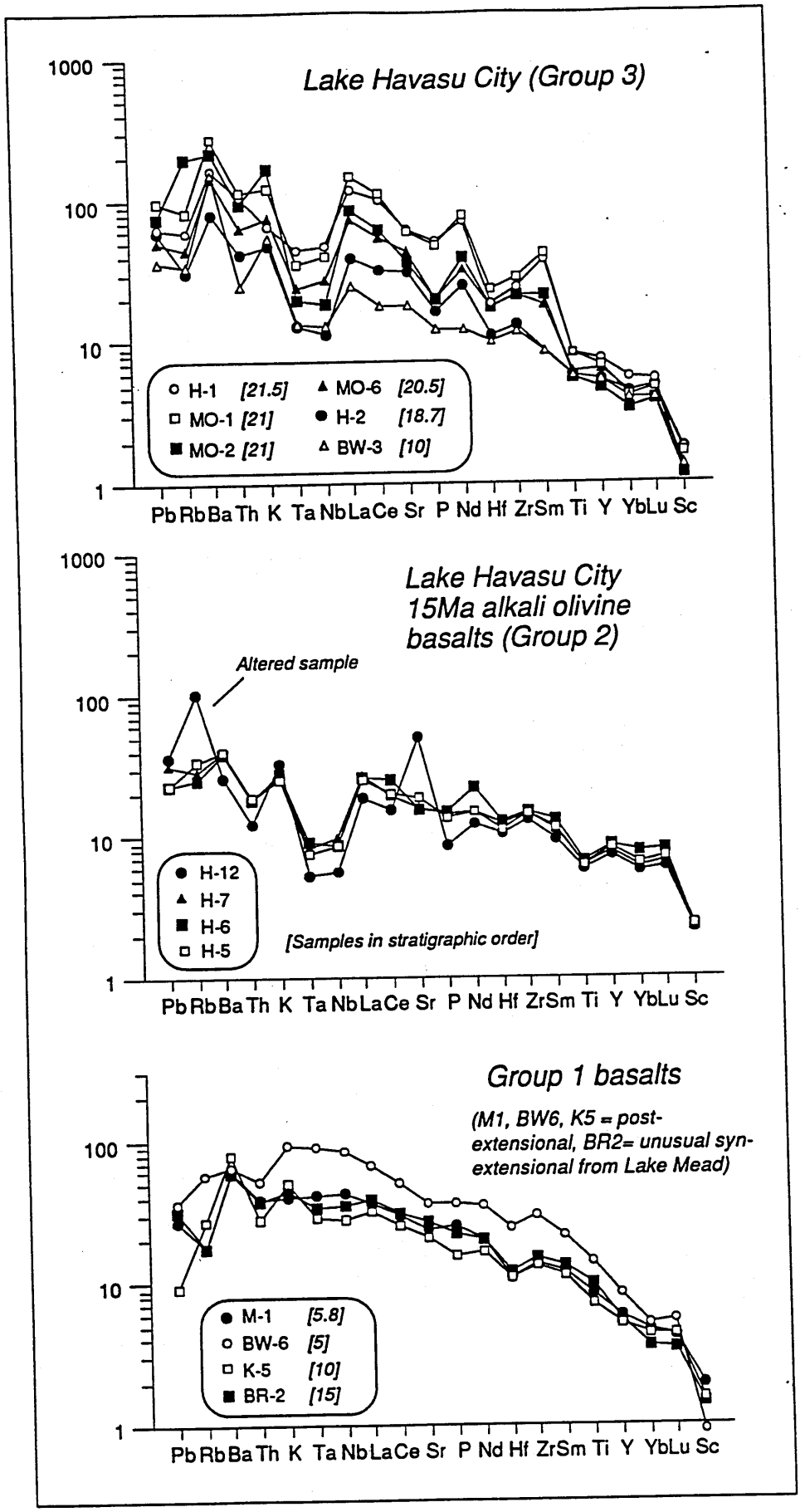

Figure 2. Primitive mantle normalised multi-element diagrams ('spidergrams') for representative samples from the CRT. (See Appendix for normalising values). Three groups of samples are indicated and these will be discussed in the text. Sample ages are given in square brackets.

The exception to these general features are a number of the most recent post-extensional samples and a few syn-extensional samples from the Lake Mead area. These samples have smoother mantle normalised patterns, again enriched above primitive mantle values and convex upwards, but they have maxima at either K_2O, Ta or Nb and do not display a Ta-Nb trough. Some of the samples also have a spike at Ba, but at lower concentrations than in the basalts described above. The basalts have some of the highest TiO_2 contents in the CRT (up to 3wt%) and this significantly reduces the size of the 'step' in the trace element patterns at Ti. On figure 3 the high Nb/La ratios and restricted and low Ba contents clearly distinguish these samples from the main basalt associations of the CRT.

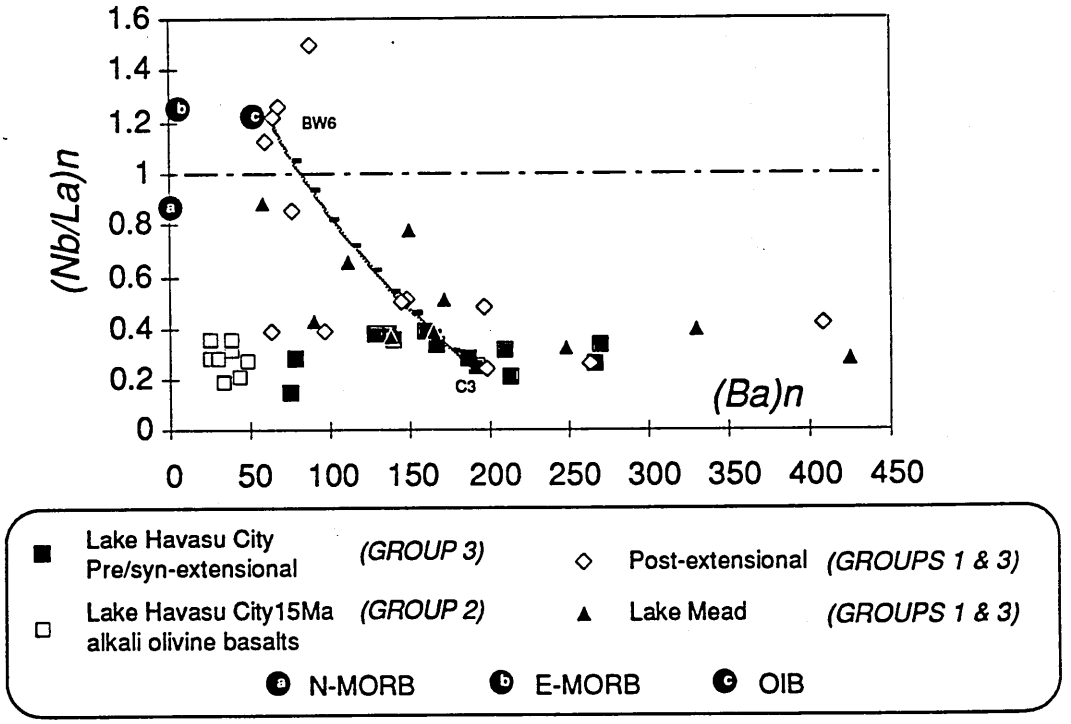

Figure 3. Primitive mantle normalised Nb/La vs Ba. Samples above Nb/La=1 do not display a Ta-Nb trough on figure 2. A hypothetical mixing line is drawn between these samples and the main group of data. Comparative positions for mantle magmas are also shown (from Sun and McDonough 1989).

A further group (group 2) can also be recognised on figure 3, having very low Ba and low Nb/La. This is a group of 15Ma alkali olivine basalts from Lake Havasu City, representing the final stages of syn-extensional magmatism for that region. Petrologically and geochemically similar basalts occur as dykes further along the axis of the extensional corridor in the Newberry Mts (see Chapter 2). Both the lavas and the dykes range from 45.5-49 wt% SiO_2, have high Al_2O_3 contents (≈ 16.4wt%) and have lower incompatible

element contents than the other CRT basalts. However, the overall mantle normalised diagram pattern is strikingly similar to that of the average pre/syn-extensional basalts (see figure 2). The difference between the two patterns is greatest for Ba, Th, K, Ta and Nb, but gradually decreases towards elements regarded as being more compatible in upper mantle assemblages. The patterns cross at Ti and the 15Ma alkali olivine basalts have higher Y, Sc and HREE contents than the other syn-and post-extensional samples. This results in much flatter REE profiles, and mantle normalised patterns which appear to have rotated about Ti (figure 2). Basalts having similar trace element patterns have rarely been described in the Basin and Range Provinces, and thus their origin will be discussed here in some detail.

To summarise, three main groups of basalts can be identified in the CRT based on their distinct trace element signatures:

1) high Nb/La, mostly post-extensional, basalts

2) relatively trace element depleted, but HREE enriched alkali olivine basalts, and

3) typical pre/syn/post-extensional basalts, which have a wide range of compositions but with fairly enriched trace element abundances, a marked Ta-Nb trough, and somewhat depleted Y, Sc and HREE contents.

These geochemical groups are emphasised in figure 4 which relates the variation of three incompatible elements, Th, Nb and Zr, normalised to primitive mantle values. Samples from each group fall in rough clusters distributed over a range of Th/Nb ratios from approximately 0.5 to 10, with the group 1 basalts having the lowest Th/Nb. The post-extensional basalts display the largest spread of Th/Nb ratios, and the group 3 basalts as a whole show a significant range of Th/Zr with little change in Nb/Zr ratios. The group 2 samples display the least variation and cluster at both the lowest Nb/Zr and Th/Zr ratios. As in figure 3, only the high Nb/La post-extensional basalts, and a few samples from Lake Mead, fall on or close to the asthenospheric array, defined by the fields for Mid-Ocean Ridge Basalts (MORB) and Ocean Island Basalts (OIB).

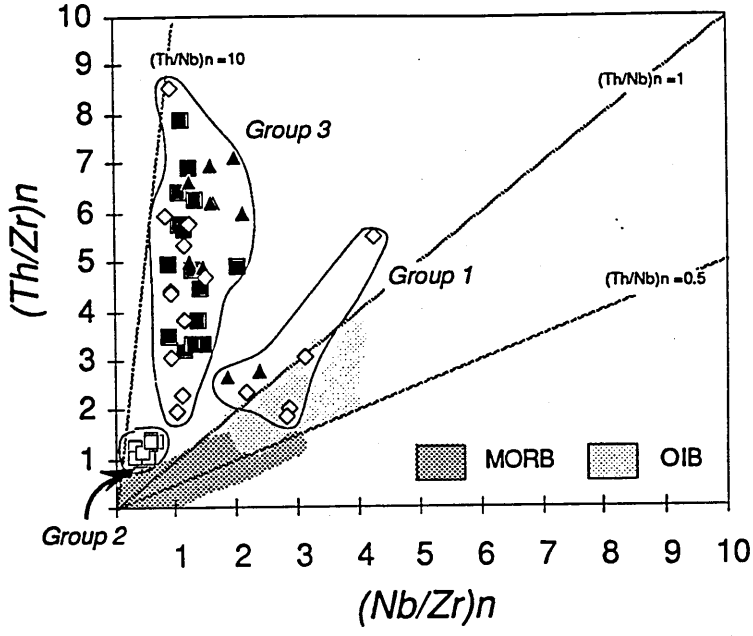

Figure 4. Th/Zr vs Nb/Zr. The three geochemical groups compared to OIB and MORB. samples have been normalised to primitive mantle values. Clustering on this diagram is consistent with samples in each group being generally comagmatic (see Chapter 6). Key as figure 3.

4.2.1 Isotope geochemistry

The bulk of the CRT samples are isotopically distinct from the asthenospheric mantle array. The mean $^{87}Sr/^{86}Sr$ ratio for all pre/syn-extensional basalts (in groups 2 and 3 above) is 0.7079±8, although the post-extensional basalts in group 3 range from 0.7065 (BW4) to 0.7092 (SL6) with a slight tendancy for the higher SiO_2 rocks to have higher $^{87}Sr/^{86}Sr$ (figure 5, on following page). The lead isotope ratios for all of the group 2 and 3 samples plot above the Northern Hemisphere Reference Line (figure 6), having elevated $^{207}Pb/^{204}Pb$ and $^{208}Pb/^{204}Pb$ ratios compared with typical MORB and OIB over a large range in $^{206}Pb/^{204}Pb$. Only the high Nb/La basalts have $^{87}Sr/^{86}Sr$ ratios which approach those of oceanic basalts (eg. BW6= 0.7047, BR1= 0.7054), and these samples also have MORB-like lead isotope ratios (figure 6).

In general, the CRT basalts have high Sr contents (the mean Sr content of 22 basalts from Lake Havasu City is 800ppm) and it is not thought that the high $^{87}Sr/^{86}Sr$ isotope ratios are the result of crustal contamination. This can be demonstrated by simple mass balance calculations, for example:

To raise the $^{87}Sr/^{86}Sr$ ratio of a group 1 sample (eg. BW6) from 0.7047, to that of a typical group 3 sample with a ratio of 0.7079 (eg. MO5) would require the addition of 55wt% of the granite NB11 (a crustal end member used in Chapter 3). This degree of contamination would result in a rock with 58 wt% SiO_2; sample MO5 is analysed at 50.87 wt% SiO_2.

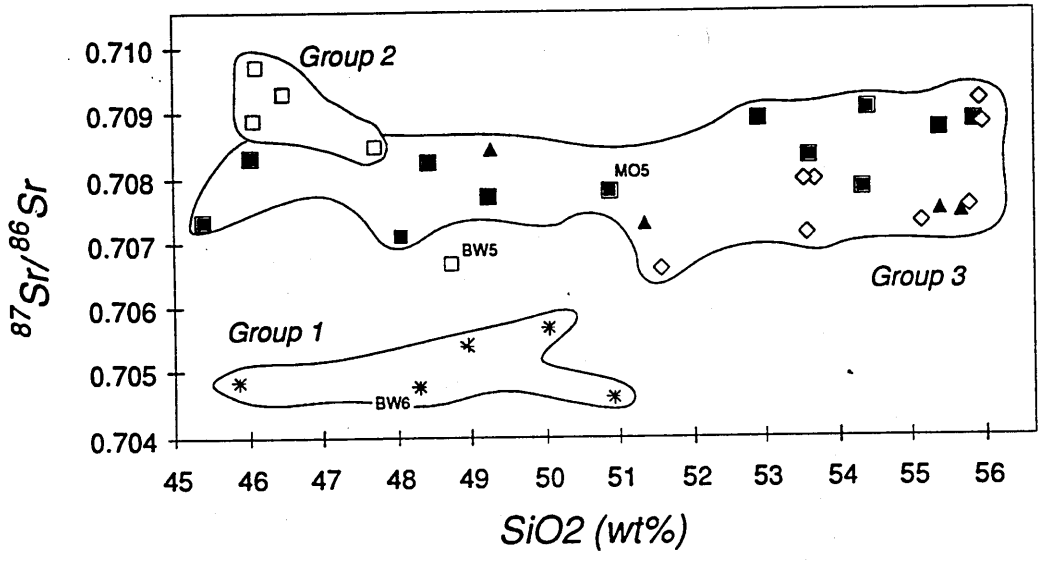

Figure 5. 87Sr/86Sr vs. SiO2. Key as figure 3. Group 1 basalts are clearly distinct from those of groups 2 and 3. There is little variation in the group 3 isotope ratios although the post-extensional samples may show a slight tendancy towards higher ratios with increasing silica. (The sample indicated as BW5 may be related to group 2 based on petrographic observations although it has a rather more evolved composition.)

4.2.2 Geochemical variations with time

The greatest range of geochemical composition with time is observed in the group 3 pre/syn- to post-extensional basalts (figures 2-6). In general the earlier basalts have the highest trace element concentrations, and they have high LILE and LREE contents relative to those of the HFSE and HREE. This results in steep and LREE enriched profiles resembling those of the more evolved trachyandesites from the CRT. With time, and the onset of extension, the LILE and LREE concentrations generally decrease, as do the concentrations of the HFSE and HREE although to a lesser extent. Consequently, the REE profiles appear to flatten progressively in successively younger rocks. Typical magma types may also change with time, from earlier alkaline basalts to subalkaline basaltic andesites.

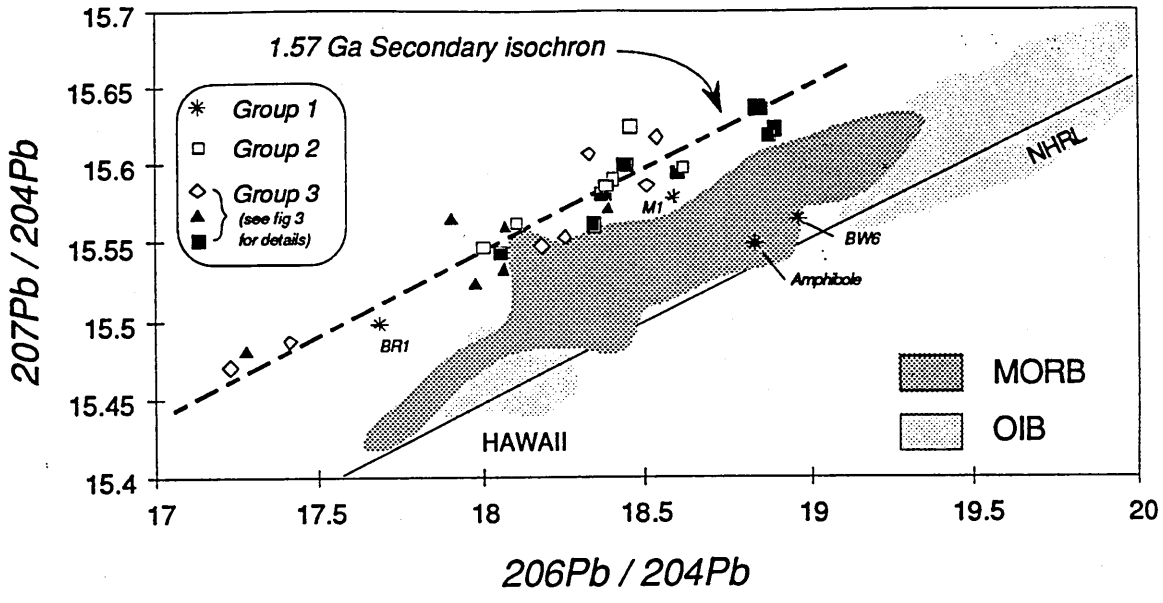

Figure 6. Lead isotope ratios determined for CRT samples. Key as figure 3. NHRL= Northern Hemisphere Reference Line from Hart (1984), fields for MORB and OIB are also shown. A secondary Pb isochron can be drawn through the samples at 1.57Ga, consistent with published ages for a lithospheric heating event in the region. The four samples highlighted are all from group 1 (the amphibole sample is a separate from basalt M2, data from Wilshire et al 1985).

Such systematic variations in composition with time are illustrated on figure 7, with the post-extensional samples and samples from the Lake Havasu City area. The Ce/Yb ratio is used as a measure of the degree of enrichment of the highly incompatible elements (eg. LREE) in the melt, relative to that of the less incompatible elements (eg. the HREE). Initially the Ce/Yb ratio is high, but this declines rapidly with time and then increases again slightly in the most recent post-extensional basalts. Comparing figure 7 with figure 2 indicates that the bulk of the early Ce/Yb variation is caused by the strong depletion in the LREE with time, relative to a smaller depletion in the HREE concentrations. The samples with the lowest Ce/Yb ratios on figure 7 are the group 2 alkali olivine basalts, which have both low LREE and high HREE concentrations.

There is no obvious variation of $^{87}Sr/^{86}Sr$ isotope ratios with time in group 3. However, there is an apparent variation in lead isotope ratios. Most of the pre/syn-extensional samples have high $^{207}Pb/^{204}Pb$ and $^{206}Pb/^{204}Pb$ (up to 16.5 and 18.8 respectively), while many of the post extensional samples have on average lower $^{207}Pb/^{204}Pb$ for the same $^{206}Pb/^{204}Pb$. The group also contains the lowest $^{207}Pb/^{204}Pb$ (<15.5) and $^{206}Pb/^{204}Pb$ (< 17.5) values.

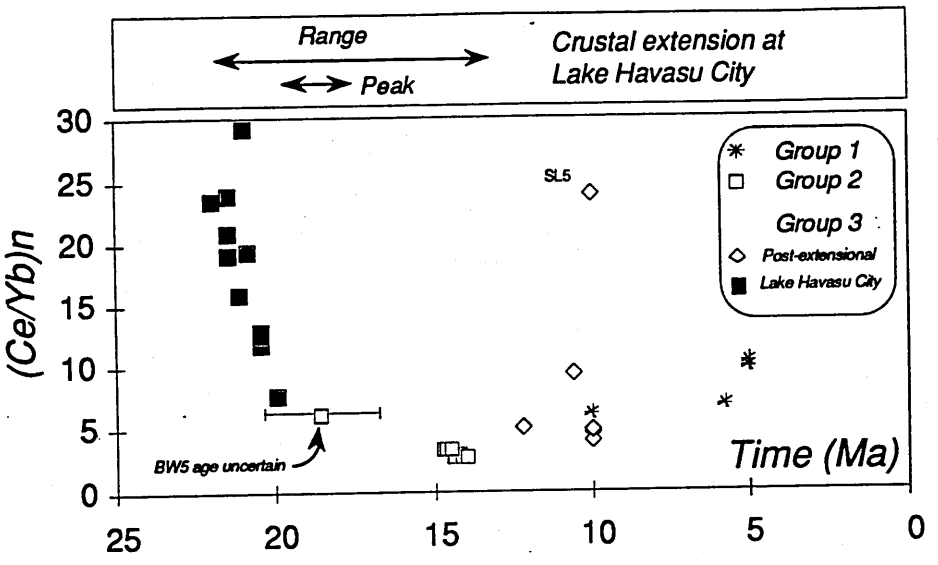

Figure 7. Primitive mantle normalised Ce/Yb vs time for Lake Havasu City and post-extensional samples only. The relationship to the main phase of crustal extension at Lake Havasu City is shown. The values for 'time' are only approximate and are mainly determined on stratigraphic relationships and the few published K-Ar and Ar-Ar dates (see Chapter 2). Where age data is restricted, the samples have been arranged in stratigraphic sequence with an arbitrary time spacing (eg. group 2 samples).

4.3 Geochemical modelling

In the previous sections, geochemical differences have been highlighted between three main groups of CRT basalts. Moreover, the variation between samples in the largest of these groups (group 3) may be time related.

This variability could reflect a number of factors, although essentially they fall into two categories as being either 'process' controlled or 'source' controlled. Source controlled variations arise from differences in source geochemistry and/or mineralogy, and whether the magmas are derived from the same or disparate sources. Process controlled variations include factors such as the degree of partial melting, whether mixing occurs between magmas from more than one source, and also the possibility of contamination. In modelling the CRT basalts all of these factors are considered, and in particular whether any of these may have varied with time.

Because the number of potential variables is high, some initial assumptions must be made around which a model can then be developed. In this respect the group 3 basalts are addressed first and it is assumed that they are derived from the same general source with a

particular mineralogy and trace element content. This is a reasonable assumption because the basalts have similar isotopic compositions and display only limited variability of the more mantle compatible elements (eg.Y, Yb and Lu). The group 3 variability is therefore thought to be process controlled, resulting from either changes in the degree of partial melting of this source or from mixing / contamination.

The partial melting equation used in this Chapter is for the simple batch melting model from Allègre and Minster (1978):

$$C_1\omega = \frac{C^{o}\omega}{D^{o}\omega + F(1-P\omega)}$$

Where $C^{o}\omega$ is the initial concentration of element ω in the mantle source and $C_1\omega$ is the concentration of ω in the magma. $D^{o}\omega$ is the bulk distribution coefficient for ω in the source and $P\omega$ represents the bulk distribution coefficient of ω for the proportion in which the source mineral phases contribute to the melt. Percent melting = 100*F.

During partial melting, and particularly at small degrees of melting, highly incompatible trace elements are preferentially concentrated in the melt relative to the more compatible elements. As the degree of melting increases, the total trace element concentration in the melt decreases, and eventually approaches that of the mantle source. The ratio of highly incompatible elements in the melt will also decrease, although the ratio of similarly incompatible elements is likely to remain fairly constant. Isotopic ratios should be unaffected by variations in percent melting. In contrast, mixing / contamination of the original basaltic magma is likely to result in changes in both trace element and isotopic compositions. Furthermore, because the added material may have been derived from a geochemically disparate source to that of the original magma, large changes in the ratios of equally compatible trace elements may also occur.

4.3.1 Group 3 basalts

The large change in the Ce/Yb ratios within group 3 (figure 7), relative to the smaller variation in Yb and the moderately low Yb concentrations, suggests that Yb is reasonably compatible in the source, and in a phase which does not significantly contribute to the melt. Suitable minerals with high $Yb_{xstal/liq}$ distribution coefficients that might be present in the mantle are pyroxene, amphibole and garnet (Pearce and Norry 1979). However, pyroxene and amphibole are usually among the first minerals to contribute to the magma as the mantle melts. Only garnet is likely to remain as a residual phase at small degrees of partial melting, although it too is expected to become exhausted above 12% melting (Cox et al 1984). A garnet bearing source would thus be more favourable and a composition similar to that of fertile garnet lherzolite xenoliths from Arizona (Ehrenberg 1982) is suggested (table 1). The proposed source is an average of a fertile garnet lherzolite analysis (FO77) from Ehrenberg (1982) and a modelled composition for the source of basic rocks in the Lebombo region of South Africa (Cox et al 1984). The resulting composite ('initial model') is within error limits of the source calculated for alkali basaltic magmatism in the Big Pine Volcanic Field of California (Ormerod 1988; Ormerod et al 1991).

	INITIAL MODEL	*PA-65G*		Source Mineralogy		Proportions entering melt	
La	2.205	.84	*MODEL*	①	②	①	②
Ce	4.9	2.0	Ol	.62	.62	.1	.1
Nd	2.667	1.5	OPX	.3	.3	.3	.3
Sm	.636	.342	CPX	.058	.08	.55	.6
Eu	.206	.119	GT	.022	0	.05	0
Tb	.104	.06					
Yb	.479	.27	*PA-65G*	③		③	
Lu	.06	.041	Ol	.6		.1	
Zr	12	na	OPX	.2		.1	
Ti	1000	na	CPX	.15		.5	
Y	2.9	2.3	SP	.05		.3	

Table 1. Proposed source comoposition (ppm), mineralogy and melting modes, see text for discussion of models. Model ① to reproduce the group 3 trends. Model ② as ① but without garnet in the source. Model ③, melting spinel lherzolite source based on the composition of xenolith PA-65G from Frey and Prinz (1978). Melting modes adapted from Beccaluva et al (1985).

The variation in the ratios of similarly incompatible elements (eg. Nb/La and Nb/Zr) is rather restricted for the group 3 (and group 2) basalts (figures 3 & 4). However, the Th/Zr, Th/Nb and, in figure 7, the Ce/Yb ratios show considerable variation. In figures 2 and 7 this variation appears to be systematic (eg. lower concentrations of the REE are matched by lower concentrations of LILE) and to vary with time. The pre/syn-extensional basalts show no systematic variation in their Pb and Sr isotope ratios, although the post-extensional basalts apparently do (figures 5 and 6). Some of these basalts also plot at considerably higher Nb/La and lower Th/Zr than the group 3 average.

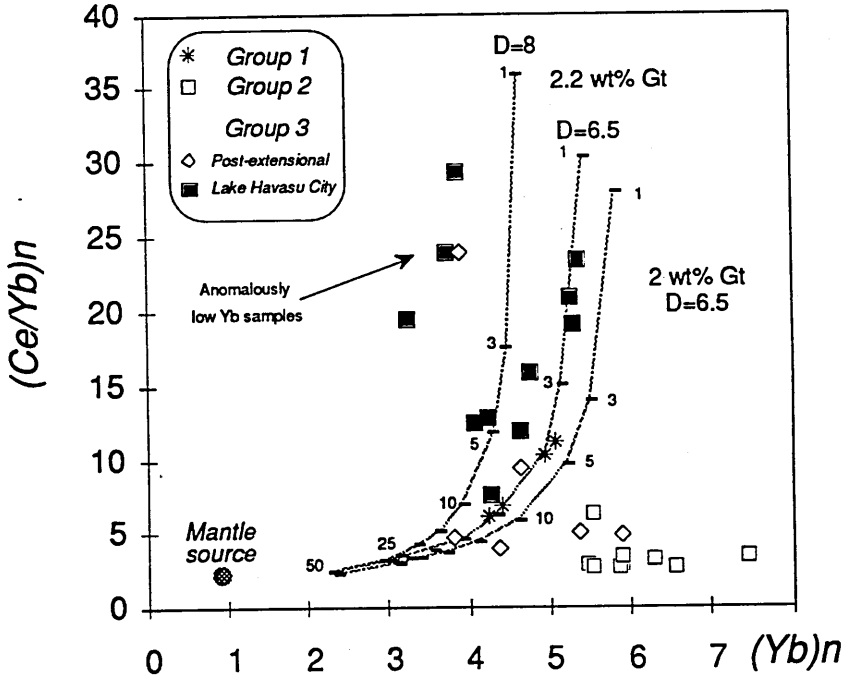

Figure 8. Primitive mantle normalised Ce/Yb vs Yb for post-extensional samples and samples from Lake Havasu City. Melting curves are displayed for melting the initial model composition in table 1 and with melting model ①. However, the Yb distribution coefficient in garnet and the proportion of garnet in the source have been varied as indicated. See text for details.

These features suggest that a few of the group 3 post-extensional basalts may have undergone at least some mixing between a trace element enriched magma and a more LILE-depleted, probably MORB or group 1 type, magma. This is illustrated by the hypothetical mixing line on figure 3. Conversely, the systematic trace element variations in the remainder of the group 3 basalts, and their limited isotopic range, are more consistent with the effects of variable degrees of partial melting. This possible relationship between the samples is demonstrated in figures 8 and 9 with the post-extensional basalts and data from

the Lake Havasu City area.

The model curves in figure 8 are based on the simple batch melting equation (Allègre and Minster 1978) with source minerals entering the melt in the proportions given for model ① in table 1 (as suggested in Beccaluva et al 1985). The best fit to the data is obtained by melting the lherzolitic mantle source containing 2-2.2 wt% garnet, and allowing for a range of $Yb_{gt/melt}$ distribution coefficients of between 6.5 and 8.0 (see table 1 for further details of this melting model). In figure 9 the model has been expanded to include a number of other elements, plotted in such a way that samples related by variable degrees of partial melting will have a straight line correlation (after Hofman and Feigenson 1983; Ormerod et al 1991).[2]

Note that diagrams of the type displayed in figure 9 are typically plotted with the most incompatible element that is available on the x-axis, and as the y-axis numerator (eg. Ormerod et al 1991 use Rb). However Pb, Rb, Ba and K_2O all potentially suffer to some degree from alteration processes which are difficult to quantify. It is also considered that Th distribution coefficient data is not yet sufficiently constrained to be useful in this sort of modelling. Thus, La is chosen as the most incompatible element and the calculated degrees of partial melting are therefore relative values, based on the assumed La source content.

Although the results from most of the samples do approximate to linear arrays on figure 9, a certain amount of scatter is observed which may be the result of fractionation. Typically this will displace samples horizontally causing them to plot below the general correlation lines. However, four samples (MO1, MO2, MH8 and SL5) all have anomalously low Yb concentrations and are consequently displaced to high positions on figures 8 and 9. This could indicate either fractionation of a phase in which Yb is highly compatible, or the retention of such a phase in the residual source. Analytical precision (of XRF data) may also be an important factor in the scatter of Y and TiO_2.

---

[2] Notice the similarity in the slope of the trace element arrays for the pre/syn-extensional and post-extensional samples in figure 9. This is consistent with the initial assumption that all the samples in group 3 are derived from the same source.

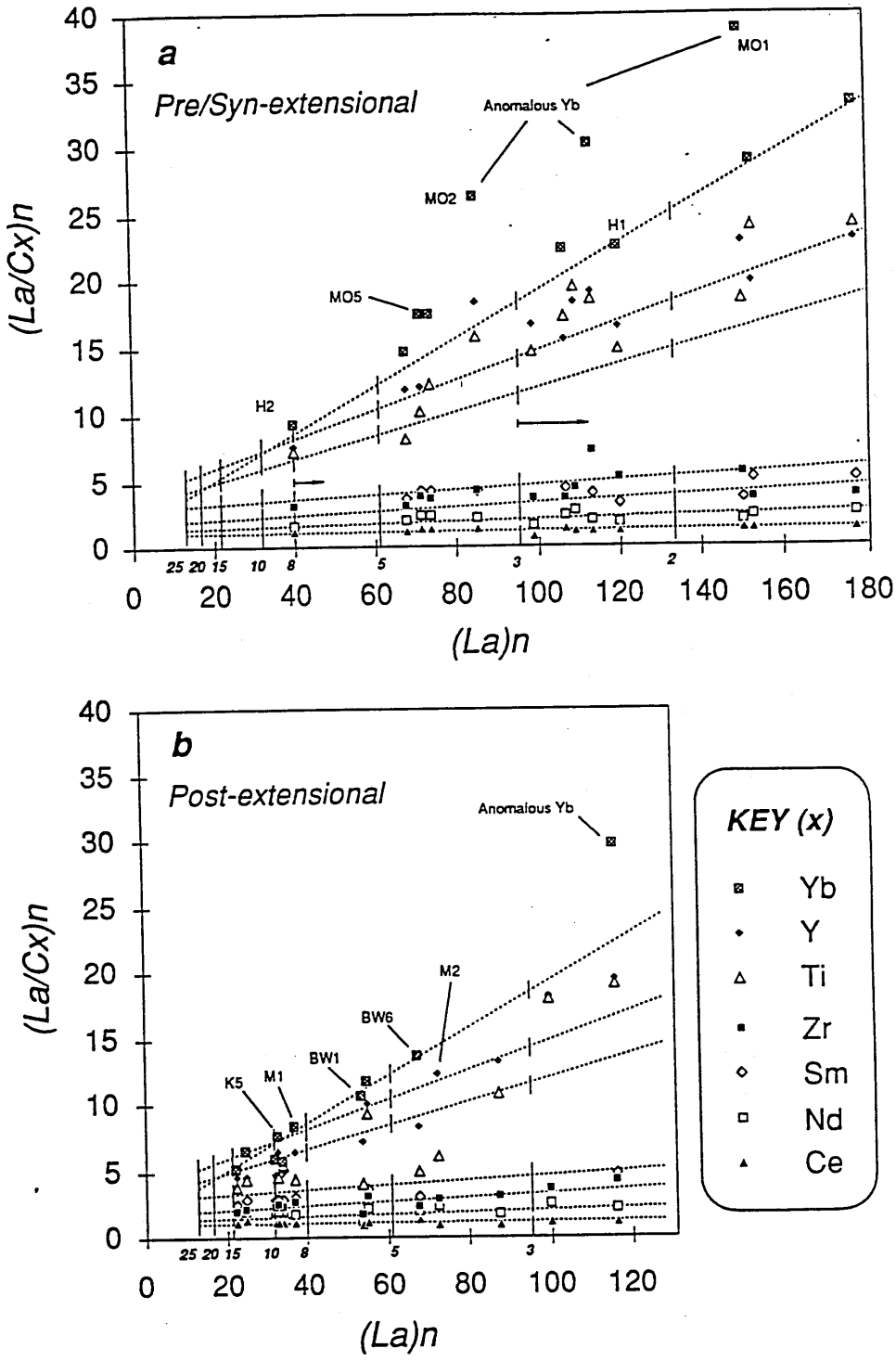

Figure 9. Primitive mantle normalised La/Cx vs La, where Cx is the concentration of the elements x listed in the key. Samples related by variable degrees of partial melting of the same source will fall on straight lines, with the same slope and intercept values. The lines shown on figure 9 are calculated from melting of the proposed initial source in table 1 (degree of melting is displayed as small figures below the x-axis). The model lines are in the same order as the elements in the key. Clearly there is reasonable correlation between the model lines and most of the actual data. TiO2 is an exception: the high Ti contents in group 1 samples cause them to plot lower on the diagram; while other samples that plot above the model lines may have fractionated ilmenite. The maximum effect of 15wt% fractionation on sample position has been indicated on 9a with small arrows (the shift is greatest for the smallest degrees of melting and hence these samples are not used in the modelling to be presented on figure 11). K5, M1, BW1, BW6 and M2 indicated on 9b are the high Nb/La, group 1, samples.

On both figures 8 and 9 the degree of partial melting of the proposed source is expressed as a percentage, calculated from just the REE data. The pre/syn-extensional basalts from Lake Havasu City can be modelled by approximately 1-8% partial melting of the source, with most samples corresponding to between 2 and 5% melting. The group 3 post-extensional basalts cover a larger melting interval (2-15%) and their sample distribution is skewed towards the higher end of this range. High Nb/La (group 1) basalts are also shown on figures 8 and 9 and they can be modelled by 4-10% partial melting of this same source.

The principal inference that can be drawn from these results is that the Ce/Yb variation in figure 7 corresponds to changes in the degree of partial melting with time. The earliest magmas apparently record the smallest degrees of melting although the extent of melting rapidly increased as extension proceeded. Following the end of extension the average degree of partial melting was somewhat higher, although rather more variable.

4.3.2 Group 2 basalts

The group 2 alkali olivine basalts occur at Lake Havasu City between the main pre/syn-extensional and post-extensional phases of group 3 type magmatism. It is therefore possible that the two magma types are related in some way. Again, this relationship may be either source or process controlled. For example, the low position of the group 2 basalts on figure 7, and the generally depleted nature of their trace element patterns (figure 2), could be consistent with greater degrees of partial melting of the proposed group 3 source. However, this does not explain the enriched Y, Sc and HREE content of the basalts. On figure 8 this forces the group 2 basalts to plot away from the garnet lherzolite melting curves towards high Yb values.

The solution may be to involve a two stage process, of melting followed by fractionation. In this way it would be possible to produce a nearly flat mantle normalised pattern from a high degree of partial melting, and then subsequently raise each trace element concentration by fractionation. The distribution of the group 2 samples on figure 8 would appear to support this hypothesis. The group 2 trend on figure 8 might therefore represent part of a

fractionation vector originating on the garnet lherzolite melting curves. If this trend is extrapolated back to the melting models it intersects them at ~25-30% melting, and 1.36ppm Yb (figure 10a).

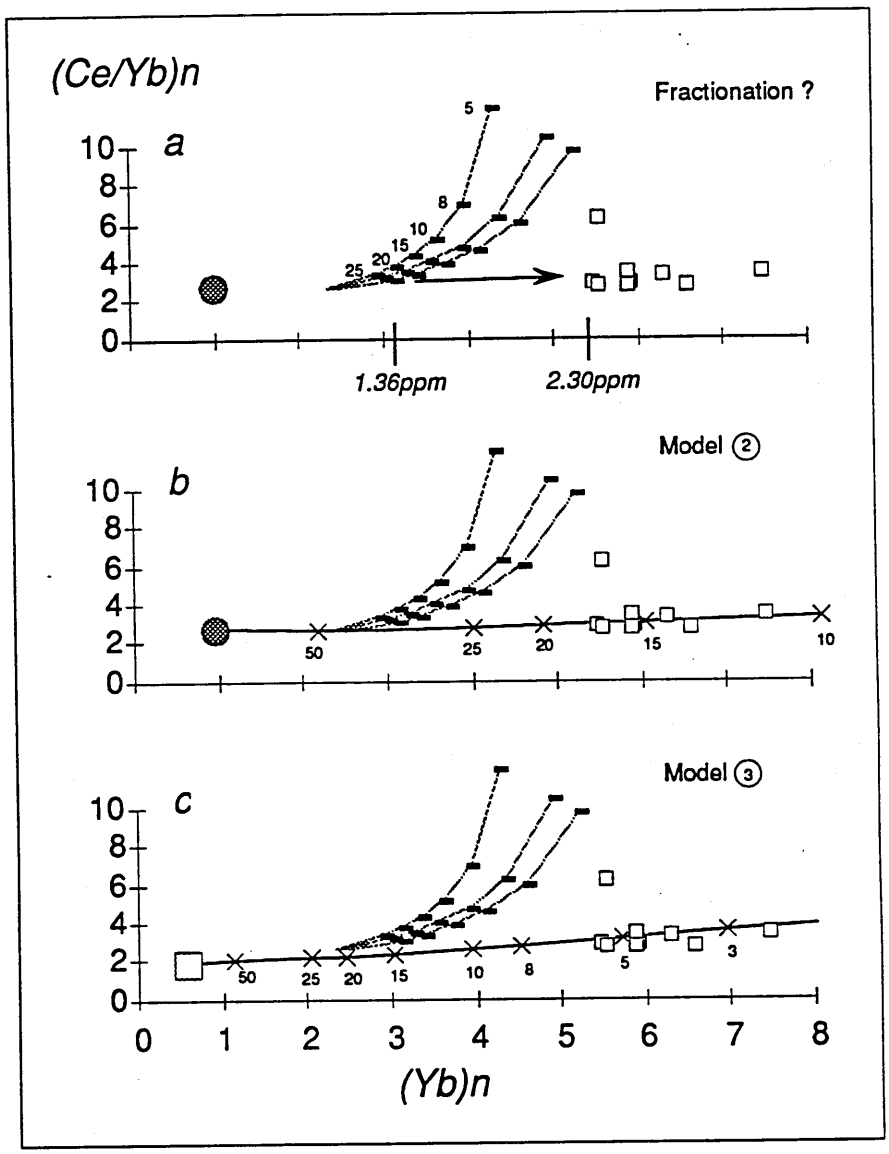

Figure 10. Expanded portion of figure 8 showing various models for generating the group 2 basalts: **a)** fractionation from the group 3 models; **b)** melting the group 3 source composition without garnet; **c)** melting a depleted spinel lherzolite source. See table 1 for models used to generate curves in **b** and **c**.

In this model the nature of the fractionating assemblage is obviously not known, but it is possible to estimate the amount of fractionation required to shift the samples from their 'starting position' at 1.36ppm Yb to their current position at ≥ 2.3ppm Yb. Assuming a bulk Yb distribution coefficient of zero for the fractionating assemblage, then the *absolute minimum* requirement is 40wt% fractionation to achieve the displacement.

In light of the low silica content of the group 2 basalts from Lake Havasu City (45.5-47.7 wt% SiO_2), and transition metal abundances indicating just 6-8wt% fractionation from primary, such a large value is improbable. Thus it is concluded that the group 2 basalts were not derived by fractionation from melts of the same source composition and mineralogy as the group 3 basalts.

However, the bulk similarity of the group 2 and 3 mantle normalised signatures (figure 2) does suggest that trace element ratios in the mantle sources for both are fairly similar. The difference between the sources may therefore be one of mineralogy. Such a situation is represented by model ② in table 1 where the garnet content of the proposed group 3 source has been set to zero. Because garnet is the principal influence on the distribution of Yb in the mantle its absence creates a situation of almost equal compatibility between Yb and Ce. Consequently the new melting model is defined by a nearly horizontal vector on the Ce/Yb vs. Yb diagram (figure 10b), this is similar to the vector produced by fractionation. The least fractionated group 2 sample (H12) can be modelled by ~18% melting of this new source, and the whole range of basalts by 12-18% melting.

Intuitively, such a melting model would appear to be reasonable because these basalts are only found along the axis of the CRT where extension is thought to have reached a maximum. This would be consistent with the positive correlation between the amount of lithospheric stretching and the size of melt fraction attained in adiabatic decompression melting models (McKenzie and Bickle 1988). Alternatively, the group 2 basalts may have been derived from a source with a lower trace element content (although with similar trace element ratios to the proposed group 3 source) by smaller degrees of partial melting. The existence of a suitable source is suggested by the predominance of trace element depleted spinel lherzolite xenoliths in the Pliocene-Recent basalt fields of southern Arizona (Wilshire et al 1985; Frey and Prinz 1978). Model ③ in table 1 is based on the most fertile, in major element terms, of these xenoliths (from Frey and Prinz 1978), and spinel lherzolite melting modes from Beccaluva et al (1985). With this model the least fractionated group 2 sample can be derived by just 6% partial melting, and the whole range of group 2 basalts by 2-6%

melting (figure 10c).

Thus, both models ② and ③ are apparently capable of reproducing some of the geochemistry of the group 2 basalts, although they require substantially different degrees of partial melting in the source. However, if the modelling is carried out using La and Sm (replacing Ce and Yb) then model ③ is favoured.

As a further, independent, test it may be possible to distinguish between the models on the basis of major element data alone. For example, Jaques and Green (1980), Klein and Langmuir (1987; 1989) and McKenzie and Bickle (1988) suggest that there is a relationship between the extent of mantle melting and the major element budget of the resulting basalt magmas. This work has generally been applied to the genesis of MORB, although it might be possible to apply the same reasoning to the CRT basalts. The main assumption that must be made is that, under the same conditions of pressure, initial mineralogy and degree of partial melting, all fertile mantle sources will melt to produce magmas of effectively the same major element composition. If this is true then direct comparisons can be made to the MORB models.

Such comparisons are presented in table 2 (overleaf) for the group 2 and 3 basalts. Following the method of Klein and Langmuir (1987), the comparisons are made at 8wt% MgO and, where necessary, the CRT sample trends have been extrapolated to this value. This helps to eliminate the effects of fractionation from the primary liquid compositions, and it permits comparison of the basalts as a group of data rather than as individual samples. The results in table 2 indicate no consistent major element features that might be reconciled with the pressure of melting, although there is consistency when the data is interpreted in terms of the degree of melting. In this case both groups 2 and 3 suggest small degrees of partial melting compared to that of typical MORB. The lower SiO_2, Ca/Al ratio and higher Na_2O (at 8wt% MgO) for group 2 may also indicate that basalts in this group are derived by smaller degrees of partial melting on average than those in group 3. Furthermore, at high degrees of partial melting, such as that indicated in model ②, sub-alkaline rather than alkaline compositions would have been anticipated for the group 2

basalts (McKenzie and Bickle 1988). Indeed all of the group 3 post-extensional basalts which can be modelled at ≥ 10% melting are sub-alkaline.

Thus, if this major element modelling is at least reasonably valid, the results suggest that the group 2 basalts are more likely to be derived by small degrees of partial melting of a trace element depleted source. This favours model ③ in table 1. The group 2 and 3 sources are therefore thought to have both different mineralogy and trace element abundances, although rather similar trace element ratios and isotopic compositions.

	Group 2	*Group 3*	*MORB*
SiO_2	46 V.LOW	~49 LOW	48-53
FeO	9.8 Moderate	7.8-9.8 Moderate	6-13
CaO	9.2 V.LOW	10.5-11 Moderate	10-13.5
Na_2O	3.3 V.HIGH	2.8 HIGH	1.5-3.5
Ca/Al	~0.55 V.LOW	0.7 Moderate	0.6-0.87

General features of mantle melting (Jaques and Green 1980; Klein and Langmuir 1987; 1989):
HIGH PRESSURE MELTING - Low SiO_2, High FeO, High Ca/Al
SMALL DEGREE MELTING - Low SiO_2, Low CaO, High Na_2O, Low Ca/Al

Analysis of CRT basalts in comparison to these general features:
GROUP 2 = Small degree partial melting
GROUP 3 = Small to moderate degree partial melting.

Table 2. Top: Wt% comparison of group 2 and 3 basalts to MORB compositions at 8wt% MgO. **Lower:** Dependence of the major element compositions of mantle melts on the degree and pressure of partial melting. The CRT group 2 and 3 basalts are interpreted in general terms based on the features outlined; both groups appear to be more consistent with small degrees of partial melting.

4.3.3 Group 1 basalts

These basalts apparently fall on the same garnet lherzolite melting curves in figure 8 as

described for the group 3 basalts, and indeed the REE profiles for the two groups are almost identical (see figure 2). But the high Nb/Zr and Nb/La ratios, low Th/Nb ratios, low Ba contents, low $^{87}Sr/^{86}Sr$ ratios, and lead isotope ratios close to the Northern Hemisphere Reference Line indicate that these basalts must be derived from a separate mantle source. This source may be mineralogically similar to the group 3 source, but it has not developed the high time-integrated isotope ratios and it has a different enrichment history for trace elements less compatible than the LREE.

However, because of the similarity between the REE profiles of these and the group 3 basalts, the trace element modelling in figures 8 and 9 may not be entirely invalidated. Thus it is suggested that these basalts are derived by reasonably small degrees of partial melting (eg. $\leq 10\%$).

4.3.4 A better approximation of mantle source compositions

Having established the degree of partial melting for the CRT basalts (figures 9 and 10), the modelling techniques can be inverted to produce more information about the mantle source. This is achieved by regressing individual sample compositions, by their calculated degrees of partial melting, to arrive at an overall source composition. Although this may appear to be a circular argument, the degrees of partial melting indicated in figure 9 are effectively determined just by the distribution of La. Therefore it is possible to calculate the abundance contents of other incompatible trace elements in the source *relative* to that of the assumed La source contents.[3]

This inverse modelling has been applied to the three CRT basalt groups to calculate the trace element patterns of their sources. Model ① in table 1 was inverted for groups 1 and 3, and model ③ for the group 2 basalts. The results are displayed as mantle normalised trace element patterns in figure 11 with the mean calculated source compositions (after regressing a number of samples, see figure caption) and fields representing 1σ error.

---

[3] These were inferred to be 2.205ppm in the group 1 and 3 sources, and 0.84ppm in the group 2 source (see table 2).

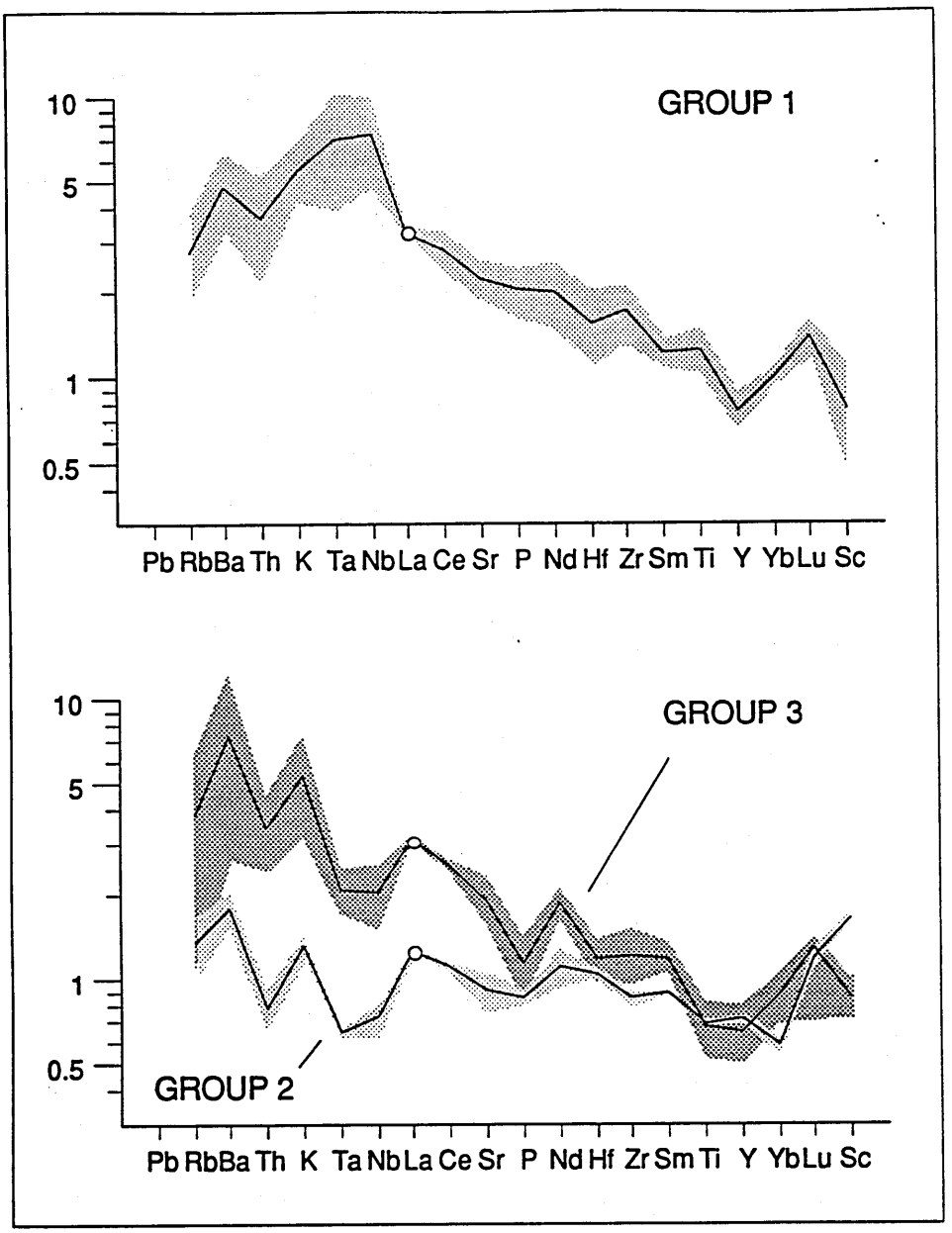

Figure 11. Calculated source compositions for the three CRT basalt groups relative to the fixed La source content of the initial model source in table 1. The lines represent mean source compositions and the shaded regions are fields for 1σ error on the inverse calculations. See text for discussion. Samples used in the inverse modelling are listed below with the degree of partial melting that each sample is regressed by: **Group 1-** BW1 (6%), BW6 (4.7%), K5 (9%), M1 (8.5%), M2 (4.4%); **Group 2-** H5 (4.25%), H6 (3.2%), H7 (4.3%); **Group 3-** MO6 (4.4%), MO1 (1.5%), MO7 (2.7%), MH8 (2.5%), MO2 (3.5%), MO5 (4.5%), H2(8%), D3 (10%), BW4 (14%). See Appendix C for source composition table.

Clearly, the group 2 and 3 basalt sources have very similar trace element patterns, particularly the troughs at Ta-Nb, P_2O_5 and Th, and the maxima at Ba, although at somewhat different abundance levels. The group 1 source has a much smaller Ba peak, high P_2O_5 and TiO_2 and a maxima at Ta-Nb. Thus it is suggested that two distinct mantle sources melt to produce the CRT magmatism and that one of these sources, characterised

by a Ta-Nb trough, has enriched and depleted fractions.

4.4 Asthenospheric versus lithospheric sources

The previous section recognised the need of two distinct mantle sources for the CRT magmatism, which raises the question of how the sources are related to each other in a physical sense. Identification of the sources as either lithospheric or asthenospheric in origin (and whether they melt in a specific order) is also important for understanding the development of the magmatism, and how this was linked to extension.

First let us consider the group 1 basalts which constitute only a small minority of the CRT samples. The smooth mantle-normalised patterns, trace element ratios identical to enriched MORB or OIB, and isotope ratios similar to MORB suggest that the group 1 basalts were derived from the asthenospheric mantle. The source was most obviously tapped during the latest episode of post-extensional magmatism, however a number of samples from the Lake Mead area (eg. BR1&2) indicate that melting of the source occurred here during the earliest syn-extensional phase at approximately 15Ma. Furthermore, the apparent mixing trends between typical group 1 basalts (eg. M1, BW1 and BW6) and earlier post-extensional basalts (eg. K5 and BW4) suggests that melting of this source was not confined to just the most recent phase of magmatism.

Basalts similar to those in group 1 are recognised in the Pliocene-Recent volcanic fields across the Great Basin and southern Arizona (eg. Lunar Craters, Lum et al 1989) and are termed the 'Basin and Range magma type' by Fitton et al (1991). Under the conditions of model ① in table 1, the most primitive Lunar Craters magma composition can be reproduced by 8% melting of the proposed group 1 source composition.

A low Th/Ta (equivalent to low Th/Nb), low $^{87}Sr/^{86}Sr$ component is also identified as the principal contributor to post 21Ma magmatism in the Mogollon Datil Volcanic Field of New Mexico (Davis 1991), and for post 11.6Ma magmas in the Rio Grande Rift of NW Colorado (Leat et al 1988). These authors also recognise an asthenospheric origin for the basalts, although there is considerable debate as to whether they represent small volume

melts of normal asthenosphere or are related to melting in a mantle plume. This controversy will be discussed in Chapter 5.

The irregular mantle-normalised trace element patterns, trace element ratios and isotope ratios which are generally distinct from MORB or OIB, suggest that the group 2 and 3 basalts are inconsistent with an asthenospheric origin. The group 3 source in particular is modelled as having a high concentration of Ba (and other LILE), and both the group 2 and 3 sources are calculated to have a depleted Ta-Nb signature. The elevated $^{207}Pb/^{204}Pb$, $^{208}Pb/^{204}Pb$ and $^{87}Sr/^{86}Sr$ isotope ratios in both basalt groups require time to develop and therefore a stable source that is isolated from the convecting asthenosphere.

The length of time that this source has been isolated from the asthenosphere can be estimated from the lead isotope ratios of samples derived from this source. These samples should fall along a secondary isochron line that defines the time since isolation. From figure 6 this is calculated at approximately 1.57Ga (see Appendix C for details). This age is probably a minimum estimate because the isochron is drawn through some of the group 3 post-extensional samples which may have had their lead isotope ratios diluted by mixing with a group 1 type magma. However, this age is still significant because it effectively rules out melting of the subducted Farallon Plate which is thought to have been <50My old beneath the CRT at the time of magmatism (Engebretson et al 1985). The 1.57Ga age is instead comparable with the time of Proterozoic lithosphere stabilisation across the continental western United States (Dudas et al 1987). Therefore it is suggested that the group 2 and 3 magmas are derived from melting of the sub-continental lithospheric mantle beneath the CRT. The group 2 basalts probably derive from a spinel-bearing fraction of this mantle and the group 3 basalts from lithosphere in which garnet is residual.

If the major and trace element models for the group 2 source are correct, then the relationship of the group 2 and 3 sources within the lithospheric mantle may be one of depth. The favoured model for the group 2 source contains spinel which is generally stable at lower pressures than garnet. Consequently, this source is likely to represent a shallower level in the lithosphere. A trace element depleted spinel lherzolite zone overlying a more

enriched garnet-bearing zone would also be consistent with currently accepted models for trace element enrichment in the sub-continental lithospheric mantle (eg. Waters and Erlank 1988). Additionally, the link between the group 2 basalt types and maximum extension may be reconciled with a depth related distribution if melting begins close to the base of the lithosphere, and then spreads to shallower levels as the degree of extension increases.

However, there are problems with inferring lithospheric mantle melting as the principal source of the CRT magmatism. McKenzie and Bickle (1988) and White and McKenzie (1989) calculate that the bulk of mantle melting will occur in the asthenosphere and thermal boundary layer during continental extension, and that any contribution from the lithosphere will be in the form of a contaminant. Ormerod (1988) also recognises the possibility of major and trace element (and therefore presumably isotopic-) decoupling during melting. Thus, melting of the asthenosphere could provide a simple basaltic magma which then picks up the lithospheric trace element and isotopic signature enroute to the surface. This new enriched signature is likely to swamp that of the trace element depleted asthenospheric melt. Subsequently, it would be difficult, if not impossible, to identify the initial contribution from the asthenosphere in these 'contaminated' basalts.

Nevertheless, if the group 1 basalts are a true representation of asthenospheric melts in the western USA then their high Ta-Nb signature at least would be expected to survive into the 'contaminated' magmas. This is because it is inherently more difficult to dilute trace element concentrations than it is to enrich them. Clearly, from figures 3 and 4, this signature is not present in the typical basalts from the CRT. Therefore it is unlikely that asthenosphere of this type has been a significant contributor to the syn-extensional magmatism.

4.5 Summary and Model for CRT Magmatism

In addition to the field classification of pre/syn- and post-extensional samples, three distinct geochemical groups of basalt have been identified in the CRT. Basalts in group 1 have isotope ratios similar to MORB or OIB and smooth mantle-normalised trace element patterns that typically peak at Ta-Nb. The group 2 and 3 basalts have elevated isotopic

compositions and more irregular mantle normalised patterns with a Ta-Nb trough. Of these, the group 2 basalts have the most depleted trace element signatures, although they are enriched in Y, Sc and the HREE.

It has been suggested that the bulk of pre/syn- and post-extensional basalts from the CRT (group 3) are likely to be related by variable degrees of partial melting from a trace element enriched lherzolitic source. This source is modelled to contain ~2wt% garnet which mostly behaves as a residual phase during melting. Such a source composition has previously been suggested for the origin of Cenozoic basalts in southern Nevada by a number of authors, including Van Kooten (1980) and Menzies et al (1983). Alkali olivine basalts erupted in the final stages of extension (group 2) are thought to be derived from a similar, but trace element depleted, source in which garnet is absent although spinel may be present instead. The trace element and isotope signatures of both the group 2 and group 3 basalts are consistent with the melting of a non-convecting mantle capable of sustaining geochemical hetereogeneities developed during the Proterozoic. Thus, the subcontinental lithospheric mantle is proposed as the predominant magma source.

The youngest post-extensional basalts (group 1) are comparable with the 'Basin and Range magma type' of Fitton et al (1991). Their trace element and isotope signature supports an asthenospheric source probably with residual garnet, and only small degrees of partial melting. Although basalts from this source only become dominant from the late Miocene in the CRT, there is evidence that similar magmas contribute to some earlier syn- and post-extensional volcanism particularly near Lake Mead.

Within the lithospheric mantle source the degree of partial melting increased with time. The trace element signature of the earliest magmas (group 3) can be reproduced by < 3% partial melting, but this increased to 3-8% melting during the main syn-extensional period (from 20-18Ma at Lake Havasu City). Post-extensional magmatism at ~10Ma is typically modelled at > 8% melting and possibly up to 15% melting, although the input of group 1 source magmas may induce some error in these figures. This increase in the degree of partial melting is thus apparently out of step with crustal extension because the largest

percent melts erupted up to 10m.y. after the peak of extension. However, in terms of extrusive volumes, the peak of magmatic activity does occur much earlier, during the main pre/syn-extensional phase (see Chapter 2).

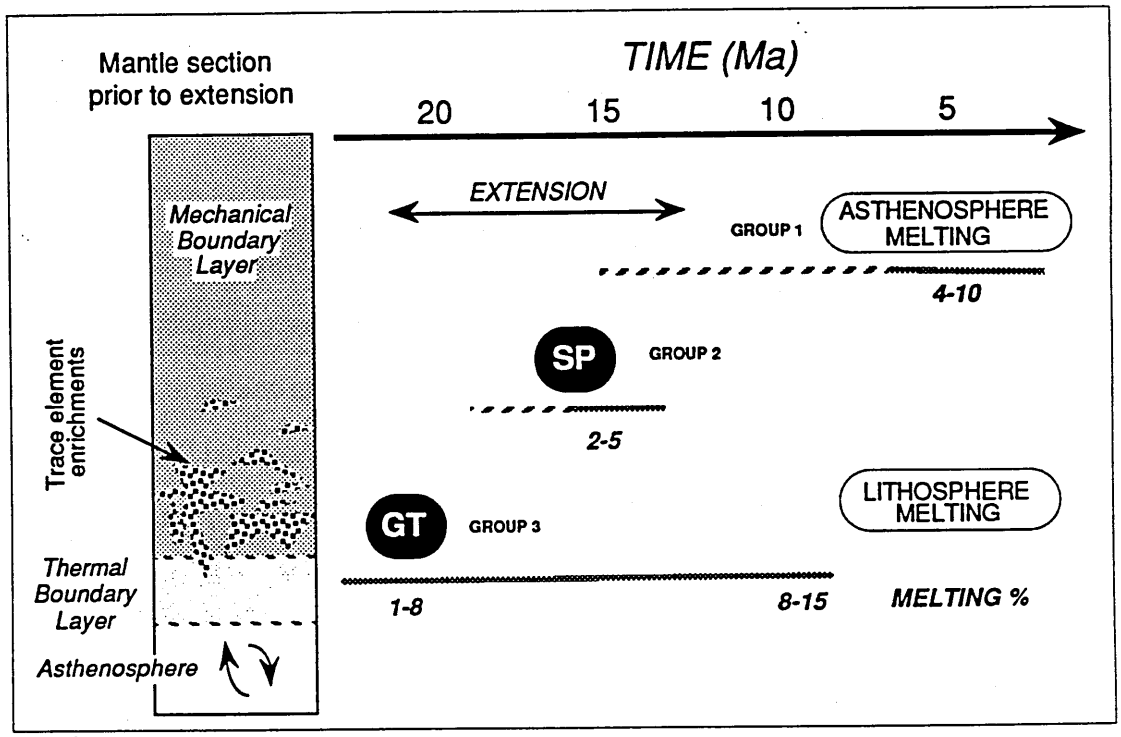

Figure 12. Summary diagram for the progression of melting in the sub-continental lithospheric mantle as suggested by the modelling in this chapter. The average degree of melting increases with time in the main source, and shallower levels of the lithosphere are available for melting at the end of the extensional period. These shallower levels are thought to have a different mineralogy and rather less trace element enrichments. Small volumes of asthenospheric melts dominate the most recent post-extensional magmatism.

Immediately after the extensional peak, group 2 type alkali basalt magmatism occurred along the axis of maximum extension in the CRT. These magmas have been interpreted as small degree partial melts from a shallower, more trace element depeleted, part of the lithospheric mantle. Such magmatism was not extensive or long-lived and group 3 type basalts again dominated during post-extensional times. In time, these magmas were themselves succeeded by asthenospheric group 1 basalts. Volumetrically the group 1 basalts are insignificant and they are only readily identified after magma generation in the other sources ceased.

A summary of this model is presented in figure 12. The main features are the dominance of lithospheric derived magmas and the progressive changes in the magmatism with time. This is apparent as both an increase in the degree of partial melting within the main lithospheric

source, and as a progression to melting shallower mantle levels along the axis of maximum extension. In the final stages of magmatism basalts with an asthenospheric origin reached the surface through the thinned lithosphere. The occurrence of similar basalts much earlier in the tectonic history at Lake Mead suggests that the Las Vegas / Lake Mead Shear Zone might be a structure that cross-cuts the whole lithosphere, providing a direct pathway for asthenospheric magmas.

A problem that has not been addressed in this chapter is the physical model of how the CRT magmatism actually relates to lithospheric extension; for instance, whether magmatism initiates extension in the lithosphere, or vice versa. Clearly this is crucial to understanding the complete tectonic and magmatic history of the CRT and the Basin and Range in general. Therefore models for the initiation of magmatism are discussed in the following chapter.

Extension and Magmatism in the Basin & Range Province, W.USA: a Role for Mantle Plumes?

5.1 Introduction

Asthenospheric mantle plumes have recently been invoked in a number of models for Cenozoic extension and magmatism in the western United States. However, geochemical evidence suggests that a significant plume contribution to early extensional magmatism is unnecessary. Plate tectonics, rather than deep seated mantle plumes, may provide the ultimate driving force for extension and magmatism.

The Cenozoic history of the western United States is dominated by magmatism and crustal extension. In the Basin and Range Province (figure 1) two distinct phases of activity can be identified. An early phase (Oligocene-Miocene) was characterised by voluminous trachy-andesitic to high silica eruptions and an estimated 100% extension (ß factor =2) across the Province. Corridors of locally intense extension are also recognised, such as the Colorado River Trough between the southern Basin and Range and the Great Basin, where extension may have exceeded 300% (see Chapter 2) and was accompanied by somewhat more mafic magmatism. The second phase of Cenozoic activity (typically late Miocene-Recent) is dominated by smaller volumes of basaltic and bimodal volcanism, and rather limited degrees of extension (<20%, eg. Stewart 1978). Calculations by Gans (1987) and Gans et al (1989) suggest that up to 5km of new material was added to the crustal thickness of the extensional provinces during the Cenozoic.

Despite the Cenozoic extension much of the western United States has undergone uplift since 17Ma, possibly by as much as 3km (Eaton 1986). The uplift is centred over the Colorado Plateau and the flanks of the Rio Grande Rift, but it also affects the Basin and Range Province (Eaton 1986; Fitton et al 1991). In these latter two areas, maximum current

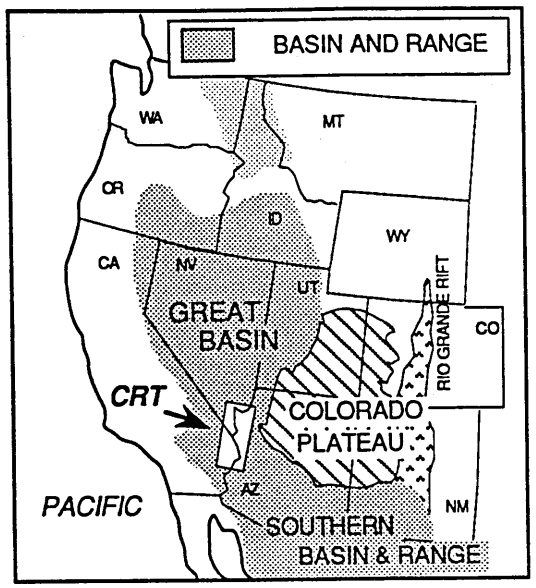

Figure 1. Cenozoic extensional provinces of the western United States in relation to the relatively undeformed Colorado Plateau. CRT= Colorado River Trough extensional corridor, with Lake Mead at its northern limit.

elevations correspond to regions of high heat flow, which may be up to three times the expected value for stable continental lithosphere (Lachenbruch and Sass 1978). This high heat flow, the Cenozoic magmatism and the anomalous topographic elevation have led a number of authors (eg. Scholz et al 1971; Fitton et al 1991) to propose the existence of a 'southern mantle plume' in the western United States that is distinct from any suggested plume related to the Colombia Plateau - Snake River Plain - Yellowstone volcanism.

Furthermore, McKenzie and Bickle (1988) consider that the volume of magma added to the crust during the Cenozoic could only be generated by decompression melting of the upper mantle if its internal potential temperature was between 1380°C and 1480°C prior to extension. For instance, at ß=2 and an asthenosphere potential temperature of 1480°C, 5-7km of melt could be generated assuming an initial lithosphere thickness of 100-120km. However, such tempertures are only usually associated with hot spot magmatism and therefore McKenzie and Bickle (1988) and Gans et al (1989) also suggest the presence of an actively upwelling mantle plume beneath the Basin and Range.

Geochemistry should be able to provide independent evidence to confirm these conclusions because the nature of magmas derived from mantle plumes is already well documented (eg.

Sun and McDonough 1989; Chaffey et al 1989; Weaver 1991). However it is important to determine at what time (if at all) a plume contribution can be identified in relation to tectonic activity. Consequently, magmatism in the Colorado River Trough (CRT) has been investigated because it represents one of the few places in the Basin and Range Province where basaltic magmas occur throughout all of the pre/syn-extensional and post-extensional phases (from 22-5Ma). The geochemistry of the CRT magmatism is described, followed by a model for the magmatism in the southern Basin and Range Province.

5.2 Characteristics of CRT magmatism

Mafic magmatism in the CRT includes a wide range of compositions from alkaline and sub-alkaline basalts to trachybasalts and basaltic andesites. Two principal magma groups are recognised on the basis of trace element and isotopic characteristics, although one of these groups accounts for over 95% by volume of the magmatism and occurs during pre/syn-extensional and early post-extensional phases. Samples in this group ('A' on figure 2) have quite variable geochemistry, but generally high concentrations of incompatible trace elements, particularly the Large Ion Lithophile Elements (LILE; eg. Rb, Ba, K) and the Light Rare Earth Elements (LREE; eg. La, Ce) which are enriched relative to the High Field Strength Elements (HFSE; eg. Ta, Nb, Zr, Ti, Y) and the Heavy Rare Earth Elements (HREE; eg. Yb, Lu).

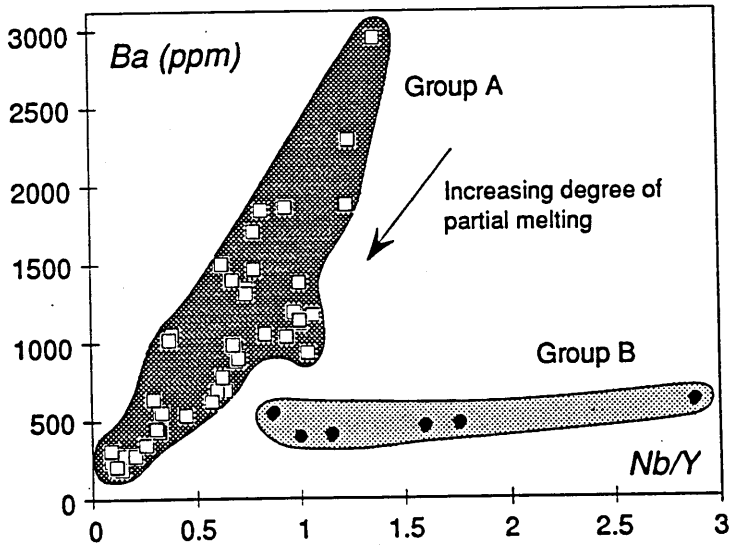

Figure 2. Nb/Y versus Ba variation for the two CRT basalt groups. Much of the variation in the group A samples can be modelled by a range in the degree of partial melting from approximately 1-15%.

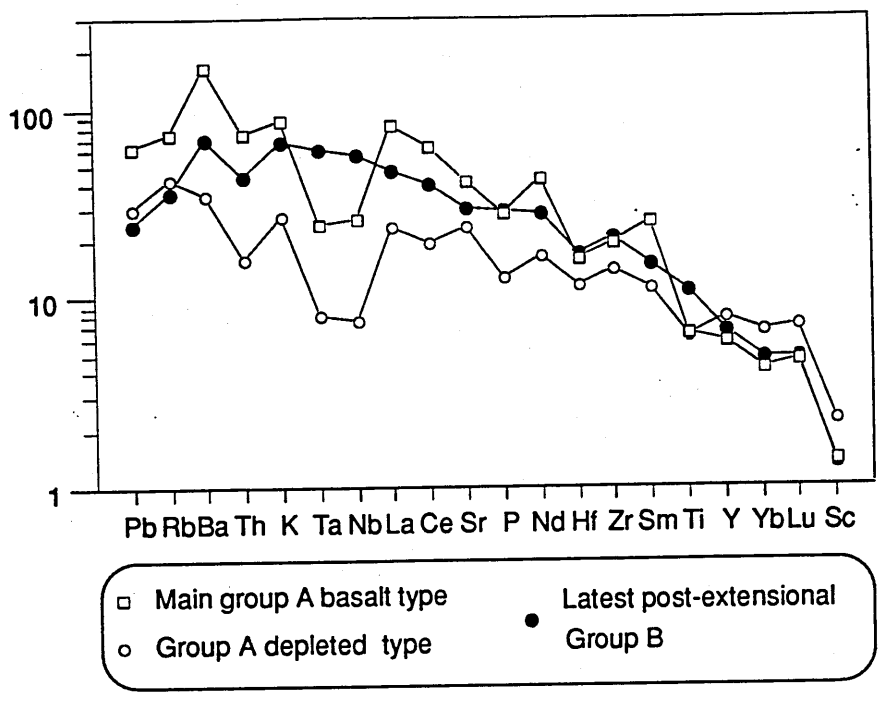

Figure 3. Average compositions of the three CRT basalt groups, normalised to the primitive mantle values of Sun and McDonough (1989). Elements are ordered from left to right with increasing compatibility in upper mantle minerals.

On mantle normalised diagrams (figure 3) these features correspond to steep REE profiles and a characteristic pattern of peaks and troughs. The most prominent troughs are at Ta-Nb (eg. low Nb/La and Ta/K) and P, and there is a prounced step between elements considered to be more and less incompatible than Ti. A subset of the main basalt group is also displayed on figure 3. These basalts represent the last syn-extensional magmatism along the axis of maximum extension. Their trace element patterns are similar to the remainder of the group A basalts although at generally lower abundances, except for the HREE, Y and Sc which are slightly enriched.

The group A basalts have high $^{87}Sr/^{86}Sr$ isotope ratios (mean = 0.7079±8), and $^{207}Pb/^{204}Pb$ and $^{208}Pb/^{204}Pb$ elevated above normal fields for Mid-Ocean Ridge Basalts and Ocean Island Basalts ('MORB' and 'OIB' respectively) over a large range in $^{206}Pb/^{204}Pb$. The samples define a Proterozoic secondary Pb isochron (~1.57Ga) and they are thus interpreted to have been derived from melting of the sub-continental lithospheric mantle. The two subsets of group A may represent melting of relatively enriched and depleted fractions of the lithosphere which probably occur at different depths. Calculated

source compositions for these magmas have many of the basalt features, including the Ta-Nb trough, low Ti and high Ba (see Chapter 4).

The sub-continental lithospheric mantle is also recognised as the primary contributor to Cenozoic basaltic volcanism in central Arizona (Wittke et al 1989), and in southwestern Nevada and Death Valley (Farmer et al 1989).

SAMPLE	Group A MO-5	Group A H-6	Group B BW-6	OIB
TiO2	1.51	1.42	2.99	2.87
K2O	1.64	0.64	2.15	1.45
P2O5	0.47	0.32	0.75	0.62
Ba	899	268	456	350
Ce	89.4	45.2	90.9	80
Eu	2.01	1.72	2.91	3.00
Hf	4.53	3.89	7.46	7.8
La	48.8	18.5	46.6	37
Lu	0.35	0.59	0.4	0.3
Nb	19	6	59	48
Nd	40.6	30.4	46.7	38.5
Pb	7.0	5.0	8.0	3.2
Rb	33	16	36	31
Sm	7.58	5.76	9.48	10.0
Sr	823	325	749	660
Ta	1.02	0.37	3.63	2.70
Tb	0.80	1.02	1.18	1.05
Th	5.26	1.69	4.72	4.00
Y	27	39	37	29
Yb	2.01	3.67	2.44	2.16
Zr	207	165	329	280

Table 1. Representative compositons of the CRT basalt types and comparison to average OIB magma of Sun and McDonough (1989). K2O, P2O5 and TiO2 as wt%, remainder as ppm. Sample H6 is from the depleted subset of group A.

The second distinct magma type ('B' on figures 2 and 3) is identified only as a few flows in the most recent, essentially post-extensional, phase of magmatism. These are alkaline basalts and like samples from group A they are trace element enriched, although the mantle normalised patterns are much smoother (figure 3). The basalts have high Nb/La ratios and

lack the troughs at Ta-Nb and P, and the step at Ti. LILE contents are lower than for the main basalt group and there is almost no variation in the Ba content of the samples (figure 2). The overall trace element abundance patterns are almost identical to that of OIB or enriched MORB (see table 1). Similarly, the calculated source composition has a maxima at Ta-Nb, a high Ti content and only a small peak at Ba. The limited Ba variation may indicate that the true Ba content of these magmas has been swamped by contamination, possibly from the enriched source of the main basalt group.

These basalts are isotopically distinct from group A, having low $^{87}Sr/^{86}Sr$ ratios (eg. 0.70486) and MORB-like Pb isotope ratios. It is thus suggested that the group B basalts represent melting of the asthenospheric mantle, and the trace element characteristics in particular would be consistent with a mantle plume origin. Relatively small volumes of similar basalts (eg. $<0.3km^3$ in NW Colorado, Leat et al 1988) are identified across the western USA extensional provinces and are the characteristic magma type of the youngest Basin and Range volcanism (Fitton et al 1988; Ormerod et al 1988; Lum et al 1989).

The bulk of the CRT magmas are clearly distinct from the typical asthenospheric endmember. Major and trace element modelling of the main CRT basalt group is consistent with small to moderate degree partial melting (eg. 1-15%) of a lithospheric source (see Chapter 4). Material input from the asthenosphere to these magmas would readily be identified by increases in the Ta and Nb contents, in particular in basalts of the trace element depleted subset to group A, but this is not apparent from figures 2 and 3. Thus it must be concluded that the bulk of CRT magmatism is not geochemically influenced by a mantle plume, although there is evidence of an OIB-type (plume?) signature in the final stages of magmatism.

5.3 Possible tectonic model

The conclusions of the previous section would appear to be inconsistent with the McKenzie and Bickle (1988) model for decompression melting of the upper mantle. In their model the bulk of magmatism would be of demonstrably OIB type, perhaps contaminated by small

volumes of lithospheric melt. How then does the lithosphere melt to produce the CRT magmas? Two possibilities are that the lithosphere itself undergoes decompression melting, or that it interacts with an 'external' medium (the asthenosphere) which provides heat, but not material input to the magmatism.

The first of these possibilities infers that Cenozoic magmatism in the western United States occurs as a response to extension. However, magmatism consistently pre-dates crustal extension by between 2 and 12m.y. in the southern Basin and Range (Gans et al 1989). Furthermore, to produce up to 5km of magma during extension, the lithosphere (with a mantle potential temperature of 1280°C) would have to decompress to, and melt within, just a few km of the Earth's surface (eg. at ≤10km, McKenzie and Bickle 1988 figure 7). Besides being an unrealistic melting depth, some of the late extensional CRT magmas record final equilibration depths much greater than this (eg. at ≥10 kb, see Chapter 2).

The second possibility, of an 'external' heat source, would therefore appear to be more favourable. However, the heat input is unlikely to have been directly from a vertical source (plume) because decompression melting would have been anticipated to produce large volumes of OIB magmas prior to and during extension. A lateral input (without significant decompression) of hot asthenosphere is thus suggested. Obviously this model assumes that there would have been relatively hot asthenosphere in a position to move laterally, and heat the base of the lithosphere, during the Oligocene-Miocene. To investigate the likelihood of this, the plate tectonic setting of the western United States during the Oligocene-Miocene must be considered.

At about 28Ma the Farallon spreading ridge and the Mendocino Fracture Zone (MFZ) arrived at the subduction zone along the Pacific margin of the United States, generating the Mendocino and Rivera Triple Junctions (Engebretson et al 1985). Although subduction continued, a strike slip boundary developed along the Pacific margin and the Mendocino Triple Junction / Fracture Zone migrated to the northwest. In so doing, this created a 'window' onto the asthenosphere beneath continental North America, which had previously been underlain by the oceanic Farallon Plate (Atwater 1970). The southern edge of this

plate, and therefore the northern edge of the window, was marked by the MFZ. In time this window has grown in response to continued spreading along the ridge sections adjacent to the MFZ. The exact spreading rate is not known because most of the Farallon Plate is now subducted, but current half spreading rates for the Gorda Ridge (figure 4a) of 1-3cm yr^{-1} and the present East Pacific Rise half spreading rate in excess of 5cm yr^{-1} indicates that 3cm yr^{-1} would not be an unreasonable estimate. At such a rate the MFZ would have lengthened by 840km since 28Ma, generating the 'slab window' as displayed in figure 4.

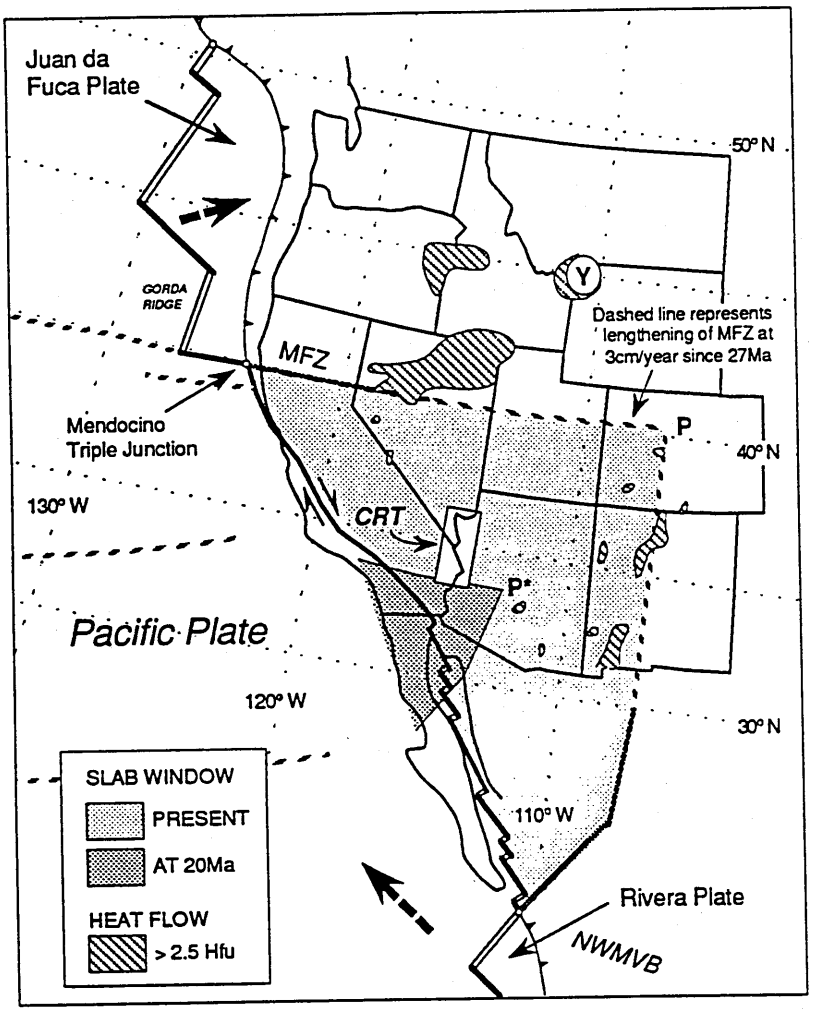

Figure 4a. Current plate tectonic setting of western North America. The positions and extent of the slab window (now and at 20Ma) have been calculated from data in Engebretson et al (1985). Heat flow data from Lachenbruch and Sass (1978). The Juan da Fuca and Rivera Plates are remnants of the Farallon Plate; spreading on the Gorda Ridge segment is 1-3cm yr-1 (Couch and Riddihough 1989). Relative motions of the Juan da Fuca and Pacific Plates are indicated by the large arrows. Y= Yellowstone, MFZ= Mendocino Fracture Zone, NWMVB= North West Mexico Volcanic Belt, P= propagating tip of slab window.

Asthenosphere at depth below the subducted Farallon Plate would be at higher temperatures than that residing between the plate and the base of the lithosphere. Thus the simplest model for the onset of magmatism in the southern Basin and Range would be for this hotter mantle to upwell into the window 'void' and flow laterally over the edge of the departing plate, displacing any asthenosphere previously trapped above the Farallon Plate. Lithospheric melting should then occur and progress northwards with the migration of the MFZ (fig. 5).

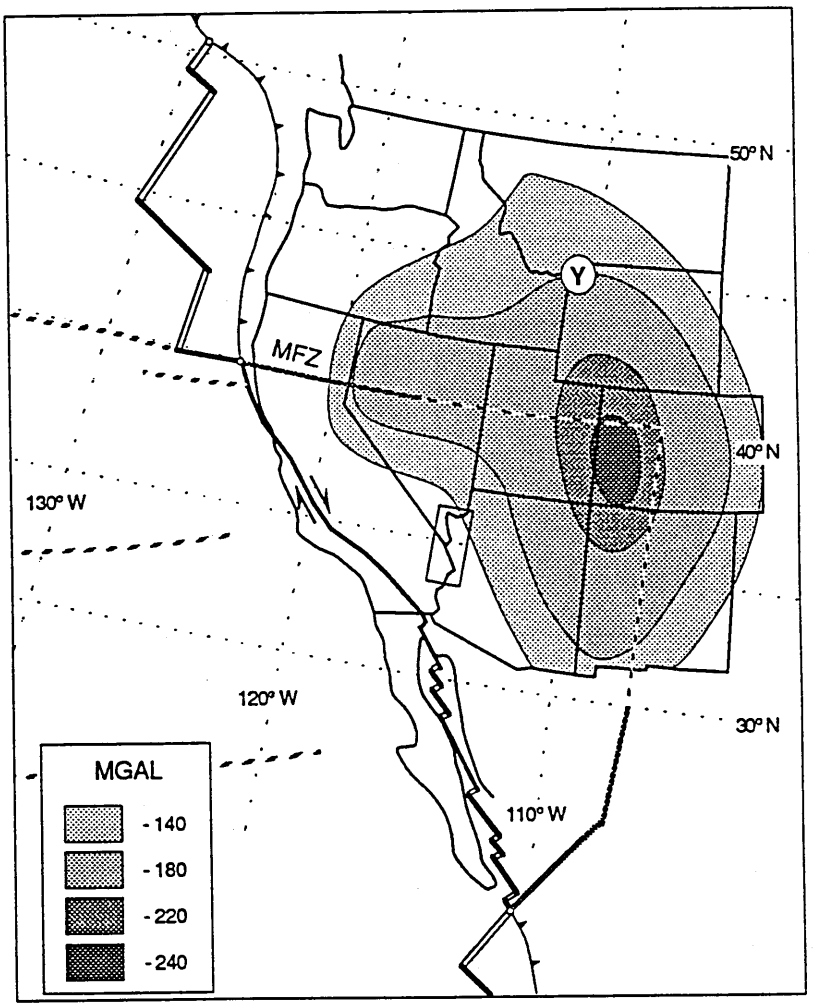

Figure 4b. Long wave length Bougouer gravity anomaly data (Kane and Godson 1989) superimposed on the slab window position. Long wave length data is used to evaluate anomalies centred at depth and to reduce the effect of localised variation.

This is precisely the pattern of magmatism observed in the southern Basin and Range (Gans et al 1989), where the onset of magmatism preceeds the passage of the MFZ by ~5m.y. The onset of bimodal or basalt-dominated volcanism in which OIB-type magmas are an important fraction, is only observed after the passage of the MFZ, presumably when

upwelling asthenosphere is in direct contact with the base of the lithosphere. Similarly, Ormerod et al (1988) observe a switch to predominatly OIB-type magmatism in the Great Basin 2-3m.y. after the passage of the MFZ beneath the area.

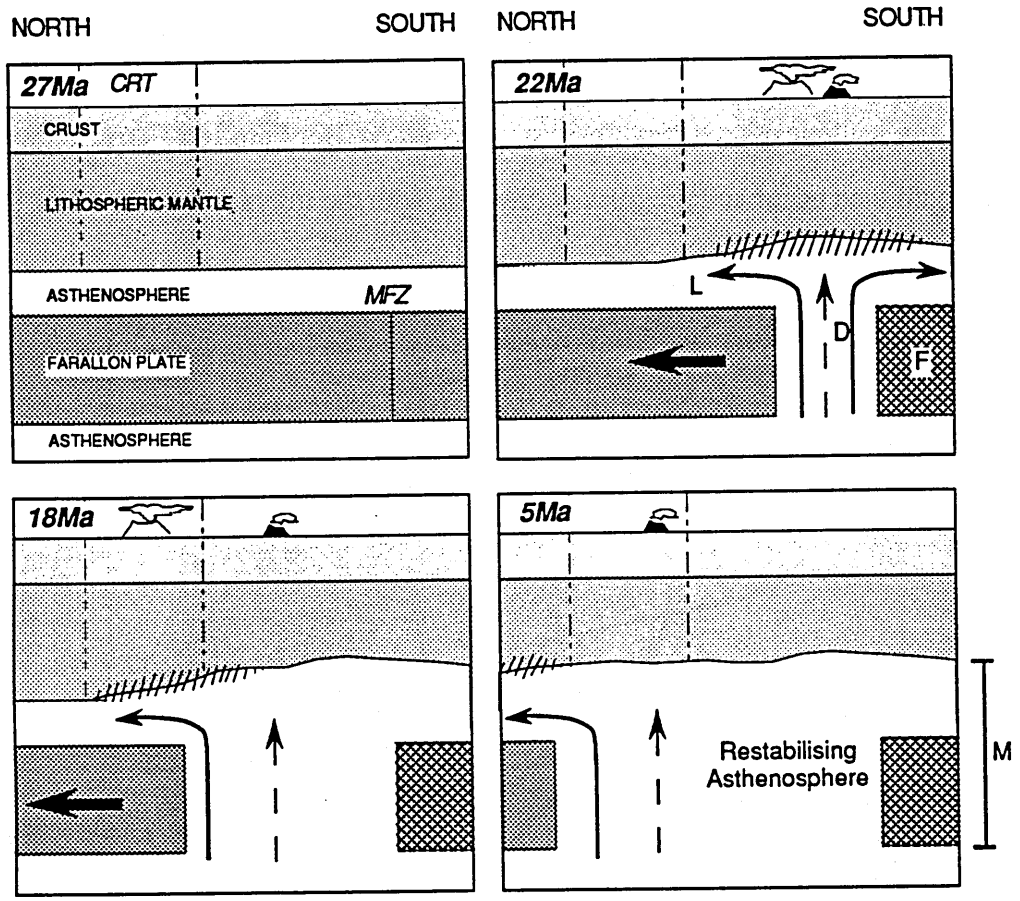

Figure 5. Tectonic model for the initiation of magmatism in the southern Basin and Range. Sections are schematic, approximately north-south through time at 115°W. Hatched areas indicate melting of the sub-continental lithospheric mantle, the site of the resulting volcanism is represented by white volcanoes. L= lateral flow of hot asthenosphere without decompression, D= decompression melting of hot asthenosphere, resulting OIB type magmatism is depicted as black volcanoes (note: sporadic OIB type magmatism may occur wherever the slab window is open). F= fixed southern portion of original Farallon Plate. M= thickness of mantle replaced by upwelling asthenosphere, see discussion section.

5.4 Discussion: a mantle plume or not?

Whether the upwelling asthenosphere could be regarded as a true mantle plume or not is a matter of conjecture. However, geophysical evidence (gravity, seismics and heat flow data) may indicate that the upwelling is just a restabilisation of the asthenosphere beneath the western United States, and not a mantle plume *sensu stricto*. Long wave length Bouguer gravity anomalies (Kane and Godson 1989) define a major kidney shaped gravity low in the upper mantle centred on NW Colorado (figure 4b). This correlates with a large decrease

in S-wave velocity (85% of which is at ≤ 200km depth) and suggests that the gravity low is caused by an upper mantle thermal anomaly. The anomaly is clearly elongated along the northern and eastern margins of the slab window, and a bulge in the anomaly through Montana and Idaho may be related to the Yellowstone hot spot. The main anomaly has its greatest definition (≥ 240 mgal) in the NE corner of the slab window, and it is least well defined to the southwest. The highest heat flow values in the western United States are also recorded along the edges of the slab window (figure 4a).

For a deep-seated mantle plume, a roughly circular gravity anomaly and high heatflow distribution would have been anticipated. However, regions where the slab window was open earliest (eg. beneath the CRT and to the southwest) now show a smaller gravity anomaly compared to NW Colorado where the propagating tip of the window is thought to be currently located (figure 4b). Thus the embayed shape of the observed anomaly would be more consistent with restabilisation of the asthenosphere through time as the slab window opened in a northeasterly direction (from P* to P in figure 4a).

The geochemical arguments for a plume, based on the identification of an OIB-type signature, may also be overstated because similar magma types are recorded in British Columbia and the Antarctic Peninsula, again in relation to the localised opening of slab windows (Hole et al 1991). Furthermore, OIB-type magmas occur with Pliocene-Recent subduction related volcanism in the North West Mexico Volcanic Belt (Verma and Nelson 1988), adjacent to the southern margin of the slab window (figure 4a). This is nearly 2000km south of the gravity anomaly centre, which is double the maximum radius of typical mantle plumes (White and McKenzie 1988). The OIB signature may therefore just represent small degree decompression melting of the asthenosphere (probably <10% melting, see Chapter 4). This would be consistent with the rather small volumes of the magma type that are generally observed across the western United States.

Therefore, the hypothesis is that a deep-seated mantle plume, with a high internal potential temperature, is not required beneath the southwestern United States. A simple test of this hypothesis is available because the excess topographic elevation (E_M) caused by a thermal

anomaly in the mantle is directly related to the temperature of the anomaly and its effective thickness (M) by the equation:

$$E_M = \alpha.\Delta T_M.M \qquad \text{(Sleep 1990)}$$

Where α is the thermal expansivity constant ($3*10^{-5}°C^{-1}$) and ΔT_M is the average temperature difference between anomalous mantle (T_1) and normal mantle temperature (T_0).

The average elevation across the anomalous region is approximately 2.0km, and the average for the United States interior is ~0.3km (Kane and Godson 1989), thus suggesting an E_M value of 1.7km. The value of M depends on the thickness of the Farallon Plate, the thickness of the continental lithosphere that is removed by melting and/or extension or related delamination processes (eg. Bird 1979; Houseman et al 1981), and the thickness of the intervening asthenosphere, all of which are assumed to be replaced by the upwelling mantle (see 'M' on figure 5). Prior to extension and magmatism, and after Laramide crustal thickening, a thickness of 120km would not have been unreasonable for the Proterozoic aged lithosphere in the western United States, although seismic evidence indicates a current thickness of ≤80km (Smith et al 1989). The thickness of the Farallon Plate is assumed to be 100km, in line with published estimates for the equilibration thickness of oceanic plates (*cf.* McKenzie and Bickle 1988), and therefore M is expected to be at least 140km. The worst constrained factor in M is the thickness of the intervening asthenosphere, however, shallow angle subduction during the Cenozoic suggests that 0-40km would be an acceptable estimate. Thus, in table 2, a range of ΔT_M is calculated for total M values of between 140 and 180km.

E_M	M	ΔT_M	T_0	T_1
1.7	140	405	1000	1405
1.7	160	354	1042	1396
1.7	180	315	1077	1392

Table 2. Calculated temperatures for a thermal anomaly in the mantle that could theoretically support an excess topographic elevation of 1.7km, see text for discussion. The T_0 values are based on assuming that the average temperature of the replaced Farallon Plate and continental lithosphere was 1000°C (from typical estimates of geothermal gradients), and that any original asthenosphere between the plate and lithosphere had a potential temperature of 1280°C. The calculated T_1 values are mantle temperatures at the average depth of the anomalous material.

The results indicate T_1 values in the region of 1400°C at a depth of 160km. Using the equations of McKenzie and Bickle (1988), this translates into a mantle potential temperature of approximately 1345°C. Such a potential temperature is <70°C greater than that proposed for normal asthenospheric mantle and thus this would appear to support the initial hypothesis. However, it must be stressed that the above calculations require a large number of assumptions. Nevertheless, asthenosphere at this potential temperture would undergo approximately 10% partial melting if it decompressed to a depth of 40km. As has already been suggested, this is consistent with modelled degrees of partial melting for OIB-type magmas in the Great Basin, where the lithosphere may be in the region of 40-60km thick.

5.5 Conclusions

The geochemistry of the bulk of Cenozoic volcanism in the western United States is inconsistent with any significant material input from a mantle plume, rather a source in the sub-continental lithospheric mantle is preferred. However it is difficult to envisage how this would melt without a heat input from the asthenosphere. A model is therefore suggested whereby asthenospheric upwelling over the edge of the subducted Farallon Plate triggered melting in the sub-continental lithospheric mantle. This may have subsequently initiated extension and magmatism in the southern Basin and Range Province.

Calculations of the internal potential temperature of the upwelling asthenosphere suggest that it need not be a mantle plume *sensu stricto*, but a transient asthensopheric re-equilibration, to fill the space vacated as the Farallon Plate moved to the north.

The adaptation of Pearce Element Ratio diagrams to complex higher silica systems

6.1 Introduction

Pearce Element Ratio (PER) diagrams have previously been used to interpret basaltic suites related by simple fractionation (Ernst *et al* 1988; Russell and Nicholls 1988). In this paper it will be shown how a number of different processes other than fractionation can be displayed on standard PER diagrams, by reference to selected suites from the western USA. An improvement is suggested to the PER scheme which enables more complex and higher silica systems to be investigated. Thus it becomes possible to recognise the effects of simple mixing between basaltic and crustal endmember melts, and of combined assimilation and fractional crystallisation. Results are of a slightly more general nature than those of previous workers because interpretations are made over several related suites, although they still remain statistically valid for petrological hypothesis testing. The statistical importance of PER modelling is already well documented (Pearce 1968; Russell and Nicholls 1988; Russell and Stanley 1990) and therefore this paper provides an expansion of ideas from a more geological stand-point.

6.2 Background

Pearce element ratios present data in the form A/ω, generally as diagrams of A/ω vs B/ω. The terms A and B may be either volume percent measurements, weight percent oxides, elemental (molar-) fractions, CIPW normative abundances, or complex functions involving more than one major element abundance. The denominator term is also a compositional abundance expressed in the same units (ie. vol%, wt% or mol%) as the numerator. The denominator differs from A and B in having the property of constant *absolute* abundance within the system under investigation. The total mass (or volume) of ω in the system must not be affected by the processes acting on this system, and thus its abundance relative to

other components will appear to increase during fractionation. Effectively this requires ω to be incompatible with the phases expected to be fractionating, and therefore the bulk distribution coefficient of ω (the bulk D_ω) will be close to zero.

The advantage of data in the form A/ω is that it provides information related to variations in absolute chemical units. This over-comes the problems of interpreting igneous systems on 'Harker variation diagrams' where data must already be correlated to some degree by its expression as a fraction of a constant sum (ie. a fraction of 100%). A condition which may result in the over emphasis of some trends, at the complete expense of others (Russell and Nicholls 1988).

The most useful form of the PER diagram utilises molar fractions and sets A and B to be formulae involving constituent elements of minerals suspected of fractionating (table 1). The general aim is to design a diagram in which fractionation of the suspected assemblage is represented by a vector with a slope (m) of 1. If the actual data statistically fit this slope then the initial hypothesis may be correct. However trends in data must also satisfy the condition of having a significant non-zero y-intercept to be accepted as valid (Pearce 1987). Linear trends that do pass through the origin are considered to be artifacts generated either when the system has become open with respect to ω (ie. when a phase fractionates in which ω is compatible), or where eutectic crystallisation is occurring (R.E.Ernst *pers comm*).

Phases \ Constituents	Si	Al	FM	Ca	Na
Albite (Ab)	3	1	0	0	1
Anorthite (An)	2	2	0	1	0
Olivine (Ol)	1	0	2	0	0
Clinopyroxene (Cpx)	2	0	1	1	0
Orthopyroxene (Opx)	1	0	1	0	0

Table 1. Constituent elements in the fractionation of common mineral phases. Numbers refer to stoichiometric abundances determined from general mineral equations. Oxygen has been excluded as a component because it is not analysed directly. Problems arising from complete solid solution between Fe and Mg compositions in ferromagnesian phases have been avoided by combining these into an 'FM' constituent.

Where a number of constituent elements are used to produce the axis functions, phases other than those directly under consideration will also have vectors in the same PER space.

For example it may be required to determine if a sample set of rocks is dominated by clinopyroxene fractionation. From its general stoichiometric formula clinopyroxene comprises 1mole Ca, 1mole FM, 2 moles Si and 6 moles of oxygen (table 1). The FM constituent considers the Fe^{2+} and Mg^{2+} ions together and therefore eliminates the effect of diopside-hedenbergite solid solution. However Ca is the distinctive feature between clinopyroxene and other ferromagnesian minerals that might also be fractionating, such as olivine and orthopyroxene; thus, the FM constituent may not need to be taken into consideration.

Placing the Si component on the x-axis (ie. B=Si) produces an x-displacement vector of $2/\omega$ (*2 moles of Si*) which must be balanced by a similar displacement vector on the y-axis with Ca to obtain the default gradient of m=1. Hence A=2·Ca (Figure 1).

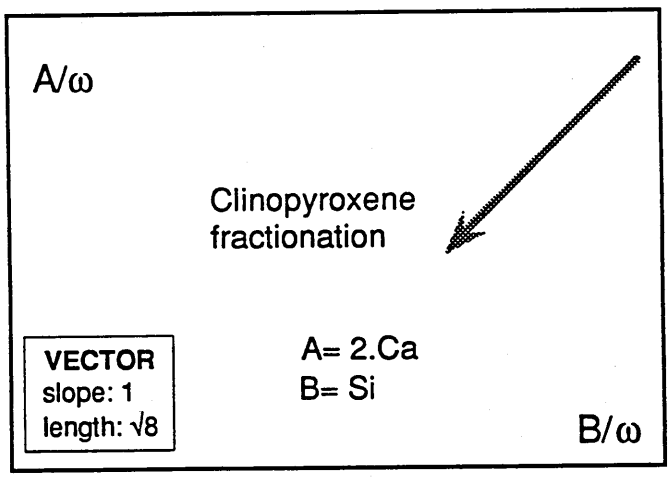

Figure 1. Simple PER diagram to express the fractionation of clinopyroxene in terms of molar compositions.

	Displacement		*Vector*	
Phase	X	Y	slope	length
Ab	3	0	0	3
An	2	2	1	√8
Ol	1	0	0	1
Cpx	2	2	1	√8
Opx	1	0	0	1
Ap	0	10	∞	10

Table 2. Other displacement vectors for common minerals on Figure 1. Vector lengths are given for fractionation of 1 mole of the mineral phases.

Other common minerals also have Ca and/or Si as constituent elements and so they too have vectors on this diagram, see table 2. It is clear that pure anorthite fractionation would produce the same result as clinopyroxene fractionation, so a modification might be made to A or B to separate the effects of these. Al is a constituent of plagioclase but not pyroxene, thus if term B is changed to 'Si+Al' then there is no effect on the clinopyroxene vector but a discrimination between clinopyroxene and plagioclase is now made (Figure 2).

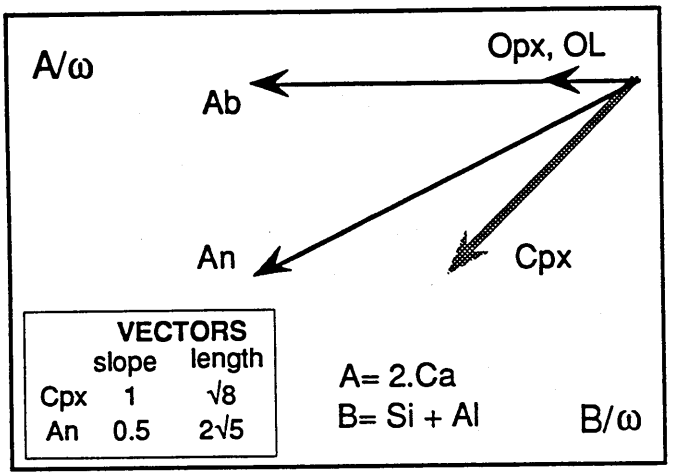

Figure 2. Modified version of Figure 1 designed to discriminate between clinopyroxene and anorthite fractionation. See text for details.

The need for specific phase composition analyses is reduced by use of the stoichiometric mineral equations and, as above, the problems of solid solution can often be avoided as well. Estimates of temperature and pressure conditions are only required if the compatibility of ω is strongly sensitive to changes in these parameters. However, PER models are usually designed so that this is not the case and therefore they can provide an inherently simple, but powerful, tool for interpreting geochemical data. As well as qualitative interpretations, quantitative assessments of fractionation are also possible. In this context it is particularly useful to define one axis function (A or B) as a CIPW normative abundance and to observe variations against an index such as SiO_2 or stratigraphic height in a sequence (Ernst *et al* 1988).

6.3 Zr as the preferred choice of ω

P,K and Ti have principally been used as ω terms in the study of alkalic and tholeiitic basalts because of their incompatibility at low weight percent silica in such rocks. However there are problems associated with each of these that can potentially restrict their usefulness in other igneous systems. Apatite and ilmenite invariably crystallise above 55 wt% SiO_2, and at even lower levels of silica in calc-alkaline or high fO_2 environments (ie. Garcia and Jacobson 1979; Bacon 1990); moreover, the accuracy of P_2O_5 analyses by some XRF techniques is poor at very low abundance levels. Potassium does remain incompatible until higher silica when biotite, amphibole, and K-feldspar may approach the liquidus and crystallise. But, potassium is also notoriously mobile in aqueous systems and it has been shown to diffuse between intrusive magma bodies and their host rocks (Blundy and Sparks 1991). Gradients on PER diagrams should not be affected by this mobility if alteration/ metasomatism occurs consistently throughout the study suite (Pearce 1987), but such effects are difficult to evaluate and they are unlikely to be so consistent. Similar caution must also be exercised in using other highly incompatible, but mobile, elements such as Ba.

A more suitable choice of ω would be an element which is generally insoluble in aqueous fluids, and is incompatible in the normal crystallising phases over a large range of silica contents. The high field strength (HFS) elements Hf and Zr are ideal, and at <60 wt% SiO_2 so are the Rare Earth Elements (REE). However, for effectiveness over the maximum silica range, and for greater availability of data, Zr proves to be the most useful.

Ernst *et al* (1988) report that a bulk D_ω value of 0.1 will induce a 10% error in PER gradients over a 50% fractionation interval. This is considered to be an acceptable error level and it indicates that Zr can be utilised under most conditions of fractionation, even if ilmenite and hornblende are principal fractionating phases (see table 3 for the details of Zr distribution coefficients). However, it is clear that minor amounts of zircon fractionation will have a substantial effect on the PER equations, so it is important to understand the behaviour of zircon in magmatic systems. (Monazite and other rare trace phases with high

D_{Zr} values also need to be considered, but the same general conclusions appear to be valid for them, as for zircon).

Phase	D_{zr}	*source*
Plagioclase	0.01	(c,d)
Ilmenite	0.3	(b)
Olivine	0.01	(a,b,d)
Clinopyroxene	0.1	(a,b,d)
Amphibole	0.45	(c)
Orthopyroxene	0.03	(a,b,d)
Zircon	3800	(c)

Table 3. Crystal / liquid distribution coefficients for Zirconium (a- Feigenson *et al* 1983; b- Ulmer 1988; c- Martin 1985; d- Pearce and Norry 1979). Only limited data is currently available for amphibole, the value given is for hornblende in tholeiitic magma.

The controlling factors on zircon fractionation are temperature, SiO_2 content and the alkalinity of the melt. Zr^{4+} ions are complexed by the alkali metals (Watson and Harrison 1983) and possibly by chlorine (G.Mahood *personal communication*), enabling higher Zr concentrations to build up before saturation levels are reached. In non-peralkaline systems the lack of suitable complexing agents inevitably results in the presence of micro zircon crystals within the melt (Watson 1979) , but fractionation can still be suppressed by high melt temperatures. Stix and Gorton (1990) report that the volatile content of the magma is also a major factor in determining the Zr saturation point.

Both higher temperatures and increased volatile contents have the effect of lowering melt viscosity by depolymerising the complex tetrahedral structure of high silica melts. The extent of melt polymerisation depends on the abundance of framework-linking oxygen bonds. These oxygen bonds may be disrupted under a number of conditions (Henderson 1986; Stix and Gorton 1990, and references therein):

i) at high temperatures (because of increased entropy in the system)

ii) when Al in the structure is complexed by hydroxyl (OH^-) ions

iii) and when the 'bridging oxygen' bonds of the silicate network are directly attacked by water or fluoride (F^-) ions. For example:

$$\equiv Si—O—Si\equiv + H_2O \rightarrow 2(\equiv Si—OH)$$

$$\equiv Si—O—Si\equiv + F^- \rightarrow \equiv Si—O^- + F—Si\equiv$$

where —O— represents single oxygen atoms linking tetrahedral silica units. Reactions of this kind provide a supply of non-bridging oxygens for which Zr^{4+} ions have a strong affinity. The activity of free Zr in the melt is subsequently reduced and the formation and fractionation of discrete zircon units is therefore suppressed.

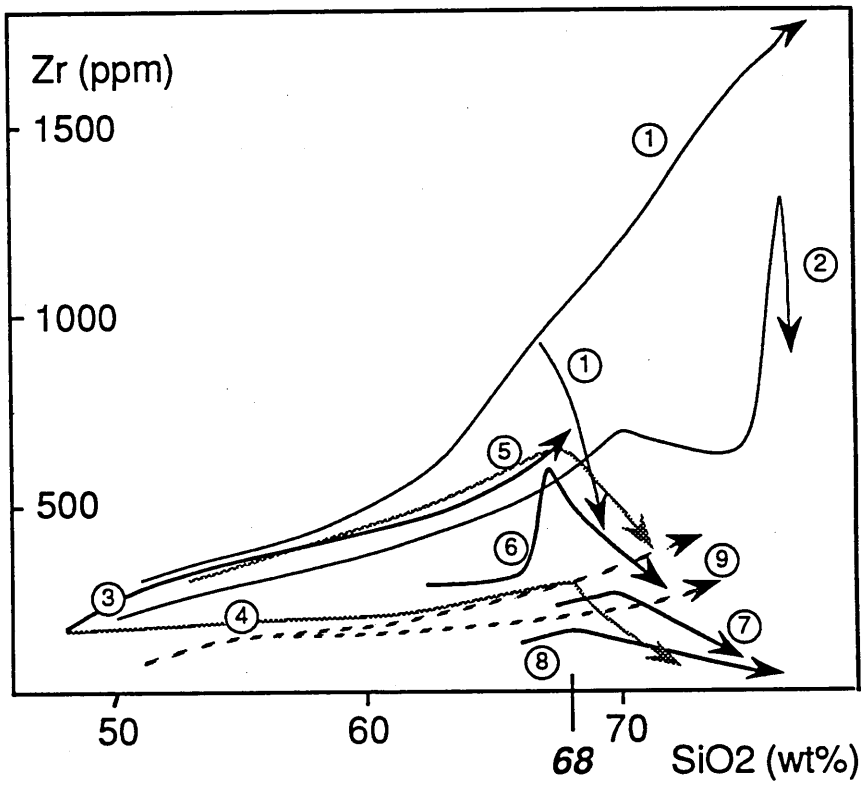

Figure 3. Zr vs silica variation diagram for a representative sample of igneous suites from various geological settings. The inverse correlation of Zr above 68 wt% SiO_2 in some suites is inferred to relate to the fractionation of zircon. It is acknowledged that agpaitic nepheline-phonolites may display increasing Zr and decreasing SiO_2 with fractionation (Hall 1987; I Parsons *pers comm*). However, these rocks are very rare and there is no indication of such extreme alkaline behaviour in the area covered by this report. Data sources: **1** Deccan (Lightfoot *et al* 1987); **2** Kane Springs Wash Caldera, W.USA (W P Leeman *pers comm*; Novak and Mahood 1986); **3** alkaline & **4** calc-alkaline suites Sanganguey Volcano, Mexico (Verma and Nelson 1989); **5** Mt. Davis volcanic group, LasVegas (Bradshaw *unpbl* data); **6** San Fransisco Volcanic Field Arizona (Bloomfield and Arculus 1989); **7** Idaho Batholith (Clarke 1990); **8** Chingezi tonalites, Archaean Zimbabwe (Luais *unpbl* data); **9** Whole range of data from the Andean volcanic arc front (Hildreth and Moorbath 1988).

The results of a survey of zircon fractionation effects in magmas from a wide variety of locations and geological settings are displayed in figure 3. Zr does not decrease and so zircon is inferred not to fractionate until at least 67 wt% SiO_2 in all cases. Most suites do

record a loss of Zr between 67 and 70 wt% SiO_2, but 68 wt% SiO_2 is probably the minimum value at which zircon fractionation would have a noticeable effect on PER models. A few alkaline and volatile-rich examples continue to concentrate Zr to extreme levels before rapid depletion occurs at or above 76 wt% SiO_2.

Thus it is proposed that Zr can be used as the standard ω factor for all conditions from mafic to high silica igneous systems, although its value may need closer assessment at very high silica (> 68 wt% SiO_2). At high silica levels the possibility of zircon fractionation can be assessed using other trace element data such as Hf/Lu ratios. Fujimaki (1986) suggests that the D_{Hf} is 1.5 to 5 times greater than the D_{Lu} between zircon and liquid, and that both partition coefficients are so extreme ($D \geq 200$) that any fractionation (≥ 0.5 wt%) will significantly affect the concentrations of these elements and their ratio in the residual liquid.

A draw back to using Zr (or any other trace element) is that the standard analytical errors on the data are usually larger than those for major elements. These errors propagate through the PER calculations and are enhanced if the trace element is used as the ω-factor. At low concentrations of a trace element ω, the propagated errors can become considerable and will therefore restrict its usefulness in petrological hypothesis testing. Hence, standard 1σ error bars have been added to the figures in the next section where appropriate.

As a further note of caution, it is recommended that the variation of Zr should be compared to that of other incompatible elements (ie. the REE) to ensure that the behaviour of zircon is as expected. For instance, a suite displaying a positive Nd-SiO_2 variation, but a negative Nd-Zr correlation, might indicate that zircon is being removed during otherwise normal conditions of fractionation.

6.4 Application

The PER approach has been applied to calc-alkaline volcanic rocks associated with Miocene extension in the Basin and Range province of the western USA (Figure 4). The whole spectrum of compositions from 45 - 80 wt% SiO_2 is available, with no major 'gaps' in the silica distribution. Trachy-andesites to higher silica volcanics are volumetrically the most

abundant and they have evolved in a range of magmatic systems up to caldera size. Magma differentiation has also undoubtedly occurred at a number of crustal levels, and thus it becomes important to have a general method of handling data applicable to all system sizes and magmatic histories. The versatility and general pressure independence of PER diagrams should make them ideal for this potentially intractable task. However, igneous rock suites such as these have not previously been investigated in this way because " it has not been obvious how [PER] diagrams for more complex systems could be constrained" (Stanley and Russell 1989).

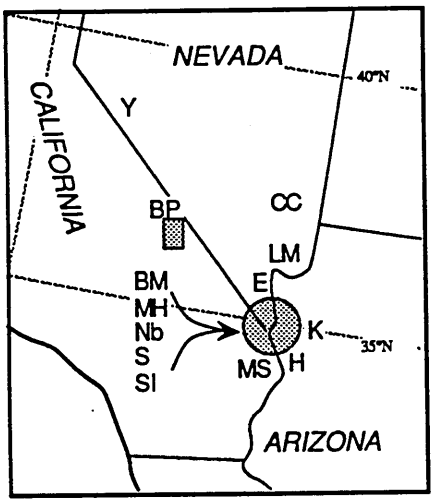

Figure 4. Western USA location map for example suites used in this study. Samples from the Mohave Mts. collected by Phil Gans of Stanford University are denoted by 'MH', other Mohave samples are denoted in the text as 'MO'. BP= Big Pine Volcanic Field - Ormerod *et al* (1991). (BM= Black Mts, CC= Caliente Caldera, E= Eldorado Mts, H= Havasu City; K= Kingman, LM= Lake Mead, MS= Mopah Springs; Nb= Newberry Mts, S= Sacramento Mts, Sl= Searchlight, Y= Yerrington).

A number of volcanic suites have been compared using PER diagrams. Samples within a suite must be co-genetic (a standard rule in using Pearce element ratios) for the specifics of fractionation to be assessed. In the same way, inter-suite comparisons may also be made if the primary basaltic magmas in each suite are related in terms of source and degree of melting.

These relationships can be determined with standard isotopic and trace element modelling techniques (eg: Leeman 1974; Fitton *et al* 1988; Hawkesworth *et al* 1988; Farmer *et al* 1989; Price *et al* 1990). In the sample suites considered here the source is thought to be subcontinental lithospheric mantle of Proterozoic age (Chapter 4). Large Ion Lithophile Element (LILE) and REE concentrations in the source are rather heterogeneous as a consequence of subduction zone fluid and small volume melt enrichments. However, sampling over a wide area (this study and Ormerod *et al* 1991, see Figure 4) suggests that,

apart from K_2O, the major element and HFS element compositions have sufficiently similar trends to permit inter-suite comparisons. Other extensional volcanic suites to the northwest have been rejected because they were developed on accreted arc terrains where chemistry, particularly that of the HFS elements, is laterally variable (eg. Yerrington in Figure 4). Each of the suites which are included on Figures 5-9 cover time periods of ≤ 3m.y.

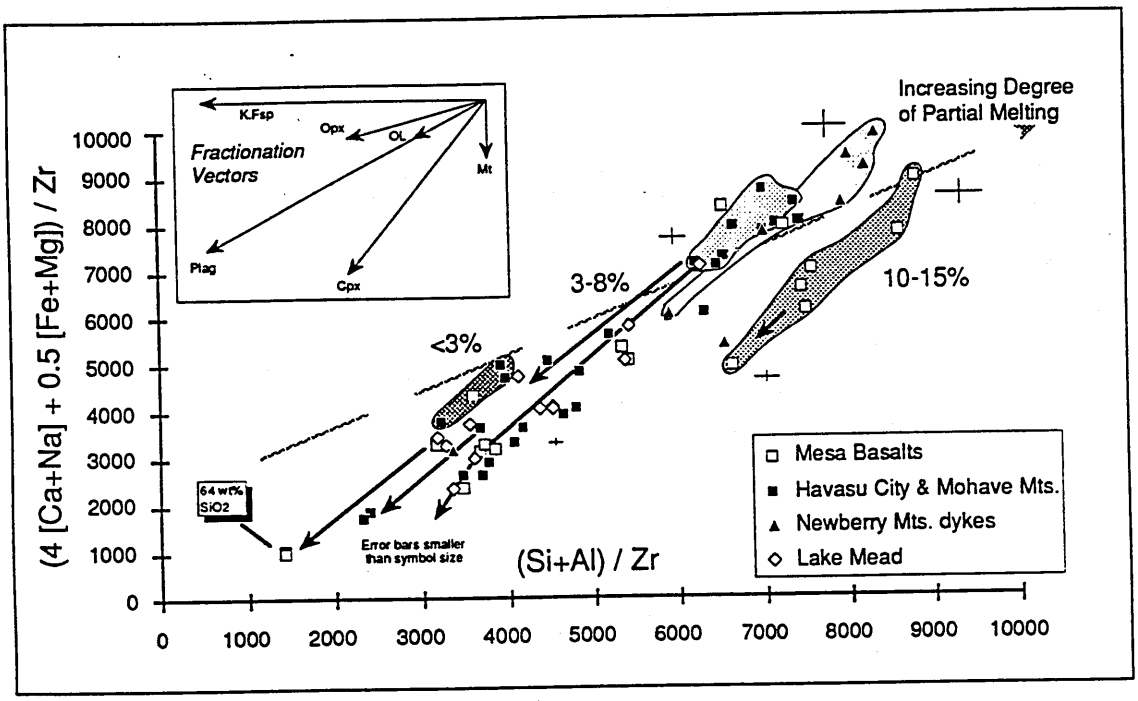

Figure 5. Molar composition PER diagram for basaltic to trachy-andesitic suites from the study area. Shaded fields and arrows highlight selected samples related by fractionation. Cross symbols are representative 1σ propagated error bars placed adjacent to samples in various positions on the diagram. Errors are dominated by Zr and are therefore larger at low Zr concentrations, towards the top and right of the diagram. Percentages indicate the degree of partial melting calculated from REE batch melting models of a standard garnet lherzolite source (Cox *et al* 1984). Large axis values on this and subsequent figures could be reduced by scaling Zr abundances to that of the most primitive sample. However, this is considered inappropriate when a large number of individual suites are being compared.

A set of basaltic to trachy-andesitic magma suites are presented in Figure 5. All samples are ≤ 60 wt% SiO_2 apart from two trachytes indicated at the end of one fractionation trend. The complex axis functions are taken from Stanley and Russell (1989), and mineral fractionation vectors are given. This set of functions can be used to test for combined olivine and/or plagioclase fractionation and it is also reasonably sensitive for distinguishing the effects of other phases, such as that of clinopyroxene from orthopyroxene. Although a number of alternative axis functions could be produced to accomplish this, those in Figure 5 have the additional feature of inhibiting the effects of solid solution in plagioclase and the

ferromagnesian minerals. An 'FM' constituent has been designated in the A function, while placing Al in the same function as Si takes account of the general $(Si, Al)_4$ unit in plagioclase.

If the evolution slopes on Figure 5 are extrapolated to intersect the the y-axis they do not pass through the origin and they therefore must be considered as valid petrological trends.

Suites have also been treated individually on a number of more explicit phase discriminant PER diagrams. However the principal fractionating assemblage is always dominated by olivine and plagioclase with variable amounts of pyroxene (usually clinopyroxene) and opaques. The axis functions in Figure 5 have been chosen to reflect this, and thus most of the magma evolution slopes approximate to unity; there is also an advantage in that over 90 wt% of the sample is represented in the equation constituents.

Consistent with the arguments outlined in the previous section, Zr is used as the ω factor, although similar patterns can also be reproduced using other incompatible elements (ie. Ce, Nd, Hf, Nb). The incompatibility of Zr in the mantle renders it highly sensitive to the degree of partial melting in the source; at low levels of silica (<50 wt%) an inverse correlation between SiO_2 wt% and Zr ppm is often observed. Thus, increased degrees of melting will force samples to plot higher and further to the right on Figure 5, along the partial melting vector indicated. The shaded "Mesa Basalt" trend is a direct consequence of this. REE modelling produces results consistent with up to 15% partial melting, whereas suites in the main fractionation trend (from Lake Mead, Havasu City and the Mohave Mts.) fit closer to 3-8% partial melting, and the few samples on the left of the diagram are thought to derive by <3% partial melting. The partial melting vector in Figure 5 has thus been positioned through the least evolved samples at the end of each of these trends. However, samples in two suites (light shading) actually fall above the expected partial melting vector for the assumed lithospheric mantle source. These are basaltic samples from the final stages of extensional magmatism in the region of greatest crustal attenuation. It is probable that they represent melting of a shallower mantle source that is slightly depleted in Zr and other trace elements (see Chapter 4).

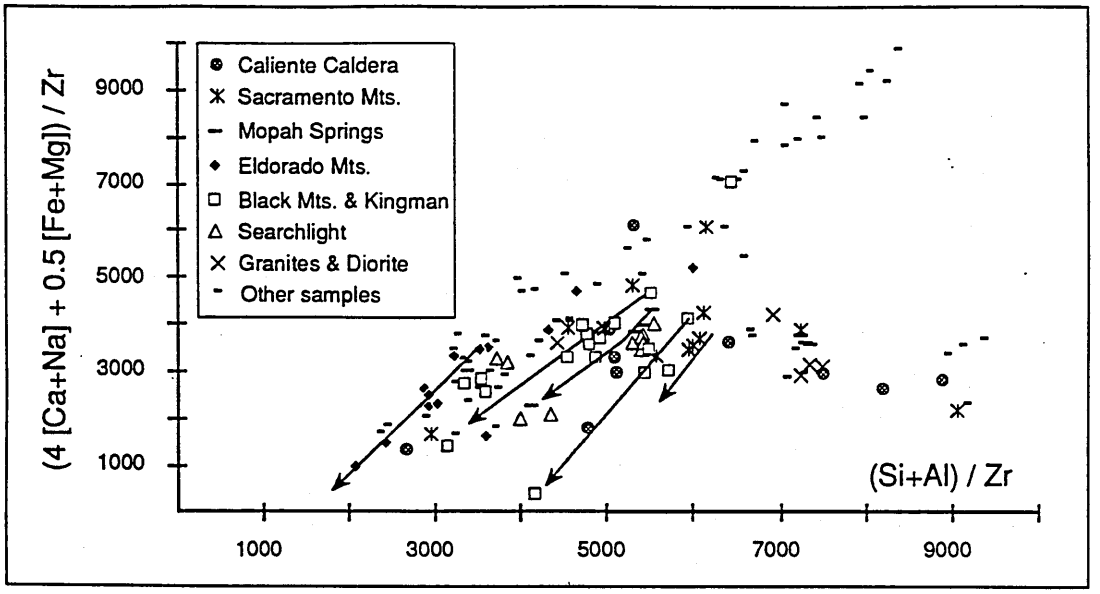

Figure 6. PER diagram as in Figure 5; all analyses from the study set are plotted, excluding the Mesa Basalts. The additions include a further basalt to trachy-andesite suite (Eldorado Mts.) and other trachy-andesite to higher silica associations. Some of the samples related by fractionation have been highlighted. Notice the negative array divergent from the main axis of basaltic fractionation.

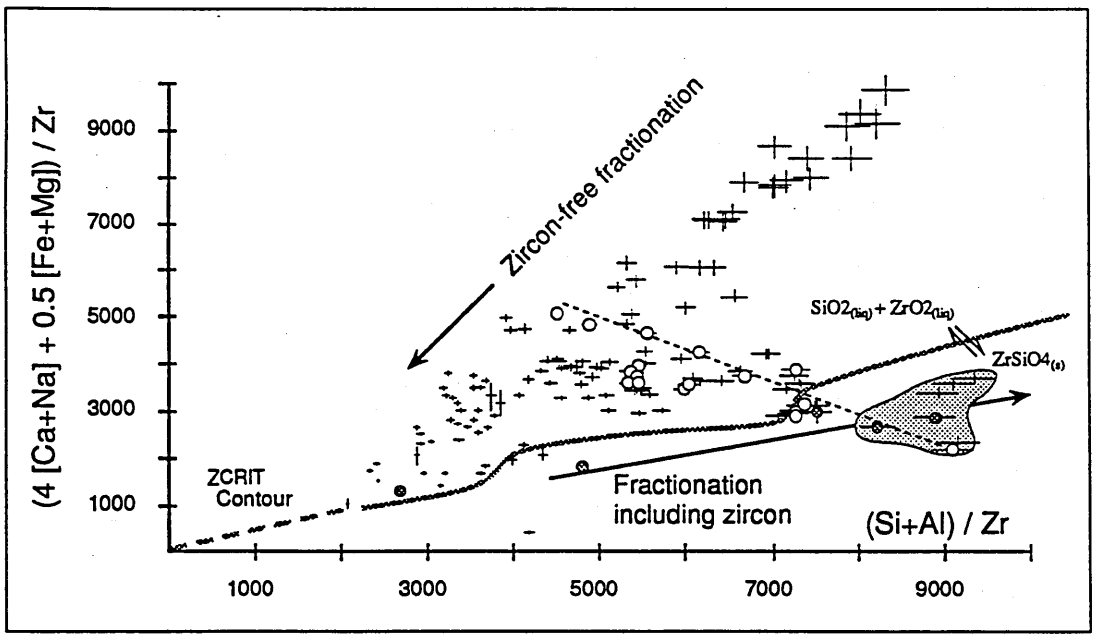

Figure 7. Data set as for Figure 6, samples have been plotted as their 1σ propagated error bars. The shaded line (ZCRIT) separates samples which plot above and below the critical silica value of 68 wt%. Above this value Zr in the melt may combine with SiO_2 to produce zircon crystals, and fractionate. A typical path for zircon fractionation is displayed by the highlighted samples from the Caliente Caldera. Samples in the shaded field artificially extend the negative array, but zircon fractionation cannot produce the main part of this array. A representative trend through the array is indicated by the dashed line, approximately orthogonal to the main direction of fractionation. The Sr isotope ratios of circled samples along this trend are presented in Figure 8 and discussed in the text.

As their name suggests, the Mesa Basalts are flat lying, post-extensional, flows erupted across the region some time (10-15m.y.) after the main group of volcanics under consideration here. These time constraints indicate that they could not have interacted with other magmas in the processes described below and so they have been omitted from subsequent figures for clarity.

In Figure 6 more of the higher silica samples and six other suites from the same area have been included. It is apparent that many samples now also scatter about a negative trending array, from which further fractionation trends are then developed. Because of the nature of the axis functions, fractionation is restricted to positive slopes (ie. m= $0 \rightarrow \infty$) on these diagrams. Thus, the recognition of a negative array is very significant, and a number of possibilities arise for the origin of this alignment:

i) continued fractionation from the end of the Mesa Basalt higher degree melting path indicated on Figure 5

ii) the ω element is no longer incompatible (ie. zircon is fractionating)

iii) magmatic evolution has changed from a closed to an open system.

The first of these is unlikely on the grounds of timing as previously discussed, and also on isotopic considerations. The Mesa basalts exhibit very homogeneous Sr isotopes with $^{87}Sr/^{86}Sr$ =0.70648 at 51.58 wt% SiO_2 and 0.70649 at 60.66 wt% SiO_2, but samples on the negative trend that might lie on the end of such a fractionation path have, for example, $^{87}Sr/^{86}Sr$ =0.70931 at 60.85 wt% SiO_2 and 0.70986 at 61.05 wt% SiO_2. A jump in the isotopic ratio of this magnitude is inconceivable by fractionation processes alone.

If Zr becomes compatible in the fractionating assemblage this reduces the denominator effect in the axis functions, the x-axis numerator is also affected by removal of $ZrSiO_4$ but this has an insignificant effect compared to that on Zr and can be ignored. During zircon fractionation samples will be displaced upward and to the right on diagrams where Zr is used as the ω value. Therefore, depending on the amount of zircon fractionation, this may cause an apparent negative trend away from the main basaltic field on Figure 6. However,

our knowledge of zircon systematics suggests that it will not fractionate until a minimum of 68 wt% SiO_2 is attained in the magma. Since Figure 6 may be contoured for silica, a 'zircon critical' (ZCRIT) contour can thus be added at 68 wt% SiO_2, Figure 7.

By its nature, the ZCRIT contour may be continued to pass through the origin on Figure 7. Because the contour then intersects the main basalt fractionation trend at coordinates *(2000,1000)*, the gradient of the contour is ≈0.5. However, some variation in this slope is expected because it is influenced by both the initial degree of partial melting and by the phases that have fractionated to bring the magma to 68 wt% SiO_2.

The samples that have fractionated zircon (based on independent Hf/Lu evidence) lie on or just below the critical line. A position far below ZCRIT indicates that zircon fractionation has remained suppressed above 68 wt% SiO_2; any subsequent loss of zircon will then occur on progressively shallower gradients in proportion to the earlier degree of suppression. An example of this suppression is displayed by samples from the Caliente Caldera, Figure 7. These samples plot just below the ZCRIT contour on a slightly shallower trend (m≈ 0.35), suggesting that zircon suppression continued until 69-70 wt% SiO_2 was attained in the magma.

It is clear from Figure 7 that a number of the Caliente, and other samples, have fractionated zircon and that some of these do artificially extend the negative sloping array. However there is still a large portion of this field between the basalt fractionation lines and the ZCRIT contour which cannot be explained in such a way. Therefore it is concluded that the evolution of these samples *has* been controlled by open system magmatic processes.

Interaction with crustal rocks is suggested by increasingly radiogenic $^{87}Sr/^{86}Sr$ values along the negative array. In Figure 8 the strontium isotope ratios for the samples indicated by open circles in Figure 7 are plotted as a representative trend through this array; their approximate positions along the array are expressed in terms of (Si + Al) / Zr. A few samples have also been regressed back along the fractionation lines shown in Figure 6 to augment the general trend, and these are clearly indicated.

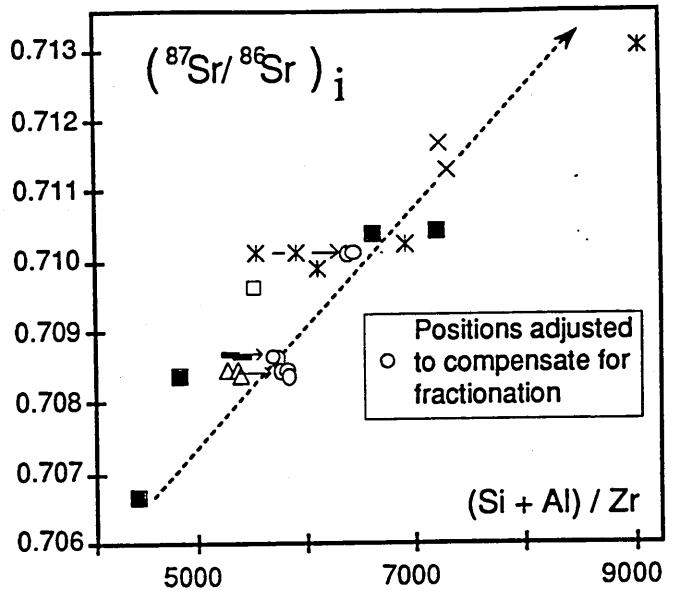

Figure 8. Initial strontium isotope ratios for selected samples in the negative array on previous diagrams (filled boxes are Lake Havasu City and Mohave Mts, other symbols as Figure 6); granite samples have been age corrected to 20Ma. Allowance has been made for samples which are inferred to have fractionated off the general negative trend (marked in Figure 7) by regressing them back along their fractionation paths. This affects the (Si + Al) / Zr value but not the $^{87}Sr/^{86}Sr$ ratio and thus produces the horizontal displacements indicated above.

Local Mesozoic granite bodies plot at the most radiogenic end of the array on Figure 8, and at the silicic end of the negative array on Figures 6 and 7. In the absence of any suitable sedimentary component, it is believed that these granites could represent the primary crustal end-member. In Figure 9 this end-member is used to generate possible evolution lines for a variety of models where combined assimilation and fractional crystallisation (AFC: DePaolo 1981) is taking place. The models are calculated using the computer programme "CHAOS" (a Macintosh™ compatible version of the "TRACE3.FOR" programme, Nielsen 1989).

Ratios of mass assimilated to mass crystallised ('r' values) of 0.3 or less are often considered appropriate in geological systems (eg.Verma and Nelson 1987), but these low values cause only minimal divergence from the normal fractionation trends. This highlights a failing of PER diagrams where geochemically important, but volumetrically insignificant, amounts of assimilation may be overlooked in the general scatter of data. The problem can be resolved by consideration of Sr isotope ratios which are sensitive to such contamination effects (as in Figure 8).

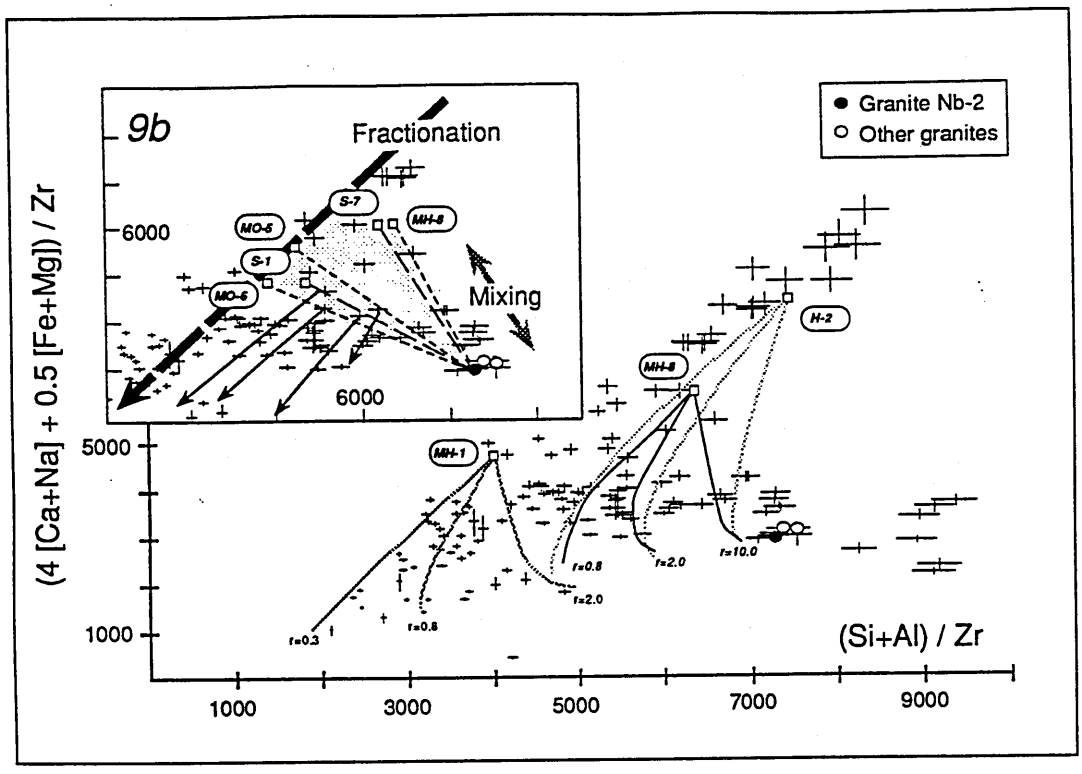

Figure 9. Samples plotted as 1σ propagated error bars. **9a.** AFC modelled curves between various basaltic end-member compositions and granitic crustal melt (r= ratio of mass assimilated to mass crystallised). Negative slopes only begin to be attained at very high r-values, and where the percentage of fractionation is large (> 80wt%). **9b.** A special case of AFC modelling where r=∞, ie. binary mixing is taking place between two magma types. Evolution lines indicate mixing between basaltic end-members and the granite Nb-2. If other potential granite contaminants are considered then any composition within the shaded field may be reproduced. The primary hybrid magmas generated in this way may then fractionate and further emphasise the negative array.

At r=0.8, some divergence is measurable above 40% fractionation, although it is not until the magma system is dominated by assimilation (r>1) that parts of the negative trend can begin to be replicated. Even under conditions of extreme r, the lower-silica, and smaller-percent partial melt basalts remain unsuitable as the mafic endmember for the models. For example, binary mixing (r=∞) from sample MH-1 will coincide with the negative array. However, this evolution path fails to pass through the least evolved samples in the array, from which further fractionation trends are seen to develop.

The most suitable mafic end-members are apparently basalts between 50 and 54 wt% SiO_2 from the main field, such as samples from the Mohave (MO-5, MO-6, MH-8) and Sacramento Mountains (S-1, S-7). If other local granites besides sample Nb-2 are used in the model, then the range of evolution lines possible between the mafic and silicic end-members (at r=∞) can adequately reproduce all the observed data. This is presented as a

shaded region on Figure 9b. Subsequently, under the appropriate conditions, fractionation of these primary 'hybrid' magmas can then occur.

It can be inferred from these results that the latent heat of crystallisation available from the fractionating mafic magmas is not a principal contributor to the heat required for crustal melting. Instead, the two distinct magma types must be present in the crust at the same time as *melts* for the conditions of binary mixing to be applicable. Thus, other processes such as advective heat transfer must be responsible for initially generating the crustal melts. The importance of this in an extensional setting is discussed in Bradshaw and Hawkesworth (1991), Chapter 3.

6.5 Discussion and Conclusions

The interpretation of geochemical data using Pearce element ratio diagrams has been successfully applied to a major province of syn-extensional magmatism in the western USA. Besides qualitative determination of mineral phase fractionation, it has also been possible to interpret more complex silicic systems. The approach develops that of previous workers (eg. Stanley and Russell 1989) by emphasising the benefits in choosing the correct denominator element (ω-value) for the Pearce Element Ratios, and it evaluates data from higher silica rocks. Zr is proposed as a standard ω-value for a number of reasons:

i) availability of data and ease of accurate analysis

ii) fluid immobility

iii) high degree of incompatibility up to 68 wt% SiO_2, and in some cases beyond this, depending on conditions in the melt

iv) and because, zircon, the mineral phase primarily responsible for removing Zr, has such an extreme D_{Zr} value that its presence is immediately recognised (and can be substantiated by changes in other trace element ratios).

The only major limitation to using Zr occurs when hornblende and ilmenite account for more than 25% of the fractionating assemblage. At this level the bulk D_{Zr} value may exceed 0.1 and induce unacceptable scatter on PER diagrams.

With Zr as the ω-value, PER's can be designed to be more resilient to alteration effects and to problems that might normally arise by variable enrichments in fluid-mobile elements within the mantle source region. The latter of these is a crucial factor when attempting to investigate suites which appear to have originated by melting in the sub-continental lithospheric mantle. Thus, in the western USA example, it is possible to use Zr for geochemical interpretations on a hierarchy of scales: to assess fractionation on an intra-suite basis and also for conducting inter-suite comparisons of a more regional nature.

PER versatility is further demonstrated by the ability to present other quantitative models on the same diagrams. In this way it is possible to predict the effects of fractionation, AFC and mixing. For our sample suites we conclude that fractionation and binary mixing have both operated, but in a mutually exclusive way (ie. not strictly AFC). Slightly evolved basalts (50-54 wt% SiO_2) apparently mix with high silica crustal melt and the resulting hybrid magmas may then also undergo fractionation.

In preliminary studies of other igneous systems (such as from the Aegean; data from Huijsmans and Barton 1989), it appears that volcanic suites often lie close to the main fractionating array in Figure 5. Similarly, other published granite analyses (see Harris *et al* 1986 for a general summary) also plot close to those used in this study; typically with the S-type granites occurring furthest to the right along the ZCRIT contour. Furthermore, the average composition of post - Archæan shales (inferred to be representative of the bulk upper continental crust composition; Taylor and McLennan 1985) falls within the field of this granite data. Thus, there is invariably a significant displacement between the trends of basaltic magmas and their potential higher silica crustal contaminants. Recognition of this displacement as a general feature should permit the investigation of further suites from a wide variety of geological settings.

This paper has attempted to highlight a number of additional uses for PER modelling and it is hoped that future applications can be made to other complex systems, and to general interpretations in a more spatial context.

Summary and Concluding Remarks

7.1 Introduction

This thesis has examined Cenozoic magmatism associated with a corridor of intense crustal extension in the Basin and Range Province of the western United States. The Colorado River Trough (CRT), between the Great Basin and the southern Basin and Range, was chosen because of the abundance of mafic magmatism recorded throughout the main episode of crustal extension. Although much has already been published about basaltic magmatism in the western United States, most of that work concerns late Miocene and Pliocene-Recent magmas associated with relatively minor extension. By contrast, the CRT region presents an opportunity to study magmatism *during* major extension, and for the contributory roles of both the crust and mantle to be assessed.

Magmatism in the CRT initiated during the late Oligocene/ early Miocene and progressed northwards with time, becoming localised near Lake Mead from around 18-6Ma. The spread of extension followed the same pattern, although lagging somewhat behind the onset of volcanism at any particular latitude. Much of the magmatism appears to be slightly bimodal, although with time and across the whole CRT, an almost continuous range of compositions from 44-80wt% silica is recorded.

7.2 Mafic magmatism

CRT mafic magmas can be divided into two groups based on the major element and petrographic arguments presented in Chapter 2. A further group is also identified by its trace element and isotopic signature, although the group is volumetrically insignificant. This group (group 1 in Chapter 4) has a characteristically smooth spidergram pattern with a broad peak across K-Nb-Ta (resulting in high Nb/Y and Nb/La on figure 1), and Sr and Pb isotope ratios indistinguishable from those of OIB or MORB. It is thought that basalts in this group represent small degrees of melting (<10%) in the asthenosphere.

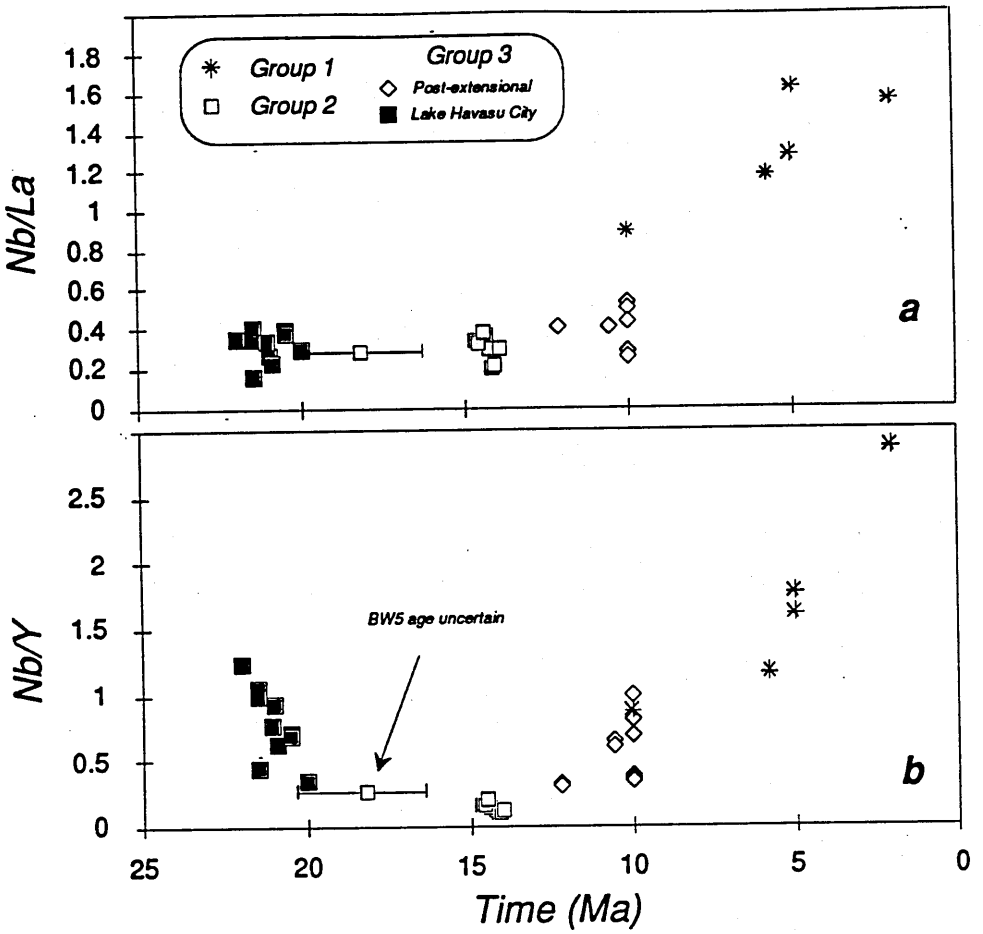

Figure 1. Nb/La and Nb/Y vs. time for Lake Havasu City and post-extensional samples having ≤56 wt% silica. In a the switch from SCLM to asthenospheric derived (group 1) magmas is marked by a jump in Nb/La ratios. Nb and La are similarly incompatible and thus the ratio should be unaffected by fractionation or degree of partial melting. In b the Lake Havasu City negative array is thought to relate to an increase in the degree of partial melting with time in a trace element enriched fraction of the SCLM. Group 2 samples are thought to be derived from a trace element depleted fraction of the SCLM. Peak magmatic activity occurred from 22-20Ma at the latitude of Lake Havasu City.

The other two magma groups (groups 2 and 3) are characterised by a pronounced Ta-Nb spidergram trough, a step from Zr/Sm to Ti, and elevated Sr and Pb isotope ratios. It is believed that both of these groups represent melting of the sub-continental lithospheric mantle (SCLM) beneath the CRT. Group 3 type magmas are the most abundant. They display a large range of trace element abundances that can be modelled by variable degrees of partial melting of a trace element enriched garnet lherzolite source (see figure 1). The degree of partial melting in this source increased with time and the onset of major crustal extension, although garnet appears to have remained as a residual phase throughout. Group 2 magmas differ from those in group 3 by displaying generally lower abundances of elements less compatible than Ti, and by having higher concentrations of Sc, Y and HREE.

Like the group 1 magmas, the group 2 magmas are volumetrically limited, although geochemically significant. Samples in group 2 are alkali olivine basalts recording a high final equilibration pressure (c.10kb). These basalts are restricted to the axis of maximum extension along the CRT and were only erupted during the final stage of syn-extensional magmatism. Major and trace element modelling indicates that these basalts cannot be derived from the same source as the group 3 basalts either by increased degrees of partial melting, or by fractionation from a group 3 primary magma. Rather it is suggested that they are derived from a relatively trace element poor fraction of the SCLM in which spinel instead of garnet is stable. These features, and the association with the most extreme extension, may be consistent with melting of a higher level in the SCLM.

7.3 Magma evolution and crustal extension

Most of the mafic magmas are alkaline and are thought to have stalled within the crust or at the Moho, fractionating either olivine or olivine plus clinopyroxene. Oxide minerals also appear to have fractionated (with the exception of the group 2 basalts), leading to the suppression of tholeiitic trends in the less abundant sub-alkaline magmas. Some of the CRT magmas may subsequently have reached the surface without further interaction with the crust, particularly along the axis of extension and around Lake Mead. In the latter area a major lithospheric shear probably acted as an important localising factor for magmatism. However, it is argued that elsewhere much of the mafic magma became stalled again in the middle crust at widespread density or stress barriers. The most likely barriers being those of 'warm' Mesozoic granite bodies intruded into the granulitic basement rocks.

At these mid-crustal levels the mafic magmas underwent significant differentiation, predominantly by the addition of high silica crustal melts. Although some fractionation also occurred, the volume of crustal melt mixed into the magmas was too great to have been produced by standard AFC processes. Major element, trace element, and isotopic trends instead suggest processes that were dominated by binary mixing between mafic and silicic endmember magmas. It is proposed that the silicic contaminant melts were themselves

generated by advective heat transfer from the stalling mafic bodies. Because most of these mafic magmas were already somewhat evolved, almost complete mixing could be achieved between the endmembers to produce a range of hybrid magma compositions.

The observed distribution and volume of hybrid magmatism suggests that crustal melting was a widespread occurrence in the CRT, and that the melting was likely to have been pervasive throughout the middle crust. In addition, the intrusion of basaltic magmas probably dominated the lower crust. A consequence of this widespread melting and intrusion would have been the thermal weakening of the middle and lower crust, and it is proposed that this provided the trigger for crustal extension. Extension reached a peak in the CRT probably as a result of 'focussing' by pre-existing structural features.

As suggested for elsewhere in the Basin and Range (eg. Gans et al 1989), the crust in the CRT apparently extended as two independent layers: ductile, symmetrical extension at depth (inferred from the magmatism); and, brittle, asymmetrical extension in the upper crust (from field observations). Such a model is consistent with geophysical evidence which indicates that material effectively flowed into the CRT region at depth, thus distributing extensional thinning over a much wider area than would have been anticipated from the surface geology.

Similar processes are likely to have operated throughout the Basin and Range, although the nature of syn-extensional magmatism there was often markedly different. For instance, the Great Basin was dominated by intermediate to high silica ash-flow tuff eruptions and the development of major caldera structures. (Calderas are absent in the CRT, although two small ones are identified on its western margin). Such features are thought to have resulted from extension that is more distributed per-unit-length and from the presence of density/ stress barriers predominantly located in supra-crustal units (that were absent in the CRT at the time of magmatism). At these higher crustal levels basaltic magmas primarily evolved by fractionation, and standard AFC processes may have operated. Some fractionation of syn-extensional magmas did occur in the CRT, mostly in the Oatman region where surface extension was at a minimum. However, because of the asymmetrical nature of the upper

crustal extension, this region is located adjacent to the highly extended CRT axis. Consequently, the fractionating magmas were intermediate silica hybrids generated by melting and mixing in the middle crust.

7.4 Geochemical changes with time

A number of geochemical changes with time are observed in the CRT magmatism. Two have already been mentioned: the increased degree of partial melting recorded in the group 3 basalts; and the tapping of a less enriched SCLM source to produce the group 2 magmatism, at the end of the main extensional phase. Following the cessation of major extension, the CRT magmatism (like that across the rest of the Basin and Range) became dominated by basalts, with subordinate amounts of rhyolite. However the magma volumes were small in comparison to those observed earlier, and unlikely to have been capable of generating significant crustal melting zones. Rather it is suggested that the bulk of the magmas either remained at depth or exploited existing fault pathways to reach the surface through the thinned crust.

In the most recent stages of magmatism, the SCLM-derived magmas were superseded by magmas of asthenospheric origin (see figure 1). A similar pattern is observed across the western US, although only in regions which had undergone earlier Cenozoic extension. In the Great Basin in particular the asthenospheric signature is observed to progress northwards during the Pliocene-Recent (Ormerod et al 1988). Where magmatism and extension are only a relatively recent phenomenon (eg. marginal to the Colorado Plateau), the magmatism is still dominated by the SCLM signature (see Fitton et al 1988).

7.5 Model for CRT magmatism and extension

As presented in section 7.3, magmatism is thought to be the motivating force behind crustal extension. The initial spread of magmatism from south to north through the CRT, followed by the more recent switch to asthenospheric magmas, apparently mirrors the passage of the edge of the subducted Farallon Plate beneath the region. It is therefore suggested that the magmatism was genetically linked to the relative plate tectonic movements. A model is

proposed in which melting of the SCLM was initiated by heat input from warmer asthenosphere as it upwelled to fill the 'void' left by the northward migration of the Farallon Plate (opening a slab window behind it). The asthenospheric upwelling was widespread although only regarded as a transient feature and not related to a deep-seated mantle plume. This may provide an explanation for the rather limited time range of peak magmatic activity observed at any area in the CRT.

7.6 A general model for the Basin and Range Province

In Chapter 1 a possible model was presented to account for the spread of volcanism (and extension) in the Great Basin. This model was based on the results and interpretations of previous workers in the Basin and Range (eg. Stewart et al 1977). In figure 2 this model is expanded to include the southern Basin and Range, as represented by the CRT region. The southern and northern halves of this model are strikingly similar in that both have components of asthenospheric in-flow to replace the Farallon Plate, which is subducting northeast and also to greater depth. In the Great Basin the main locus of volcanism approximates to the position of a developing warp in the Farallon Plate. To the south the locus is determined by the position of the Farallon Plate edge. It is proposed that in both regions the asthenospheric in-flow initiated melting in the SCLM. The resulting magmas subsequently triggered melting and extension in the overlying crust.

Lithospheric extension is likely to have been enhanced by the slowing of eastward subduction (into the page on figure 2) during the Cenozoic. This produced a state of relative tension along the Pacific margin, following the regime of extreme compression at the time of the Laramide Orogeny (Engebretson et al 1984).

From figure 2, it is clear that the two components of asthenospheric in-flow should have merged between approximately 36°N and 37°N. Abundant magmatism might therefore have been anticipated at this site from around 10Ma. However, the region actually coincides with an east-west corridor in which no magmatism occurred. Moreover, this region has continued to be 'amagmatic' during the Quaternary and Recent even though sporadic

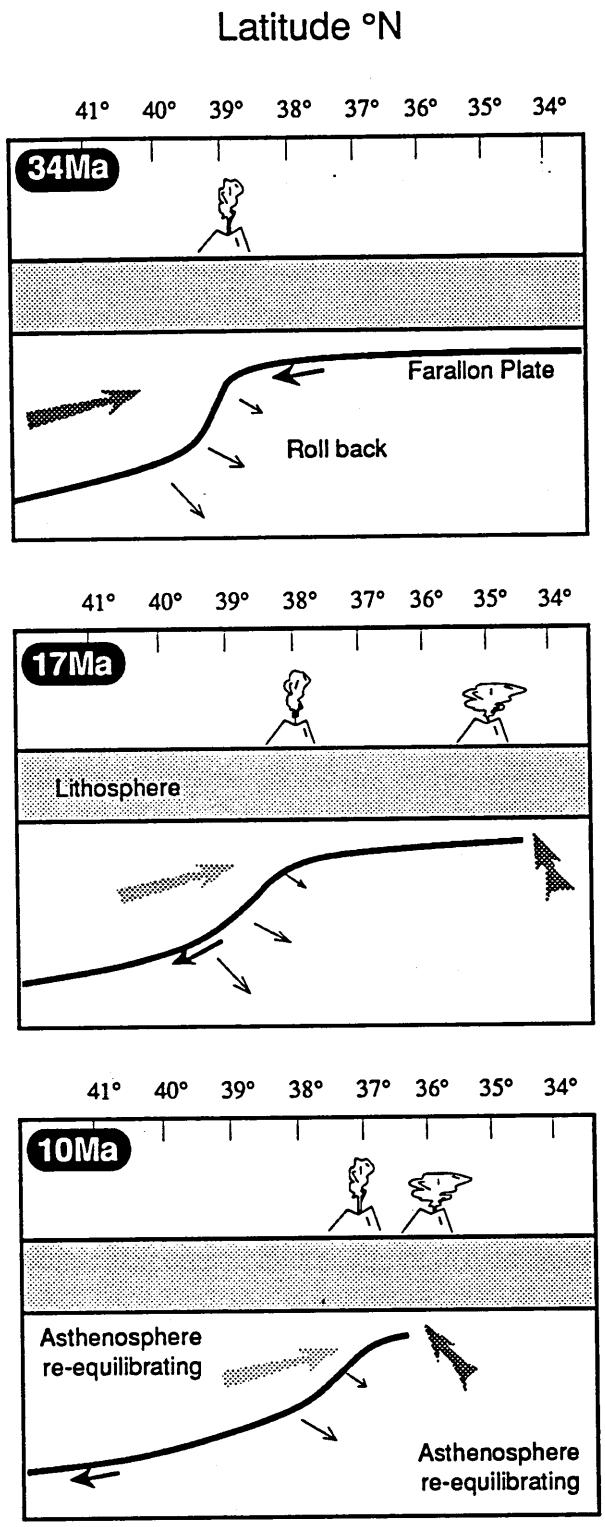

Figure 2. Tectonic model for the onset of magmatism in the the Basin and Range Province. Sections are schematic approximately north-south along longitude 115°W. Large arrows represent in-flow of asthenospheric material to the base of the SCLM. The black arrows indicate the northward migration of the Farallon Plate edge and the southward development of a warp in the plate with time See text for discussion. The Colorado River Trough lies between approximately 34 and 36°N.

basaltic volcanism has occurred throughout much of the rest of the western United States. A possible explanation for this paradox may lie in how the Farallon Plate is likely to have responded to bending stresses as the structural warp developed. If the plate behaved as a thin brittle-plastic sheet, then it is anticipated that bending would have become increasingly difficult as the warp approached the plate edge. (Attempting to propagate a warp down the length of a long plastic ruler makes a good analogy). When the plate was no longer able to respond by bending it probably fractured. Thus, the amagmatic corridor may correspond to an area that is still underlain by a detached fragment of the Farallon Plate.

7.7 Final remarks

The principal conclusion of this thesis is that extension and magmatism in the Basin and Range Province, and in the Colorado River Trough in particular, were controlled by plate tectonic processes. Magmas were predominantly derived by melting of the sub-continental lithospheric mantle (SCLM), although an asthenospheric contribution became important following the development of a no-slab window.

However, most of the ideas that have been presented are based on geochemical modelling of magmatism in the vicinity of Lake Havasu City. Clearly then there is a need to corroborate the models with similarly detailed studies in other parts of the Basin and Range. For instance, corridors of major extension were active throughout east-central Nevada during the Oligocene-Miocene. Although basaltic magmatism is scarce or non existent here, basaltic inclusions are observed in the higher silica magmas (eg. Feeley and Grunder 1991). Thus it should be possible to model these in terms of source components, and/or melting and evolution processes.

REFERENCES

Alibert C., Michard A., & Albarede F. (1986) Isotope and trace element geochemistry of Colorado Plateau volcanics *Geochim et Cosmochim* **50** 2735-2750

Allègre C.J. & Minster J.F. (1978) Quantitative models of trace element behaviour in magmatic processes *EPSL* **38** 1-25

Allmendinger R.W., Sharp J.W., von Tish D., Serpa L., Brown L., Kaufman S. & Oliver J. (1983) Cenozoic and Mesozoic structure of the Eastern Basin and Range Province, Utah, from COCORP seismic-reflection data *Geology* **11** 532-536

Anderson L.J., Barth A.P. & Young E.D. (1988) Mid-crustal Cretaceous roots of Cordilleran metamorphic core complexes *Geology* **16** 366-369

Anderson R.E. (1971) Thin skin distension in Tertiary rocks of south eastern Nevada *Geol. Soc. Am. Bull.* **82** 43-58

Anderson R.E., Longwell C.R., Armstrong R.E. & Marvin R.F. (1972) Significance of K-Ar ages of Tertiary rocks from the Lake Mead Region, Nevada-Arizona *Geol. Soc. Am. Bull.* **83** 273-288

Angelier J. & Colletta B. (1983) Tension fractures and extensional tectonics *Nature* **301** 49-51

Armstrong R.L, Ekren E.B., McKee E.H. & Noble D.C. (1969) Space-time relations of Cenozoic silicic volcanism in the Great Basin of the western United States *Am. J. of Science* **267** 478-49

Arndt N.T. & Goldstein S.L. (1987) Use and abuse of crust formation ages *Geology* **15** 893-895

Atwater T. (1970) Implications of plate tectonics for the Cenozoic tectonic evolution of western North America *Geol. Soc. Am. Bull.* **81** 3513-3536

Bacon C.R. (1990) Calk-alkaline, shoshonitic, and primitive tholeiitic lavas from monogenetic volcanoes near Crater Lake, Oregon *J.Pet* **31** 135-166

Bacon C.R. & Metz J. (1984) Magmatic inclusions in Rhyolites, contaminated basalts and compositional zonation beneath the Coso volcanic field, California *Contr. Min. Pet.* **85** 366-375

Bailey R.A. (1987) Long Valley Caldera, eastern California *in: Geol. Soc. Am. Centennial Field Guide- Cordilleran Section* 163-168

Beccaluva L., Gabbionelli G., Lucchini F., Rossi P.L. & Savell C. (1985) Petrology and K/Ar ages of volcanics dredged from the Eolian seamounts: implications for geodynamic evolution of the southern Tyrrhenian basin *EPSL* **74** 187-208

Ben-Avraham Z., Nur A., Jones D., & Cox A. (1981) Continental accretion from oceanic plateaus to allochthonous terrains *Science* **213** 47-54

Bender E.E., Anderson J.L., Wooden J.L., Howard K.A. & Miller C.F. (1988) Correlation of 1.7Ga granitoid plutonism in the lower Colorado River region *Abstr. Geol. Soc. Am.* **20** 142

Bennett V.C. & DePaolo D.J. (1987) Proterozoic crustal history of the western United States as determined by neodymium isotopic mapping *Geol. Soc. Am. Bull.* **99** 674-685

Best M.G. & Brimhall W.H. (1974) Late Cenozoic alkalic basalt magmas in the Western Colorado Plateaus and the Basin and Range Transition Zone, USA, and their bearing on mantle dynamics *Geol. Soc. Am. Bull.* **85** 1667-1690

Best M.G., Christiansen E.H., Deino A.L., Grommé C.S., McKee E.H. & Noble D.C. (1989) Eocene through Miocene volcanism in the Great Basin of the western United States *in: Field excursions to volcanic terrains in the western United States vol 2- Cascades and Intermontaine West.* **NBMG memoir 147** 91-133 Editors: Chapin C.E. & Zidek J.

Bird P. (1984) Laramide crustal thickening event in the Rocky Mountains foreland and Great Plains *Tectonics* **3** 741-758

Bird P. (1979) Continental delamination and the Colorado Plateau *J. Geophys. Res.* **84** 7561-7571

Block L. & Royden L.H. (1990) Core complex geometries and regional scale flow in the lower crust *Tectonics* **9** 557-567

Bloomfield A.L. & Arculus R.J. (1989) Magma mixing in the SanFransisco Volcanic Field, Arizona *Contr. Min. Pet.* **102** 429-453

Blundy A.L. & Sparks R.S.J. (1991) Interaction of mafic and felsic magmas in the plutonic environment: An example from the Adamello Massif, Italy *Geol Soc Lond Volc Stud Grp Abstr Prog* pg7

Buesch D.C. & Valentine G.A. (1986) Peach Springs Tuff and volcanic stratigraphy of the southern Cerbat Mountains, Kingman, Arizona *in: Cenozoic stratigraphy, structure and mineralisation in the Mojave Desert. Guide book and volume of the 82nd annual meeting of the Cordilleran Section of the Geol. Soc. Am.* 7-14

Burchfiel B.C. & Davis G.A. (1981) Mojave Desert and environs *in: The geotectonic development of California* **Rubey Volume I** 217-252 Editor: Ernst W.G.

Burchfiel B.C. & Davis G.A. (1988) Mesozoic thrust faults and Cenozoic low-angle normal faults, Eastern Spring Mountains, Nevada, and Clark Mountains thrust complex, California *in: This Extended Land - Geological Journeys in the Southern Basin and Range. (Geol. Soc. Am. Cordilleran Section guidebook, field trips 5 & 6)* 87-106

Busby-Spera C.J. (1988) Speculative tectonic model for the early Mesozoic arc of the southwest Cordilleran United States *Geology* **16** 1121-1125

Christiansen R.L., Lipman P.W., Carr W.J., Byers F.M., Orkild P.P. & Sargent K.A. (1976) The Timber Mountain -Oasis Valley Caldera complex of southern Nevada *Geol. Soc. Am. Bull.* **88** 934-959

Chaffey D.J., Cliff R.A. & Wilson B.M. (1989) Characterisation of the St.Helena magma source *in: Magmatism in the Ocean Basins. Geol. Soc. Lond. Spec. Publ.* **42** 257-275

Clarke C.B. (1990) The geochemistry of the Atlanta Lobe of the Idaho Batholith in the western United States Cordillera *PhD. Thesis: The Open University, UK* 370pp

Coats R.R. (1987) Geology of Elko County, Nevada *NBMG Bull.* **101** 112pp

Coney P.J., Jones D.L. & Monger J.H.W. (1980) Cordilleran suspect terrains *Nature* **288** 329-333

Couch R.W. & Riddihough R.P. (1989) The crustal structure of the western continental margin of North America *in: Geophysical framework of the continental United States. Geol. Soc. Am. Memoir* **172** 103-128 Editors: Pakiser L.C & Mooney W.D.

Cox K.G., Bell J.D. & Pankhurst R.J. (1979) The interpretation of igneous rocks *George Allen & Unwin Publishers* 450pp

Cox K.G., Duncan A.R., Bristow J.W., Taylor S.R. & Erlank A.J. (1984) Petrogenesis of the basic rocks of the Lebombo *Spec Publ Geol Soc S.Africa* **13** 149-169

Dann J.C. (1991) Early Proterozoic ophiolite, central Arizona *Geology* **19** 590-593

Davis G.A. & Lister G.S. (1988) Detachment faulting in continental extension; perspectives from the southwestern U.S. Cordillera *Geol. Soc. Am. Special Paper* **218** 133-160 Editors: Clark S.P., Burchfiel B.C. & Suppe J.

Davis G.H. & Vandendolder E.M. (1987) Geologic diversity of Arizona and its margins: excursions to choice areas *Geol. Soc. Am. Field trip guide book*

Davis J.M. (1991) The geochemical evolution of basic and intermediate mid- to late Tertiary volcanism of the Mogollon-Datil volcanic field, southwestern New Mexico, USA *PhD thesis. The Open University* 270pp

Deer W.A., Howie R.A. & Zussman J. (1977) An introduction to the rock-forming mineral. 10th edition. Longman Press 528pp

DePaolo D.J. (1981) Trace element and isotopic effects of combined wallrock assimilation and fractional crystallisation *EPSL* **53** 189-202

DePaolo D.J., Linn A.M. & Schubert G. (1991) The continental crustal age distribution: methods of determining mantle separation ages from Sm-Nd isotopic data and application to the southwestern United States *J. Geophys. Res.* **96** 2071-2088

Dewey J.F. (1988) Extensional collapse of orogens *Tectonics* **7** 1123-1139

Dickenson W.R., Klute M.A., Hayes M.J., Janecke S.U., Lundin E.R., McKittrick M.A. & Olivares M.D. (1988) Palaeogeographic and palaeotectonic setting of Laramide sedimentary basins in the central Rocky Mountain region *Geol. Soc. Am. Bull* **100** 1023-1039

Drewes H. (1967) Geology of the Connors Pass Quadrangle Schell Creek Range East-Central Nevada *Geol. Soc. Am. Spec. Paper* **557** 93pp

Dudas F.O., Carlson R.W. & Eggler D.H. (1987) Regional middle Proterozoic enrichment of the subcontinental mantle source of igneous rocks from central Montana *Geology* **15** 22-25

Duebendorfer E.M. & Wallin E.T. (1991) Basin development and syntectonic sedimentation associated with kinematically coupled strike-slip and detachment faulting, southern Nevada *Geology* **19** 87-90

Eaton G.P. (1986) A tectonic redefinition of the southern Rocky Mountains *Tectonophysics* **132** 163-193

Ehrenberg S.N. (1982). Rare earth element geochemistry of garnet lherzolite and megacrystalline nodules from minette of the Colorado Plateau province *EPSL* **57** 191-210

Ehrenberg S.N. (1982a) Petrogenesis of garnet lherzolite and megacrystalline nodules from the Thumb, Navajo Volcanic field *J.Pet* **23** 507-547

Engebretson D.C., Cox A. & Gordon R.G. (1985) Relative motions between oceanic and continental plates in the Pacific Basin *Geol. Soc. Am. Special Paper* **206** 59 pp.

Engebretson D.C., Cox A. & Thompson G.A. (1984) Correlation of plate motions with continental tectonics: Laramide to Basin and Range *Tectonics* **3** 115-119

England P.C. & Houseman G.A. (1988) The mechanics of the Tibetan Plateau *Phil.Trans.R.Soc.Lond.* **A326** 301-320

Ericksen M.C. & Slingerland R. (1990) Numerical simulations of tidal and wind-driven circulation in the Cretaceous Interior Seaway of North America *Geol. Soc. Am. Bull* **102** 1499-1516

Ernst R.E., Fowler A.D. & Pearce T.H. (1988) Modelling of igneous fractionation and other processes using Pearce diagrams *Contr. Min. Pet.* 12-18

Farmer G.L. & DePaolo D.J. (1983) Origin of Mesozoic and Tertiary Granite in the western USA and implications for pre-Mesozoic crustal structures: 1. Nd and Sr isotopic studies in the geocline of the Northern Great Basin *J. Geophys. Res.* **88** 3379-3401

Farmer G.L., Perry F.V., Semken S., Crowe B., Curtis. & DePaolo D.J. (1989) Isotopic evidence on the structure and origin of subcontinental lithospheric mantle in southern Nevada *J. Geophys. Res.* **94** 7885-7898

Faulds J.E., Hillemeyer F.L. & Smith E.I. (1988) Geometry and kinematics of a Miocene "Accommodation Zone" in the central Black and southern Eldorado Mountains *in: 'This Extended Land'. Geol. Soc. Am. Cordilleran Section. Field trip guide book* 293-310 Editors: Weide D.L. & Faber M.L.

Faure G. (1986) Principals of isotope geology. 2nd edition *J.Wiley & Sons Publishers* 589pp

Feeley T.C. & Grunder A.L. (1991) Mantle contribution to the evolution of middle Tertiary silicic magmatism during early stages of extension: the Egan Range volcanic complex, east central Nevada *Contr. Min. Pet.* **106** 154-169

Feigenson M.D., Hofmann A.W. & Spera F.J. (1983) Case studies on the origin of basalt: II. The transition from tholeiitic to alkaline volcanism on Kohala Volcano, Hawaii *Contr. Min. Pet.* **84** 390-405

Fitton J.G., James D. & Leeman W.P. (1991) Basic magmatism associated with late Cenozoic extension in the western United States: compositional variations in space and time *J. Geophys. Res.*

Fitton J.G., James D., Kempton P.D., Ormerod D.S. & Leeman W.P. (1988) The role of Lithospheric mantle in the Generation of late Cenozoic basic magmas in the Western United States *J.Petrology* **Special Lithosphere issue** 331-349

Frey F.A. & Prinz M. (1978) Ultramafic inclusions from San Carlos, Arizona: Petrologic and geochemical data bearing on their petrogenesis *EPSL* **38** 129-176

Fujimaki H. (1986) Partition coefficients of Hf, Zr and REE between zircon, apatite and liquid *Contr. Min. Pet.* **94** 42-45

Gans P.B. (1987) An open-system, two-layer crustal stretching model for the Eastern Great Basin *Tectonics* **6** 1-12

Gans P.B., Mahood G.A. & Schermer E. (1989) Synextensional magmatism in the Basin and Range Province: A case study from the Eastern Great Basin *Geol. Soc. Am. Special Paper* **233** 54 pp.

Gans P.B., Miller E.L., McCarthy J. & Ouldcott M.L. (1985) Tertiary extensional faulting and evolving ductile - brittle transition zones in the northern Snake Range and vicinity: new insights from seismic data *Geology* **13** 189-193

Garcia M.O. & Jacobson S.S. (1979) Crystal clots, amphibole fractionation and the evolution of calc-alkaline magmas *Contr. Min. Pet.* **69** 319-327

Geissman J.W., Van der Voo R. & Howard K.L. Jr (1982) A Palaeomagnetic study of structural deformation in the Yerrington District, Nevada *Am. J. Science* **282** 1042-1109

Gill J.B. (1981) Orogenic andesites and plate tectonics *Springer Verlag, Berlin* 385pp

Glazner A.F. (1988) Stratigraphy, structure and potassic alteration of Miocene volcanic rocks in the Sleeping Beauty area, Central Mojave Desert, California *Geol. Soc. Am. Bull.* **100** 424-435

Glazner A.F. (1989) Recycling of continental crust in Miocene volcanic rocks from the Mojave block, southern California *Geol. Soc. Am. Memoir* **174** (in press)

Glazner A.F. & Bartley J.M. (1984) Timing and tectonic setting of Tertiary low-angle normal faulting and associated magmatism in the southwestern United States *Tectonics* **3** 385-396

Glazner A.F., Nielson J.E., Howard K.A. & Miller D.M. (1986) Correlation of the Peach Springs Tuff, a large-volume Miocene ignimbrite sheet in California and Arizona *in: Cenozoic stratigraphy, structure and mineralisation in the Mojave Desert. Guide book and volume of the 82nd annual meeting of the Cordilleran Section of the Geol. Soc. Am.* 65-68

Glazner A.F. & O'Neil J.R. (1989) Crustal structure of the Mojave Desert, California: Inferences from Sr and O isotope studies of Miocene volcanic rocks *J. Geophys. Res.* **94** 7861-7870

Glazner A.F. & Ussler W. III (1989) Crustal extension, crustal density, and the evolution of Cenozoic magmatism in the Basin and Range Province of the Western United States *J. Geophys. Res.* **94** 7952-7960

Glazner A.F. & Ussler W. III (1988) Trapping of magma at mid-crustal density discontinuities *Geophys. Res. Letts.* **15** 673-675

Glazner A.F., Bartley J.M. & Walker J.D. (1989) Magnitude and significance of Miocene crustal extension in the central Mojave Desert, California *Geology* **17** 50-53

Green D.H., Edgan H.D., Beasley P., Kiss E. & Ware N.G. (1974) Upper mantle source for some hawaiites, mugaerites and benmorites *Contr. Min. Pet.* **48** 33-43

Grove T.L. & Baker M.B. (1984) Phase equilibria controls on the tholeiitic vs. calc-alkaline differentiation trends *J. Geophys. Res.* **89** 3253-3274

Gudmundsson A. (1986) Formation of crustal magma chambers in Iceland *Geology* **14** 164-166

Hall A. (1987) Igneous Petrology *Longman Scientific and Technical Publishers* 573pp

Hamelin B., Manhes G., Albarede F. & Allègre C.J. (1985) Precise lead isotope measurements by the double spike technique: A reconsideration *Geochim. et Cosmochim.* **49** 173-182

Hamilton W. (1987) Crustal extension in the Basin and Range Province, southwestern United States *in: Continental Extensional Tectonics. Geol. Soc. Lond. Spec. Publ.* **28** 155-176 Editors: Coward M.P., Dewey J.F. & Hancock P.L.

Hamilton W. & Myers W.B. (1966) Cenozoic tectonics of the western U.S. *Rev. Geophys.* **5** 509-549

Harris N.B.W., Pearce J.A. & Tindle A.G. (1986) Geochemical characteristics of collision-zone magmatism *in: Collision Tectonics Geol. Soc. Lond. Spec. Publ.* **19** 67-81 Editors: Coward M.P. & Ries A.C.

Hart S.R. (1984) A large scale isotopic anomaly in the Southern Hemisphere mantle *Nature* **309** 753-757

Harvey P.K. & Atkins B.P. (1982) Automated X-ray fluorescence analysis *in: sampling and analysis for the mining industry. IMM London* 17-26

Hauser E.C., Potter C., Hauge T., Burgess S., Burtch S., Mutschler J., Allmendinger R., Brown L., Kaufman S. & Oliver S. (1987) Crustal structure of eastern Nevada from COCORP deep seismic reflection data *Geol. Soc. Am. Bull* **99** 833-844

Hauser E.C. & Lundy J. (1989) COCORP deep reflections: MOHO at 50km (16s) beneath the Colorado Plateau *J. Geophys. Res.* **94** 7071-7081

Hawkesworth C.J., Mantovani M. & Peate D. (1988) Lithospheric remobilisation during Parana CFB magmatism *J.Petrology* **Special Lithosphere issue** 205-223

Hazlett R.W. (1986) Geology of the central Mopah Range; a guide for excursions in the Mopah Spring area *in: Cenozoic stratigraphy, structure and mineralisation in the Mojave Desert. Guide book and volume of the 82nd annual meeting of the Cordilleran Section of the Geol. Soc. Am.* 33-43

Henderson P. (1986) Inorganic Geochemistry [2nd reprint]. *Pergamon Press, Oxford UK* 353pp

Hildreth W. (1979) The Bishop Tuff: evidence for the origin of compositional zoning in magma chambers *Geol. Soc. Am. Special Paper* **180** 43-75

Hildreth W. & Moorbath S. (1988) Crustal contributions to arc magmatism in the Andes of Central Chile *Contr. Min. Pet.* **98** 455-489

Hillhouse J.W. & Wells R.E. (1991) Magnetic fabric, flow directions, and source area of the lower Miocene Peach Springs Tuff in Arizona, California, and Nevada *J. Geophys. Res.* **96** 12443-12460

Hofmann A.W. & Feigenson M.D. (1983) Case studies on the origin of basalt: I. Theory and reassessment of Grenada basalts *Contr. Min. Pet.* **88** 382-389

Hole M.J., Rogers G., Saunders A.D. & Storey M. (1991) Relation between alkalic volcanism and slab-window formation *Geology* **19** 657-660

Houseman G.A., McKenzie D.P. & Molnar P. (1981) Convective instability of a thickened boundary layer and its relevance for the thermal evolution of continental convergent belts *J. Geophys. Res.* **86** 6115-6132

Howard K.A. & John B.E. (1987) Crustal extension along a rooted system of imbricate low-angle faults; Colorado River extensional corridor, California and Arizona *in: Continental Extensional Tectonics. Geol. Soc. Lond. Spec. Publ.* **28** 299-311 Editors: Coward M.P., Dewey J.F. & Hancock P.L.

Huijsmans J.P.P. & Barton M. (1989) Polybaric geochemical evolution of two shield volcanoes from Santorini, Aegean Sea, Greece: evidence for zoned magma chambers from cyclic compositional variations *J.Pet* **30** 583-625

Huppert H.E. & Sparks S.J. (1988) The generation of granitic magmas by intrusion of basalt into the continental crust *J.Petrology* **29** 599-624

Irvine T.N. & Baragar W.R.U. (1971) A guide to the chemical classification of the common volcanic rocks *Can.J.Earth.Sci.* **8** 523-548

Irving A.J. (1978) A Review of experimental studies of crystal/liquid trace element partitioning *Geochim. et Cosmochim.* **42** 743-770

Irving A.J. & Frey F.A. (1978) Distribution of trace elements between garnet megacrysts and host volcanic liquids of kimberlitic to rhyolitic composition *Geochim. et Cosmochim.* **42** 771-787

Irving A.J. & Frey F.A. (1984) Trace element abundances in megacrysts and their host basalts: Constraints on partition coefficients and megacryst genesis *Geochim. et Cosmochim.* **48** 1201-1221

Jackson J.A. & McKenzie D.P. (1983) The geometrical evolution of normal fault systems *J. Struct. Geol.* **5** 471-482

Jaques A.L. & Green D.H. (1980) Anhydrous melting of peridotite at 0-15kb pressure and the genesis of tholeiitic basalts *Contrib. Min. Pet* **73** 287-310

John B.E (1987) Geometry and evolution of a mid-crustal extensional fault system: Chemehuevi Mountains, southeastern California *in: Continental Extensional Tectonics. Geol. Soc. Lond. Spec. Publ.* **28** 313-335 Editors: Coward M.P., Dewey J.F. & Hancock P.L.

Kane M.F. & Godson R.H. (1989) A crust/mantle structural framework of the conterminous United States based on gravity and magnetic trends *in: Geophysical framework of the continental United States. Geol. Soc. Am. Memoir* **172** 383-403 Editors: Pakiser L.C. & Mooney W.D.

Keen C.E. (1985) The dynamics of rifting: deformation of the lithosphere by active and passive forces *Geophys J.R. Astr. Soc.* **80** 95-120

Kempton P.D., Harmon R.S., Hawkesworth C.J. & Moorbath S. (1990) Petrology and geochemistry of lower crustal granulites from the Geronimo Volcanic Field, southeastern Arizona *Geochim et Cosmochim Acta* **54** 3401-3426

Kistler R.W. & Peterman Z.E. (1973) Reconstruction of crustal blocks of California on the basis of initial strontium isotopic compositions of Mesozoic granitic rocks *U.S. Geol. Surv. Prof. Paper* **1071** 17pp

Klein E.M. & Langmuir C.H. (1987) Global correlations of Ocean Ridge Basalt Chemistry with axial depth and Crustal Thickness *JGR* **92** 8089-8115

Klein E.M. & Langmuir C.H. (1989) Local versus global correlations of ocean ridge basalt composition *JGR* **94** 4241-4252

Koyaguchi T. (1986) Evidence for two stage mixing in magmatic inclusions and rhyolitic lava domes on Niijima Island, Japan *J. Volc. Geotherm. Res.* **29** 71-98

Kruse S., McNutt M., Phipps-Morgan J., Royden L. & Wernicke B.P. (1991) Lithospheric extension near Lake Mead, Nevada. A model for ductile flow in the lower crust *J. Geophys. Res.* **96** 4435-4456

Kuznir N.J. & Park R.G. (1987) The extensional strength of the continental lithosphere: its dependence on geothermal gradient, and crustal composition and thickness *in: Continental Extensional Tectonics. Geol. Soc. Lond. Spec. Publ.* **28** 35-52 Editors: Coward M.P., Dewey J.F. & Hancock P.L.

Lachenbruch A.H. & Sass J.H. (1978) Models of an extending lithosphere and heat flow in the Basin and Range Province *Geol. Soc. Am. Memoir* **152**

Larsen L.L. & Smith E.I. (1990) Mafic enclaves in the Wilson Ridge Pluton, Northwestern Arizona: Implications for the generation of a Calc-alkaline Intermediate Pluton in an Extensional Environment *J. Geophys. Res.* **95** 17693-17716

Leat P.T., Thompson R.N., Morrison M.A., Hendry G.L. & Dickin A.P. (1988) Compositionally diverse Miocene-Recent rift related magmatism in NW Colorado: partial melting, and mixing of mafic magmas from 3 different asthenospheric and lithospheric mantle sources *J.Pet. Special Vol.* 351-378

LeBas M.J., le Maitre R.W., Streckeisen A. & Zanettin B. (1986) A chemical classification of volcanic rocks based on the total-alkali silica diagram *J.Pet* **27** 745-750

Leeman W.P. (1974) Late Cenozoic Alkali-rich basalt from the Western Grand Canyon area, Utah and Arizona: Isotopic composition of Strontium *Bull. Geol. Soc. Am.* **85** 1691-1696

LeMaitre R.W. (1981) Genmix- a generalised petrological mixing model program *Computers & Geosciences* **7** 229-247

Lightfoot P.C., Hawkesworth C.J. & Sethna S.F. (1987) Petrogenesis of rhyolites and trachytes from the Deccan Traps: Sr, Nd, & Pb isotope, and trace element evidence *Contr. Min. Pet.* **95** 44-54

Lipman P.W. (1980) Cenozoic volcanism in the Western United States: Implications for Continental Tectonics *in: Continental Tectonics. Washington DC National Academy of Sciences.* 161-174

Lipman P.W., Prostka H.J. & Christiansen R.L. (1972) Cenozoic volcanism and plate tectonic evolution of the western United States 1: early and middle Cenozoic *Phil.Trans.R.Soc.Lond* **A271** 217-248

Lum C.C.L., Leeman W.P., Foland K.A., Kargel J.A. & Fitton J.G. (1989) Isotopic variations in continental basaltic lavas as indicators of mantle heterogeneity: examples from the western U.S. Cordillera *J. Geophys. Res.* **94** 7871-7884

Martin H. (1985) Nature, origine et évolution d'un segment de croute continentale archéene: contraintes chimiques et isotopiques. exemple de la Finlande orientale *PhD Thesis: Rennes* 345pp

McClay K.R. & Ellis P.G. (1987) Geometries of extensional fault systems developed in model experiments *Geology* **15** 341-344

McKenzie D.P. & Bickle M.J. (1988) The volume and composition of melt generated by extension of the lithosphere *J.Petrology* **29** 625-679

Menzies M.A., Leeman W.P. & Hawkesworth C.J. (1983) Isotope geochemistry of Cenozoic volcanic rocks reveals mantle heterogeneity below the western USA *Nature* **303** 205-209

Meyer J. & Foland K.A. (1991) Magmatic-tectonic interaction during early Rio Grande rift extension at Questa, New Mexico *Geol. Soc. Am. Bull.* **103** 993-1006

Mickus K.L. & James W.C. (1991) Regional gravity studies in southeastern California, western Arizona, and southern Nevada *J. Geophys. Res.* **96** 12333-12350

Miller C.F. & Bradfish L.J. (1980) An inner Cordilleran belt of muscovite-bearing plutons *Geology* **8** 412-416

Miller E., Gans P.B. & Garing J. (1983) The Snake Range Decollement: an exhumed mid-Tertiary ductile - brittle transition *Tectonics* **2** 239-263

Miller M.G. (1991) High-angle origin of the currently low-angle Badwater Turtleback fault, Death Valley California *Geology* **19** 372-375

Moyer T.C. & Esperança S. (1989) Geochemical and isotopic variations in a bimodal magma system: The Kaiser Spring Volcanic Field, Arizona *J. Geophys. Res.* **94** 7841-7859

Mutter J.C., Buck W.R. & Zehnder C.M. (1988) Convective partial melting 1. A model for the formation of thick basaltic sequences during the initiation of spreading *J. Geophys. Res.* **93** 1031-1048

Nielsen R.L. (1989) Phase equilibria constraints on liquid lines of descent generated by paired assimilation and fractional crystallisation: Trace elements and Sr and Nd isotopes *J. Geophys. Res.* **94** 787-794

Nielson J.E. (1986) Miocene stratigraphy of the Mohave Mountains, Arizona, and correlation with adjacent ranges *in: Cenozoic stratigraphy, structure and mineralisation in the Mojave Desert. Guide book and volume of the 82nd annual meeting of the Cordilleran Section of the Geol. Soc. Am.* 15-32

Nielson J.E., Lux D.R., Dalrymple G.B. & Glazner A.F. (1990) Age of the Peach Springs Tuff, SE. California and W.Arizona *J. Geophys. Res.* **95** 571-580

Nielson J.E. & Turner R.D. (1986) Miocene rocks of the northern Turtle Mountains, San Bernardino County, California *in: Cenozoic stratigraphy, structure and mineralisation in the Mojave Desert. Guide book and volume of the 82nd annual meeting of the Cordilleran Section of the Geol. Soc. Am.* 25-32

Novak S.W. (1984) Eruptive history of the rhyolitic Kane Springs Wash volcanic centre, Nevada *J. Geophys. Res.* **89** 8603-8615

Novak S.W. & Mahood G.A. (1986) Rise and fall of a basalt-trachyte-rhyolite magma system at the Kane Springs Wash Caldera, Nevada *Contrib. Min. Pet* **94** 352-373

O'Hara M.J. (1968) The bearing of phase equilibria studies on the origin and evolution of basic and ultrabasic rocks *Earth Sci. Rev.* **4** 69-133

Oldow J.S., Bally A.W., Ave Lallemant H.G. & Leeman W.P. (1989) Phanerozoic evolution of the North American Cordillera; United States and Canada *in: The Geology of North America - An overview. Geol.Soc.Am. Volume A* 139-232 Editors: Bally A.W. & Palmer A.R.

Ormerod D.S. (1988) Late- to post- Subduction Magmatic Transitions in the Western Great Basin, USA *PhD. Thesis (Open University)* 313 pp

Ormerod D.S., Rogers N.W. & Hawkesworth C.J. (1991) Melting in the lithospheric mantle: Inverse modelling of alkali-olivine basalts from the Big Pine Volcanic Field, California *Contrib. Min. Pet* **108** 305-317

Ormerod D.S., Hawkesworth C.J., Rogers N.W., Leeman W.P. & Menzies M.A. (1988) Tectonic and magmatic transitions in the Western Great Basin, USA *Nature* **333** 349-353

Pakiser L.C. (1989) Geophysics of the intermontaine system *in: Geophysical framework of the continental United States. Geol. Soc. Am. Memoir* 235-248 Editors: Pakiser L.C & Mooney W.D.

Patiño Douce A.E., Humphreys E.D. & Johnston A.D. (1990) Anatexis and metamorphism in tectonically thickened continental crust exemplified by the Sevier hinterland, western North America *EPSL* **97** 290-315

Pearce J.A. & Norry M.J. (1979) Petrogenetic implications of Ti, Zr, Y and Nb variations in volcanic rocks *Contrib. Min. Pet* **69** 33-47

Pearce T.H. (1987) The identification and assessment of spurious trends in Pearce-type variation diagrams: a discussion of some statistical arguements *Contrib. Min. Pet* **97** 529-534

Pearce T.H. (1968) A contribution to the theory of variation diagrams *Contrib. Min. Pet* **19** 142-157

Perry F.V., Baldridge W.S. & DePaolo D.J. (1987) Role of asthenosphere and lithosphere in the genesis of late Cenozoic basaltic rocks from the Rio Grande Rift and adjacent regions of the southwestern United States *J. Geophys. Res.* **92** 9193-9213

Potts P.J., Thorpe O.W. & Watson (1981) Determination of the rare earth element abundances in 29 international rock standards by instrumental neutron activation analysis: a critical appraisal of calibration errors *Chem. Geol.* **34** 331-352

Potts P.J., Thorpe O.W., Isaacs M.C. and Wright D.W. (1985) High precision neutron activation analysis of geological samples employing simultaneous counting with both planar and coaxial detectors *Chem. Geol.* **48** 145-155

Potts P.J., Webb P.C. & Watson J.S. (1984) Energy dispersive x-ray fluorescence analysis of silicate rocks for major and trace elements *X-ray Spectrom.* **13** 2-15

Presnall D.C., Dixon S.A., Dixon J.R., O'Donnell T.H., Brenner N.L. Schrock R.L. & Dycus D.W. (1978) Liquidus phase relations on the join diopside-forsterite-anorthite from 1 atm to 20 kbar: their bearing on the generation and crystallisation of basaltic magma *Contrib. Min. Pet* **66** 203-220

Price R.C., Johnson L.E. & Crawford A.J. (1990) Basalts of the North Fiji basin: the generation of back arc basin magmas by mixing of evolved mantle sources *Contrib. Min. Pet* **105** 106-121

Prodehl C. & Lipman P.W. (1989) Crustal structure of the Rocky Mountain region *in: Geophysical framework of the continental United States. Geol. Soc. Am. Memoir* **172** 249-284 Editors: Pakiser L.C. & Mooney W.D.

Proffett J.M. (1977) Cenozoic geology of the Yerrington district, Nevada, and implications for the nature of Basin and Range faulting *Geol.Soc Am. Bull* **88** 247-266

Proffett J.M. & Dilles (1984) Geologic map of the Yerrington district, Nevada *NBMG* **Map 77**

Rehrig W.A. (1986) Processes of regional Tertiary extension in the western Cordillera: Insights from the metamorphic core complexes *Geol. Soc. Am. Special Paper* **208** 97-121

Reynolds S.J., Richard S.M., Haxel G.B., Tosdal R.M. & Laubach S.E. (1988) Geologic setting of Mesozoic and Cenozoic metamorphism in Arizona *in: Metamorphism and crustal evolution of the Western United States* 466-501 Editor: Ernst W.G.

Roden M.F., Smith D. & Mc.Dowell F.W. (1979) Age and extent of potassic volcanism on the Colorado Plateau *EPSL* **43** 279-284

Russell J.K. & Nicholls J. (1988) Analysis of petrologic hypotheses with Pearce element ratios *Contrib. Min. Pet* **99** 25-35

Russell J.K. & Stanley C.R. (1990) A theoretical basis for the development and use of chemical variation diagrams *Geochim et Cosmochim Acta* **54** 2419-2431

Saleeby J.B. (1983) Accretionary tectonics of the North American Cordillera *Ann. Rev. Earth Planet Sci* **15** 45-73

Scholz C.H., Barazangi S. & Sbar M.L. (1971) Late Cenozoic evolution of the Great Basin, W. USA, as an ensialic interarc basin *Geol.Soc Am. Bull* **82** 2979-2990

Simpson C., Schweitzer J. & Howard K.A. (1991) A reinterpretation of the timing, position and significance of part of the Sacramento Mountains detachment fault, southeastern California *Geol.Soc Am. Bull* **103** 751-761

Sleep N.H. (1990) Hotspots and Mantle Plumes: some phenomenology *J. Geophys. Res.* **95** 6715-6736

Smith I.E., Feuerbach D.L., Naumann T.R. & Mills J.G. (1990) Mid Miocene volcanic and plutonic rocks in the Lake Mead area of Nevada and Arizona *Geol.Soc Am. Memoir* **174** 169-194

Smith R.B., Nagy W.C., Julander A.K., Viveiros J.J., Barker C.A. & Gants D.G. (1989) Geophysical and tectonic framework of the eastern Basin and Range-Colorado Plateau- Rocky Mountain transition *in: Geophysical framework of the continental United States. Geol. Soc. Am. Memoir* **172** 205-234 Editors: Pakiser L.C & Mooney W.D.

Snyder W.S., Dickinson W.R. & Silberman M.L. (1976) Tectonic implications of space-time patterns of Cenozoic magmatism in the western United States *EPSL* **32** 91-106

Sonder L.J., England P.C., Wernicke W.P. & Christiansen R.L. (1987) A physical model for Cenozoic extension of western North America *in: Continental Extensional Tectonics. Geol. Soc. Lond. Spec. Publ.* **28** 187-201 Editors: Coward M.P., Dewey J.F. & Hancock P.L.

Sparks R.S.J. & Marshall L.A. (1986) Thermal and mechanical constraints on mixing between mafic and silicic magmas *J. Volc. Geotherm. Res.* **29** 99-124

Speed R.C. (1979) Collided Palaeozoic platelet in the western United States *Geology* **87** 279-292

Spencer J.E. (1985) Miocene low-angle normal faulting and dyke emplacement, Homer Mountains and surrounding areas, southeastern California and southernmost Nevada *Geol.Soc Am. Bull* **96** 1140-1155

Spencer J.E. & Chase C.G. (1989) Role of crustal flexure in the initiation of low angle normal faults and implications for structural evolution of the Basin and Range Province *J. Geophys. Res.* **94** 1765-1775

Spurr J.E. (1903) Descriptive geology of Nevada south of the fortieth parallel and adjacent portions of California *USGS Bull* **208**

Stanley C.R. & Russell J.K. (1989) Petrologic hypothesis testing with Pearce Element Ratio diagrams: derivation of diagram axes *Contr. Min. Pet.* **103** 78-89

Stewart J.H. (1980) Geology of Nevada: A discussion to accompany the Geologic Map of Nevada *NBMG Spec. Publ.* **4**

Stewart J.H. (1978) Basin-range structure in western North America: a review *Geol. Soc. Am. Memoir* **152** 31pp

Stewart J.H. & Carlson J.E. (1976) Cenozoic rocks of Nevada *NBMG Map*

Stewart J.H., Moore W.J. & Zeitz I. (1977) East-west patterns of Cenozoic igneous rocks, aeromagnetic anomalies, and mineral deposits, Nevada and Utah *Geol. Soc. Am. Bull.* **88** 67-77

Stix J. & Gorton M.P. (1990) Changes in silicic melt structure between the two Bandelier caldera - forming eruptions, New Mexico, USA: evidence from zirconium and light rare earth elements *J.Pet* **31** 1261-1283

Sun S-s. & McDonough W.F. (1989) Chemical and isotopic systematics of oceanic basalts: implications for mantle composition and processes *in: Magmatism in the Ocean Basins. Geol. Soc. Am. Spec. Publ.* **42** 313-345 Editors: Saunders A.D. & Norry M.J.

Suneson N.H. & Luchitta I. (1983) Origin of bimodal volcanism, Southern Basin and Range Province, west-central Arizona *Geol. Soc. Am. Bull.* **94** 1005-1019

Taylor S.R. & McClennan S.M. (1985) The continental crust: its composition and evolution *Blackwell Sci Publ.* 312pp

Thomas W.M., Clark H.S., Young E.D., Suzanne O.E. & Anderson J.L. (1988) Proterozoic high-grade metamorphism in the Colorado River region, Nevada, Arizona and California *in: Metamorphism and crustal evolution of the Western United States. (Rubey Vol.7)* 527-537 Editor: Ernst W.G.

Thompson R.N., Morrison M.A., Dickin A.P. & Hendry G.L. (1983) Continental flood basalts ... arachnids rule ok? *in: Continental basalts and mantle xenoliths* 158-185 Editors: Hawkesworth C.J. & Norry M.J.

Turner R.D. & Glazner A.F. (1991) Miocene volcanism, folding and faulting in the Castle Mountains, southern Nevada and eastern California *Geol. Soc. Am. Memoir* **176** (in press)

Tuttle O.F. & Bowen N.L. (1958) Origin of granite in the light of experimental studies in the system NaAlSi3O8- KAlSi3O8- SiO2- H2O *Geol. Soc. Am. Memoir* **74**

Ulmer P. (1989) Partitioning of high field strength elements among olivine, pyroxenes, garnet and calc-alkaline picro basalt: experimental results in an application *Ann. Rpt. Dir. Geophys. Lab. Carnegie Inst.* 42-47

Van Kooten G. (1980) Mineralogy, petrology and geochemistry of an ultrapotassic basaltic suite, central Sierra Nevada, California, USA *J.Pet.* **21** 651-684

Verma S.V. & Nelson S. (1989) Isotopic and trace element constraints on the origin and evolution of calc-alkaline magmas in the northwestern Mexican Volcanic Belt *J. Geophys. Res.* **94** 4531-4544

Volborth A. (1973) Geology of the granite complex of the Eldorado, Newberry and Northern Dead Mountains, Clark County, Nevada *NBMG Bull.* **80** 40 pp

Walker J.D. (1988) Permian and Triassic rocks of the Mojave Desert and their implications for timing and mechanisms for continental truncation *Tectonics* **7** 685-709

Waters F.G. & Erlank A.J. (1988) Assessment of the vertical extent and distribution of mantle metasomatism below Kimberley, South Africa *J.Petrology (Special Lithosphere Issue)* 185-204

Watson B.E. (1979) Zircon saturation in felsic liquids: experimental results and applications to trace element geochemistry *Contr. Min. Pet.* **70** 407-419

Watson B.E. & Harrison T.M. (1983) Zircon saturation revisited: temperature and composition effects in a variety of crustal magma types *EPSL* **64** 295-304

Weaver B.L. (1991) Trace element evidence for the origin of ocean-island basalts *Geology* **19** 123-126

Weber M.E. & Smith E.I. (1987) Structural and geochemical constraints on the reassembly of disrupted mid-Miocene volcanoes in the Lake Mead - Eldorado Valley area of southern Nevada *Geology* **15** 553-556

Weide D.L. & Faber M.L. (1988) This Extended Land. Geological journeys in the southern Basin and Range *Geol. Soc. Am. Cordilleran Section. Field trip guide book* 330pp

Wells R.E., & Hillhouse J.W. (1989) Palaeomagnetism and tectonic rotation of the lower Miocene Peach Springs Tuff: Colorado Plateau, Arizona to Barstow, California *Geol. Soc. Am. Bull.* **101** 846-863

Wernicke B.P. (1981) Low-angle normal faults in the Basin and Range Province: Nappe tectonics in an extending orogen *Nature* **291** 645-648

Wernicke B.P., Axen G.J. & Snow J.K. (1988) Basin and Range extensional tectonics at the latitude of LasVegas, Nevada *Geol. Soc. Am. Bull.* **100** 1738-1757

Wernicke B.P., Christiansen R.L., England P.C. & Sonder L.J. (1987) Tectonomagmatic evolution of Cenozoic extension in the North American Cordillera *in: Continental Extensional Tectonics. Geol. Soc. Lond. Spec. Publ.* **28** 203-221 Editors: Coward M.P., Dewey J.F. & Hancock P.L.

White R.S. & McKenzie D.P. (1989) Magmatism at rift zones: the generation of volcanic continental margins and flood basalts *J. Geophys. Res.* **94** 7685-7730

Wilshire H.G., Meyer C.E., Nakata J.K., Calk L.C., Shervais J.W., Nielson J.E. & Schwarzman E.C. (1985) Mafic and ultramafic rocks of the western United States *USGS Open File rpt* **85**

Wilson C.J.N & Hildreth W. (1991) Hybrid fall/surge deposits in the Bishop tuff, California *Volc. Stud. Grp. Prog & Abs*

Winkler H.G.F. (1979) Petrogenesis of metamorphic rocks (chapter 18) *Springer Verlag Publ* **5th ed** 348pp

Wittke J.H., Smith D. & Wooden J.L. (1989) Origin of Sr, Nd and Pb isotopic systematics in high-Sr basalts from central Arizona *Contr. Min. Pet.* **101** 57-68

Woodhead J.D. (1988) The origin of geochemical variations in Mariana lavas: a general model for petrogenesis in intra oceanic island arcs *J.Pet* **29** 805-830

Wright T.L. & Doherty P.C. (1970) A linear programming and least squares computer method for solving petrologic mixing problems *Geol.Soc Am. Bull.* **81** 1995-2008

Wust S.L. (1986) Regional correlation of extension directions in Cordilleran metamorphic core complexes *Geology* **14** 828-830

Young E.D., Anderson J.L. Clarke H.S. & Thomas W.M. (1989) Petrology of biotite-cordierite-garnet gneiss of the McCullough Range, Nevada I. Evidence for Proterozoic low-pressure fluid-absent granulite grade metamorphism in the Southern Cordillera *J.Pet* **30** 39-60

Data Appendix: Major Element, Trace Element, CIPW Norm, and Sr and Pb Isotope Analyses

The following pages contain all of the analytical data that has been produced as part of this study. The samples are listed geographically as three principal groups, 'Yerrington', 'Caliete Caldera' and 'Colorado River Trough'. The Colorado River Trough (CRT) samples are further subdivided into pre/syn-extensional and post-extensional groups and are again listed geographically. The coding for general sample locations is as follows:

YER	Yerrington	CAL	Caliente Caldera
ELD	Eldorado Mts.	OAT	Oatman (Black Mts.)
LHC	Lake Havau City	SEARCH	Searchlight
(GRAN),	(DYKES)	Granite samples & basaltic dykes from the Newberry Mts.	
GOFFS	Goffs Butte	MEAD	Lake Mead
MOPAH	Mopah Springs	SAC	Sacramento Mts. and environs
KING	Kingman	DEAD	Dead Mts.

Major elements (XRF) are given as weight percent oxides with total Fe contents expressed as Fe_2O_3. Loss on ignition (LOI) and Mg#s are shown. Mg# is calculated assuming FeO= 0.85*Total Fe, thus:

$$Mg\#= 100^* \left(\frac{\frac{MgO}{40.304}}{\frac{MgO}{40.304} + \frac{Fe_2O_3t}{93.936}} \right)$$

Weight percent CIPW norm data was calculated using the VAX programme 'CIPWNORM' written by D.Wright at The Open University. Major element data for clinopyroxene phenocrysts (electron microprobe) are given at the end of this appendix. Trace elements are expressed in parts per million (ppm) and subdivided into determinations made by XRF and INAA. Note that, where determinations exist for the same element by both techniques, the INAA data is used in preference because of its greater precision (see Appendix D). Sr and Pb isotope analyses and initial Sr ratios are listed with 1σ errors (eg: 0.70756 ± 2 is equivalent to 0.70756 ± 0.00002).

Yerrington west-central Nevada 30-8Ma (samples YR-1,2,14 are post-extensional)

SAMPLE	Y-1	Y-2	Y-3A	Y-5	Y-6	Y-7	Y-8	Y-9
REGION	YER	YER	YER	YER	YER	YER	YER	YER
SiO2	59.92	52.35	62.08	58.45	57.62	52.78	52.98	61.54
TiO2	0.62	0.67	0.64	0.67	0.67	0.91	0.90	0.57
Al2O3	16.91	12.80	15.74	16.44	16.28	14.37	14.58	17.04
Fe2O3	5.28	8.09	7.44	6.96	7.04	7.98	7.94	4.28
MnO	0.10	0.14	0.04	0.13	0.10	0.12	0.14	0.08
MgO	2.64	12.38	2.55	3.75	3.90	8.97	8.45	1.83
CaO	3.14	8.08	0.75	6.65	6.76	7.63	7.65	5.18
Na2O	6.20	2.28	6.19	3.57	3.69	3.20	3.14	4.18
K2O	3.14	0.82	2.47	2.28	2.25	1.69	1.71	2.30
P2O5	0.29	0.25	0.26	0.25	0.28	0.38	0.39	0.27
LOI	1.78	1.22	1.65	0.75	1.12	2.08	2.03	2.84
Total	**100.02**	**99.08**	**99.81**	**99.88**	**99.71**	**100.11**	**99.91**	**100.13**
Mg#	53.83	78.08	44.36	55.64	56.35	72.36	71.25	49.91
NORM								
Quartz	0.3	0.0	8.0	8.2	6.6			13.8
Corundum			2.1					
Orthoclase	18.6	4.8	14.6	13.5	13.3	10.0	10.1	13.6
Albite	52.4	19.3	52.4	30.2	31.2	27.1	26.6	35.4
Anorthite	9.1	22.3	2.0	22.1	21.2	19.8	20.6	20.9
Nepheline								
Diopside	3.8	12.9		7.6	8.6	12.5	11.9	2.5
Hypersthene	10.6	34.2	14.9	13.6	13.6	19.2	22.1	8.0
Olivine						4.4	1.6	
Magnetite	1.1	1.8	1.6	1.5	1.5	1.7	1.7	0.9
Ilmenite	1.2	1.3	1.2	1.3	1.3	1.7	1.7	1.1
Apatite	0.7	0.6	0.6	0.6	0.7	0.9	0.9	0.6
XRF								
Ba	1143	700	745	793	789	943	969	1307
Ce	26	39	149	35	33	40	55	46
Co	12	42	17	25	25	40	38	14
Cr	30	793	27	85	110	390	383	23
La	11		49	21	17	17	11	13
Nb	4	4	3	6	5	6	6	4
Nd	14	18	56	19	29	28	32	22
Ni	16	319	20	19	18	201	198	14
Pb	21	10	7	15	19	16	13	19
Rb	70	45	40	64	61	40	37	41
Sr	629	1202	187	737	753	802	832	982
Th	6	4	7	10	5	7	9	3
Y	14	15	15	16	19	18	16	11
Zn	68	74	19	68	72	74	78	63
Zr	133	90	99	119	120	137	138	114
INAA								
Ce								
Co								
Cr								
Cs								
Eu								
Hf								
La								
Lu								
Nd								
Sc								
Sm								
Ta								
Tb								
Th								
U								
Yb								
ISOTOPES								
87Sr/86Sr								
(87Sr/86Sr)i								
206Pb/204Pb								
207Pb/204Pb								
208Pb/204Pb								

SAMPLE	Y-10	Y-11	Y-12	Y-13	Y-14	Y-15	Y-16A	Y-16B
REGION	YER	YER	YER	YER	YER	YER	YER	YER
SiO2	66.78	53.47	68.83	77.37	62.04	76.45	61.68	60.73
TiO2	0.40	1.03	0.37	0.13	0.52	0.14	0.51	0.53
Al2O3	15.66	15.69	15.48	12.69	17.09	12.49	16.85	17.03
Fe2O3	3.63	7.68	3.07	1.07	4.90	1.11	4.85	4.94
MnO	0.07	0.14	0.05	0.03	0.08	0.05	0.10	0.13
MgO	1.52	3.90	0.90	0.29	2.24	0.20	2.46	2.65
CaO	2.55	5.45	2.32	0.67	4.56	0.73	4.90	5.35
Na2O	4.94	3.39	4.10	2.92	4.28	2.76	4.41	4.48
K2O	3.30	2.34	4.23	4.84	2.32	4.92	2.37	2.36
P2O5	0.17	0.42	0.14	0.05	0.25	0.03	0.26	0.27
LOI	1.13	5.69	1.60	1.52	1.48	1.39	1.87	2.48
Total	**100.14**	**99.21**	**101.09**	**101.57**	**99.77**	**100.27**	**100.27**	**100.94**
Mg#	49.38	54.17	40.56	38.65	51.58	29.33	54.16	55.58
NORM								
Quartz	16.4	5.4	21.3	39.6	13.5	39.2	11.7	9.5
Corundum			0.3	1.6		1.4		
Orthoclase	19.5	13.8	25.0	28.6	13.7	29.1	14.0	14.0
Albite	41.8	28.7	34.7	24.7	36.2	23.4	37.3	37.9
Anorthite	10.8	20.7	10.5	3.0	20.6	3.4	19.2	19.4
Nepheline								
Diopside	0.6	3.0			0.3		2.8	4.5
Hypersthene	7.6	16.6	5.7	1.9	11.0	1.8	10.3	10.1
Olivine								
Magnetite	0.8	1.7	0.7	0.2	1.1	0.2	1.1	1.1
Ilmenite	0.8	2.0	0.7	0.2	1.0	0.3	1.0	1.0
Apatite	0.4	1.0	0.3	0.1	0.6	0.1	0.6	0.6
XRF								
Ba	1034	1747	1200	137	1212	224	1134	1337
Ce		51	53	107		82	40	51
Co	16	25	5		13	3	15	15
Cr	22	84	13	13	50	11	41	42
La		20	21	31	12	26		
Nb	4	7	9	13	4	14	4	4
Nd	15	25	24	32	10	26	10	21
Ni	7	55	2	1	13	3	12	12
Pb	14	5	25	27	18	33	16	15
Rb	84	90	128	187	55	194	55	56
Sr	562	495	357	59	750	77	750	731
Th	14	7	18	24	4	29	9	6
Y	11	28	16	20	14	22	14	14
Zn	36	84	47	32	63	40	66	67
Zr	90	170	164	103	133	112	133	135
INAA								
Ce								
Co								
Cr								
Cs								
Eu								
Hf								
La								
Lu								
Nd								
Sc								
Sm								
Ta								
Tb								
Th								
U								
Yb								
ISOTOPES								
87Sr/86Sr								
(87Sr/86Sr)i								
206Pb/204Pb								
207Pb/204Pb								
208Pb/204Pb								

SAMPLE	YR-1	YR-2	YR-6	YR-7	YR-11B	YR-14
REGION	YER	YER	YER	YER	YER	YER
SiO2	53.41	53.21	60.41	63.32	63.69	54.33
TiO2	0.94	1.00	0.71	0.57	0.59	0.95
Al2O3	18.50	18.32	17.34	16.75	17.63	17.89
Fe2O3	8.42	8.70	5.47	4.33	4.34	7.71
MnO	0.16	0.15	0.07	0.08	0.05	0.12
MgO	4.35	4.43	1.52	2.29	1.36	3.33
CaO	8.42	8.35	5.89	4.64	3.99	8.53
Na2O	2.94	3.42	4.57	4.72	4.80	3.89
K2O	1.35	1.21	2.49	2.30	2.22	1.43
P2O5	0.39	0.32	0.36	0.27	0.32	0.37
LOI	0.45	1.18	1.42	0.28	2.85	0.92
Total	**99.33**	**100.29**	**100.24**	**99.56**	**101.84**	**99.48**
Mg#	54.60	54.27	39.27	55.15	42.31	50.15
NORM						
Quartz	4.6	2.4	9.3	13.0	15.5	2.9
Corundum					0.8	
Orthoclase	8.0	7.2	14.7	13.6	13.1	8.4
Albite	24.9	28.9	38.6	40.0	40.6	32.9
Anorthite	33.3	31.0	19.5	17.7	17.7	27.1
Nepheline						
Diopside	4.9	6.8	6.2	2.9		10.6
Hypersthene	18.0	17.5	6.6	9.0	8.1	11.6
Olivine						
Magnetite	1.8	1.9	1.2	0.9	0.9	1.7
Ilmenite	1.8	1.9	1.3	1.1	1.1	1.8
Apatite	0.9	0.8	0.8	0.6	0.8	0.9
XRF						
Ba	766	610	1327	1268	1233	765
Ce	59	61	47	33	43	28
Co	22	26	13	16	9	22
Cr	25	33	38	44	19	22
La	22		25	19	21	
Nb	3	3	5	3	4	3
Nd	33	26	26	17	21	24
Ni	5	1	17	26	8	7
Pb	8	11	26	22	17	9
Rb	15	14	35	44	39	19
Sr	1405	1399	1158	945	1077	1541
Th	5	3	8	5	3	9
Y	25	23	14	11	13	18
Zn	92	91	62	66	65	80
Zr	130	107	137	118	132	97
INAA						
Ce						
Co						
Cr						
Cs						
Eu						
Hf						
La						
Lu						
Nd						
Sc						
Sm						
Ta						
Tb						
Th						
U						
Yb						
ISOTOPES						
87Sr/86Sr						
(87Sr/86Sr)i						
206Pb/204Pb						
207Pb/204Pb						
208Pb/204Pb						

Caliente Caldera southern Nevada 30-25Ma pre/syn-extensional

SAMPLE	LN-23	CC-1	CC-3	CC-4	CC-5	CC-6	CC-7	CC-8
REGION	CAL	CAL	CAL	CAL	CAL	CAL	CAL	CAL
SiO2	47.85	58.84	64.84	73.12	73.93	70.51	62.90	61.18
TiO2	2.18	1.03	0.90	0.16	0.20	0.32	0.72	1.01
Al2O3	16.52	16.12	15.86	13.73	13.65	14.24	15.25	15.52
Fe2O3	12.48	8.11	4.28	1.53	1.77	1.67	5.44	6.43
MnO	0.18	0.15	0.08	0.07	0.03	0.06	0.08	0.11
MgO	5.66	3.59	1.12	0.46	0.53	0.45	2.56	2.65
CaO	9.38	7.52	2.63	1.25	1.37	1.09	4.27	4.91
Na2O	3.84	3.02	3.81	2.94	2.93	3.64	3.10	3.48
K2O	0.94	1.70	5.43	5.37	5.06	5.75	3.91	3.78
P2O5	0.40	0.40	0.26	0.04	0.04	0.05	0.28	0.32
LOI	1.55	0.90	2.69	2.84	5.15	2.84	2.29	1.22
Total	**100.96**	**101.37**	**101.90**	**101.51**	**104.67**	**100.62**	**100.80**	**100.61**
Mg#	51.36	50.77	37.86	41.01	40.89	38.79	52.27	48.97
NORM								
Quartz		12.4	13.7	31.4	33.0	23.7	15.7	11.3
Corundum				0.9	1.0	0.2		
Orthoclase	5.6	10.0	32.1	31.7	29.9	34.0	23.1	22.3
Albite	27.8	25.6	32.2	24.9	24.8	30.8	26.2	29.4
Anorthite	25.1	25.4	10.1	5.9	6.5	5.1	16.1	15.6
Nepheline	2.5							
Diopside	15.5	7.7	1.0				2.6	5.6
Hypersthene		14.1	6.4	3.0	3.3	2.8	11.0	10.6
Olivine	14.1							
Magnetite	2.7	1.8	0.9	0.3	0.4	0.4	1.2	1.4
Ilmenite	4.1	2.0	1.7	0.3	0.4	0.6	1.4	1.9
Apatite	0.9	0.9	0.6	0.1	0.1	0.1	0.7	0.8
XRF								
Ba	266	663	1306	795	1493	1102	1033	932
Ce	39	113	231	91	127	129	91	102
Co	48	20	6	8	9	7	18	21
Cr	58	75	3	11	3	6	51	43
La	19	28	86	43	50	58	43	26
Nb	17	12	26	17	13	16	11	15
Nd	27	39	74	37	44	51	32	42
Ni	72	9	2	5	4	4	27	33
Pb	4	11	34	28	27	36	27	23
Rb	12	34	200	195	153	196	114	136
Sr	499	888	457	201	272	246	667	667
Th	1	2	41	28	30	39	28	27
Y	33	42	39	25	21	26	24	24
Zn	93	85	68	43	32	38	68	64
Zr	194	235	481	155	168	285	195	240
INAA								
Ce								
Co								
Cr								
Cs								
Eu								
Hf								
La								
Lu								
Nd								
Sc								
Sm								
Ta								
Tb								
Th								
U								
Yb								
ISOTOPES								
87Sr/86Sr								
(87Sr/86Sr)i								
206Pb/204Pb								
207Pb/204Pb								
208Pb/204Pb								

			Colorado River Trough pre/syn-extensional					
SAMPLE	CC-9	CC-10	E-1	E-2	E-3	E-4	E-5	E-6
REGION	CAL	CAL	ELD	ELD	ELD	ELD	ELD	ELD
SiO2	61.53	70.86	57.42	57.66	58.95	72.09	50.75	54.38
TiO2	0.85	0.42	0.74	1.05	0.73	0.13	1.52	1.39
Al2O3	16.11	14.64	15.42	14.75	15.83	12.27	13.85	15.61
Fe2O3	5.54	2.57	4.94	6.82	4.91	0.75	8.67	7.33
MnO	0.07	0.05	0.07	0.07	0.06	0.04	0.13	0.10
MgO	2.40	0.86	2.94	3.17	3.60		7.65	5.03
CaO	4.64	1.91	6.04	5.33	4.35	0.97	8.39	7.14
Na2O	3.07	3.32	4.62	5.08	7.22	3.85	3.21	3.87
K2O	4.02	4.42	2.87	2.60	1.35	3.91	2.94	3.77
P2O5	0.33	0.12	0.36	0.48	0.46		0.85	0.73
LOI	1.73	1.20	4.14	2.01	1.84	6.08	2.01	1.33
Total	**100.30**	**100.38**	**99.57**	**99.02**	**99.30**	**100.10**	**99.97**	**100.69**
Mg#	50.21	43.75	58.08	52.03	63.04	n/a	67.29	61.53
NORM								
Quartz	13.6	28.4	4.1	3.0		32.3		
Corundum		1.2						
Orthoclase	23.8	26.1	16.9	15.3	7.9	23.1	17.4	22.3
Albite	26.0	28.1	39.1	43.0	61.1	32.6	26.8	32.7
Anorthite	18.3	8.7	12.9	9.8	6.8	4.6	14.7	14.1
Nepheline							0.2	
Diopside	2.1		12.0	11.1	9.6	0.2	17.3	13.5
Hypersthene	10.8	4.8	6.7	9.5	4.3	0.7		2.1
Olivine					3.8		14.1	8.1
Magnetite	1.2	0.6	1.1	1.5	1.1	0.2	1.9	1.6
Ilmenite	1.6	0.8	1.4	2.0	1.4	0.2	2.9	2.6
Apatite	0.8	0.3	0.9	1.1	1.1		2.0	1.7
XRF								
Ba	1059	850	1274	1072	875		1493	1519
Ce	115	46	116	150		84	222	237
Co	11	9	27	29		2	46	32
Cr	24	16	384	147		40	396	116
La	53	30	16	51		33	78	78
Nb	14	15	10	12	13	34	23	27
Nd	45	23	46	67		18	92	81
Ni	24	8	88	75	84	4	239	107
Pb	23	23	24	22	20	35	17	28
Rb	163	130	57	58	25	304	61	96
Sr	813	366	1231	1011	1129	136	1170	1241
Th	28	17	9	17	13	40	14	23
Y	23	16	17	24	17	20	26	27
Zn	59	36	65	59	76	29	95	71
Zr	244	181	201	272	261	119	323	388
INAA								
Ce					143.9		170.9	
Co					16.1		35.7	
Cr					122		413	
Cs					1.11		1.25	
Eu					2.36		3.20	
Hf					6.35		7.05	
La					78.6		88.6	
Lu					0.23		0.29	
Nd					65.1		82.0	
Sc					10.4		21.2	
Sm					10.02		13.16	
Ta					0.70		1.25	
Tb					0.94		1.14	
Th					12.23		11.86	
U								
Yb					1.36		1.76	
ISOTOPES								
87Sr/86Sr					.710925±3		.70756±2	
(87Sr/86Sr)i					.710873±3		.70751±2	
206Pb/204Pb							18.388±5	
207Pb/204Pb							15.573±4	
208Pb/204Pb							38.746±10	

SAMPLE	E-7	E-8	E-9	E-10A	E-10B	E-11	E-12	E-13
REGION	ELD	ELD	ELD	ELD	ELD	ELD	ELD	ELD
SiO2	52.29	66.74	70.98	55.70	57.20	53.42	55.04	63.43
TiO2	1.49	0.57	0.38	1.21	1.18	1.52	1.30	0.88
Al2O3	16.41	16.40	15.12	15.50	15.52	16.41	15.90	17.42
Fe2O3	8.39	2.41	1.69	6.42	5.99	8.65	7.27	3.73
MnO	0.10	0.08	0.06	0.09	0.08	0.13	0.10	0.08
MgO	4.76	0.32		4.00	3.72	4.79	3.91	1.25
CaO	7.89	1.42	0.86	6.33	6.01	7.37	6.61	3.34
Na2O	3.72	4.45	4.68	3.30	3.56	4.28	3.87	4.59
K2O	2.52	6.38	6.22	4.41	4.39	2.62	3.65	4.98
P2O5	0.69	0.14	0.08	0.66	0.62	0.51	0.68	0.23
LOI	1.38	0.71	0.53	2.19	2.15	1.84	1.61	0.56
Total	**99.65**	**99.61**	**100.60**	**99.80**	**100.43**	**101.56**	**99.95**	**100.49**
Mg#	56.90	23.40		59.19	59.12	56.33	55.60	43.85
NORM								
Quartz		12.3	18.0	1.8	3.0			8.3
Corundum								
Orthoclase	14.9	37.7	36.8	26.1	26.0	15.5	21.6	29.4
Albite	31.4	37.6	39.6	27.9	30.2	36.2	32.7	38.8
Anorthite	20.7	5.9	1.9	14.5	13.4	17.8	15.2	12.2
Nepheline								
Diopside	11.4	0.2	1.6	10.3	10.1	12.6	10.8	2.4
Hypersthene	7.8	3.0	0.8	11.3	10.2	0.9	11.7	5.4
Olivine	5.1					10.0	0.1	
Magnetite	1.8	0.5	0.4	1.4	1.3	1.9	1.6	0.8
Ilmenite	2.8	1.1	0.7	2.3	2.2	2.9	2.5	1.7
Apatite	1.6	0.3	0.2	1.6	1.5	1.2	1.6	0.5
XRF								
Ba	1174	1362	514	1363	1392	1022	1696	2102
Ce	183	396	182	175	206	152	230	219
Co	28	5	1	25	25	37	28	9
Cr	72	16	154	20	192	155	80	4
La	66	158	74	89	97	63	103	97
Nb	18	28	43	29	28	23	25	34
Nd	63	114	56	59	70	52	90	68
Ni	60	5	12	72	67	107	67	8
Pb	15	39	38	25	28	17	23	25
Rb	55	136	182	146	148	66	96	129
Sr	979	357	145	946	945	814	1233	877
Th	11	35	41	27	26	15	23	24
Y	33	30	32	31	27	30	31	31
Zn	72	43	34	68	67	81	78	47
Zr	306	635	374	395	385	314	391	525
INAA								
Ce			176.6	177.5				
Co			1.6	21.3				
Cr			192	150				
Cs			2.60	2.60				
Eu			1.49	2.73				
Hf			9.98	8.90				
La			108.7	97.0				
Lu			0.47	0.39				
Nd			64.5	71.5				
Sc			3.4	15.0				
Sm			10.15	12.04				
Ta			2.33	1.53				
Tb			1.05	1.16				
Th			37.18	24.25				
U								
Yb			2.44	2.11				
ISOTOPES								
87Sr/86Sr				.70839±1				
(87Sr/86Sr)i				.70827±1				
206Pb/204Pb								
207Pb/204Pb								
208Pb/204Pb								

SAMPLE	BM-3	BM-4	BM-5	BM-6	BM-7	BM-8	BM-9	BM-10
REGION	OAT	OAT	OAT	OAT	OAT	OAT	OAT	OAT
SiO2	62.19	58.89	58.96	59.94	63.56	64.63	60.85	60.21
TiO2	0.97	0.96	1.07	1.04	0.90	0.84	0.93	0.98
Al2O3	18.03	17.37	15.83	16.53	14.70	14.97	16.49	17.60
Fe2O3	4.60	6.18	6.73	5.97	5.07	4.93	5.39	5.78
MnO	0.13	0.05	0.10	0.12	0.11	0.05	0.08	0.09
MgO	1.33	2.23	4.53	2.95	1.13	1.19	1.83	2.05
CaO	3.60	4.79	6.42	5.50	5.53	4.05	4.55	5.36
Na2O	5.26	4.24	4.13	4.13	3.84	3.19	4.06	4.34
K2O	4.03	3.49	2.05	3.00	1.90	3.08	2.93	2.83
P2O5	0.48	0.46	0.33	0.33	0.35	0.35	0.36	0.38
LOI	1.46	1.71	1.10	1.86	1.88	3.05	2.19	1.86
Total	**102.06**	**100.38**	**101.25**	**101.38**	**98.97**	**100.34**	**99.66**	**101.49**
Mg#	40.21	45.64	61.07	53.48	34.14	35.93	44.17	45.29
NORM								
Quartz	6.0	6.2	6.7	8.0	20.7	22.6	12.5	8.8
Corundum								
Orthoclase	23.8	20.6	12.1	17.7	11.2	18.2	17.3	16.7
Albite	44.5	35.9	34.9	34.9	32.5	27.0	34.4	36.7
Anorthite	13.7	18.1	18.6	17.7	17.3	17.4	18.1	20.2
Nepheline								
Diopside	0.9	2.2	9.0	6.1	6.7	0.3	1.8	3.3
Hypersthene	7.4	10.9	13.9	10.5	4.7	7.8	9.2	9.4
Olivine								
Magnetite	1.0	1.3	1.5	1.3	1.1	1.1	1.2	1.3
Ilmenite	1.8	1.8	2.0	2.0	1.7	1.6	1.8	1.9
Apatite	1.1	1.1	0.8	0.8	0.8	0.8	0.8	0.9
XRF								
Ba	2050	1520	1179	1139	1227	1308	1394	1301
Ce	211	174	98	104	119	121	140	123
Co	12	27	33	20	19	17	20	18
Cr		11	131	97	42	21	27	25
La	72	83	37	63	47	56	55	40
Nb	25	13	16	13	13	13	16	14
Nd	80	62	44	34	54	55	51	52
Ni		26	127	63	27	21	23	27
Pb	24	20	19	19	15	23	25	21
Rb	87	100	60	74	52	78	64	62
Sr	1210	1280	958	867	966	829	1078	920
Th	20	13	8	11	12	14	12	11
Y	27	26	20	22	21	19	23	25
Zn	84	74	75	74	53	66	83	76
Zr	350	269	213	247	213	236	257	258
INAA								
Ce	32.2	159.7	77.8	98.3		110.9	124.7	109.8
Co	40.0	18.3	23.4	19.2		12.5	13.4	15.7
Cr	229	12	169	127		23	27	25
Cs	0.20	8.15	1.59	2.88		3.23	0.89	3.46
Eu	1.25	2.32	1.62	1.80		1.85	2.05	1.90
Hf	3.05	6.27	4.88	5.64		5.33	6.07	5.92
La	17.0	84.3	41.4	53.5		58.1	65.1	58.3
Lu	0.29	0.31	0.26	0.30		0.29	0.28	0.34
Nd	16.2	66.9	35.5	43.6		45.8	53.5	46.7
Sc	23.0	11.0	15.5	16.3		8.4	9.4	12.3
Sm	3.67	10.65	5.99	7.10		7.78	8.92	7.93
Ta	0.52	0.72	0.79	0.82		0.83	0.93	0.77
Tb	0.63	0.90	0.69	0.75		0.72	0.81	0.84
Th	2.24	11.34	5.68	9.13		9.15	10.33	9.26
U	0.84	2.40	1.10	2.02		1.90	2.40	1.40
Yb	1.88	1.78	1.51	1.67		1.53	1.75	2.07
ISOTOPES								
87Sr/86Sr		.710142±6	.70956±1			.709344±7	.709313±7	.710215±6
(87Sr/86Sr)i		.710078±6	.70955±1			.709267±7	.709264±7	.710160±6
206Pb/204Pb			18.108±3					
207Pb/204Pb			15.563±2					
208Pb/204Pb			38.830±6					

SAMPLE	BM-11	BM-12	BM-13	BM-14	BM-15	BM-16	H-1	H-2
REGION	OAT	OAT	OAT	OAT	OAT	OAT	LHC	LHC
SiO2	63.81	63.53	70.78	58.18	80.25	67.08	45.40	49.26
TiO2	0.73	0.69	0.51	1.17	0.06	0.40	1.74	1.21
Al2O3	16.67	15.72	13.07	16.68	10.98	16.14	16.37	15.73
Fe2O3	4.12	4.35	2.75	6.44	0.55	2.76	10.83	9.86
MnO	0.07	0.05	0.03	0.09	0.01	0.07	0.17	0.11
MgO	1.83	1.15	0.63	3.54	0.21	0.75	5.57	7.34
CaO	3.96	3.45	0.67	5.21	0.16	1.57	11.21	9.72
Na2O	4.23	3.37	0.55	4.65		3.94	3.40	2.90
K2O	3.09	3.99	9.30	2.98	8.68	5.93	1.49	1.06
P2O5	0.26	0.26	0.20	0.65		0.12	1.05	0.34
LOI	1.70	4.22	1.36	3.08	0.38	1.91	2.62	3.01
Total	**100.47**	**100.78**	**99.87**	**102.67**	**101.28**	**100.66**	**99.86**	**100.54**
Mg#	50.87	38.12	34.71	56.13	46.77	38.68	54.52	63.42
NORM								
Quartz	15.1	18.2	28.9	3.4	46.1	16.0		
Corundum		0.2	1.4		1.3	0.7		
Orthoclase	18.3	23.6	55.0	17.6	51.3	35.0	8.8	6.3
Albite	35.8	28.5	4.7	39.3		33.3	17.2	24.5
Anorthite	17.4	15.4	2.0	15.8	0.8	7.0	25.0	26.8
Nepheline							6.3	
Diopside	0.5			4.7			19.5	15.7
Hypersthene	8.5	7.4	4.3	13.0	1.1	4.9		9.5
Olivine							11.4	8.8
Magnetite	0.9	0.9	0.6	1.4	0.1	0.6	2.4	2.1
Ilmenite	1.4	1.3	1.0	2.2	0.1	0.8	3.3	2.3
Apatite	0.6	0.6	0.5	1.5		0.3	2.5	0.8
XRF								
Ba	1322	1336	1562	1867	290	2032	1114	552
Ce	93	107	161	274	32	211	226	84
Co	10	16	3	30	4	9	49	49
Cr	31	21		14	17		24	285
La	39	48	70	109	21	90	58	30
Nb	15	14	23	14	38	16	33	8
Nd	42	35	55	98	10	69	86	37
Ni	18	18	13	27	3	2	45	171
Pb	25	23	21	26	45	41	14	13
Rb	70	121	632	86	342	160	37	19
Sr	881	574	501	1236	118	847	1250	639
Th	16	9	12	21	28	21	16	3
Y	17	18	29	22	16	21	33	24
Zn	68	57	59	91	29	72	99	82
Zr	234	226	319	355	96	422	258	142
INAA								
Ce							180.6	57.5
Co							36.6	42.1
Cr							20	321
Cs							40.12	0.70
Eu							4.06	1.70
Hf							5.54	3.32
La							82.3	27.3
Lu							0.39	0.35
Nd							94.1	33.4
Sc							20.4	29.5
Sm							16.05	4.60
Ta							1.74	0.51
Tb							1.56	0.80
Th							9.57	3.76
U								
Yb							2.62	2.10
ISOTOPES								
87Sr/86Sr							.70733±1	.70777±1
(87Sr/86Sr)i							.70731±1	.70769±1
206Pb/204Pb							18.897±9	18.839±7
207Pb/204Pb							15.623±7	15.636±6
208Pb/204Pb							39.024±18	39.005±14

Pb isotope	repeat data
H-1	H-2
18.878±2	18.847±1
15.619±2	15.636±1
39.058±5	39.063±2

SAMPLE	H-3	H-4	H-5	H-6	H-7	H-8A	H-8B	H-9
REGION	LHC	LHC	LHC	LHC	LHC	LHC	LHC	LHC
SiO2	66.97	65.88	46.50	47.70	46.70	72.14	44.68	46.09
TiO2	0.37	0.45	1.36	1.42	1.33	0.33	2.59	1.26
Al2O3	14.23	15.24	16.28	16.60	16.30	14.50	14.57	16.31
Fe2O3	2.17	3.02	11.28	11.67	11.22	2.05	10.48	11.40
MnO	0.04	0.06	0.19	0.18	0.18	0.03	0.12	0.18
MgO	0.73	1.05	8.20	8.22	8.39	0.54	10.13	8.28
CaO	3.04	2.93	8.74	9.52	8.51	1.95	10.51	8.88
Na2O	2.58	4.21	3.31	3.36	3.34	3.33	2.01	3.41
K2O	2.87	3.43	0.57	0.64	0.60	4.69	1.65	0.49
P2O5	0.12	0.18	0.29	0.32	0.30	0.11	0.34	0.26
LOI	7.75	3.67	2.96	1.14	2.93	0.45	1.31	3.10
Total	**100.88**	**100.12**	**99.67**	**100.76**	**99.80**	**100.12**	**98.39**	**99.67**
Mg#	43.79	44.68	62.87	62.13	63.51	38.14	69.23	62.85
NORM								
Quartz	32.7	19.7				29.2		
Corundum	1.6					0.7		
Orthoclase	17.0	20.3	3.4	3.8	3.6	27.7	9.7	2.9
Albite	21.8	35.6	27.2	26.2	27.9	28.2	12.7	25.7
Anorthite	14.3	12.6	27.9	28.3	27.7	8.9	25.9	27.8
Nepheline			0.4	1.2	0.2		2.3	1.7
Diopside		0.6	11.1	13.7	10.2		19.3	11.9
Hypersthene	4.1	5.5				3.5		
Olivine			20.1	19.4	20.7		18.2	20.2
Magnetite	0.5	0.7	2.5	2.5	2.4	0.4	2.3	2.5
Ilmenite	0.7	0.9	2.6	2.7	2.5	0.6	4.9	2.4
Apatite	0.3	0.4	0.7	0.7	0.7	0.3	0.8	0.6
XRF								
Ba	907	1405	272	268	274	1166	676	211
Ce	71	67	77	42	45	30	142	36
Co	3	12	50	44	49	3	62	48
Cr	13	15	149	147	142	21	96	121
La	32	28		13	18	12	34	
Nb	15	10	6	6	7	9	10	4
Nd	23	33	31	27	18	15	59	24
Ni	4	3	132	130	122	6	125	140
Pb	15	27	5	5	7	27	12	8
Rb	98	109	21	16	18	98	35	16
Sr	512	638	393	325	336	377	895	364
Th	13	13	5	1	5	7	2	4
Y	17	15	37	39	35	24	33	34
Zn	40	59	75	73	75	37	70	72
Zr	194	199	158	165	160	146	123	139
INAA								
Ce		76.1	36.6	45.2	35.6			32.0
Co		5.8	44.9	45.7	43.9			48.4
Cr		13	177	168	179			149
Cs		2.98	14.60	2.90	15.70			9.82
Eu		1.14	1.45	1.72	1.45			1.51
Hf		4.65	3.41	3.89	3.75			3.45
La		42.6	17.8	18.5	18.7			13.6
Lu		0.23	0.51	0.59	0.48			0.56
Nd		31.4	20.2	30.4	20.4			22.6
Sc		5.5	40.4	39.2	39.2			39.3
Sm		5.08	5.00	5.76	4.84			4.51
Ta		0.64	0.30	0.37	0.33			0.40
Tb		0.57	0.84	1.02	0.81			1.07
Th		9.35	1.74	1.69	1.67			1.22
U								
Yb		1.26	3.10	3.67	2.90			3.24
ISOTOPES								
87Sr/86Sr		.71037±1	.709345±6	.70853±1			.70837±1	.708930±7
(87Sr/86Sr)i		.70984±1	.709306±6	.70849±1			.70834±1	.708894±7
206Pb/204Pb			18.429±14					18.404±25
207Pb/204Pb			15.645±12					15.590±22
208Pb/204Pb			39.159±30					39.004±54

SAMPLE	H-10	H-11	H-12	H-13	BW-5	C-1	C-2	C-3
REGION	LHC	LHC	LHC	LHC	LHC	LHC	LHC	LHC
SiO2	45.82	46.10	45.54	45.56	48.87	55.86	55.41	51.43
TiO2	1.29	1.35	1.27	1.28	1.81	1.21	1.38	1.46
Al2O3	16.44	16.50	16.41	16.28	17.01	15.41	15.23	15.60
Fe2O3	11.46	11.76	11.19	11.33	10.07	6.83	7.21	8.20
MnO	0.18	0.18	0.17	0.17	0.16	0.08	0.10	0.09
MgO	8.46	7.81	8.38	7.94	6.08	3.45	4.23	4.96
CaO	8.73	9.14	9.49	9.44	9.95	6.38	6.48	8.63
Na2O	4.28	3.70	2.81	2.81	3.61	3.67	3.02	3.28
K2O	0.51	0.96	0.76	1.17	0.93	3.74	3.70	2.92
P2O5	0.16	0.20	0.18	0.18	0.57	0.56	0.63	0.66
LOI	3.96	3.13	3.83	4.21	1.30	1.66	1.95	2.85
Total	**101.29**	**100.82**	**100.03**	**100.39**	**100.35**	**98.87**	**99.33**	**100.09**
Mg#	63.23	60.71	63.58	62.01	58.41	54.09	57.73	58.50
NORM								
Quartz						2.7	4.4	
Corundum								
Orthoclase	3.0	5.7	4.5	6.9	5.5	22.1	21.9	17.3
Albite	21.9	20.5	21.8	19.6	29.9	31.1	25.6	27.8
Anorthite	24.1	25.6	29.9	28.4	27.5	14.5	17.0	19.2
Nepheline	7.8	5.8	1.1	2.3	0.3			
Diopside	14.8	15.1	13.0	14.1	14.9	11.1	8.9	15.8
Hypersthene						10.0	13.3	3.8
Olivine	19.5	18.4	19.7	18.7	13.2			6.6
Magnetite	2.5	2.6	2.4	2.5	2.2	1.5	1.6	1.8
Ilmenite	2.4	2.6	2.4	2.4	3.4	2.3	2.6	2.8
Apatite	0.4	0.5	0.4	0.4	1.3	1.3	1.5	1.6
XRF								
Ba	308	232	179	181	336	1336	1161	1306
Ce	22	42	73	60	84	159	237	225
Co	49	53	50	52	38	33	32	28
Cr	121	117	112	122	72	107	101	117
La				28	21	75	84	68
Nb	3	3	4	5	9	20	37	20
Nd	22	24	21	22	36	56	78	82
Ni	140	150	146	142	52	96	88	89
Pb	7	2	8	8	5	18	32	20
Rb	19	58	64	100	12	172	152	50
Sr	353	510	1045	466	629	1210	933	1424
Th	1	3	4	2	6	17	27	13
Y	34	35	33	35	36	27	35	27
Zn	67	76	71	74	77	71	85	90
Zr	145	153	146	143	237	284	474	297
INAA								
Ce	28.4	30.7	28.0	26.8	61.2		195.3	
Co	45.6	47.7	47.0	46.4	35.8		25.1	
Cr	148	145	130	146	57		145	
Cs	13.10	4.92	7.34	6.13	0.76		8.53	
Eu	1.37	1.37	1.31	1.30	2.07		2.65	
Hf	3.21	3.45	3.22	3.26	5.17		10.93	
La	13.8	15.0	13.4	13.7	32.0		104.9	
Lu	0.51	0.49	0.44	0.51	0.46		0.43	
Nd	18.5	18.9	16.9	17.4	33.8		85.1	
Sc	38.2	39.3	37.0	38.2	28.3		16.7	
Sm	4.37	4.48	4.09	4.05	6.97		13.41	
Ta	0.22	0.20	0.21	0.19	0.56		2.03	
Tb	0.79	0.81	0.77	0.74	0.96		1.17	
Th	1.14	1.49	1.13	1.16	2.50		24.86	
U					0.40			
Yb	2.89	2.91	2.69	2.72	2.72		2.60	
ISOTOPES								
87Sr/86Sr		.709801±5			.706659±9	.70899±1	.70885±1	
(87Sr/86Sr)i		.709707±5			.706643±9	.70887±1	.70871±1	
206Pb/204Pb		18.385±31			18.614±8			
207Pb/204Pb		15.586±26			15.598±7			
208Pb/204Pb		39.028±66			38.815±17			

SAMPLE	C-4	MH-1	MH-6	MH-8	MO-1	MO-2	MO-4	MO-5
REGION	LHC	LHC	LHC	LHC	LHC	LHC	LHC	LHC
SiO2	55.87	46.03	71.07	54.34	48.46	52.92	79.99	50.87
TiO2	1.58	1.80	0.25	1.32	1.74	1.17	0.10	1.51
Al2O3	17.85	13.34	13.73	16.05	12.83	13.68	11.09	16.06
Fe2O3	6.11	11.13	1.59	8.17	9.11	7.34	0.68	9.55
MnO	0.06	0.14	0.04	0.12	0.13	0.07	0.02	0.10
MgO	1.84	10.24	0.44	5.53	8.03	7.52	0.21	5.93
CaO	4.79	11.48	1.26	7.77	10.69	7.07	0.49	8.36
Na2O	4.26	1.62	3.83	3.91	2.50	2.60	2.64	4.15
K2O	4.84	1.14	4.79	1.95	2.79	3.81	4.96	1.64
P2O5	0.79	0.75	0.06	0.47	0.99	0.41		0.47
LOI	1.69	1.87	3.45	0.36	2.70	3.81	0.78	2.78
Total	**99.69**	**99.54**	**100.52**	**99.97**	**99.97**	**100.39**	**100.96**	**101.42**
Mg#	41.25	68.19	39.28	61.19	67.26	70.46	41.63	59.12
NORM								
Quartz	0.1		26.5				43.9	
Corundum			0.1				0.5	
Orthoclase	28.6	6.7	28.3	11.5	16.5	22.5	29.3	9.7
Albite	36.1	13.7	32.4	33.0	17.7	22.0	22.3	33.2
Anorthite	15.3	25.8	5.9	20.5	15.5	14.4	2.4	20.3
Nepheline					1.9			1.0
Diopside	2.8	21.3		12.2	25.0	14.5		14.7
Hypersthene	8.5	8.4	2.8	16.1		13.7	1.3	
Olivine		13.3		0.1	12.2	4.0		12.8
Magnetite	1.3	2.4	0.3	1.8	2.0	1.6	0.1	2.1
Ilmenite	3.0	3.4	0.5	2.5	3.3	2.2	0.2	2.9
Apatite	1.9	1.8	0.1	1.1	2.3	1.0		1.1
XRF								
Ba	1883	959	1064	523	1858	1489		899
Ce	239	94	68	183	181	103		117
Co	16	33	9	60	41	45		45
Cr	4	150	7	378	268	287		237
La	116	26	34	65	93	65		32
Nb	43	18	16	12	28	13		19
Nd	94	41	23	74	81	49		40
Ni	14	79	4	227	133	214		158
Pb	33	10	27	11	21	16		7
Rb	146	33	121	18	51	124		33
Sr	1086	823	235	1348	1224	757		823
Th	28	10	21	10	17	12		5
Y	35	26	18	27	30	21		27
Zn	87	73	36	90	91	79		77
Zr	511	242	189	177	307	227		207
INAA								
Ce	221.7	97.3		159.5	201.5	111.7	54.8	89.4
Co	12.9	28.3		49.7	35.7	30.1	0.4	33.8
Cr	10	176		488	370	328	3	300
Cs	3.05	0.57		5.72	1.40	6.88	3.33	1.39
Eu	3.30	2.10		3.12	4.10	2.10	0.27	2.01
Hf	11.41	5.18		4.06	6.96	5.23	3.05	4.53
La	121.8	46.4		77.8	103.3	58.6	33.5	48.8
Lu	0.46	0.33		0.28	0.34	0.28	0.16	0.35
Nd	94.6	46.1		81.0	102.1	52.2	13.2	40.6
Sc	9.8	19.7		27.6	28.2	19.5	1.2	23.4
Sm	15.13	8.30		12.42	18.18	9.18	2.08	7.58
Ta	2.43	1.07		0.88	1.39	0.77	1.30	1.02
Tb	1.30	0.96		1.29	1.39	0.76	0.28	0.80
Th	24.25	5.88		8.62	10.41	8.55	16.44	5.26
U					2.50	2.20	2.80	2.30
Yb	2.64	2.28		1.85	1.91	1.60	1.04	2.01
ISOTOPES								
87Sr/86Sr		.70836±1	.710420±4	.70782±1	.708271±7	.709007±8		.70781±1
(87Sr/86Sr)i		.70833±1	.709997±4	.70781±1	.708237±7	.708872±8		.70777±1
206Pb/204Pb		18.344±5			18.604±9			18.444±1
207Pb/204Pb		15.561±4			15.595±8			15.600±2
208Pb/204Pb		38.803±10			38.807±19			38.936±1

SAMPLE	MO-6	MO-7	FS-1	FS-2	FS-3	FS-4	FS-5	SL-1
REGION	LHC	LHC	LHC	LHC	LHC	LHC	LHC	SEARCH
SiO2	53.62	54.41	76.83	58.96	59.48	56.26	53.36	62.33
TiO2	1.31	1.33	0.12	1.03	1.07	1.32	1.33	0.73
Al2O3	16.20	16.18	13.24	15.98	16.28	16.20	15.70	15.42
Fe2O3	8.24	7.38	0.76	5.69	5.98	7.51	7.28	4.27
MnO	0.13	0.08	0.02	0.15	0.14	0.12	0.11	0.09
MgO	5.16	4.58	0.28	1.14	2.13	3.83	3.84	2.28
CaO	8.33	6.40	0.76	4.05	3.34	7.08	5.13	2.54
Na2O	3.89	2.96	3.99	5.15	4.94	3.59	4.59	3.17
K2O	1.72	4.66	4.44	3.86	4.09	3.56	3.19	6.87
P2O5	0.41	0.55	0.03	0.34	0.36	0.48	0.54	0.25
LOI	1.32	2.23	1.20	4.55	4.01	1.78	5.84	2.59
Total	**100.33**	**100.77**	**101.67**	**100.89**	**101.82**	**101.73**	**100.91**	**100.55**
Mg#	59.33	59.09	46.00	31.80	45.39	54.30	55.10	55.43
NORM								
Quartz			34.3	4.0	3.8	1.7		8.2
Corundum			0.6					
Orthoclase	10.2	27.5	26.2	22.8	24.2	19.4	18.9	40.6
Albite	32.9	25.0	33.8	43.6	41.8	28.0	38.8	26.8
Anorthite	21.7	17.1	3.6	9.1	10.2	16.2	12.8	7.6
Nepheline								
Diopside	13.9	9.0		7.4	3.4	10.9	7.5	2.8
Hypersthene	13.8	12.1	1.5	4.9	9.8	10.5	5.4	8.7
Olivine	0.6	1.7					5.8	
Magnetite	1.8	1.6	0.2	1.2	1.3	1.5	1.6	0.9
Ilmenite	2.5	2.5	0.2	2.0	2.0	2.3	2.5	1.4
Apatite	1.0	1.3	0.1	0.8	0.8	1.0	1.3	0.6
XRF								
Ba	984	1466	518	1254	1425	873	1040	1695
Ce	96	155	67	176	144	119	134	131
Co	32	31	5	14	15	27	25	16
Cr	141	124	12	20	24	83	54	34
La	57	76	39	50	68		38	37
Nb	19	24	19	23	23	20	24	19
Nd	55	62	32	56	47	47	53	50
Ni	67	100	3	10	12	45	35	42
Pb	11	23	14	13	22	20	16	30
Rb	28	155	127	150	143	96	84	229
Sr	874	807	71	268	316	499	551	685
Th	9	23	18	11	15	9	8	18
Y	28	31	16	26	28	29	29	24
Zn	74	90	14	142	236	63	70	107
Zr	230	327	113	325	330	246	275	288
INAA								
Ce	96.2	134.4						125.5
Co	29.4	24.4						12.1
Cr	176	175						42
Cs	0.63	4.22						5.25
Eu	2.01	2.45						1.81
Hf	5.26	7.39						7.05
La	50.8	73.2						67.2
Lu	0.35	0.36						0.27
Nd	43.1	60.8						51.2
Sc	21.1	19.1						8.7
Sm	7.75	10.63						8.19
Ta	0.93	1.37						1.15
Tb	0.81	1.12						0.80
Th	5.79	14.04						13.25
U		2.80						2.90
Yb	2.09	2.35						1.75
ISOTOPES								
87Sr/86Sr	.708336±8	.70908±3						.709961±5
(87Sr/86Sr)i	.708310±8	.70904±3						.709686±5
206Pb/204Pb	18.375±7							
207Pb/204Pb	15.581±6							
208Pb/204Pb	38.779±15							

SAMPLE	SL-3	SL-4	SL-7	SL-8	SL-9	SL-10	NB-1	NB-2
REGION	SEARCH	SEARCH	SEARCH	SEARCH	SEARCH	SEARCH	(GRAN)	(GRAN)
SiO2	60.73	63.61	63.97	63.03	63.96	62.73	62.41	74.79
TiO2	0.85	0.77	0.76	0.74	0.74	0.73	0.72	0.19
Al2O3	15.87	15.64	16.67	16.70	16.62	16.78	18.77	13.73
Fe2O3	5.36	4.81	4.76	4.68	4.69	4.66	3.83	1.01
MnO	0.06	0.07	0.08	0.08	0.08	0.08	0.09	0.04
MgO	2.71	2.24	1.99	2.20	2.06	2.25	1.30	0.31
CaO	5.30	4.23	4.64	4.91	4.62	4.80	2.91	0.54
Na2O	3.97	4.01	4.35	4.33	4.50	4.00	5.90	4.38
K2O	3.57	4.09	3.23	3.00	3.04	3.19	4.44	5.07
P2O5	0.30	0.35	0.30	0.29	0.29	0.29	0.28	0.03
LOI	1.62	1.30	0.85	0.82	0.44	1.54	0.49	0.80
Total	**100.34**	**101.12**	**101.61**	**100.79**	**101.05**	**101.06**	**101.13**	**100.87**
Mg#	54.11	51.97	49.38	52.24	50.56	52.94	44.05	41.79
NORM								
Quartz	8.9	12.2	13.0	12.3	12.8	13.0	2.2	27.9
Corundum								0.1
Orthoclase	21.1	24.2	19.1	17.7	18.0	18.9	26.2	30.0
Albite	33.6	33.9	36.8	36.6	38.1	33.8	49.9	37.1
Anorthite	14.9	12.6	16.4	17.3	16.2	18.4	11.6	2.5
Nepheline								
Diopside	7.7	5.0	3.8	4.3	4.0	2.9	0.8	
Hypersthene	8.5	8.1	8.0	8.3	8.1	9.1	6.7	1.8
Olivine								
Magnetite	1.2	1.0	1.0	1.0	1.0	1.0	0.8	0.2
Ilmenite	1.6	1.5	1.4	1.4	1.4	1.4	1.4	0.4
Apatite	0.7	0.8	0.7	0.7	0.7	0.7	0.7	0.1
XRF								
Ba	1249	1507	1338	1308	1330	1232	1692	171
Ce	103	121	116	90	80	85	118	70
Co	21	22	16	13	18	15	4	4
Cr	41	41	33	20	27	28		17
La	47	46	53	68	40	26	41	39
Nb	13	15	14	11	12	13	19	33
Nd	38	45	40	39	45	32	38	24
Ni	41	44	24	17	22	22	2	5
Pb	22	22	24	23	22	23	23	51
Rb	81	90	74	64	68	69	61	167
Sr	849	917	992	1041	1007	1018	568	44
Th	15	17	8	12	12	10	9	20
Y	20	19	21	19	19	20	31	26
Zn	59	64	55	61	47	56	68	68
Zr	221	232	238	232	234	233	446	191
INAA								
Ce			88.5		89.4	85.8		104.2
Co			11.3		11.9	11.3		0.4
Cr			31		35	29		5
Cs			1.67		0.99	1.29		1.70
Eu			1.62		1.69	1.60		0.63
Hf			5.77		5.42	5.43		6.87
La			46.0		47.1	46.0		59.4
Lu			0.25		0.22	0.24		0.39
Nd			38.4		40.9	36.8		35.9
Sc			9.0		9.2	8.8		2.2
Sm			6.61		6.88	6.42		5.95
Ta			0.76		0.74	0.73		2.17
Tb			0.69		0.69	0.65		0.73
Th			9.07		8.97	8.73		22.22
U			2.60		1.90	2.00		2.50
Yb			1.60		1.57	1.50		2.49
ISOTOPES								
87Sr/86Sr			.708428±8		.708446±5	.708349±5		.714652±4
(87Sr/86Sr)i			.708367±8		.708391±5	.708293±5		.711510±4
206Pb/204Pb								
207Pb/204Pb								
208Pb/204Pb								

SAMPLE / *REGION*	NB-11 (GRAN)	NB-11A (GRAN)	NB-14 (GRAN)	NB-15 (GRAN)	G-2 GOFFS	NB-3 (DYKES)	NB-4 (DYKES)	NB-5 (DYKES)
SiO2	65.09	57.87	70.95	71.94		50.17	49.08	48.04
TiO2	0.63	1.31	0.35	0.28		1.66	1.24	1.30
Al2O3	16.09	17.43	14.32	14.26		17.07	16.90	17.23
Fe2O3	4.10	6.77	2.39	2.09		8.93	9.99	10.46
MnO	0.07	0.15	0.05	0.04		0.14	0.16	0.16
MgO	2.25	3.35	0.75	0.60		4.85	7.89	8.05
CaO	3.71	4.89	2.14	1.70		6.57	10.07	10.37
Na2O	4.18	4.92	3.49	3.64		4.85	3.68	3.52
K2O	3.70	3.22	4.48	4.50		2.87	0.61	0.44
P2O5	0.25	0.64	0.11	0.07		0.53	0.20	0.21
LOI	0.66	1.03	1.54	0.73		3.73	1.43	1.79
Total	**100.73**	**101.58**	**100.57**	**99.86**		**101.38**	**101.26**	**101.58**
Mg#	56.12	53.52	42.09	40.27		55.87	64.78	64.19
NORM								
Quartz	14.6	1.1	26.9	28.2				
Corundum			0.1	0.5				
Orthoclase	21.9	19.0	26.5	26.6		17.0	3.6	2.6
Albite	35.4	41.6	29.5	30.8		28.2	27.2	25.0
Anorthite	14.2	16.0	9.9	8.0		16.3	27.8	29.9
Nepheline						7.0	2.1	2.6
Diopside	2.1	3.4				10.5	16.9	16.4
Hypersthene	8.9	13.5	4.4	3.8				
Olivine						11.6	16.3	17.2
Magnetite	0.9	1.5	0.5	0.5		1.9	2.2	2.3
Ilmenite	1.2	2.5	0.7	0.5		3.2	2.4	2.5
Apatite	0.6	1.5	0.3	0.2		1.3	0.5	0.5
XRF								
Ba	1539	1376	1007	824	1428	806	319	382
Ce	95	103	36	81	562	84	47	58
Co	13	22	5	8	12	38	46	53
Cr	39	20	17	11	19	71	160	164
La	37	30	23	26	207	19	17	32
Nb	11	16	14	14	24	14	7	4
Nd	39	43	20	29	174	40	20	22
Ni	44	47	9	8	15	47	124	122
Pb	20	14	25	25	29	11	9	11
Rb	88	97	136	149	151	100	14	13
Sr	997	1125	288	255	298	975	399	458
Th	12	8	19	17	97	3	4	3
Y	18	18	22	22	40	22	26	30
Zn	59	89	37	30	84	75	70	67
Zr	185	268	184	182	512	186	131	125
INAA								
Ce	99.1		87.2					35.0
Co	11.3		4.0					41.7
Cr	48		13					192
Cs	0.76		0.75					
Eu	1.64		0.99					1.36
Hf	5.38		4.72					2.72
La	52.7		48.1					16.1
Lu	0.21		0.29					0.43
Nd	42.3		32.1					19.6
Sc	7.9		4.7					38.5
Sm	6.61		5.44					4.32
Ta	0.74		1.05					0.29
Tb	0.64		0.66					0.76
Th	10.01		14.84					1.89
U	1.60		1.90					
Yb	1.23		1.72					2.89
ISOTOPES								
87Sr/86Sr	.709983±5		.711642±7		.73916±1			.707111±6
(87Sr/86Sr)i	.709910±5		.711254±7		-			.707090±6
206Pb/204Pb							18.004±1	18.054±1
207Pb/204Pb							15.549±1	15.545±1
208Pb/204Pb							38.759±2	38.740±2

SAMPLE	NB-6	NB-7	NB-8	NB-9	NB-10	NB-12	NB-13	MC-2
REGION	(DYKES)	(DYKES)	(DYKES)	(DYKES)	(DYKES)	(DYKES)	(DYKES)	MEAD
SiO2	48.79	72.47	51.49	52.42	65.90	56.45	48.24	64.18
TiO2	1.27	0.26	1.28	1.63	0.78	1.10	1.41	0.87
Al2O3	17.19	14.20	16.65	16.54	15.39	16.17	16.94	15.94
Fe2O3	10.44	2.05	10.00	8.08	4.90	7.52	10.92	4.19
MnO	0.16	0.04	0.16	0.12	0.08	0.13	0.17	0.07
MgO	7.77	0.79	6.72	4.92	1.81	4.86	7.75	1.24
CaO	10.11	1.71	9.25	6.86	3.53	6.95	10.05	3.35
Na2O	3.16	3.43	3.55	4.20	4.08	3.45	3.02	3.19
K2O	0.73	4.73	0.99	2.54	3.32	2.15	0.61	6.43
P2O5	0.18	0.06	0.18	0.73	0.16	0.19	0.19	0.32
LOI	1.67	0.91	1.47	2.41	0.95	1.83	1.45	1.29
Total	101.47	100.65	101.75	100.45	100.90	100.80	100.74	101.08
Mg#	63.43	49.52	61.00	58.64	46.22	60.09	62.31	40.88
NORM								
Quartz		26.2			17.9	5.2		12.0
Corundum		0.8						
Orthoclase	4.3	24.1	5.9	15.0	19.6	12.7	3.6	38.0
Albite	26.7	26.0	30.0	35.5	34.5	29.2	25.6	27.0
Anorthite	30.6	6.9	26.6	18.8	13.9	22.3	30.9	10.2
Nepheline								
Diopside	15.0		14.8	8.6	2.2	8.9	14.5	3.6
Hypersthene	0.1	3.9	8.1	4.8	8.6	15.8	2.8	5.3
Olivine	17.1		9.1	8.1			15.6	
Magnetite	2.3	0.4	2.2	1.8	1.1	1.6	2.4	0.9
Ilmenite	2.4	0.4	2.4	3.1	1.5	2.1	2.7	1.7
Apatite	0.4	0.1	0.4	1.7	0.4	0.4	0.4	0.8
XRF								
Ba	392	983	754	1357	1026	600	380	1425
Ce	38	58	23	183	69	79		156
Co	52	9	41	27	17	33	46	10
Cr	162	18	146	66	25	101	156	4
La		13		79	38	19		60
Nb	4	12	5	24	11	11	5	25
Nd	15	28	11	68	31	21	17	59
Ni	121	8	84	71	9	76	126	9
Pb	7	30	10	15	19	15	6	23
Rb	21	136	27	44	68	57	20	174
Sr	365	263	348	1242	345	351	391	495
Th	1	15	4	9	13	5	5	22
Y	31	18	32	30	26	30	30	29
Zn	69	36	71	92	72	73	74	39
Zr	128	150	136	333	208	177	149	344
INAA								
Ce								
Co								
Cr								
Cs								
Eu								
Hf								
La								
Lu								
Nd								
Sc								
Sm								
Ta								
Tb								
Th								
U								
Yb								
ISOTOPES								
87Sr/86Sr								
(87Sr/86Sr)i								
206Pb/204Pb								
207Pb/204Pb								
208Pb/204Pb								

SAMPLE	MC-3	M-3	M-4	M-5	M-6	M-7	M-8	M-9
REGION	MEAD	MEAD	MEAD	MEAD	MEAD	MEAD	MEAD	MEAD
SiO2	65.65	53.82	52.03	68.55	50.92	47.78	55.26	67.92
TiO2	0.67	1.45	1.60	0.48	1.54	1.77	1.37	0.41
Al2O3	16.62	16.71	16.34	15.42	16.17	13.87	16.66	15.30
Fe2O3	3.16	8.26	8.61	2.76	8.87	9.99	6.57	2.76
MnO	0.05	0.13	0.07	0.01	0.16	0.14	0.12	0.06
MgO	0.80	4.33	3.45	1.10	6.22	8.82	3.43	1.19
CaO	2.39	7.44	5.92	2.27	9.54	8.14	7.41	2.85
Na2O	4.17	4.09	5.73	5.07	3.38	3.71	4.28	3.53
K2O	5.16	2.23	2.24	3.84	1.38	1.62	2.50	4.08
P2O5	0.17	0.86	0.90	0.21	0.55	0.76	0.47	0.16
LOI	0.64	0.79	2.42	0.71	0.67	2.61	1.37	2.73
Total	**99.49**	**100.11**	**99.31**	**100.42**	**99.40**	**99.23**	**99.44**	**100.99**
Mg#	37.04	54.98	48.29	48.05	62.02	67.27	54.84	50.24
NORM								
Quartz	14.4			17.6			1.4	23.0
Corundum	0.2							0.3
Orthoclase	30.5	13.2	13.2	22.7	8.2	9.6	14.8	24.1
Albite	35.3	34.6	41.3	42.9	28.6	26.8	36.2	29.9
Anorthite	10.7	20.6	12.2	8.0	24.8	16.4	18.9	13.1
Nepheline			3.9			2.5		
Diopside		8.8	9.3	1.6	15.4	15.4	12.2	
Hypersthene	5.0	14.8		4.7	8.7		9.0	5.9
Olivine		0.1	9.2		6.1	17.9		
Magnetite	0.7	1.8	1.9	0.6	1.9	2.2	1.4	0.6
Ilmenite	1.3	2.8	3.0	0.9	2.9	3.4	2.6	0.8
Apatite	0.4	2.0	2.1	0.5	1.3	1.8	1.1	0.4
XRF								
Ba	1501	1678	1736	1588	633	964	1159	1522
Ce	160	168	162	20	71	127	124	93
Co	11	30	35	10	37	45	22	10
Cr	8	17	25	117	170	275	77	6
La	73	67	75	30	36	77	67	52
Nb	29	38	25	17	16	29	27	18
Nd	59	53	64	10	31	58	39	35
Ni	7	25	23	16	82	220	58	7
Pb	32	8	13	12	12	13	20	31
Rb	145	45	59	64	31	46	56	103
Sr	544	1216	986	465	749	817	729	579
Th	28	16	12	13	10	5	14	20
Y	28	21	32	16	28	28	27	17
Zn	34	83	34	13	91	90	127	39
Zr	410	210	316	200	199	244	265	186
INAA								
Ce								
Co								
Cr								
Cs								
Eu								
Hf								
La								
Lu								
Nd								
Sc								
Sm								
Ta								
Tb								
Th								
U								
Yb								
ISOTOPES								
87Sr/86Sr		.708202±5			.70758±1			
(87Sr/86Sr)i		.708170±5			.70755±1			
206Pb/204Pb						18.068±3		
207Pb/204Pb						15.535±2		
208Pb/204Pb						38.428±6		

SAMPLE	M-10	M-11	BR-1	BR-2	BR-3	BR-6	BR-7	R-1
REGION	MEAD	MEAD	MEAD	MEAD	MEAD	MEAD	MEAD	MEAD
SiO2	55.68	55.41	57.45	48.94	55.47	58.09	46.14	51.37
TiO2	1.34	1.36	1.63	2.09	1.10	1.39	1.81	1.46
Al2O3	16.40	16.77	16.14	14.88	15.61	16.91	13.77	15.63
Fe2O3	6.91	7.23	7.25	11.37	8.46	8.46	8.77	8.32
MnO	0.11	0.09	0.11	0.16	0.09	0.02	0.12	0.11
MgO	3.72	4.18	2.80	6.05	4.45	2.67	1.88	4.24
CaO	7.25	7.83	5.63	9.35	7.23	1.44	10.28	8.43
Na2O	4.16	3.61	4.53	3.49	3.30	5.67	5.09	3.57
K2O	2.62	2.38	2.33	1.02	2.30	3.89	4.41	3.00
P2O5	0.48	0.52	0.54	0.47	0.34	0.51	0.63	1.04
LOI	1.73	1.83	1.98	2.45	1.18	2.19	8.61	1.80
Total	**100.40**	**101.21**	**100.39**	**100.27**	**99.53**	**101.26**	**101.50**	**98.98**
Mg#	55.64	57.39	47.39	55.36	55.05	42.38	33.29	54.28
NORM								
Quartz	1.7	3.3	6.0		4.9	0.7		
Corundum						2.0		
Orthoclase	15.5	14.1	13.8	6.0	13.6	23.0	26.1	17.7
Albite	35.2	30.5	38.3	29.6	27.9	48.0	4.9	30.2
Anorthite	18.3	22.5	16.8	21.9	21.0	3.8	1.7	17.8
Nepheline							20.7	
Diopside	11.9	10.6	6.3	17.5	10.4		26.0	14.2
Hypersthene	10.3	12.4	10.6	4.6	15.2	15.2		2.9
Olivine				9.7				6.7
Magnetite	1.5	1.6	1.6	2.5	1.8	1.8	1.9	1.8
Ilmenite	2.5	2.6	3.1	4.0	2.1	2.6	3.4	2.8
Apatite	1.1	1.2	1.3	1.1	0.8	1.2	1.5	2.4
XRF								
Ba	1198	1047	904	408	787	1508	1333	2309
Ce	130	114	100	39	59	110	120	299
Co	29	31	25	51	34	18	25	17
Cr	125	165	23	240	126	9	8	62
La	51	32	50	20	22	37	57	103
Nb	27	26	35	25	15	43	49	42
Nd	42	51	40	24	25	36	47	105
Ni	95	125	13	158	96	9	10	51
Pb	21	31	15	7	8	6	8	34
Rb	71	58	63	11	51	69	55	55
Sr	747	752	711	570	470	232	406	1606
Th	12	12	13	7	6	13	16	18
Y	28	28	27	25	24	24	29	34
Zn	124	147	154	101	76	69	84	175
Zr	256	254	329	165	162	357	337	332
INAA								
Ce				55.7				
Co				38.7				
Cr				288				
Cs								
Eu				1.78				
Hf				3.63				
La				27.3				
Lu				0.25				
Nd				27.2				
Sc				24.2				
Sm				5.72				
Ta				1.36				
Tb				0.76				
Th				3.48				
U				0.89				
Yb				1.70				
ISOTOPES								
87Sr/86Sr	.70745±2	.70749±4	.705482±8					.70727±2
(87Sr/86Sr)i	.70737±2	.70743±4	.705410±8					.70727±2
206Pb/204Pb		17.980±2	17.692±2	18.076±2				17.907±3
207Pb/204Pb		15.525±2	15.500±2	15.560±2				15.565±3
208Pb/204Pb		38.766±4	38.153±5	38.210±5				38.533±6

SAMPLE	R-2	MS-1	MS-2	MS-3	MS-4	MS-5	MS-6	MS-7A
REGION	MEAD	MOPAH	MOPAH	MOPAH	MOPAH	MOPAH	MOPAH	MOPAH
SiO2	49.29	53.81	52.70	60.33	60.33	68.11	69.80	68.40
TiO2	1.33	1.70	1.24	1.06	1.02	0.58	0.40	0.42
Al2O3	14.40	17.98	14.48	16.59	16.40	16.08	14.84	14.74
Fe2O3	8.58	7.36	7.39	5.62	5.07	3.03	2.48	2.55
MnO	0.18	0.10	0.08	0.06	0.08	0.03	0.04	0.05
MgO	4.61	2.95	5.04	2.12	3.23	0.66	0.58	0.95
CaO	9.15	6.57	7.61	5.18	5.31	2.38	2.80	2.39
Na2O	3.48	4.03	2.93	4.22	3.93	4.68	4.14	3.85
K2O	3.25	3.37	4.37	3.33	3.11	4.15	4.45	4.23
P2O5	1.12	0.81	0.76	0.38	0.34	0.17	0.15	0.15
LOI	2.44	2.33	2.59	1.39	1.37	0.75	1.30	2.59
Total	**97.83**	**101.01**	**99.21**	**100.29**	**100.17**	**100.60**	**101.01**	**100.32**
Mg#	55.58	48.23	61.39	46.82	59.74	33.50	35.35	46.58
NORM								
Quartz				8.8	9.5	18.1	22.0	22.5
Corundum								
Orthoclase	19.2	19.9	25.8	19.7	18.4	24.5	26.3	25.0
Albite	23.4	34.1	24.8	35.7	33.2	39.6	35.0	32.6
Anorthite	14.1	21.0	13.5	16.5	18.0	10.6	8.8	10.4
Nepheline	3.2							
Diopside	19.7	5.2	15.7	5.6	5.0	0.1	3.5	0.4
Hypersthene		9.8	5.1	8.1	10.6	4.6	2.3	4.8
Olivine	8.0	1.3	5.4					
Magnetite	1.9	1.6	1.6	1.2	1.1	0.7	0.5	0.6
Ilmenite	2.5	3.2	2.3	2.0	1.9	1.1	0.8	0.8
Apatite	2.6	1.9	1.8	0.9	0.8	0.4	0.4	0.3
XRF								
Ba	2968	1256	1826	1356	1383	1444	1212	1254
Ce	377	198	261	92	108	96	88	76
Co	25	20	32	22	23	4	9	4
Cr	26	40	225	55	50	7	14	7
La	162	78	117	42	21	18	39	36
Nb	45	29	17	17	15	17	13	12
Nd	136	80	114	47	39	36	27	29
Ni	47	68	135	63	63	5	8	7
Pb	72	26	31	24	22	26	27	25
Rb	56	57	84	77	79	101	114	104
Sr	1821	1283	1590	1034	1055	457	442	483
Th	14	15	23	8	9	17	14	14
Y	33	30	26	19	18	20	18	17
Zn	168	86	95	66	67	55	36	40
Zr	332	353	324	227	230	321	184	182
INAA								
Ce	290.2							
Co	29.0							
Cr	35							
Cs	4.40							
Eu	4.49							
Hf	7.87							
La	154.1							
Lu	0.39							
Nd	129.4							
Sc	19.0							
Sm	18.52							
Ta	1.85							
Tb	1.46							
Th	15.04							
U								
Yb	2.28							
ISOTOPES								
87Sr/86Sr	.708449±4			.708621±5	.708665±6			
(87Sr/86Sr)i	.708423±4			.708560±5	.708608±6			
206Pb/204Pb								
207Pb/204Pb								
208Pb/204Pb								

SAMPLE	MS-7B	S-1	S-2	S-3	S-4	S-5A	S-5B	S-5C
REGION	MOPAH	SAC	SAC	SAC	SAC	SAC	SAC	SAC
SiO2	67.78	50.25	51.27	55.35	61.05	64.12	64.53	62.99
TiO2	0.40	1.27	1.27	1.14	0.81	0.66	0.65	0.76
Al2O3	14.83	15.66	17.43	13.44	15.26	15.64	15.43	16.13
Fe2O3	2.54	7.76	7.16	6.30	5.03	3.81	3.71	4.36
MnO	0.05	0.10	0.11	0.09	0.07	0.06	0.06	0.10
MgO	0.97	5.12	3.55	6.16	3.62	2.00	1.77	2.15
CaO	2.45	6.40	5.66	6.13	4.35	3.56	3.42	4.01
Na2O	3.88	3.76	3.58	3.63	4.11	4.17	4.04	3.75
K2O	4.12	2.45	3.14	2.75	2.96	3.34	3.42	3.24
P2O5	0.16	0.61	0.40	0.73	0.28	0.22	0.23	0.27
LOI	3.25	6.95	6.90	3.89	2.76	2.48	2.68	2.85
Total	100.42	100.32	100.47	99.61	100.30	100.06	99.93	100.61
Mg#	47.13	60.60	53.58	69.49	62.58	55.03	52.57	53.49
NORM								
Quartz	22.0			3.4	10.7	15.8	17.2	15.8
Corundum								
Orthoclase	24.3	14.5	18.5	16.3	17.5	19.7	20.2	19.2
Albite	32.8	31.8	30.3	30.8	34.8	35.3	34.2	31.7
Anorthite	10.9	18.6	22.2	12.2	14.4	14.1	13.8	17.6
Nepheline								
Diopside	0.2	7.5	2.7	10.8	4.3	1.7	1.4	0.4
Hypersthene	5.0	8.7	13.0	16.5	12.1	8.0	7.5	9.7
Olivine		6.2	1.3					
Magnetite	0.6	1.7	1.6	1.4	1.1	0.8	0.8	0.9
Ilmenite	0.8	2.4	2.4	2.2	1.5	1.2	1.2	1.5
Apatite	0.4	1.4	0.9	1.7	0.7	0.5	0.5	0.6
XRF								
Ba	1278	1205	1360	1434	1292	1149	1166	1164
Ce	64	71	90	152	71	37	63	91
Co	8	36	31	28	19	13	11	12
Cr	9	273	110	273	138	36	43	35
La	64	58	30	61	63	26	49	31
Nb	12	13	10	26	10	14	11	12
Nd	25	40	32	63	39	23	31	34
Ni	6	80	26	172	108	30	29	31
Pb	25	16	69	14	21	28	28	52
Rb	99	39	65	42	57	72	78	71
Sr	482	1036	789	864	965	701	679	717
Th	16	10	5	8	8	11	12	10
Y	19	23	25	22	16	17	18	21
Zn	43	94	127	69	76	63	64	90
Zr	183	211	235	248	201	212	218	229
INAA								
Ce		123.0			80.0		85.3	82.2
Co		26.9			17.7		9.3	10.8
Cr		130			137		29	26
Cs		0.44			0.83		0.74	1.10
Eu		2.43			1.38		1.36	1.41
Hf		4.89			4.72		5.17	5.37
La		65.5			41.6		45.9	44.3
Lu		0.26			0.21		0.25	0.29
Nd		57.8			35.1		36.0	34.4
Sc		15.8			10.5		6.9	8.3
Sm		9.34			5.69		5.98	5.94
Ta		0.66			0.52		0.87	0.79
Tb		0.88			0.53		0.66	0.63
Th		8.13			6.47		10.28	8.98
U		1.70			1.22			2.20
Yb		1.59			1.11		1.53	1.58
ISOTOPES								
87Sr/86Sr				.708668±6	.70986±1		.71012±1	.71010±1
(87Sr/86Sr)i				.708630±6	.70982±1		.71003±1	.71003±1
206Pb/204Pb								
207Pb/204Pb								
208Pb/204Pb								

SAMPLE	S-5D	S-6	S-7	ST-1	ST-2	ST-3	K-1	K-2
REGION	SAC	SAC	SAC	SAC	SAC	SAC	KING	KING
SiO2	65.55	65.50	52.36	66.11	60.39	66.02	58.76	59.05
TiO2	0.57	0.60	1.21	0.68	0.88	0.68	1.12	1.03
Al2O3	15.27	15.93	16.67	16.58	14.18	15.03	14.57	14.33
Fe2O3	3.59	3.68	9.48	3.75	4.57	4.03	6.66	6.48
MnO	0.06	0.06	0.16	0.05	0.04	0.04	0.09	0.08
MgO	1.99	1.77	5.58	0.85	0.83	0.49	3.60	5.12
CaO	3.30	3.34	8.42	2.55	4.55	4.36	5.73	5.30
Na2O	3.56	4.42	3.59	4.64	3.47	3.78	4.01	4.00
K2O	3.33	3.25	2.41	4.46	2.67	3.79	3.19	2.98
P2O5	0.19	0.26	0.21	0.20	0.27	0.25	0.47	0.40
LOI	3.05	2.41	0.90	0.84	1.89	2.39	1.42	1.84
Total	**100.48**	**101.22**	**100.98**	**100.71**	**93.75**	**100.88**	**99.62**	**100.62**
Mg#	56.30	52.82	57.83	34.46	29.66	22.20	55.78	64.78
NORM								
Quartz	20.8	16.7		14.2	18.9	19.8	6.6	5.9
Corundum	0.3							
Orthoclase	19.7	19.2	14.2	26.4	15.8	22.4	18.9	17.6
Albite	30.1	37.4	30.4	39.3	29.4	32.0	33.9	33.8
Anorthite	15.1	14.0	22.3	11.2	15.2	12.8	12.3	12.3
Nepheline								
Diopside		0.7	14.9	0.1	4.7	6.1	10.7	9.2
Hypersthene	8.7	7.9	0.8	5.8	4.1	2.2	10.6	15.0
Olivine			11.8					
Magnetite	0.8	0.8	2.1	0.8	1.0	0.9	1.4	1.4
Ilmenite	1.1	1.1	2.3	1.3	1.7	1.3	2.1	2.0
Apatite	0.5	0.6	0.5	0.5	0.6	0.6	1.1	0.9
XRF								
Ba	1211	1251	653	1404	1289	1167	1390	1390
Ce	63	75	62	149	91	92	164	119
Co	14	12	35	9	17	13	35	33
Cr	66	52	142	11	15	21	244	383
La	30	28		78	31	24	65	48
Nb	9	12	9	35	19	16	19	14
Nd	29	32	26	57	49	32	63	46
Ni	38	25	91	6	12	15	250	349
Pb	42	25	9	29	20	23	22	21
Rb	68	69	64	132	65	78	67	55
Sr	618	825	487	576	855	853	1087	998
Th	9	10	5	20	8	8	9	9
Y	15	15	29	31	18	12	22	17
Zn	89	62	120	69	54	64	84	75
Zr	180	187	178	442	233	216	247	229
INAA								
Ce	62.8	95.6						
Co	9.5	8.5						
Cr	61	30						
Cs	0.51	0.30						
Eu	1.09	1.38						
Hf	4.58	4.99						
La	33.4	50.2						
Lu	0.20	0.21						
Nd	27.3	39.2						
Sc	7.5	6.9						
Sm	4.65	6.21						
Ta	0.55	0.75						
Tb	0.49	0.56						
Th	7.04	9.43						
U	1.50	2.04						
Yb	1.14	1.30						
ISOTOPES								
87Sr/86Sr		.710203±6					.70856±1	
(87Sr/86Sr)i		.710131±6					.70851±1	
206Pb/204Pb							18.281±3	18.198±3
207Pb/204Pb							15.580±2	15.574±2
208Pb/204Pb							38.915±5	38.894±6

			Colorado River Trough post-extensional group 3 (see Chapter 4)				
SAMPLE	**K-3**	**K-4**	**BM-1**	**BM-2**	**MH-9**	**MH-10**	**BW-3**
REGION	KING	KING	OAT	OAT	LHC	LHC	LHC
SiO2	59.32	59.36	51.14	75.96	53.70	53.54	53.59
TiO2	1.13	1.17	1.31	0.12	1.28	1.27	1.21
Al2O3	16.00	15.13	16.73	13.19	15.54	15.32	15.28
Fe2O3	6.34	6.89	9.62	0.74	8.42	8.36	10.85
MnO	0.08	0.06	0.15	0.03	0.12	0.13	0.16
MgO	3.75	4.08	6.80	0.26	6.61	6.44	6.11
CaO	5.61	5.58	10.00	0.55	8.63	8.33	8.06
Na2O	4.24	4.54	3.42	3.61	3.52	3.06	2.84
K2O	3.40	3.21	0.91	5.17	1.73	1.76	1.24
P2O5	0.44	0.47	0.22	0.03	0.39	0.38	0.25
LOI	0.65	2.06	0.56	0.66	1.17	0.75	0.05
Total	**100.97**	**102.56**	**100.87**	**100.32**	**101.11**	**99.33**	**99.63**
Mg#	57.94	57.97	62.20	45.18	64.63	64.24	56.72
NORM							
Quartz	4.6	3.6		33.3		2.0	4.0
Corundum				0.7			
Orthoclase	20.1	19.0	5.4	30.6	10.3	10.4	7.3
Albite	35.9	38.4	28.9	30.5	29.8	25.9	24.0
Anorthite	14.6	11.4	27.6	2.5	21.5	22.8	25.3
Nepheline							
Diopside	8.5	10.8	16.7		15.2	13.0	10.7
Hypersthene	11.6	11.9	6.4	1.5	15.6	18.6	22.1
Olivine			9.3		1.7		
Magnetite	1.4	1.5	2.1	0.2	1.8	1.8	2.4
Ilmenite	2.1	2.2	2.5	0.2	2.4	2.4	2.3
Apatite	1.0	1.1	0.5	0.1	0.9	0.9	0.6
XRF							
Ba	1363	1373	2853	206	693	680	1041
Ce	193	131	59	79	71	75	47
Co	24	21	42	1	38	40	45
Cr	65	234	157	15	216	213	173
La	73	65	24	31		30	
Nb	23	22	10	21	16	15	9
Nd	68	68	26	21	40	31	14
Ni	70	202	91	4	119	119	92
Pb	25	21	10	34	14	14	8
Rb	94	67	18	139	37	39	21
Sr	960	1041	552	50	603	602	369
Th	21	8	4	21	9	11	1
Y	26	21	30	13	25	25	24
Zn	77	74	68	24	76	70	84
Zr	334	247	167	110	205	204	127
INAA							
Ce		116.9	50.6			76.8	32.2
Co		20.3	36.7			34.0	40.0
Cr		208	218			266	229
Cs		1.30				0.56	0.20
Eu		2.43	1.50			1.85	1.25
Hf		5.97	3.87			4.61	3.05
La		63.3	23.3			37.8	17.0
Lu		0.26	0.44			0.37	0.29
Nd		57.4	23.3			35.7	16.2
Sc		7.2	34.0			25.4	23.0
Sm		9.90	5.22			6.66	3.67
Ta		1.18	0.62			0.97	0.52
Tb		0.85	0.77			0.92	0.63
Th		8.11	3.87			5.87	2.24
U		2.50	0.73				0.84
Yb		1.53	2.91			2.29	1.88
ISOTOPES							
87Sr/86Sr	.70957±1	.70859±1			.707960±3	.70766±2	.70714±1
(87Sr/86Sr)i	.70948±1	.70854±1			.707935±3	.70765±2	.70712±1
206Pb/204Pb		18.250±3	18.332±4		18.510±1	18.533±1	
207Pb/204Pb		15.558±2	15.606±3		15.586±1	15.618±1	
208Pb/204Pb		38.858±6	39.190±8		39.057±3	39.155±1	

SAMPLE	BW-4	D-1	D-2	D-3	G-1	K-6	K-7	SL-2
REGION	LHC	DEAD	DEAD	DEAD	GOFFS	KING	KING	SEARCH
SiO2	51.58	55.81	55.35	55.15	60.66	55.98	62.18	69.18
TiO2	1.25	1.13	1.12	1.15	0.90	1.21	1.13	0.32
Al2O3	15.23	15.92	15.75	16.17	17.51	15.49	16.74	15.19
Fe2O3	11.40	8.36	8.43	8.82	6.02	7.22	5.19	1.81
MnO	0.16	0.12	0.10	0.14	0.10	0.11	0.11	0.06
MgO	6.50	4.10	4.19	4.79	2.53	5.03	2.05	0.78
CaO	8.71	7.32	7.95	7.69	5.82	6.95	4.04	1.79
Na2O	3.14	3.04	3.60	3.34	4.09	3.55	4.58	4.43
K2O	0.93	2.02	2.09	1.92	2.85	3.14	4.24	5.43
P2O5	0.26	0.17	0.15	0.17	0.14	0.47	0.44	0.11
LOI	0.02	1.47	1.97	1.49	1.19	0.54	1.55	2.70
Total	**99.18**	**99.46**	**100.70**	**100.83**	**101.81**	**99.68**	**102.25**	**101.82**
Mg#	57.05	53.33	53.64	55.84	49.47	61.85	47.99	50.23
NORM								
Quartz		7.4	3.2	3.8	8.7	2.0	7.6	17.6
Corundum								
Orthoclase	5.5	11.9	12.4	11.3	16.8	18.6	25.1	32.1
Albite	26.6	25.7	30.5	28.3	34.6	30.0	38.8	37.5
Anorthite	24.7	23.8	20.6	23.5	21.0	17.1	12.6	5.5
Nepheline								
Diopside	13.8	9.4	14.7	11.2	5.8	11.7	3.8	2.2
Hypersthene	21.9	14.6	12.3	16.1	9.9	14.3	8.2	2.8
Olivine	0.3							
Magnetite	2.5	1.8	1.8	1.9	1.3	1.6	1.1	0.4
Ilmenite	2.4	2.1	2.1	2.2	1.7	2.3	2.1	0.6
Apatite	0.6	0.4	0.4	0.4	0.3	1.1	1.0	0.3
XRF								
Ba	1009	641	421	443	765	1390	1353	1854
Ce	57	42	61	47	82	148	168	105
Co	45	39	37	35	16	32	10	3
Cr	202	128	131	138	15	144	8	
La				15	33	69	65	54
Nb	8	9	9	9	14	17	25	21
Nd	16	27	21	12	32	54	60	47
Ni	105	94	100	101	1	102	5	4
Pb	10	14	15	14	21	18	23	28
Rb	11	52	51	49	69	58	93	126
Sr	335	399	345	366	590	949	726	261
Th	10	10	5	7	12	14	8	13
Y	22	31	28	30	22	25	32	25
Zn	86	69	64	67	59	73	62	47
Zr	121	154	150	152	185	310	355	335
INAA								
Ce	31.3			48.0				
Co	45.6			31.4				
Cr	475			166				
Cs				0.51				
Eu	1.25			1.24				
Hf	2.91			3.68				
La	15.3			22.2				
Lu	0.32			0.38				
Nd	16.1			23.1				
Sc	25.0			22.8				
Sm	3.80			5.04				
Ta	0.52			0.63				
Tb	0.70			0.83				
Th	1.81			5.00				
U	0.46			1.01				
Yb	2.15			2.65				
ISOTOPES								
87Sr/86Sr	.706595±5	.70753±1		.707324±8	.706487±5	.70881±1	.70888±1	
(87Sr/86Sr)i	.706587±5	.70747±1		.707269±8	.706394±5	.70879±1	.70883±1	
206Pb/204Pb	17.233±7			17.413±2		18.258±2		
207Pb/204Pb	15.471±6			15.487±2		15.554±2		
208Pb/204Pb	37.351±16			38.120±4		38.831±5		

SAMPLE	SL-5	SL-6	SA-1	MS-8	R-3A	R-3B	BR-4	BR-5
REGION	SEARCH	SEARCH	SAC	MOPAH	MEAD	MEAD	MEAD	MEAD
SiO2	56.05	55.94	71.59	58.51	73.23	75.43	56.47	58.30
TiO2	1.32	1.75	0.26	0.95	0.22	0.23	1.14	1.00
Al2O3	15.92	16.49	13.81	16.52	13.33	13.06	16.24	15.45
Fe2O3	7.00	7.96	1.84	6.23	1.28	1.32	8.32	7.54
MnO	0.09	0.10	0.03	0.09	0.04	0.05	0.13	0.12
MgO	3.44	2.18	0.61	3.68	0.31	0.25	4.30	3.75
CaO	6.75	6.34	1.16	6.41	0.50	0.91	7.18	6.10
Na2O	3.57	4.53	1.97	3.62	2.56	3.82	3.55	3.88
K2O	3.62	3.26	7.73	2.68	7.96	5.45	2.56	2.54
P2O5	0.66	0.70	0.09	0.28	0.06	0.09	0.38	0.33
LOI	1.06	1.50	1.80	0.78	0.85	0.41	0.90	0.73
Total	**99.50**	**100.76**	**100.89**	**99.74**	**100.33**	**101.04**	**101.19**	**99.75**
Mg#	53.39	38.91	43.39	57.92	36.19	30.99	54.63	53.68
NORM								
Quartz	3.2	1.4	26.5	7.7	26.1	29.9	3.8	6.9
Corundum			0.3					
Orthoclase	21.4	19.3	45.7	15.8	47.0	32.2	15.1	15.0
Albite	30.2	38.3	16.6	30.7	21.6	32.4	30.1	32.8
Anorthite	16.7	15.0	5.2	20.9	1.4	2.4	20.8	17.2
Nepheline								
Diopside	10.2	9.9		7.4	0.6	1.3	10.1	8.9
Hypersthene	10.5	8.0	3.5	12.1	1.8	1.4	14.7	13.2
Olivine								
Magnetite	1.5	1.7	0.4	1.4	0.3	0.3	1.8	1.6
Ilmenite	2.5	3.3	0.5	1.8	0.4	0.4	2.2	1.9
Apatite	1.6	1.7	0.2	0.7	0.1	0.2	0.9	0.8
XRF								
Ba	1841	1376	1422	954	669	691	885	980
Ce	208	139	87	76	84	89	94	51
Co	30	25	6	27	6	3	28	28
Cr	19	15	14	31	11	10	71	72
La	82	60	39	29	46	27	39	31
Nb	22	30	16	9	22	24	21	16
Nd	71	63	34	36	25	23	44	35
Ni	28	19	3	29	2	1	43	47
Pb	23	18	15	16	29	40	13	13
Rb	67	71	206	49	181	145	41	52
Sr	1280	874	122	665	120	170	665	419
Th	21	11	20	10	25	25	5	8
Y	27	30	27	21	17	18	29	25
Zn	72	85	19	63	23	22	72	69
Zr	300	309	149	217	149	154	185	177
INAA								
Ce	166.0							
Co	22.6							
Cr	25							
Cs	0.79							
Eu	2.36							
Hf	6.99							
La	79.8							
Lu	0.31							
Nd	69.9							
Sc	14.2							
Sm	10.60							
Ta	1.26							
Tb	0.93							
Th	12.20							
U	2.07							
Yb	1.93							
ISOTOPES								
87Sr/86Sr		.709231±6	.71302±1					
(87Sr/86Sr)i		.709197±6	.71163±1					
206Pb/204Pb		18.185±3					17.284±1	
207Pb/204Pb		15.548±2					15.482±1	
208Pb/204Pb		38.906±6					37.931±3	

Post-extensional group 1 (see Chapter 4)

SAMPLE	BW-1	BW-2	BW-6	BW-7	K-5	M-1	M-2 AMPHIBOLE
REGION	PARKER	PARKER	PARKER	PARKER	KING	MEAD	MEAD (M2)
SiO2	48.19	63.56	48.30	64.16	50.06	45.87	44.55
TiO2	2.92	0.38	2.99	0.40	1.56	1.81	2.56
Al2O3	16.38	15.56	16.56	15.88	15.49	15.33	15.19
Fe2O3	11.82	6.23	12.07	6.34	11.40	12.09	9.15
MnO	0.19	0.23	0.19	0.23	0.16	0.18	0.15
MgO	4.07		4.06	0.38	6.53	8.40	4.11
CaO	7.56	1.94	7.59	1.72	9.29	10.93	8.25
Na2O	4.03	6.28	3.97	6.02	3.35	3.11	4.31
K2O	2.22	5.44	2.15	5.48	1.15	0.91	2.72
P2O5	0.80	0.13	0.75	0.09	0.32	0.52	0.72
LOI	1.68	0.07	1.89	0.05	0.35	0.59	8.33
Total	**99.84**	**99.82**	**100.55**	**100.76**	**99.68**	**99.75**	**100.03**
Mg#	44.47		43.95	12.38	57.15	61.82	51.11
NORM							
Quartz		1.3		2.3			
Corundum							
Orthoclase	13.1	32.2	12.7	32.4	6.8	5.3	16.1
Albite	30.1	49.7	30.5	50.9	28.3	17.5	16.8
Anorthite	20.1		21.0	0.1	23.8	25.2	14.1
Nepheline	2.1		1.7			4.8	10.7
Diopside	10.1	7.8	9.7	6.9	16.5	20.9	18.2
Hypersthene		4.4		5.2	6.2		
Olivine	11.6		11.9		10.4	17.2	6.7
Magnetite	2.6		2.6	1.4	2.5	2.6	2.0
Ilmenite	5.5	0.7	5.7	0.8	3.0	3.4	4.9
Apatite	1.9	0.3	1.8	0.2	0.8	1.2	1.7
XRF							
Ba	484	164	456	267	540	417	621
Ce	148	173	148	214	69	68	115
Co	33	6	37	4	45	52	26
Cr	30	15	16	13	223	287	62
La	37	59	49	73	16		50
Nb	60	86	59	89	20	30	78
Nd	61	54	57	60	25	31	43
Ni	10	3	1	4	100	136	62
Pb	3	14	8	13	2	6	7
Rb	36	93	36	95	17	11	49
Sr	729	16	749	24	436	495	1112
Th	8	13	5	14	5	4	12
Y	34	50	37	52	23	26	27
Zn	105	103	99	109	86	79	63
Zr	329	867	329	874	144	150	287
INAA							
Ce	100.5		90.9	137.0	46.5	54.2	26.2
Co	28.0		27.9	0.3	41.9	45.0	40.8
Cr	9		5	5	262	327	905
Cs	0.36		0.30	0.65			
Eu	3.08		2.91	1.74	1.46	1.57	1.82
Hf	7.49		7.46	16.90	3.29	3.35	2.42
La	37.0		46.6	69.9	22.5	25.6	11.0
Lu	0.40		0.40	0.78	0.32	0.31	0.24
Nd	57.2		46.7	61.4	22.7	27.0	21.3
Sc	13.8		15.6	13.1	26.1	32.9	43.2
Sm			9.48	11.90	4.85	5.19	5.47
Ta	4.02		3.63	4.88	1.14	1.63	1.59
Tb	1.29		1.18	1.55	0.72	0.76	0.89
Th	5.11		4.72	9.64	2.56	3.51	0.79
U			1.23	2.09		1.49	
Yb	2.50		2.44	4.70	2.09	2.18	1.57
ISOTOPES							
87Sr/86Sr	.70477±1		.70477±1		.705710±5	.70487±2	
(87Sr/86Sr)i	.70475±1		.70475±1		.705694±5	.70486±2	
206Pb/204Pb			18.969±1			18.589±3	
207Pb/204Pb			15.565±1			15.579±2	
208Pb/204Pb			38.850±3			38.634±6	

Electron Microprobe analyses of clinopyroxene

SAMPLE	E-5 CORE	E-6 RIM (a)	E-6 CORE (a)	E-6 RIM (b)	E-6 CORE (b)	E-10 RIM (a)	E-10 CORE (a)	E-10 RIM (b)
SiO2	51.83	51.89	51.05	52.18	51.87	51.10	51.23	51.66
TiO2	1.29	1.11	1.27	1.16	0.79	1.12	1.16	2.94
Al2O3	3.16	2.49	2.78	2.67	2.92	2.84	2.79	1.16
FeO	7.68	7.77	7.86	7.90	6.92	8.94	8.64	9.00
MnO	0.20	0.24	0.24	0.25	0.17	0.27	0.25	0.28
MgO	15.01	15.25	15.01	14.95	15.75	15.37	15.16	15.28
CaO	20.22	20.27	20.52	19.96	20.63	19.29	19.42	19.17
Na2O	0.54	0.41	0.46	0.47	0.39	0.53	0.53	0.54
K2O								
Cr	0.02		0.02	0.02	0.14	0.02	0.03	0.03
Ni				0.01	0.01	0.01		
Total	99.95	99.43	99.21	99.57	99.59	99.49	99.21	100.06

SAMPLE	E-10 RIM (c)	E-10 RIM (d)	E-7 RIM (a)	E-7 CORE (a)	E-7 RIM (b)	E-7 CORE (b)	E-7 RIM (c)	E-7 RIM (d)
SiO2	51.31	51.30	51.05	51.24	50.79	50.90	51.23	50.79
TiO2	1.18	1.14	1.14	1.16	1.12	0.99	1.16	1.14
Al2O3	2.94	2.87	2.92	2.84	2.83	2.78	2.79	2.89
FeO	9.02	8.76	9.01	8.65	9.13	8.68	8.64	8.95
MnO	0.25	0.28	0.27	0.25	0.27	0.25	0.25	0.27
MgO	15.19	15.20	15.20	15.20	15.35	15.34	15.16	15.38
CaO	19.12	18.93	19.18	19.87	18.96	19.24	19.42	19.33
Na2O	0.53	0.51	0.51	0.51	0.50	0.51	0.53	0.51
K2O								
Cr	0.02	0.02	0.02	0.03	0.02	0.21	0.03	0.03
Ni	0.03	0.01	0.01	0.01	0.01			0.01
Total	99.59	99.02	99.31	99.76	98.98	98.90	99.21	99.30

Clinopyroxene classification diagram from Deer et al (1977).

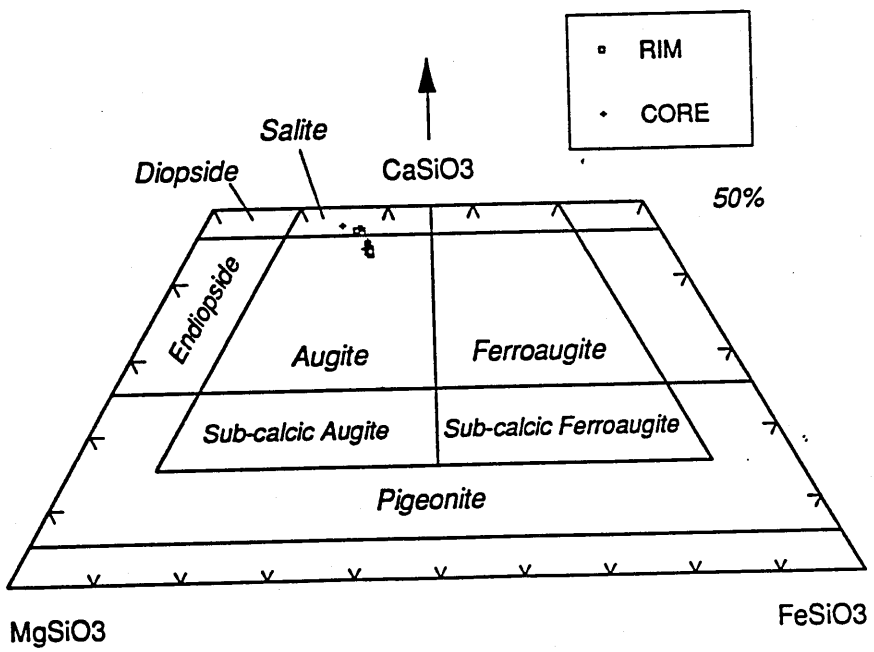

Sample Localities and Thin Section Descriptions

This section provides more general information about the samples collected, including breif descriptions and a precise location in terms of latitude (°N) and longitude (given as negative values because all samples were collected from west of the Greenwich Meridian). Samples are presented in the same order as Appendix A. Useful topographic maps are also listed.

B.1 Yerrington (West central Nevada)

See Nevada Bureau of Mines and Geology Map 77 (Proffett and Dilles 1984) for detail of localities. Samples indicated as YR were collected by Phil Gans.

Y-1 Longitude: -119.26139°. Latitude: 39.05013°N. *Classification: Trachy andesite.* Phenocrysts= hornblende 15%, plag 5-10%.

Y-2 Longitude: -119.26069°. Latitude: 39.05056°N. *Classification: Basaltic andesite.* Olivine phyric 15-20%. Some polycrystalline quartz with reaction rims of cpx.

Y-3A Longitude: -119.25944°. Latitude: 39.05425°N. *Classification: Trachy andesite.* Plag dominated K-alteration. Phenocrysts= plag 10%, biotite + hornblende 5%.

Y-5 Longitude: -119.2417°. Latitude: 39.03125°N. *Classification: Andesite.* Plag and Cpx phyric. Some large patches of opaques.

Y-6 Longitude: -119.01361°. Latitude: 39.0293°N. *Classification: Andesite.* Cpx and plagioclase phyric.

Y-7 Longitude: -119.32833°. Latitude: 39.01172°N. *Classification: Basaltic andesite.* Olivine phyric 30% (highly altered phenocrysts).

Y-8 Longitude: -119.33306°. Latitude: 39.00673°N. *Classification: Basaltic andesite.* Olivine phyric 15-20% plus cpx microphenocrysts.

Y-9 Longitude: -119.33014°. Latitude: 39.00977°N. *Classification: Trachy andesite.* See Chapter 2. Phenocrysts= plag 35%, biotite 5%.

Y-10 Longitude: -119.31222°. Latitude: 39.06836°N. *Classification: Rhyolite.* Biotite and plag phyric. Pervasive alteration.

Y-11 Longitude: -119.2925°. Latitude: 39.05013°N. *Classification: Basaltic andesite.* Phenocrysts= plag 30% (large rectangular with complex zoning), hornblende 5%.

Y-12 Longitude: -119.28556°. Latitude: 39.06288°N. *Classification: Rhyolite.* Vitric G.mass. Phenocrysts= plag- Qz- sanidine 30% (all ≥2mm), biotite 5%.

Y-13 Longitude: -119.28361°. Latitude: 39.06228°N. *Classification: Rhyolite.* Phenocrysts= sanidine and Qz 20%, minor biotite.

Y-14 Longitude: -119.27417°. Latitude: 39.08746°N. *Classification: Trachy andesite.* G.mass dominated by equant plag. Phenocrysts= plag few%, hornblende <5%.

Y-15 Longitude: -119.27583°. Latitude: 39.0855°N. *Classification: Rhyolite*..As Y-13 but with some lithic fragments.

Y-16A Longitude: -119.25958°. Latitude: 39.08735°N. *Classification: Trachy andesite.* Plag and hornblende phyric.

Y-16B Longitude: -119.25958°. Latitude: 39.08735°N. *Classification: Trachy andesite.* Plag and hornblende phyric.

YR-1 Longitude: -119.22°. Latitude: 38.94°N. *Classification: Basaltic andesite.* Cpx phyric (euhedral, some with complex zoning and multiple sector twinning).

YR-2 Longitude: -119.22139°. Latitude: 38.93902°N. *Classification: Basaltic andesite.* Plag, Cpx, Opx phyric.

YR-6 Longitude: -119.25556°. Latitude: 38.98633°N. *Classification: Trachy andesite.* Phenocrysts= Biotite 10%.

YR-7 Longitude: -119.32792°. Latitude: 39.00217°N. *Classification: Trachy andesite.* Phenocrysts= plag 45%, biotite 10%.

YR-11B Longitude: -119.3685°. Latitude: 39.0383°N. *Classification: Dacite.* Phenocrysts= plag 30%, hornblende 5%.

YR-14 Longitude: -118.9422°. Latitude: 38.9685°N. *Classification: Basaltic andesite.* Equant plagioclase dominated G.mass. Phenocrysts= amphibole <5%.

B.2 Caliente Caldera (Southeastern Nevada)

All localities on Caliente quadrangle 1:100 000 topographic sheet (Nevada-Utah).

LN-23 Longitude: -115.0199°. Latitude: 37.1923°N. *Classification: Alkali basalt.* Granular G.mass of Cpx and micro plag laths (50:50) + opaques. Phenocrysts= plagioclase 20% (laths) and olivine 15% (euhedral altered to iddingsite)

CC-1 Longitude: -115.0185°. Latitude: 37.8982°N. *Classification: Andesite.* Flow textured, partially devitrified G.mass. Phenocrysts= hornblende 10% (altered euhedral) and Opx (euhedral fresh).

CC-3 Longitude: -115.0185°. Latitude: 37.8982°N. *Classification: Trachyte.* Vitrophyre.

CC-4 Longitude: -115.0213°. Latitude: 37.8529°N. *Classification: Rhyolite.* Crystal rich vitrophyre ("Petroglyph Ignimbrite").

CC-5 Longitude: -115.0213°. Latitude: 37.8529°N. *Classification: Rhyolite.* Crystal rich vitrophyre ("Monotony Tuff Lower").

CC-6 Longitude: -115.0355°. Latitude: 37.8382°N. *Classification: Rhyolite.* Vitrophyre ("Monotony Tuff Upper").

CC-7 Longitude: -114.3141°. Latitude: 37.6169°N. *Classification: Trachy andesite.* Intrusive pod. Vitric G.mass. Phenocrysts= plag 40% (equant to rectangular up to 1.5mm, some rounded with complex zoning and twinning), hornblende 10% (badly altered) + quartz (equant, rounded and embayed, no reaction rims).

CC-8 Longitude: -114.4972°. Latitude: 37.6556°N. *Classification: Trachy andesite.* G.mass= plag and Cpx. Phenocrysts= plagioclase 30% (large rectangular complex zoning and fine twinning), and Cpx + Opx 5-10% (rounded/ subhedral or as glomerocrysts with plag and Ksp).

CC-9 Longitude: -114.5°. Latitude: 37.6555°N. *Classification: Trachy andesite.* Crystal rich vitrophyre (Phenocrysts= biotite and plag).

CC-10 Longitude: -114.7098°. Latitude: 37.6075°N. *Classification: Rhyolite.* (Quartz biotite tuff).

B.3 Colorado River Trough

Useful topographic maps at 1:100 000 scale- Lake Mead (Az), Boulder City (Nv-Az), Mesquite Lake (Ca-Nv), Davis Dam (Az-Nv-Ca), Needles (Ca-Az), Ivanpah (Ca-Az), Parker (Az-Ca), Amboy (Ca), Blythe (Ca-Az). 1:250 000 scale- Kingman (sheet NI 11-3), Williams (sheet NI 12-1).

B.3.1 Eldorado Mts.

E-1 Longitude: -114.8905°. Latitude: 35.7491°N. *Classification: Trachy andesite.* Very altered. G.mass= fine crystalline plag (some large patches of calcite). Phenocrysts= hornblende 5-10% (altered) + some large equant to rectangular plag.

E-2 Longitude: -114.8866°. Latitude: 35.7491°N. *Classification: Trachy andesite.* G.mass= microcrystalline plag laths + Cpx and opaques (square-granular), some alteration and minor calcite. Phenocrysts= augite 5%, olivine <2% (euhedral altered, mostly to iddingsite), few hornblende and plag.

E-3 Longitude: -114.8905°. Latitude: 35.7491°N. *Classification: Trachy andesite.* G.mass= microcrystalline, altered plus calcite). Phenocrysts= hornblende 15% (euhedral, abundant microphenocrysts), plag 20%, Ksp 10%, few Cpx.

E-4 Longitude: -114.8335°. Latitude: 35.7274°N. *Classification: Rhyolite.* Vitrophyre. Intensely flow banded, holohyaline.

E-5 Longitude: -114.8319°. Latitude: 35.7278°N. *Classification: Alkali basalt.* G.mass= dominated by microcrsytalline plag laths, + minor pyroxene and olivine. Phenocrysts= plag 20% (altered), Cpx 10% (euhedral, some with distinct cores containing high relief inclusions overgrown by inclusion-free rims), plus some Opx and olivine.

E-6 Longitude: -114.828°. Latitude: 35.7301°N. *Classification: Trachy andesite.* Reasonably fresh! G.mass= crystalline, coarser than E-5: plag laths + minor Cpx. Phenocrysts= plag 20%, Cpx 10% (some with cores). Few larger plag crystals appear to be strained.

E-7 Longitude: -114.818°. Latitude: 35.7369°N. *Classification: Trachy andesite.* G.mass= dominated by micro plag laths and intergranular Cpx. Phenocrysts= plag 25%, augite 10%, plus small % of olivine (iddingsitised), Opx, and sanidine (?).

E-8 Longitude: -114.8186°. Latitude: 35.7369°N. *Classification: Trachyte.* G.mass= devtrified and altered. Abundant microphenocrysts and phenocrysts of plag. V.few biotite crystals. Some polycrystalline rock fragments (fiamme).

E-9 Longitude: -114.8252°. Latitude: 35.7373°N. *Classification: Rhyolite.* Rather altered: G.mass= dominated by micro plag laths but 20-30% secondary minerals. Phenocrysts= plag 30% (some as glomerocrysts), v.rare Opx.

E-10A Longitude: -114.8252°. Latitude: 35.731°N. *Classification: Trachy andesite.* Vesicular (abundant zeolite) and highly altered. G.mass= bulk of rock. Phenocrysts= plag 10% (subhedral, often ragged), Cpx 10% (in clusters).

E-10B Longitude: -114.8252°. Latitude: 35.731°N. *Classification: Trachy andesite.* As E-10A but rather less alteration. Fresh Cpx phenocrysts (some are large up to 4mm with oxide and apatite inclusions), some sanidine and relict olivine (euhedral <2%, now as iddingsite).

E-11 Longitude: -114.823°. Latitude: 35.737°N. *Classification: Trachy andesite.*

E-12 Longitude: -114.823°. Latitude: 35.737°N. *Classification: Trachy andesite.*

E-13 Longitude: -114.8833°. Latitude: 35.809°N. *Classification: Trachy andesite.* G.mass= partially devitrified. Phenocrysts= plag 15%, hornblende 5% (altered), Cpx <5%. Cpx and plag often as glomerocrysts. Some large partially resorbed and ragged plag crystals with complex zoning.

B.3.2 Black Mts. (Oatman)

BM-3 Longitude: -114.4123°. Latitude: 34.959°N. *Classification: Trachy andesite.* Vitrophyre.

BM-4 Longitude: -114.4118°. Latitude: 34.959°N. *Classification: Trachy andesite.* Intense flow texture, devitrified G.mass. Phenocrysts= Cpx + Opx (few %, some secondary hornblende). Some poly crystalline quartz material.

BM-5 Longitude: -114.411°. Latitude: 34.9595°N. *Classification: Andesite.*

BM-6 Longitude: -114.411°. Latitude: 34.96°N. *Classification: Trachy andesite.* G.mass= plag and Cpx + opaques. Phenocrysts= plag 40% (equant), Cpx 10% (subhedral-euhedral often as glomerocrysts with plag), plus few % hornblende and relict olivine. Large plag xenocryst (altered) with clear overgrowth rim.

BM-7 Longitude: -114.4099°. Latitude: 34.9608°N. *Classification: Dacite.* Plag phyric.

BM-8 Longitude: -114.4098°. Latitude: 34.961°N. *Classification: Dacite.* Plag phyric.

BM-9 Longitude: -114.4095°. Latitude: 34.9613°N. *Classification: Trachy andesite.* G.mass= partially devitrified (plag + amphibole and opaques). Phenocrysts= plag 15% (large, complex zoning and twinning, often rounded some Ksp content) and hornblende 5% (sub-euhedral altered).

BM-10 Longitude: -114.4106°. Latitude: 34.964°N. *Classification: Trachy andesite.* G.mass= devitrified; equant to rectangular plag microphenocrysts + Cpx and opaques. Phenocrysts= plag 15% (bulk >2mm, some sieve textured). Largest plag phenocrysts as glomerocrysts with interstitial Cpx. Few quartz fragments.

BM-11 Longitude: -114.4095°. Latitude: 34.9658°N. *Classification: Trachy andesite.*

BM-12 Longitude: -114.4063°. Latitude: 34.9649°N. *Classification: Trachy andesite.* Plag phyric (altered phenocrysts).

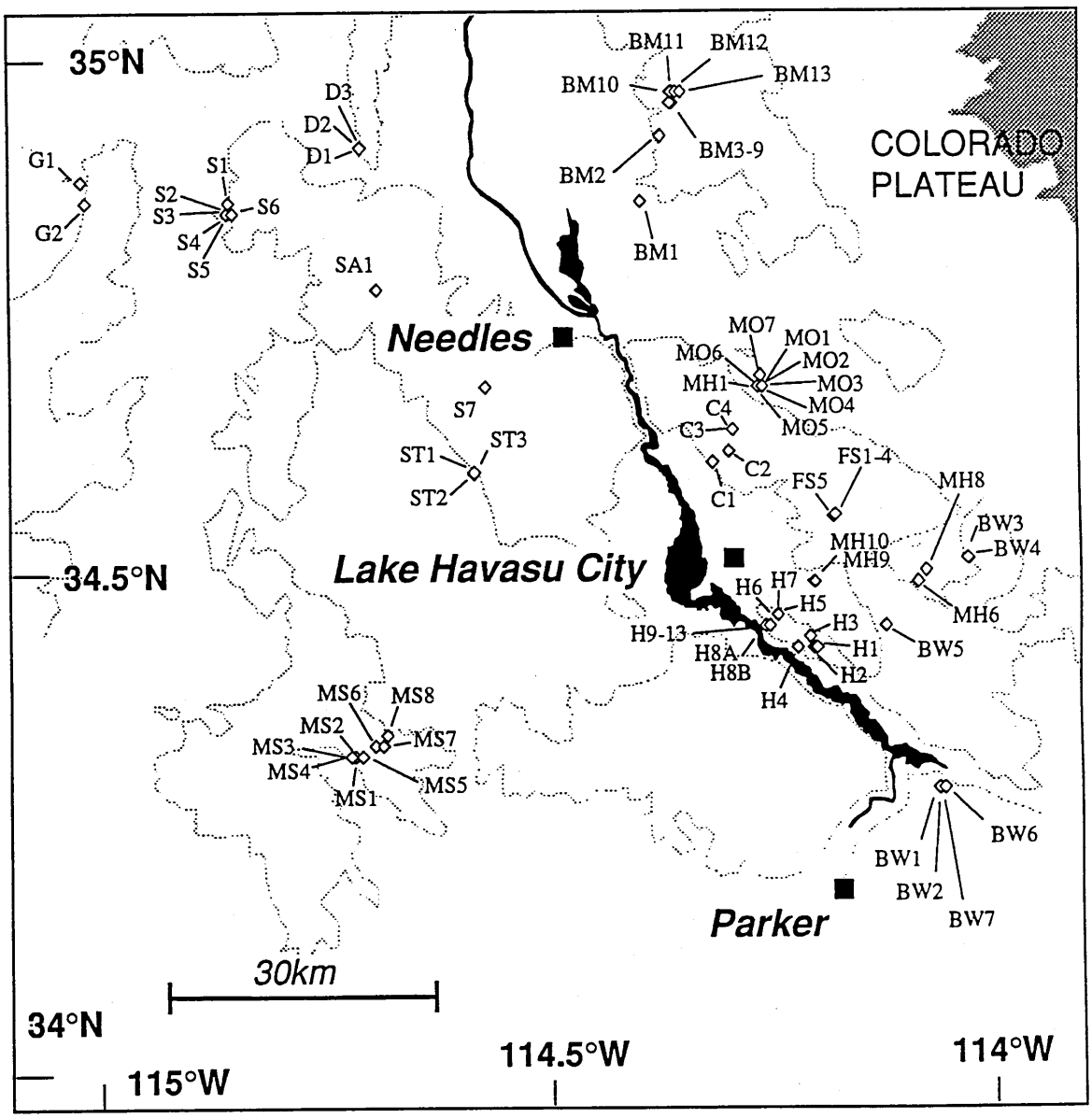

Location map for samples in the vicinity of Lake Havasu City

BM-13 Longitude: -114.4046°. Latitude: 34.9653°N. *Classification: Rhyolite.* Aphyric.

B.3.2.1 Black Mts. (Union Pass)

BM-14 Longitude: -114.4119°. Latitude: 35.2117°N. *Classification: Trachy andesite.*

BM-15 Longitude: -114.413°. Latitude: 35.2135°N. *Classification: Rhyolite.*

BM-16 Longitude: -114.4152°. Latitude: 35.2095°N. *Classification: Trachyte.*

B.3.3 Lake Havasu City region

See location map for detail: H= Aubrey Hills; C= Chemehuevi Mts; MO= Mohave Mts (MH= collected by Phil Gans); BW= Bill Williams Mts; FS= Falls Spring Wash.

H-1 Longitude: -114.2504°. Latitude: 34.4248°N. *Classification: Alkali basalt.* G.mass= 50:50 finely crystalline plag laths and granular Cpx + opaques. Intergranular texture. Phenocrysts= few % Cpx (euhedral zoned and twinned), few fresh olivine (rounded), and Opx + plag (angular).

H-2 Longitude: -114.2543°. Latitude: 34.4253°N. *Classification: Basalt.* G.mass= as H1 but slightly coarser and more opaques. Phenocrysts= olivine 5-10%.

H-3 Longitude: -114.2581°. Latitude: 34.4266°N. *Classification: Dacite.* Intensely flow textured holohyaline G.mass (dark). Phenocrysts= plag 15% (equant to rectangular, or laths [up to 4mm] with complex twinning and zoning, some rounded or have rounded cores), biotite 5-8%.

H-4 Longitude: -114.2728°. Latitude: 34.4235°N. *Classification: Dacite.* Clear holohyaline G.mass. As H3 but rather more euhedral and rectangular plag with distinct cores. Phenocrysts= plag 15%, biotite 10%, hornblende <5%.

H-5 Longitude: -114.2945°. Latitude: 34.4511°N. *Classification: Basalt/ alkali basalt.* Coarse crystalline. Sub-ophitic texture dominated by slightly pleochroic (pinkish) Cpx and plag laths.Some intergranular olivines (typically in patches), opaques as wedges along crystal boundaries, some chloritic alteration of G.mass. Phenocrysts= olivine few % (fresh).

H-6 Longitude: -114.3021°. Latitude: 34.4457°N. *Classification: Basalt.* See figure in Chapter 2. As above but rather more ol phenocrysts (<5%). Less alteration.

H-7 Longitude: -114.3021°. Latitude: 34.4457°N. *Classification: Basalt/ alkali basalt.* As H-5 and H-6 but more altered and some vesicles filled with chloritic material.

H-8A Longitude: -114.3075°. Latitude: 34.4443°N. *Classification: Proterozoic Schist* Intense parallel fabric. Granular quartz and larger areas of Ksp.

H-8B Longitude: -114.3075°. Latitude: 34.4443°N. *Classification: Alkali basaltic (intrusive) Cretaceous?.* Coarsely crystalline G.mass= plag and hornblende (≥2mm), with some coarse interstitial sphene (2mm) and euhedral apatite. Total % of rock: plag 20%, hornblende (some >20mm) 75%, sphene and opaques 5%.

H-9 Longitude: -114.3059°. Latitude: 34.4447°N. *Classification: Basalt.* As H-5 but slightly vesicular and some analcime in G.mass.

H-10 Longitude: -114.3055°. Latitude: 34.4448°N. *Classification: Alkali basalt.* As H5.

H-11 Longitude: -114.304°. Latitude: 34.4457°N. *Classification: Alkali basalt.* As H5.

H-12 Longitude: -114.3038°. Latitude: 34.4458°N. *Classification: Basalt/ alkali basalt.* As H5. But rather more altered.

H-13 Longitude: -114.303°. Latitude: 34.4459°N. *Classification: Basalt/ alkali basalt.* As H5. But rather more altered.

BW-5 Longitude: -114.1725°. Latitude: 34.4407°N. *Classification: Basalt.* Dominated by v.fine granular G.mass (plag, pyroxene and high % of opaques). Also microphenocrysts of olivine and plag. Phenocrysts= plag 5% (most rectangular labradorite) some have resorbed margins.

C-1 Longitude: -114.3646°. Latitude: 34.6037°N. *Classification: Trachy andesite.* G.mass= finely crystalline plag and Cpx + opaques (granular). Phenocrysts= Opx 2%, Cpx 5% (zoned euhedral, few with inclusions), plag 10% (laths [1-3mm] to rectangular some embayed and rounded. Few glomerocrysts of Opx and plag.

C-2 Longitude: -114.3493°. Latitude: 34.6137°N. *Classification: Trachy andesite.* G.mass= dark partially devitrified, with granular opaques and plag microlaths. Phenocrysts= plag 8-10% (most have sieve textured cores filled with G.mass) some rounded, Cpx 8-10% (augite with melt and opaque inclusions) almost all are rounded, few Opx.

C-3 Longitude: -114.3417°. Latitude: 34.6327°N. *Classification: Basalt.* G.mass= finely crystalline granular Cpx +opaques and plag microlaths. Phenocrysts= ol 5% (iddingsitised, euhedral), Opx few % (complex zoning), plag 20% (laths up to 3mm), Cpx 5-10% (bimodal size distribution: <1mm, ≥4mm some with distinct cores and melt + opaque inclusions).

C-4 Longitude: -114.3433°. Latitude: 34.6304°N. *Classification: Trachy andesite.* G.mass= crystalline, plag lath dominated plus opaques and some granular Cpx, flow textured. Phenocrysts= olivine <1% (iddingsitised), Cpx few large, plag 5-10% (laths to rectangular, complex twinning and zoning, some complex overgrowths) flow orientated.

MH-1 Longitude: -114.3117°. Latitude: 34.6807°N. *Classification: Basalt.* G.mass dominated, plag microlaths and granular Cpx + opaques. Few microphenocrysts of olivine and Cpx. Phenocrysts= olivine 2% (sub-euhedral rimmed with iddingsite). Few irregular feldspar xenocrysts with ragged margins.

MH-6 Longitude: -114.1356°. Latitude: 34.4846°N. *Classification: Rhyolite.* G.mass= vitric with fine equant microphenocrysts of plag and biotite. Flow textured. Phenocrysts= plag 10% (often complex zoning), biotite <2%, minor hornblende. Some polycrystalline fldsp xenocrysts (strained extinction, ragged, sieve texture).

MH-8 Longitude: -114.1269°. Latitude: 34.4992°N. *Classification: Basaltic andesite.* G.mass= v.fine crystalline plag and Cpx plus abundant opaques. Phenocrysts= angular or slightly rounded: Cpx 5-8%, Opx <2%, few olivine (fresh).

MO-1 Longitude: -114.3107°. Latitude: 34.6833°N. *Classification: Alkali basalt.* G.mass= crystalline, dominated by granular Cpx and opaques, plus plag microlaths and interstitial. Some glomerocrysts of Cpx and Opx microphenocrysts Phenocrysts= Opx 2%, Cpx few%, olivine 5% (highly altered).

MO-2 Longitude: -114.3109°. Latitude: 34.683°N. *Classification: Trachy andesite.* G.mass= flow textured, plag microlaths plus granular Cpx and opaques. Phenocrysts= olivine 5-8% (all altered, some iddingsite).

MO-4 Longitude: -114.311°. Latitude: 34.6825°N. *Classification: Rhyolite.* G.mass= holohyaline, complex flow texture. Few crystals of sanidine, Qz and biotite.

MO-5 Longitude: -114.3117°. Latitude: 34.6821°N. *Classification: Alkali basalt.*

MO-6 Longitude: -114.3118°. Latitude: 34.682°N. *Classification: Basaltic andesite.* G.mass= as MO-2 but slightly coarser (micro plag laths to 0.5mm) Phenocrysts= olivine ≤5% (fresh to totally iddingsitised), Cpx few % (as glomerocrysts). Few polycrystalline quartz xenocrysts up to 4mm with pyroxene reaction rims and patches of melting (see figure in Chapter 2).

MO-7 Longitude: -114.3135°. Latitude: 34.6847°N. *Classification: Trachy andesite.* G.mass= finely crystalline but pervasive deep grey birefringence suggests mild potassic alteration. Phenocrysts= Cpx 5% (euhedral plus melt + oxide inclusions), Opx 2%, plag 15% (large altered laths), olivine <2% (altered and iddingsitised).

FS-1 Longitude: -114.2303°. Latitude: 34.5518°N. *Classification: Rhyolite.*

FS-2 Longitude: -114.2305°. Latitude: 34.5514°N. *Classification: Trachy andesite.*

FS-3 Longitude: -114.2312°. Latitude: 34.5508°N. *Classification: Trachy andesite.* Pervasive alteration.

FS-4 Longitude: -114.2316°. Latitude: 34.5505°N. *Classification: Alkali basalt.*

FS-5 Longitude: -114.2319°. Latitude: 34.5495°N. *Classification: Trachy andesite.*

B.3.4 Searchlight

SL-1 Longitude: -114.7517°. Latitude: 35.4883°N. *Classification: Trachyte.* Potassic alteration. Altered devitrified G.mass (with sericite + calcite). Phenocrysts= 15% (altered plag and microphenocrysts of hornblende). Large polycrystalline oligiclase and Ksp xenocrysts.

SL-3 Longitude: -114.7941°. Latitude: 35.3739°N. *Classification: Trachy andesite.* Volcanic breccia.

SL-4 Longitude: -114.7952°. Latitude: 35.3811°N. *Classification: Trachy andesite.*

SL-7 Longitude: -114.9105°. Latitude: 35.4262°N. *Classification: Trachy andesite.* Biotite and plag phyric.

SL-8 Longitude: -114.9106°. Latitude: 35.4264°N. *Classification: Trachy andesite.* Mixing textures. Some large biotite phenocrysts.

SL-9 Longitude: -114.9108°. Latitude: 35.426°N. *Classification: Trachy andesite.* G.mass= devitrified + plag micro phenocrysts. Phenocrysts= plag 25% (fresh, rectangular to equant, most are ~0.25mm; largest crystals v.irregular with corroded margins and complex zoning), hornblende 10% (altered sub-euhedral) and Cpx 5% (rounded with inclusion trails).

SL-10 Longitude: -114.9112°. Latitude: 35.4262°N. *Classification: Trachy andesite.* G.mass= devitrified + plagioclase. Phenocrysts= plag 25% (mostly equant-rectangular), Cpx 5% (irregular to rounded some with low relief inclusions [apatite?], often as glomerocrysts with Opx [plag interstitial]), and hornblende 5% (subhedral). Plag xenocrysts with sieve texture.

B.3.5 Newberry Mountains 'granites'

NB-1 Longitude: -114.6806°. Latitude: 35.1694°N. *Classification: Granodiorite.* Sphene and biotite rich, from small pod intruding main granite.

NB-2 Longitude: -114.7687°. Latitude: 35.2595°N. *Classification: Biotite granite.* Some large Ksp phenocrysts.

NB-11 Longitude: -114.683°. Latitude: 35.2248°N. *Classification: Granodiorite.* K-feldspar rich (some plag overgrowth rims), hornblende and biotite.

NB-11a Longitude: -114.683°. Latitude: 35.2246°N. *Classification: Diorite.* Hornblende rich fraction of Nb11.

NB-14 Longitude: -114.6949°. Latitude: 35.2275°N. *Classification: Granite.* Leucogranite, homogenous fine grained.

NB-15 Longitude: -114.7126°. Latitude: 35.1712°N. *Classification: Granite.* As NB14.

G-2 Longitude: -115.0614°. Latitude: 34.8542°N. *Classification: Gneiss.*

B.3.6 Newberry Mountains 'dykes'

NB-3 Longitude: -114.7676°. Latitude: 35.2604°N. *Classification: Alkali basalt.*

NB-4 Longitude: -114.6806°. Latitude: 35.2243°N. *Classification: Basalt.* Micro plag laths and v.altered mafics.

NB-5 Longitude: -114.681°. Latitude: 35.2243°N. *Classification: Basalt.*

NB-6 Longitude: -114.683°. Latitude: 35.2243°N. *Classification: Basalt.* Homogenous finely crystalline, sub-ophitic texture. Roughly 50:50 plag laths and Cpx plus granular opaques. All Cpx altered to green hornblende an /or chlorite.

NB-7 Longitude: -114.684°. Latitude: 35.2243°N. *Classification: Rhyolite.*

NB-8 Longitude: -114.6845°. Latitude: 35.2243°N. *Classification: Basaltic andesite.*

NB-9 Longitude: -114.685°. Latitude: 35.2243°N. *Classification: Trachy andesite.*

NB-10 Longitude: -114.6856°. Latitude: 35.2243°N. *Classification: Dacite.* Vitric G.mass. Plag and biotite phyric.

NB-12 Longitude: -114.6878°. Latitude: 35.2252°N. *Classification: Andesite.* Coarse crystalline, plagioclase dominated plus interstitial Cpx (altered). Overall deep grey birefringence suggests some potassic alteration.

NB-13 Longitude: -114.6922°. Latitude: 35.2261°N. *Classification: Basalt.* As NB-6 but with some relict olivine in G.mass, and some larger plag phenocrysts (laths).

B.3.7 Lake Mead region

See location map for detail: MC= McCullough Mts; M= Lake Mead south; BR= Black Range; R= River Mts.

MC-2 Longitude: -114.9922°. Latitude: 36.0081°N. *Classification: Trachyte.* Crystal rich vitrophyre (biotite and plag).

MC-3 Longitude: -114.992°. Latitude: 36.0078°N. *Classification: Trachyte.* As MC-2 but slightly altered.

M-3 Longitude: -114.635°. Latitude: 35.9995°N. *Classification: Tertiary Diorite.* Coarse crystalline. Total% of rock= Ksp 70%, hornblende and biotite 20%, sphene 4%, plus: opaques, apatite and zircon.

M-4 Longitude: -114.6344°. Latitude: 35.9982°N. *Classification: Alkali basalt.* Pervasively altered, devitrified G.mass (plag rich).

M-5 Longitude: -114.6355°. Latitude: 35.9982°N. *Classification: Rhyolite.* G.mass= fine granular feldspar dominated plus Qz and some opaques, microgranitic texture. Phenocrysts= biotite 8-10% (some zircon inclusions and apatite), amphibole 5% (green, some overgrowing biotite), feldspar 20% (complex twining and zoning, probably some Ksp component).

M-6 Longitude: -114.6372°. Latitude: 35.9982°N. *Classification: Basalt.* Pervasive alteration. Secondary green amphibole= 35% of rock.

M-7 Longitude: -114.7155°. Latitude: 36.0012°N. *Classification: Alkali basalt.* Olivine phyric (iddingsitised).

M-8 Longitude: -114.7157°. Latitude: 36.001°N. *Classification: Trachy andesite.*

M-9 Longitude: -114.7133°. Latitude: 36.0018°N. *Classification: Rhyolite.* Crystal rich vitrophyre (plag/ sanidine, plus hornblende and biotite).

M-10 Longitude: -114.7122°. Latitude: 36.0036°N. *Classification: Trachy andesite.* As M11 but with some calcite and zeolite in vesicles. Few large Cpx phenocrysts.

M-11 Longitude: -114.7178°. Latitude: 36.0005°N. *Classification: Andesite.* G.mass= finely crystalline plag dominated, plus Cpx + opaques. Phenocrysts= olivine 5% (euhedral relicts). Few large ragged plag crystals with sieve texture. Some small glomerocrysts of Opx, Cpx and plag.

BR-1 Longitude: -114.6687°. Latitude: 36.1771°N. *Classification: Trachy andesite.* G.mass= vitric with abundant micro plag laths, some alteration. Phenocrysts and micro-phenocrysts= plag 15% (complex twinning), sanidine 5% (clear and zoned), Opx and Cpx 5%, biotite 2-5%, plus opaques and some relict olivines.

BR-2 Longitude: -114.7113°. Latitude: 36.1757°N. *Classification: Basalt.* G.mass= crystalline, dominated by micro plag laths, plus granular Cpx and opaques. Phenocrysts= few relict olivines.

BR-3 Longitude: -114.729°. Latitude: 36.1748°N. *Classification: Basalt.* G.mass= 50:50 micro plag and alteration material plus opaques. Vesicular with zeolites. Potassic metasomatised. Some altered plag phenocrysts.

BR-6 Longitude: -114.4872°. Latitude: 36.2455°N. *Classification: Trachy andesite.*

BR-7 Longitude: -114.487°. Latitude: 36.2453°N. *Classification: Alkali basalt.* Pervasive alteration, messy!

R-1 Longitude: -114.8553°. Latitude: 36.0915°N. *Classification: Basaltic andesite.* G.mass= fine crystalline dominated by plag laths plus intergranular Cpx and opaques. Some altered microphenocrysts of olivine and Opx. Phenocrysts= augite 5-8%, Opx few%, plag 10% (larger laths often ragged).

R-2 Longitude: -114.855°. Latitude: 36.0914°N. *Classification: Basaltic andesite.* G.mass= dominated by altered plag laths, plus granular opaques and minor Cpx. Phenocrysts= amphibole 5-10% (large crystals with granular opaque oxide rims, possible kaersutite), Opx few%, plag 10% (intensely altered), Cpx few% (may be glomerocrystic). Used as marker horizon because of distinctive amphibole.

B.3.8 Mopah Springs

MS-1 Longitude: -114.7749°. Latitude: 34.3143°N. *Classification: Trachy andesite.* Vesicular with zeolites. G.mass= v.fine crystalline, plag laths with some granular Cpx and abundant opaques (10% of rock). Phenocrysts= plag 15-20% (large laths and rectangles up to 4mm, may form glomerocrysts), augite 5-8%.

MS-2 Longitude: -114.7766°. Latitude: 34.3161°N. *Classification: Alkali basalt.* G.mass= partially devitrified with micro plag laths and granular opaques. Phenocrysts= plag laths 20%, Cpx 10% (euhedral, some with exsolution lamellae), olivine 2% (euhedral but altered), Opx few%.

MS-3 Longitude: -114.7793°. Latitude: 34.3159°N. *Classification: Trachy andesite.* G.mass= 'merocrystalline' (50:50 glass and crystals). Phenocrysts and micro phenocrysts= plag 35% (laths, semi skeletal), Cpx 15% (subhedral, twinned).

MS-4 Longitude: -114.7793°. Latitude: 34.3134°N. *Classification: Trachy andesite.* Merocrystalline, similar mineral proportions to MS-3.

MS-5 Longitude: -114.7652°. Latitude: 34.3175°N. *Classification: Rhyolite.* G.mass= pale brown partially devitrified. Phenocrysts= sanidine and plag 20%, hornblende 5%, biotite 2%. Plus minor opaques.

MS-6 Longitude: -114.7543°. Latitude: 34.3252°N. *Classification: Rhyolite.* Merocrystalline with abundant micro plag laths (flow textured). Phenocrysts= biotite few%, plag and sanidine 45%, minor hornblende.

MS-7A Longitude: -114.744°. Latitude: 34.3261°N. *Classification: Rhyolite.* G.mass= partially devitrified. Phenocrysts= biotite and hrnbl 5-8%, sanidine and plag 20%.

MS-7B Longitude: -114.7435°. Latitude: 34.3261°N. *Classification: Rhyolite.* Fresh vitrophyre. Phenocrysts= biotite and hornblende 2-4%, feldspar 10%.

B.3.9 Sacramento Mts region

See location map for detail: S= Northern Sacramento Mts; ST= Snaggletooth

S-1 Longitude: -114.9159°. Latitude: 34.8555°N. *Classification: Alkali basalt.* Fine equigranular plag dominated. Pervasive alteration (sericite and calcite).

S-2 Longitude: -114.9165°. Latitude: 34.8542°N. *Classification: Alkali basalt.* Similar to S-1 but micro plag lath texture in groundmass.

S-3 Longitude: -114.9165°. Latitude: 34.854°N. *Classification: Trachy andesite.* G.mass= v.fine granular plag dominated but rather altered. Micro phenocrysts of amphibole appear to be secondary minerals.

S-4 Longitude: -114.9154°. Latitude: 34.8528°N. *Classification: Trachy andesite.* Crystalline equigranular, plag dominated (0.25mm, almost all are zoned and some alteration to sericite) with some opaques and secondary amphibole.

S-5A Longitude: -114.9127°. Latitude: 34.8514°N. *Classification: Dacite.* G.mass= fine granular feldspar dominated plus biotite, some calcite replacement of G.mass. Feldspar phenocrysts (rectangular or prismatic from G.mass size to ≥4mm, largest crystals heavily altered).

S-5B Longitude: -114.913°. Latitude: 34.8514°N. *Classification: Dacite.* As S-5A but rather less alteration and coarser G.mass, biotite phenocrysts= 8%, some large plag phenocrysts up to 10mm and glomerocrystic.

S-5C Longitude: -114.9125°. Latitude: 34.8514°N. *Classification: Trachy andesite.* G.mass= fine crystalline plag microlaths plus some biotite. Plag ≥80% rock, 10% as phenocrysts (often equant, zoned with distinct cores).

S-5D Longitude: -114.9131°. Latitude: 34.8514°N. *Classification: Dacite.* Plagioclase dominated similar to S-5A but pervasively altered (calcite, sericite and chlorite).

S-6 Longitude: -114.9154°. Latitude: 34.8542°N. *Classification: Dacite.* G.mass= v.fine grained crystalline feldspar dominated, minor alteration. Phenocrysts= sanidine <2%, biotite 5-8% (altered), plag 10-15% (complex zoning).

S-7 Longitude: -114.6272°. Latitude: 34.6757°N. *Classification: Basaltic andesite.*

ST-1 Longitude: -114.6382°. Latitude: 34.5914°N. *Classification: Trachyte.* (Peach Springs Tuff, see Chapter 2). Large biotite and zoned sanidine phenocrysts.

ST-2 Longitude: -114.638°. Latitude: 34.5914°N. *Classification: Andesite.* Prominent flow banding and mixing textures. Fine agate vein mineralisation.

ST-3 Longitude: -114.6382°. Latitude: 34.5923°N. *Classification: Dacite.* Crystal tuff.

B.3.10 Kingman

K-1 Longitude: -114.0913°. Latitude: 35.1712°N. *Classification: Trachy andesite.*

K-2 Longitude: -114.0916°. Latitude: 35.1712°N. *Classification: Trachy andesite.* Flow banded with mixing textures.

K-3 Longitude: -114.0985°. Latitude: 35.1698°N. *Classification: Trachy andesite.* Vesicular. G.mass= devitrified (oxide rich). Phenocrysts= plag 15%, pyroxene 10% (Cpx: sub-euhedral, Opx: rounded). Some disequilibrium textured plag phenocrysts, one large Cpx-Opx-Ksp-plag xenocryst.

K-4 Longitude: -114.0935°. Latitude: 35.1696°N. *Classification: Trachy andesite.*

B.4 Post-extensional from CRT

B.4.1 Group 3 type

BM-1 Longitude: -114.4468°. Latitude: 34.8541°N. *Classification: Basalt.* Fresh vesicular flow top.

BM-2 Longitude: -114.4265°. Latitude: 34.918°N. *Classification: Rhyolite.* Flow banded vitric with Qz and sanidine (?) phenocrysts.

MH-9 Longitude: -114.2511°. Latitude: 34.4857°N. *Classification: Basaltic andesite.* G.mass= coarse crystalline micro plag laths (0.5mm) with plag interstitial and granular Cpx + opaques. Few microphenocrysts of olivine. Phenocrysts= olivine 10% (fresh euhedral), minor Cpx. Slightly vesicular. Number of large polycrystalline Qz + feldspar xenocrysts with thin reaction rims. Some sieve textured plag phenocrysts.

MH-10 Longitude: -114.2511°. Latitude: 34.4857°N. *Classification: Basaltic andesite.* Similar to MH-9 but G.mass in patches is dominated by either plag or Cpx. Most olivine phenocrysts are euhedral but some are embayed.

BW-3 Longitude: -114.0753°. Latitude: 34.51°N. *Classification: Basaltic andesite.* Fine sub-ophitic texture, cpx + plag laths (cpx is clear, non pleochroic unlike H-5), some interstitial plag, granular opaques. Phenocrysts= plag <5% (rectangular with sieve textured cores and clear overgrowth rims), olivine <2% (some up to 1mm, iddingsite margins), few Opx.

BW-4 Longitude: -114.0755°. Latitude: 34.5105°N. *Classification: Basaltic andesite.* G.mass= granular appearance but sub-ophitic as BW-3. Patches may be dominated by Cpx or plag laths giving 'ophimottled'. Some microphenocrysts of olivine. Phenocrysts= olivine <2%, plag <5% (few laths but mostly equant with sieve textured cores [see figure in Chapter 2]).

D-1 Longitude: -114.765°. Latitude: 34.9105°N. *Classification: Andesite.*

D-2 Longitude: -114.7648°. Latitude: 34.9104°N. *Classification: Andesite.*

D-3 Longitude: -114.7649°. Latitude: 34.9106°N. *Classification: Basaltic andesite.*

G-1 Longitude: -115.0658°. Latitude: 34.882°N. *Classification: Trachy andesite.* Fresh, hornblende, pyroxene phyric with rounded Qz.

K-6 Longitude: -114.266°. Latitude: 35.4261°N. *Classification: Trachy andesite.*

K-7 Longitude: -114.2662°. Latitude: 35.4262°N. *Classification: Trachy andesite.* Plagioclase phyric, vitric G.mass.

SL-2 Longitude: -114.7957°. Latitude: 35.3721°N. *Classification: Rhyolite.* Biotite and plagioclase phyric.

SL-5 Longitude: -114.8027°. Latitude: 35.38°N. *Classification: Trachy andesite.* As SL-6 but less zeolite.

SL-6 Longitude: -114.8029°. Latitude: 35.3802°N. *Classification: Trachy andesite.* Vesicular, some zeolites. G.mass= devitrified, oxide rich. Mostly plag micro laths and opaques. Phenocrysts= plag (v.few).

SA-1 Longitude: -114.7478°. Latitude: 34.7766°N. *Classification: Rhyolite.* G.mass= vitric plus grains of Qz and feldspar. Phenocrysts= biotite 5%, Qz 5-8%, sanidine and plag 20%. (Collected by Phil Gans from Eagle Peak in the Sacramento Mts).

MS-8 Longitude: -114.7381°. Latitude: 34.3297°N. *Classification: Trachy andesite.* Dark, partially devitrified G.mass with opaques, abundant micro plag laths. Microphenocrysts of Cpx 5% (often clustered). Vesicular.

R-3A Longitude: -114.8515°. Latitude: 36.0917°N. *Classification: Rhyolite.* Devitrified, complex flow textured, abundant multi-granular Qz patches and disaggregating Qz + feldspar (lithic fragments). Phenocrysts= biotite 2%, Qz 5-10%, sanidine 5%.

R-3B Longitude: -114.8518°. Latitude: 36.0919°N. *Classification: Rhyolite.*Similar to R-3A but darker G.mass.

BR-4 Longitude: -114.7384°. Latitude: 36.1793°N. *Classification: Andesite.* G.mass= partially devitrified with micro plag laths and granular opaques. Phenocrysts= plag 2-5%. Abundant Qz xenocrysts. Pyroxene granular mostly microphenocrysts (up to 8% of rock), mostly in small clusters after total replacement of Qz xenocrysts.

BR-5 Longitude: -114.7378°. Latitude: 36.1775°N. *Classification: Trachy andesite.* G.mass= crystalline, micro plag lath dominated, plus granular Cpx and opaques. Few Cpx microphenocrysts. Some mixing textures. Phenocrysts= plag , Cpx and Opx few% (some clusters). Qz xenocrysts with reaction rims.

B.4.2 Group 1 type

BW-1 Longitude: -114.1112°. Latitude: 34.2844°N. *Classification: Alkali basalt.* Flow orientated G.mass and phenocrysts. G.mass= dominated by micro laths of plag, plus granular opaques. Few microphenocrysts of Cpx. Phenocrysts= plag 25% (1mm laths), olivine 5% (subhedral, bright red iddingsite).

BW-2 Longitude: -114.1112°. Latitude: 34.284°N. *Classification: Trachyte.* G.mass= fine crystalline dominated by plagioclase, some granular Cpx. Phenocrysts= few Cpx. Some large Ksp xenocrysts (strained, occasionally polycrystalline with Qz).

BW-6 Longitude: -114.1113°. Latitude: 34.2844°N. *Classification: Alkali basalt.* As BW-1, possibly same flow.

BW-7 Longitude: -114.1081°. Latitude: 34.2843°N. *Classification: Trachyte.* As BW-2.

K-5 Longitude: -114.1582°. Latitude: 35.7162°N. *Classification: Trachy andesite.*

M-1 Longitude: -114.6051°. Latitude: 35.8691°N. *Classification: Alkali basalt.* G.mass= plag laths and granular Cpx + opaques. Phenocrysts= olivine 5% (up to 2mm, fresh euhedral).

M-2 Longitude: -114.6399°. Latitude: 35.9215°N. *Classification: Alkali basalt.* G.mass= fine crystalline (blotchy differential alteration), plag laths plus calcite and abundant opaques (equant crystals). Some rounded Opx micro phenocrysts. Phenocrysts/ xenocrysts of kaersutite (up to 50mm) surrounded by granular opaque reaction rims. Sample also contains small lithic fragments and micro xenoliths of granular olivine ± Cpx. Some fine calcite veining, intense in places.

Miscellaneous

C.1 Distribution coefficients

The following table is a compilation of crystal/ liquid distribution coefficients for trace elements that have been used for geochemical modelling in the course of preparing this thesis. References: Henderson (1986); Cox et al (1984); Pearce and Norry (1979); Irving and Frey (1984, 1987); Irving (1978); Feigenson et al (1983); Ulmer (1988); T.Elliott *pers comm.* Additional D-values for Zr in various minerals are also presented in Chapter 6.

	OL	*OPX*	*CPX*	*GT*	*SP*	*AMPH*	*IL*
La	0.0002	0.002	0.069	0.01	0	0.27	0.01
Y	0.001	0.04	0.3	2	0.02	0.89	0.01
Nd	0.001	0.0065	0.18	0.08	0	0.5	0.01
Sm	0.0013	0.013	0.26	0.217	0	0.91	0.01
Nb	0.001	0.15	0.1	0.1	0	1.3	0.8
Zr	0.001	0.03	0.1	0.3	0	1.1	0.01
Tb	0.0015	0.02	0.3	0.7	0.007	1.4	0.01
TiO2	0.02	0.1	0.3	0.3	0	0.5	0.01
Yb	0.0015	0.049	0.28	7	0.007	0.97	0.01
Ce	0.0005	0.003	0.098	0.021	0	0.34	0.01
Rb	0.0001	0.001	0.05	0.01	0	0.25	0.01
Ba	0.0001	0.001	0.05	0.01	0	0.31	0.01
Th	0.001	0.01	0.01	0.02	0		
K2O	0.007	0.015	0.03	0	0	0.6	0
Ta	0.001	0.15	0.07	0.1	0	1.3	0.8
Sr	0.001	0.01	0.1	0.01	0	0.57	0.01
P2O5	0.001	0.008	0.14	0.09	0		
Hf	0.001	0.04	0.31	0.3	0		
Lu	0.001	0.11	0.8	10	0		
Sc	0.17	1.1	2.7	4	0		

C.2 Primitive mantle normalising values

Where data has been expressed in relation to the composition of the 'primitive mantle', the normalising values used were taken from Sun and McDonough (1989). These values are reproduced below.

Pb	0.185	*Ta*	0.041	P_2O_5	0.021	*Y*	4.55
Rb	0.635	*Nb*	0.713	*Nd*	1.354	*Yb*	0.493
Ba	6.989	*La*	0.687	*Hf*	0.309	*Lu*	0.074
Th	0.085	*Ce*	1.775	*Zr*	11.20	*Sc*	17.1
K_2O	0.023	*Sr*	21.10	TiO_2	0.217		

C.3 Errors used in PER modelling (Chapter 6)

SiO2	0.16	*Fe2O3*	0.07	*CaO*	0.08	*P2O5*	0.01
TiO2	0.01	*MnO*	0.01	*Na2O*	0.07	ω	ppm
Al2O3	0.12	*MgO*	0.01	*K2O*	0.11	*Zr*	4

Errors are 1σ values based on XRF analysis, data presented as wt% for oxides and as ppm for Zr (the standard ω element). These errors were used to calculate the standard propogated errors that arise through the use of complex axes coefficients in the Pearce Element Ratio (PER) modelling of Chapter 6.

C.4 Source compositions calculated in Chapter 4

In Chapter 4, three distinct mantle source compositions were calculated to model the geochemistry of basaltic volcanism in the Colorado River Trough. Source 1 is predicted to be asthenospheric, sources 2 and 3 are assumed to be in the sub-continental lithospheric mantle and be responsible for the bulk of the magmatism. Source 3 is modelled as a garnet-bearing lherzolite while source 2 is trace element depleted and may contain spinel. The following table presents the calculated source data (mean and 1σ errors) used to construct figure 11 in Chapter 4.

	Group 1	1σ	Group 2	1σ	Group 3	1σ
La	2.205	——	0.84	——	2.205	——
Y	3.413	0.482	3.231	0.095	2.939	0.666
Nd	2.711	0.704	1.505	0.224	2.541	0.289
Sm	0.532	0.067	0.396	0.009	0.524	0.069
Nb	5.182	1.871	0.522	0.074	1.448	0.366
Zr	18.902	4.421	9.435	0.761	13.620	2.981
Tb	0.090	0.015	0.074	0.005	0.074	0.017
TiO2	0.271	0.049	0.150	0.003	0.145	0.033
Yb	0.474	0.022	0.277	0.017	0.418	0.084
Ce	5.172	0.864	2.047	0.035	4.613	0.215
Rb	1.753	0.544	0.850	0.208	2.397	1.688
Ba	33.246	10.095	12.478	1.768	51.815	33.254
Th	0.340	0.139	0.073	0.011	0.318	0.095
K2O	0.124	0.027	0.030	0.003	0.123	0.048
Ta	0.284	0.125	0.026	0.001	0.084	0.014
Sr	46.301	6.728	19.326	3.598	40.300	8.354
P2O5	0.043	0.009	0.018	0.001	0.024	0.006
Hf	0.478	0.144	0.324	0.017	0.363	0.062
Lu	0.101	0.014	0.087	0.007	0.095	0.009
Sc	13.236	5.049	28.039	0.453	14.848	2.381

La contents are fixed, see Chapter 4 for rationale. Data presented as ppm for trace elements and as wt% values for oxides.

C.5 Lead isochron calculation

The secondary lead isochron (time lapsed since stabilisation of the mantle source) displayed in Chapter 4 is calculated by the method presented in Faure (1986). The age is determined from the slope of the sample array on a diagram of $^{207}Pb/^{204}Pb$ versus $^{206}Pb/^{204}Pb$ using the following relationship:

$$Age = -3.0135 + 89.802m - 584.48m^2 + 1506.2m^3$$

Where m is the slope of the sample array, and the age is calculated in Ga. For samples collected in the Colorado River Trough region the slope, m, is calculated to be 0.096721,

which produces an age of approximately 1.57Ga. However, because the CRT sample array is slightly scattered on the $^{207}Pb/^{204}Pb$ versus $^{206}Pb/^{204}Pb$ diagram, the m value has a least squares fit of only 0.894 (eg. roughly 11% error). Such an error in m indicates that the actual age may range between 1.35 and 1.75Ga.

This age range is consistent with the widespread lithospheric heating event suggested by Dudas et al (1987), although the maximum age is still less than that of the 2.0-2.3Ga Nd model age calculated from Proterozoic gneiss outcrops in the region (Bennet and DePaolo 1987, see Chapter 2). An inference from this may be that the sub-continental lithospheric mantle in the CRT was reheated following its initial stabilisation, but that the crust was generally not affected by this event.

C.6 Sr isotope age correction

Although the Rb/Sr ratios in most of the CRT samples are rather low (eg. typically <0.05), and the time available for additional Rb decay since eruption is short (from the Miocene), samples have been back corrected to give initial Sr isotope ratios $(^{87}Sr/^{86}Sr)_i$. It is these values that are plotted on all of the Sr isotope ratio diagrams throughout the thesis. The correction is most valuable when considering the high silica samples, and particularly the contaminant material in mixing processes, where Rb/Sr ratios are higher (eg. sample SA-1 has an Rb/Sr ratio of 1.68). Pre/syn-extensional and granite samples were time corrected to 20Ma, and all of the post-extensional samples were corrected to 10Ma using the equation below:

$$(^{87}Sr/^{86}Sr)_i = (^{87}Sr/^{86}Sr) - (^{87}Rb/^{86}Sr)\ (e^{\lambda t}-1)$$

where t is time in years (eg. 20Ma= $20*10^6$ a), and λ is the decay constant for ^{87}Rb, which is $1.42*10^{-11}$ a^{-1}. The value of $^{87}Rb/^{86}Sr$ is:

$$^{87}Rb/^{86}Sr = Rb/Sr\ (2.6939 + 0.2832*^{87}Sr/^{86}Sr).$$

Analytical Techniques

D.1 Sample preparation

Samples were initially split by hand or using a variety of hardened steel and pneumatic jaw crushers. The resulting pieces were reduced to <5mm chips and then a 'coned and quartered' 100g fraction was ground to <200 mesh size in an agate tema. At each crushing stage chips containing altered material, weathering surfaces, amygdales or any obvious secondary mineralisation were rejected to eliminate possible sources of contamination.

D.2 X-Ray Fluorescence (XRF) analysis

D.2.1 Sample preparation

The rock powders were dried overnight in an oven at 110°C to eliminate moisture. For trace element analyses approximately 8g of dried sample were mixed with a 'Moviol' binder and then formed into 3cm diameter pellets using a hydraulic press. These pellets were again dried for at least 24 hours before analysis. For major element analyses 0.4g of dried sample were carefully mixed in a 1:6 ratio with the fluxing agent 'Spectroflux 100B' (lithium tetraborate-metaborate). These mixtures were then fused for 12 minutes at 1100°C in a muffle furnace using platinum-gold alloy crucibles. The melt was thoroughly mixed during this time (using a special technique developed at the OU) and then poured onto a heated brass mould to form a 3cm diameter glass disc. The discs were allowed to cool slowly.

Loss on ignition (LOI) data were calculated by igniting 1-2g of dried sample in pre-ignited silica crucibles at 1000°C for 20 minutes, and then measuring the percentage mass loss.

D.2.2 Major element analysis

Glass discs were analysed for major elements at the Open University using energy-dispersive (ED-XRF) techniques on a Link Systems Meca 10-44 ED-XRF spectrometer.

Instrument drift was corrected using the international standard MONAGV-1. A number of other international standards, covering a wide range of compositions, were used for calibration purposes (eg. BHVO-1, GSP-1, QAB-1 and G-2). Details of the Open University analytical techniques are to be found in Potts et al (1984).

D.2.3 Trace element analysis

Pressed powder pellets were analysed for trace elements at Nottingham University on a Phillips PW-1400 wavelength dispersive (WD-XRF) spectrometer. A rhodium X-ray tube was used and the operating conditions were varied to ensure optimum analysis over the range of elements listed in Appendix A. Again, various international standards were employed for calibration and drift correction. Details of the Nottingham University analytical techniques are presented in Harvey and Atkins (1982). Analytical precision is better than 2% at the 100ppm level and the accuracy is thought to be approximately double this value. See table 1 (section D3) for detection limits.

D.3 Instrumental Neutron Activation Analysis

REE, Hf, Ta, Th, U, Co, Cr, Cs and Sc were determined using Instrumental Neutron Activation Analysis (INAA). Full details of the analytical techniques are described in Potts et al (1981; 1985).

Dried rock powder aliquots (0.3g) were sealed inside polyethylene capsules and then stacked into a polyethylene casing tube for irradiation. Eleven sample capsules were placed in each tube along with two capsules containing standard powders. A lacquered disc of pure iron foil was placed between each capsule to monitor the neutron flux along the tube. The standard powders were the calibration standard AC-2 (Ailsa Craig microgranite) and the internal standard WS (Whin Sill dolerite), which was analysed as an 'unknown' sample.

Samples were irradiated at the Imperial College Reactor Centre near Ascot in a thermal neutron flux of $5*10^{12}$n cm^{-2} sec^{-1} for 24-30 hours. After 'cooling' to allow short lived

radio-nucleides to decay, samples were counted at the Open University. Two detectors were used in tandem: a coaxial Ge(Li) detector and a planar low-energy photon spectrometer (LEPS). Two sets of counting were performed on each sample over a period of approximately one month. The initial stage ('short counts') lasted for 800sec and this was followed by a second stage, two to four weeks after irradiation, lasting for between 6 and 10 hours ('long counts'). This second stage was employed to increase precision on the longer lived isotopes.

	XRF	INAA		XRF	INAA
Ba	24	60	Rb	3	10
Ce	30	1.5	Sc	8	0.03
Co	6	0.14	Sm		0.1
Cr	10	1.5	Sr	3	
Cs		0.17	Ta		0.07
Eu		0.05	Tb		0.09
Hf		0.17	Th	9	0.22
La	15	0.5	W		30
Lu		0.1	U		0.5
Nb	6		Y	3	
Nd	36	4.6	Yb		0.14
Ni	6		Zn	9	
P	60		Zr	6	
Pb	6				

Table 1. Comparison of six sigma detection limits for trace elements analysed in this study using XRF and INAA techniques. Values given as ppm.

D.4 Radiogenic isotope analysis

All the analytical procedures described below were undertaken in the clean chemistry labs in the Earth Science Department at the Open University. Sample beakers were not normally opened outside of laminar flow fume cupboards, and only then for the minimum amount of time. All reagents used were either two-stage quartz distilled or teflon distilled (TD). Unless otherwise stated, solutions were made up with Milli-Q reverse osmosis purified water (RO water).

D.4.1 Beaker cleaning

All beakers were rigourously cleaned for at least 24 hours in HNO_3, then rinsed with RO water, allowed to stand in RO water for a further day, and rinsed again before use. For the Pb chemistry dedicated beakers were used and an additional cleaning procedure was observed: beakers were pre-cleaned with heated 6M HCl and rinsed with RO water before the HNO_3 stage; just prior to use, beakers were removed from the RO water and sealed with 2ml TD HNO_3 on a hot plate for 1 hour before finally rinsing again with RO and then TD water.

D.4.2 Strontium chemistry

Approximately 150mg aliquots of rock powder were weighed into clean teflon beakers of the Sevalex™ type with screw top lids. Samples were wetted with a few drops of 15M TD HNO_3 and then allowed to stand cold overnight with ≤4ml of 40% TD HF.

The HF/rock solutions were then evaporated slowly under heating lamps in a compressed air supply until they attained a colloidal consistency. At this point 2-3ml of 15M TD HNO_3 were added. This solution was evaporated to dryness before adding a further 2ml of 15M TD HNO_3. Following further evaporation of the solution (this time to insipient dryness), ~6ml of TD 6M HCl were added. With the beaker lids tightly screwed on, the HCl/rock solutions were then pressure cooked under the heat lamps to ensure total dissolution of the sample. This was normally achieved after about 30min of pressure cooking, although on a few samples it became necessary to repeat the process a number of times. Once total dissolution had been achieved the HCl/rock solutions could again be evaporated to dryness.

Samples were then dissolved in ~2ml of 2.5M HCl, transferred to acid cleaned and rinsed centrifuge tubes, and centrifuged for around 5min to remove any residue. 1ml of the centrifuged solutions were carefully loaded onto 10ml columns of preconditioned ion-exchange resin for Sr separation. Samples were allowed to sink into the top of the resin beds and were then washed with two 1ml aliquots of 2.5M HCl, and allowed to settle

again. 48ml of 2.5M HCl was eluted through each column to remove the Rb fraction of the samples. The Sr fraction was subsequently collected in 10ml of 2.5M HCl, evaporated to dryness and stored for later analysis.

D.4.3 Lead chemistry

Approximately 130mg aliquots of sample powder were weighed into clean Sevalex beakers, to which 1ml twice teflon distilled (2*TD) 16M HNO_3 and then 3ml 2*TD HF were added. Beakers were sealed and left to stand cold overnight. The solutions were then evaporated as for the Sr procedure before adding 2ml 2*TD 16M HNO_3 and again evaporating to dryness. 2ml of 2*TD 6M HCl were then added and the samples 'pressure cooked' on a hot plate. If necessary this stage and the previous HNO_3 stage were repeated to ensure complete sample dissolution. The HCl/rock solutions were evaporated to dryness and then 1ml of 1M HBr was added. These solutions were left to stand overnight.

To separate the Pb fraction, micro ion exchange columns were made from 1ml pipette tips and 3 drops of resin. These columns were twice cleaned with 6M HCl and TD water and then preconditioned with 0.5 column volumes (cv) of 1M HBr. The sample solutions were carefully added to the columns ensuring that no residue was incorporated. After allowing the solutions to elute through the columns, 0.75cv of 1M HBr were added and again allowed to elute through . The Pb fraction could then be collected with 2ml 2*TD 6M HCl; a few drops of 2*TD 6M HNO_3 were added to this to remove the bromine, and then the solutions were evaporated to dryness. At this point a few drops of HBr were added to the samples and then the column washing, conditioning and elution procedures were repeated. In this second ion exchange stage the Pb fractions were collected with 2.5ml 2*TD 6M HCl and, in addition to the HNO_3, 1µl of phosphoric acid (H_3PO_4) was added to each solution before final evaporation. Because the H_3PO_4 resists evaporation, the Pb should become concentrated in this drop of acid. Samples were then stored for later analysis.

D.4.4 Mass spectrometry

All samples were analysed on a Finnigan MAT261 multi-collector mass spectrometer

running software developed by D.W Wright and P.W.C van Calsteren at the Open University.

For Sr isotope analysis samples were loaded onto outgassed single Ta filaments with 1 drop of H_3PO_4, after dissolving the samples in a small drop of TD water. For Pb analysis, samples (in their drops of H_3PO_4) were loaded onto single Re filaments. These filaments having been preconditioned with a drop of mixed silica gel and H_3PO_4 to help secure the Pb. The actual detail of these loading procedures was adjusted as necessary to optimise results.

Total procedure blanks for Pb and Sr were analysed on a Vacuums Generators Isomass 54E solid source mass spectrometer. Throughout the course of this study the blanks were below 3.8ng for Sr and 1ng for Pb. While these values are obviously not fantastic they were deemed to be sufficiently low considering the high Sr and Pb concentrations in most of the analysed samples.

Raw Sr isotope ratios were corrected for mass fractionation by assuming that $^{86}Sr/^{88}Sr= 0.1194$. Repeat analyses of the Sr standard NBS 987 gave a mean of $^{87}Sr/^{86}Sr= 0.710246$ and 1σ error of 0.000017.

Samples for Pb analysis were consistently run at 1100°C and then corrected for two types of error. The first of these errors is induced by the small size of the ^{204}Pb peak relative to the ^{206}Pb, ^{207}Pb and ^{208}Pb peaks. If the beam intensity is low then the error increases dramatically, producing even greater errors on diagrams where the heavier isotopes are divided by ^{204}Pb. Thus samples which ran with low beam intensities ($\leq$1pico amp) were rejected from this study.

The second correction is for mass fractionation. This can be approximated by the linear equation: $R= Rm (1+ \varepsilon\delta m)$. Where R is the real value of, for instance, $^{206}Pb/^{204}Pb$, Rm is the measured value, ε is a mass discrimination coefficient per mass unit, and δm is the mass difference between the two isotopes (eg. 206-204= 2). To correct for fractionation at least two Pb standards (NBS 981) were included for analysis on every magazine of 13 samples.

According to a number of isotope labs (including the ANU) the 'real' isotope ratios for NBS 981 are $^{206}Pb/^{204}Pb$= 16.937, $^{207}Pb/^{204}Pb$= 15.491 and $^{208}Pb/^{204}Pb$= 36.7.

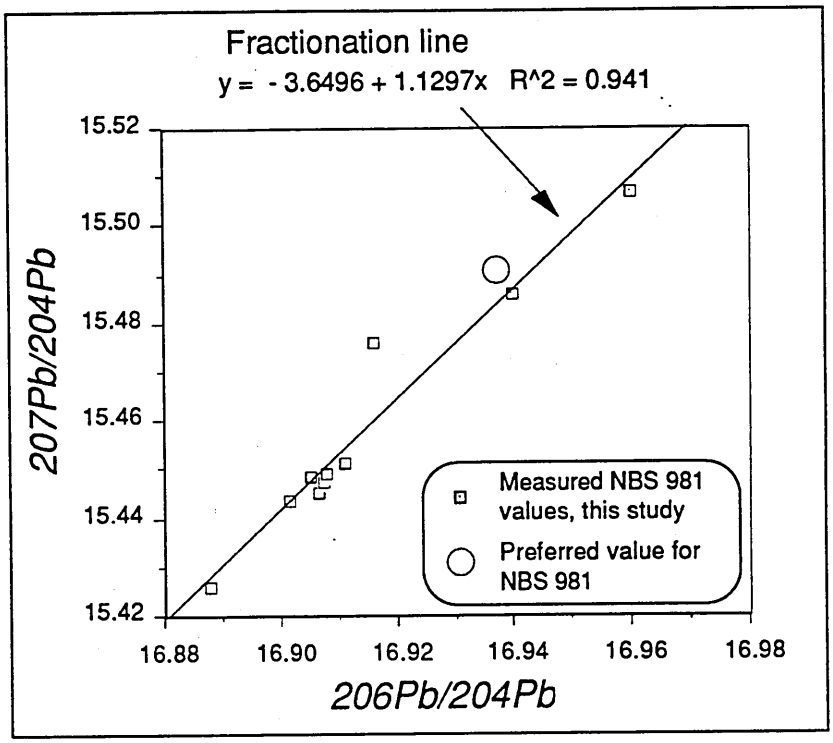

Table 2. Measured NBS 981 values from this study and the calculated fractionation line for $^{207}Pb/^{204}Pb$ versus $^{206}Pb/^{204}Pb$. Samples were corrected to the preferred values for NBS 981 using the procedure below.

Thus, three solutions for ε could be calculated for each NBS 981 run based on these preferred 'real' ratios for the standard. From these values average correction factors (equivalent to the 1 + εδm term in the equation described above) were calculated, and the measured isotope ratios adjusted accordingly. The average correction factors calculated in this study were as follows:

$$^{206}Pb/^{204}Pb = Rm * 1.00180$$

$$^{207}Pb/^{204}Pb = Rm * 1.00282$$

$$^{208}Pb/^{204}Pb = Rm * 1.00393$$

Further details of the mass spectrometry techniques used to analyse for Pb isotopes can be found in Hamelin et al (1985).

Published Abstracts

E.1 Abstract to Chapter 6

Bradshaw (1992): Contributions to Mineralogy and Petrology

Pearce Element Ratios (PER's, of Pearce 1968) express geochemical data in a form where variations in absolute compositions of an igneous suite can be evaluated. Generally the denominator value in the ratio is taken as a major element abundance, but it is argued here that Zr provides a more suitable choice. Zr remains incompatible in magmatic systems up to $\approx$ 68 wt% SiO_2 because zircon fractionation can be suppressed by high melt temperatures and increased volatile contents. The use of Zr thus permits PER modelling to be extended to much higher levels of silica than previously investigated. However, such systems are more complex than those just involving simple basaltic magmas. Besides fractionation, the processes of magma mixing, combined assimilation and fractional crystallisation, and the initial degree of partial melting in the mantle source must also be considered.

To distinguish and evaluate these processes a set of example suites are investigated from a complex syn-extensional calc-alkaline province in the western USA. Samples within most individual suites can be modelled by fractionation, however a significant trend orthogonal to the main fractionation vector is also apparent, and open system processes are inferred. Successful modelling is achieved on an inter-suite basis using diagrams with axis functions of (4[Ca + Na] + 0.5[Fe + Mg])/ Zr vs. (Si + Al)/ Zr. Potential open system evolution paths between mafic end-members and crustal contaminants are also displayed and evaluated on these same diagrams. The encouraging results suggest that such PER diagrams may be employed as a versatile tool for investigating the systematics of related igneous suites over a wide area.

E.2 Volcanic Studies Group Abstract, Cardiff

Bradshaw and Hawkesworth (1991): The nature of crustal extension inferred from the geochemistry of coeval volcanism: an example from the western USA.

Geochemistry can provide a valuable tool in assessing the relative importance of brittle and ductile stretching regimes *within* extending crust. Whole-crustal models may then be developed, which are not limited by surface observations of structure.

A Miocene extensional corridor, along the Colorado River (34-36°N) is taken as an example. Axial volcanism is dominated by a basaltic suite that has reached the surface without modification from 8kb (based on normative modelling). Higher silica (56-70wt%) volcanics are prevalent to either side of this axis. Their major and trace element variations are consistent with hybrid magmas developed by mixing between basaltic and crustal endmember melts. Cretaceous granodiorite bodies in the middle crust are an ideal 'crustal' source, but mixing models indicate upwards of 35wt% of this material in the modal hybrid magma; a significant volume even if generated by melting over a large area. Clearly, in a tensional regime, ductile stretching processes will be favoured here.

Only along the central axis does major faulting provide adequate magma-pathways to bypass the ductile-hybridisation zone. East of the axis, hybrid magmas fractionate in the upper crust (at ≈2kb). However, no high level fractionation occurs along the axis or to the west, suggesting highly unstable conditions in the upper crust, that prevent magma chamber development.

Thus, major and trace element characteristics of syn-extensional volcanism support ductile stretching at depth, but it can be inferred from process modelling that brittle extension in the upper crust is heterogenous, and asymmetrical about the centre of the corridor. A two-layer stretching model (cf Gans 1987) is therefore preferred to the traditional McKenzie or Wernicke models.

E.3 EUG VI Abstract, Strasbourg

Bradshaw and Hawkesworth (1991a): Terra Abstracts Vol.3, pp 49-50.

Geochemistry of Miocene volcanics coeval to high extension (in a narrow corridor along the Colorado River: 34-36°N) reveals a progression to shallower melting levels in the mantle with time, consistent with mantle processes driving the extension.

Volcanism is dominantly basaltic to trachy-andesitic, accompanied by small volumes of crustal melts. These define a calc-alkaline trend with enriched trace element patterns similar to arc-like shoshonites (high LILE/HFSE, LREE/HREE, and [La/Nb]mn >1, but HFSE at ~25 times primitive mantle). Combined with 87Sr/86Sr ≥ 0.7080 and Pb isotopes moderately above the Northern Hemisphere Reference Line (a Proterozoic source age is calculated) this suggests melting of LIL element enriched subcontinental lithospheric mantle (SCLM) and thermal boundary layer material. Magmas are consistent with a fertile garnet - phlogopite lherzolite source and an increasing degree of melting with time. The latest tholeiites are comparatively trace element depleted and 87Sr/86Sr decreases to 0.7071, and then to 0.7043, as the enriched component becomes exhausted. In the region of highest extension, slightly alkaline (~1% Ne norm) basalts are associated with these tholeiites. Trace element depletion, flattening of REE patterns and increased HREE contents reflect a change in melting depth into the spinel lherzolite field. It is proposed that the previous source zone may have become physically removed into the convecting asthenosphere; thus higher, less enriched, levels of SCLM are exposed to melting.

Around 5Ma a new type of alkali basalt magma appeared in isolated flows along the main extensional axis. The trace element signature is of an ocean island basalt type (Zr/Ba > 0.4, [La/Nb]mn <1) and Pb isotope ratios are consistent with an asthenospheric, E-MORB, source; their chemistry is broadly comparable to incipient ridge volcanism in the North Fiji Basin. Clearly this occurrence, following the high degree of melting in the lithospheric mantle, suggests they would have represented the precursors to typical back-arc spreading magmatism, had extension continued after 10Ma.